

Syracuse University

SURFACE

Dissertations - ALL

SURFACE

December 2016

High-energy Neutron Backgrounds for Underground Dark Matter Experiments

Yu Chen

Syracuse University

Follow this and additional works at: <https://surface.syr.edu/etd>



Part of the [Physical Sciences and Mathematics Commons](#)

Recommended Citation

Chen, Yu, "High-energy Neutron Backgrounds for Underground Dark Matter Experiments" (2016).

Dissertations - ALL. 569.

<https://surface.syr.edu/etd/569>

This Dissertation is brought to you for free and open access by the SURFACE at SURFACE. It has been accepted for inclusion in Dissertations - ALL by an authorized administrator of SURFACE. For more information, please contact surface@syr.edu.

ABSTRACT

Direct dark matter detection experiments usually have excellent capability to distinguish nuclear recoils, expected interactions with Weakly Interacting Massive Particle (WIMP) dark matter, and electronic recoils, so that they can efficiently reject background events such as gamma-rays and charged particles. However, both WIMPs and neutrons can induce nuclear recoils. Neutrons are then the most crucial background for direct dark matter detection. It is important to understand and account for all sources of neutron backgrounds when claiming a discovery of dark matter detection or reporting limits on the WIMP-nucleon cross section. One type of neutron background that is not well understood is the cosmogenic neutrons from muons interacting with the underground cavern rock and materials surrounding a dark matter detector.

The Neutron Multiplicity Meter (NMM) is a water Cherenkov detector capable of measuring the cosmogenic neutron flux at the Soudan Underground Laboratory, which has an overburden of 2090 meters water equivalent. The NMM consists of two 2.2-tonne gadolinium-doped water tanks situated atop a 20-tonne lead target. It detects a high-energy ($>\sim 50\text{ MeV}$) neutron via moderation and capture of the multiple secondary neutrons released when the former interacts in the lead target. The multiplicity of secondary neutrons for the high-energy neutron provides a benchmark for comparison to the current Monte Carlo predictions. Combining with the Monte Carlo simulation, the muon-induced high-energy neutron flux above 50 MeV is measured to be $(1.3 \pm 0.2) \times 10^{-9} \text{ cm}^{-2}\text{s}^{-1}$, in reasonable agreement with the model prediction. The measured multiplicity spectrum agrees well with that of Monte Carlo simulation for multiplicity below 10, but shows an excess of approximately a factor of three over Monte Carlo prediction for multiplicities $\sim 10 - 20$.

In an effort to reduce neutron backgrounds for the dark matter experiment SuperCDMS SNO-LAB, an active neutron veto was developed. It is estimated that the current design of the neutron

veto with a 40 cm thick layer of boron-doped liquid scintillator can achieve a $> 90\%$ efficiency for tagging the single-scatter neutrons. In addition, a one-quarter scale prototype detector for neutron veto has been built and tested.

HIGH-ENERGY NEUTRON BACKGROUNDS
FOR UNDERGROUND
DARK MATTER EXPERIMENTS

YU CHEN

B.S., BEIJING INSTITUTE OF TECHNOLOGY, BEIJING, CHINA (2006)

M.S., BEIJING NORMAL UNIVERSITY, BEIJING, CHINA (2009)

DISSERTATION

SUBMITTED IN PARTIAL FULFILLMENT
OF THE REQUIREMENTS FOR THE DEGREE OF
DOCTOR OF PHILOSOPHY IN PHYSICS

SYRACUSE UNIVERSITY

DECEMBER 2016

©Copyright by Yu Chen 2016

All Rights Reserved

To my Mother, Father, and Wife.

Acknowledgements

First and foremost, my deepest gratitude goes to my advisor Richard Schnee for his mentoring, support, and encouragement. He not only taught me knowledge and skills of particle physics, but also guided me towards the career of a physicist. Without his tireless help and unwavering support I would not have completed my graduate study.

It was a great pleasure to work with the former Dark Matter Detection group at Syracuse University. I would especially like to thank Ray Bunker for his great advising on data analysis and on many other aspects. His experience and insight have always been enlightening and helpful. Thanks to Marek Kos for teaching me ROOT and Geant4, and helping me set up my very first detector simulation. Thanks to Joseph Kiveni for sharing his experience on data analysis. Particular thanks to Boqian Wang for the great help on C++ and all the interesting discussions on physics and many other topics. Without his brilliance I would have been much more lonely in my journey of pursuing a Ph.D. Thanks to Michael Bowles for the pleasant experience of working with him.

I would like to thank the SuperCDMS collaboration and the Neutron Multiplicity Meter collaboration for the opportunity of witnessing and working in a more widely collaborative style. I especially appreciate the opportunity to work with and receive guidance from Dan Bauer, Rob Calkins, Jodi Cooley, Prisca Cushman, Mike Kelsey, Ben Loer, Amy Roberts, Joel Sander, Silvia Scorza, Melinda Sweany, and Anthony Villano.

Finally, I owe my family a debt of gratitude for their unconditional love and support. I would like to gratefully thank my parents for their encouragement and patience on my every step along the way. And a great big thank you to my wife Yaxin Liu. Her love is my biggest comfort and strongest motivation.

Syracuse, New York

December, 2016

Contents

List of Figures	x
List of Tables	xvii
1 Dark Matter	1
1.1 The Standard Cosmology and the Dark Matter Problem	1
1.2 Weakly Interacting Massive Particles	10
1.3 Direct Dark Matter Detection	12
1.3.1 Spin-independent and Spin-dependent Cross Sections	12
1.3.2 The WIMP Recoil Energy Spectrum	14
1.3.3 Direct Detection Technologies	16
2 Neutron Backgrounds	18
2.1 Radiogenic Neutrons	19
2.2 Cosmogenic Neutrons	21
3 The Neutron Multiplicity Meter at the Soudan Underground Laboratory	26
3.1 Motivation	26
3.2 Detection Technique	28
3.3 Detector Description	29
3.3.1 Main Components	29

3.3.2	Trigger, Electronics, and DAQ	31
3.4	Data and Reduction	32
3.4.1	Types of Events	32
3.4.2	Useful Data Runs	34
4	Monte Carlo Study of the Neutron Multiplicity Meter	36
4.1	Detector Responses and Energy Scale	37
4.1.1	Modeling Gadolinium Neutron Capture Gamma Emission	38
4.1.2	Recalibration of Energy Scale Factors	42
4.1.3	Recalibration of Smearing Parameters	46
4.2	A Comprehensive Simulation of Cosmic Muons and Muon-induced Neutrons . . .	57
4.2.1	Simulation Setup	57
4.2.2	Data Processing	58
4.2.3	Monte Carlo Truth Analysis	61
4.2.4	Muon Rejection Cut Study	70
4.2.5	Multiplicity Spectrum	76
4.2.6	Neutron Flux Reconstruction	79
5	Fast Neutron Search Analysis for the Neutron Multiplicity Meter Experiment	86
5.1	Pulse Height Likelihood Analysis	87
5.1.1	Pulse Height Likelihood Cut	88
5.1.2	Pulse Height Log-Likelihood Ratio (LLR) Fit	92
5.1.3	Component Modeling for the LLR Fit	94
5.2	Data Quality Cuts	99
5.2.1	Muon Pulse and Afterpulsing with Mis-coincidence	99
5.2.2	Removing Noise Pulses: Integral-Amplitude Ratio Cut	101
5.3	Results of Log-Likelihood-Ratio (LLR) Fit	113
5.4	Benchmark of High-energy Neutron Multiplicity Spectrum	134

5.5	Measurement of the High-energy Neutron Flux at the Soudan Underground Laboratory	144
6	Active Neutron Veto for SuperCDMS Experiment at SNOLAB	148
6.1	Passive Shielding for SuperCDMS SNOLAB	148
6.2	Active Neutron Veto	151
6.2.1	Design	151
6.2.2	Monte Carlo Evaluation	153
6.3	Prototyping of the Neutron Veto	157
6.3.1	The Quarter-Scale Prototype	157
6.3.2	Monte Carlo Model	158
6.3.3	Demonstration Runs	164
	References	167
	Vita	177

List of Figures

1.1	Constraint on the baryon density from Big Bang Nucleosynthesis.	5
1.2	Rotation curves of galaxy M31 and galaxy M33.	7
1.3	A slice through the Sloan Digital Sky Survey 3-dimensional map of the distribution of galaxies with the Earth at the center.	8
1.4	Power spectrum, i.e. the variance $\Delta^2 \equiv k^3 P(k)/2\pi^2$ of the Fourier transform of the galaxy distribution as a function of scale wave number k	9
1.5	Comoving number density of WIMP dark matter in the early Universe.	10
1.6	Expected spin-independent integrated event rates for a 100 GeV WIMP with cross section $\sigma_{SI} = 10^{-44} \text{ cm}^2$	15
2.1	The energy spectrum for neutrons produced with (α, n) reactions in the cavern rock compared to those induced by muon interactions in the rock with and without shielding.	22
2.2	The total muon flux measured for the various underground laboratories.	23
2.3	The differential energy spectrum for muon-induced neutrons at the various underground laboratories.	24
3.1	The profile drawing of the Neutron Multiplicity Meter (NMM).	30

4.1	The previously tuned detector response of ^{252}Cf neutron calibration in Monte Carlo with Geant4.9.4.p04 and the Monte Carlo detector response based on the same parameters with Geant4.9.5.p01.	39
4.2	The comparison of individual gamma emission spectra of gadolinium neutron captures from Geant4 simulations and measurements.	41
4.3	Fit of muon pulse height spectrum in MC with the measured muon pulse height spectrum from low-gain data set for tuning the low-gain energy scale factor in MC offline processor.	44
4.4	Fit of muon pulse height spectrum in MC with the measured muon pulse height spectrum from high-gain data set for tuning the high-gain energy scale factor in MC offline processor.	45
4.5	Fit of the PMT asymmetry distribution from ^{252}Cf neutron simulation with that from ^{252}Cf calibration run during the time of low PMT gain for the south tank to tune the East-West Adjustment on PMT energy factors.	49
4.6	Fit of the PMT asymmetry distribution from ^{252}Cf neutron simulation with that from ^{252}Cf calibration run during the time of low PMT gain for the north tank to tune the East-West Adjustment on PMT energy factors.	50
4.7	Fit of the PMT asymmetry distribution from ^{252}Cf neutron simulation with that from ^{252}Cf calibration run during the time of high PMT gain for the south tank to tune the East-West Adjustment on PMT energy factors.	51
4.8	Fit of the PMT asymmetry distribution from ^{252}Cf neutron simulation with that from ^{252}Cf calibration run during the time of high PMT gain for the north tank to tune the East-West Adjustment on PMT energy factors.	52
4.9	Fit of the PMT asymmetry distribution from ^{252}Cf neutron simulation with that from ^{252}Cf calibration run during the time of low PMT gain for tuning the smearing parameter s_1	53

4.10	Fit of the PMT asymmetry distribution from ^{252}Cf neutron simulation with that from ^{252}Cf calibration run during the time of high PMT gain for tuning the smearing parameter s_1	54
4.11	The comparison of ^{252}Cf neutron pulse height spectra from simulations with tuned PMT energy scale and smearing parameters in this work and the pulse height spectra measured in ^{252}Cf neutron data.	55
4.12	Primary muons in the comprehensive simulation. On the top is the energy spectrum of the primary muons used in this simulation.	59
4.13	The difference in time between a pulse and the MC truth “event” taking place right before the pulse time.	62
4.14	Pulse multiplicity spectra of the events in different types based on MC truth.	65
4.15	Pulse spectra of the maximum pulse in each event for different event types.	67
4.16	Pulse time distributions of neutron capture pulses and muon pulses in different types of events.	69
4.17	Efficiencies of muon cut for neutron capture events with low PMT gain as a function of the cut pulse height.	72
4.18	Efficiencies of muon cut for neutron capture events with high PMT gain as a function of the cut pulse height.	73
4.19	Muon pulse spectrum from the events of muons accompanied by neutron captures.	75
4.20	Multiplicity distributions of the events selected for the fast neutron search in the comprehensive muon simulation.	78
4.21	Muon-induced neutron flux through three surfaces in the comprehensive muon simulation.	81
4.22	Primary neutron energy spectrum of the accepted events, normalized with tank top surface area and MC live time.	82
4.23	2-dimensioanl histograms of event multiplicity vs. primary neutron energy.	84

4.24	The multiplicity distributions of the accepted events, split into the events of real high-energy neutrons and the events of neutron bundles, with the overall distribution plotted together.	85
5.1	Comparison of background gammas and high-energy neutrons in event rate with respect to multiplicity.	89
5.2	Comparison of the pulse spectra of neutron captures and background gammas. . . .	91
5.3	Distribution of “pulse-height likelihood” estimator $L \equiv \frac{n}{n+g}$ for the multiplicity 5 events from the 1st fast neutron search data.	93
5.4	Representation of neutron likelihood in log-likelihood ratio (LLR) $\log_{10} \left(\frac{n}{g} \right)$ for the multiplicity-5 candidate events in the 1st fast neutron search data.	95
5.5	LLR component distribution of multiplicity 5 for each combination of neutron captures and gamma pulses.	97
5.6	An example of mis-coincident muon event with afterpulsing, shown with waveforms in the four PMT channels.	100
5.7	An example of an electronic noise event, shown with waveforms in the four PMT channels.	103
5.8	The scatter plots of pulse integral to amplitude ratio (IAR) vs pulse height of the 1st fast neutron search data and the low-gain run of ^{252}Cf calibration.	104
5.9	The scatter plots of pulse integral to amplitude ratio (IAR) vs pulse height of the 2nd fast neutron search data and the high-gain run of ^{252}Cf calibration.	105
5.10	The scatter plots of pulse integral to amplitude ratio (IAR) vs pulse height of the 3rd fast neutron search data and the high-gain run of ^{252}Cf calibration.	106
5.11	The histograms of pulse integral to amplitude ratio (IAR) for the 1st fast neutron search data and the low-gain run of ^{252}Cf calibration.	107
5.12	The histograms of pulse integral to amplitude ratio (IAR) for the 2nd fast neutron search data and the high-gain run of ^{252}Cf calibration.	108

5.13	The histograms of pulse integral to amplitude ratio (IAR) for the 3rd fast neutron search data and the high-gain run of ^{252}Cf calibration.	109
5.14	Scatter plot of the IAR against multiplicity for the events of multiplicity 9 or greater having passed the muon rejection cut from all the three fast neutron searches. . . .	110
5.15	The efficiency of the data quality cut of $\text{IAR} < 0.18$, defined as the acceptance fraction for good ^{252}Cf calibration events.	112
5.16	Least-squares fit of the LLR distribution for the multiplicity 5 events in the 1st fast neutron search data.	116
5.17	Least-squares fit of the LLR distribution for the multiplicity 6 events in the 1st fast neutron search data.	117
5.18	Least-squares fit of the LLR distribution for the multiplicity 7 events in the 1st fast neutron search data.	118
5.19	Least-squares fit of the LLR distribution for the multiplicity 8 events in the 1st fast neutron search data.	119
5.20	Least-squares fit of the LLR distribution for the multiplicity 9 events in the 1st fast neutron search data.	120
5.21	Least-squares fit of the LLR distribution for the multiplicity 10 events in the 1st fast neutron search data.	121
5.22	Least-squares fit of the LLR distribution for the multiplicity 6 events in the 2nd fast neutron search data.	122
5.23	Least-squares fit of the LLR distribution for the multiplicity 7 events in the 2nd fast neutron search data.	123
5.24	Least-squares fit of the LLR distribution for the multiplicity 8 events in the 2nd fast neutron search data.	124
5.25	Least-squares fit of the LLR distribution for the multiplicity 9 events in the 2nd fast neutron search data.	125

5.26	Least-squares fit of the LLR distribution for the multiplicity 10 events in the 2nd fast neutron search data.	126
5.27	Least-squares fit of the LLR distribution for the multiplicity 5 events in the 3rd fast neutron search data.	127
5.28	Least-squares fit of the LLR distribution for the multiplicity 6 events in the 3rd fast neutron search data.	128
5.29	Least-squares fit of the LLR distribution for the multiplicity 7 events in the 3rd fast neutron search data.	129
5.30	Least-squares fit of the LLR distribution for the multiplicity 8 events in the 3rd fast neutron search data.	130
5.31	Least-squares fit of the LLR distribution for the multiplicity 9 events in the 3rd fast neutron search data.	131
5.32	Least-squares fit of the LLR distribution for the multiplicity 10 events in the 3rd fast neutron search data.	132
5.33	The LLR distribution of two data groups with multiplicity greater than 10 in 3rd fast neutron search data.	133
5.34	Multiplicity spectrum of the 1st fast neutron search data, compared with the multiplicity spectrum of the low-PMT-gain MC.	138
5.35	Multiplicity spectrum of the 2nd fast neutron search data, compared with the multiplicity spectrum of the high-PMT-gain MC.	139
5.36	Multiplicity spectrum of the 3rd fast neutron search data, compared with the multiplicity spectrum of the high-PMT-gain MC.	140
5.37	Multiplicity spectrum of the combined fast neutron search (FNS) data, compared with the MC multiplicity spectrum.	143
6.1	Conceptual design of the SuperCDMS SNOLAB cryogenic and shielding system. .	149
6.2	Schematic graphs for the layout of the active neutron veto modules.	152
6.3	Neutron capture times in the active neutron veto with different boron concentrations.	153

6.4	Estimated neutron tagging efficiency, plotted together with capture time, both as functions of boron concentration.	154
6.5	Veto efficiency for tagging single-scatter neutron-induced iZIP events as a function of threshold energy in keV _{ee} , for veto time window 10 μs, 30 μs, 100 μs, and 300 μs.	156
6.6	The photographs of the quarter-scale neutron-veto prototype.	158
6.7	Screenshots of a 3D visualization for the veto prototype geometry.	159
6.8	The 9 locations of radioactive sources for calibration.	160
6.9	Energy spectra for a Monte Carlo simulation of the veto prototype exposed with ¹³⁷ Cs at three different locations.	162
6.10	The left column shows the fraction of PE response of individual channels over the total PE. The right column shows channel number vs the PE fraction, with the color representing event rate.	163
6.11	The measured spectrum of ¹³⁷ Cs compared to a Geant4 ¹³⁷ Cs spectrum smeared using parameters derived from ¹³⁷ Cs and SiPM response.	164
6.12	The measured energy spectrum for data collected without any radioactive source present.	165

List of Tables

4.1	Summary of best-fit values of energy scales and smearing parameters in the MC offline processor. The values of overall energy scale result from the fits shown in Figure 4.3 and 4.4. The East-West Adjustment is the value added to the east PMT and subtracted from the west PMT of the best fit energy scale factor for a PMT gain setting, to fine-tune the energy scale factors for the single PMTs. The fits of East-West Adjustment are shown in Figure 4.5, 4.6, 4.7, and 4.8. Smearing parameters s_1 is defined with Eq. (4.2) and the fits for the values are shown in Figure 4.9 and 4.10.	56
4.2	Event numbers in each MC event type with each selection requirement found in the comprehensive muon simulation with 138.8 days of live time.	77

Chapter 1

Dark Matter

There is compelling evidence for the existence of dark matter from astronomical and cosmological observations. In this chapter, I will briefly present modern cosmology and introduce the evidence for dark matter, following [1, 2]. In general, I will take the convention of natural units in which the speed of light is set to one ($c = 1$). I then discuss the most important dark matter candidate, the Weakly Interacting Massive Particle (WIMP), and direct detection experiments.

1.1 The Standard Cosmology and the Dark Matter Problem

Cosmology was an ancient and mysterious topic, but only became a real discipline of science after Einstein's discovery of general relativity in the early 20th century. General relativity describes gravitation as a geometric property of spacetime—the curvature, which is directly related to the energy and momentum of the content of the universe, e.g. matter and radiation. The relation is specified by Einstein's equation

$$G_{\mu\nu} = 8\pi G T_{\mu\nu}, \tag{1.1}$$

where $G_{\mu\nu}$ is the Einstein tensor representing spacetime curvature, G is Newton's constant, and $T_{\mu\nu}$ is the energy-momentum tensor for all fields.

Besides Einstein's equation, modern cosmology is based on a fundamental idea known as the cosmological principle—the universe is homogeneous and isotropic on large scales. The cosmological principle is not only a hypothesis for simplifying discussions but also supported by many astronomical observations. The early observation of the cosmic microwave background (CMB) by COBE found that the anisotropy of the early universe at the time of recombination of protons and electrons is only $\sim 10^{-5}$.

In the 1920s, Hubble found that the redshifts of celestial objects were proportional to the distances of the objects away from Earth. The redshift was interpreted as the linear expansion of the velocity of the objects. This relationship is known as Hubble's law

$$v = H_0 D, \quad (1.2)$$

where v is the velocity of the object, D is its distance from Earth, and H_0 is called the Hubble constant. Hubble's law implies that the universe expands uniformly everywhere as time evolves. We can imagine a frame with *comoving coordinates*, in which the *comoving distance* between two points in space remains constant. However, the physical distance is proportional to a scale factor, $a(t)$, and the physical distance does evolve with time. To quantify the change in the scale factor, it is useful to define the Hubble rate

$$H(t) := \frac{da/dt}{a} \equiv \frac{\dot{a}}{a}, \quad (1.3)$$

which measures how rapidly the scale factor changes. The Hubble constant is nothing but the present value of Hubble rate, $H_0 = H(t_0)$.

The smooth, expanding universe may be described by the Robertson-Walker (RW) metric

$$ds^2 = -dt^2 + a^2(t) \left[\frac{dr^2}{1 - kr^2} + r^2(d\theta^2 + \sin^2\theta d\phi^2) \right], \quad (1.4)$$

where t, r, θ, ϕ are comoving coordinates. The parameter k determines the curvature of the space: $k = +1$ for a spherical, or closed, universe, $k = 0$ for a flat universe, and $k = -1$ for a hyperbolic, or open, universe.

The energy-momentum tensor $T_{\mu\nu}$ on the right-hand side of Einstein's equation is made of energy density ρ and pressure p in the universe. With the RW metric, the solution of Einstein's equation leads to the two independent Friedmann equations:

$$H^2(t) \equiv \left(\frac{\dot{a}}{a}\right)^2 = \frac{8\pi G}{3} \left[\rho(t) + \frac{\rho_{\text{cr}} - \rho_0}{a^2(t)} \right], \quad (1.5)$$

and

$$\frac{\ddot{a}}{a} = -\frac{4\pi G}{3} \left(\rho(t) + 3p(t) \right), \quad (1.6)$$

where ρ_0 is the present value of energy density. The *critical density*

$$\rho_{\text{cr}} \equiv \frac{3H_0^2}{8\pi G}. \quad (1.7)$$

The flat universe is one in which the present energy density is equal to the critical density. If the energy density is higher than the critical density, then the universe is closed; if the energy density is lower than this value, then the universe is open. There is persuasive observational evidence, e.g. the anisotropy spectrum of the CMB measured by Planck [3], that strongly supports the flatness of the universe. With an equation of state $p = \omega\rho$ (constant $\omega = 1/3$ for radiation, and $\omega = 0$ for matter), the scale factor evolving over time is then solved from the Friedmann equations,

$$\begin{aligned} a &\propto t^{1/2} \quad (\text{for radiation}); \\ a &\propto t^{2/3} \quad (\text{for matter}). \end{aligned} \quad (1.8)$$

Besides, according to the properties of $T_{\mu\nu}$ for radiation and matter, the relationship between energy

density and the scale factor can be found as

$$\begin{aligned}\rho &\sim a^{-4} \quad (\text{for radiation}); \\ \rho &\sim a^{-3} \quad (\text{for matter}).\end{aligned}\tag{1.9}$$

At early times, the scale factor must have been very small, and the energy density very high. In the standard cosmology, we believe that the universe began from the earliest known periods with a state of very high density and high temperature, and expanded over time. At early times, the energy in the universe was dominated by radiation, and the scale factor evolved as a^{-4} . As the universe expanded, the energy density and temperature dropped, and the density of radiation dropped faster than that of matter. At later times, nonrelativistic matter dominates the content of energy density, and the universe then expanded as $t^{2/3}$. Then at more recent times, another form of energy, known as dark energy, becomes dominant, making the expansion of the universe accelerate. I will ignore dark energy for a while until completing the discussion on the evidence of dark matter.

When the universe was much hotter and denser with the temperature at the order of MeV/k_B at the earliest times, there were no neutral atoms or even nuclei. As the universe cooled below the binding energies of typical nuclei, light elements began to form. This process is known as Big Bang Nucleosynthesis (BBN). The standard cosmology predicts how the density and temperature dropped over the early times, and therefore can give precise predictions on the light element abundances through BBN. Figure 1.1 shows the predictions of BBN and the astronomical measurements of abundances of four light elements [4]. The measurements are consistent with the predictions, and provide another confirmation of the standard cosmology. In addition, BBN provides a way of measuring the baryon density, which is the combined proton plus neutron density, in the universe. In particular, the measurement of deuterium pins down the baryon density accurately to only $\sim 4\%$ of the critical density. But the total energy density has to be the critical energy for a flat universe, which is strongly supported by many observations. This implies the existence of nonbaryonic matter in the universe, or known as dark matter.

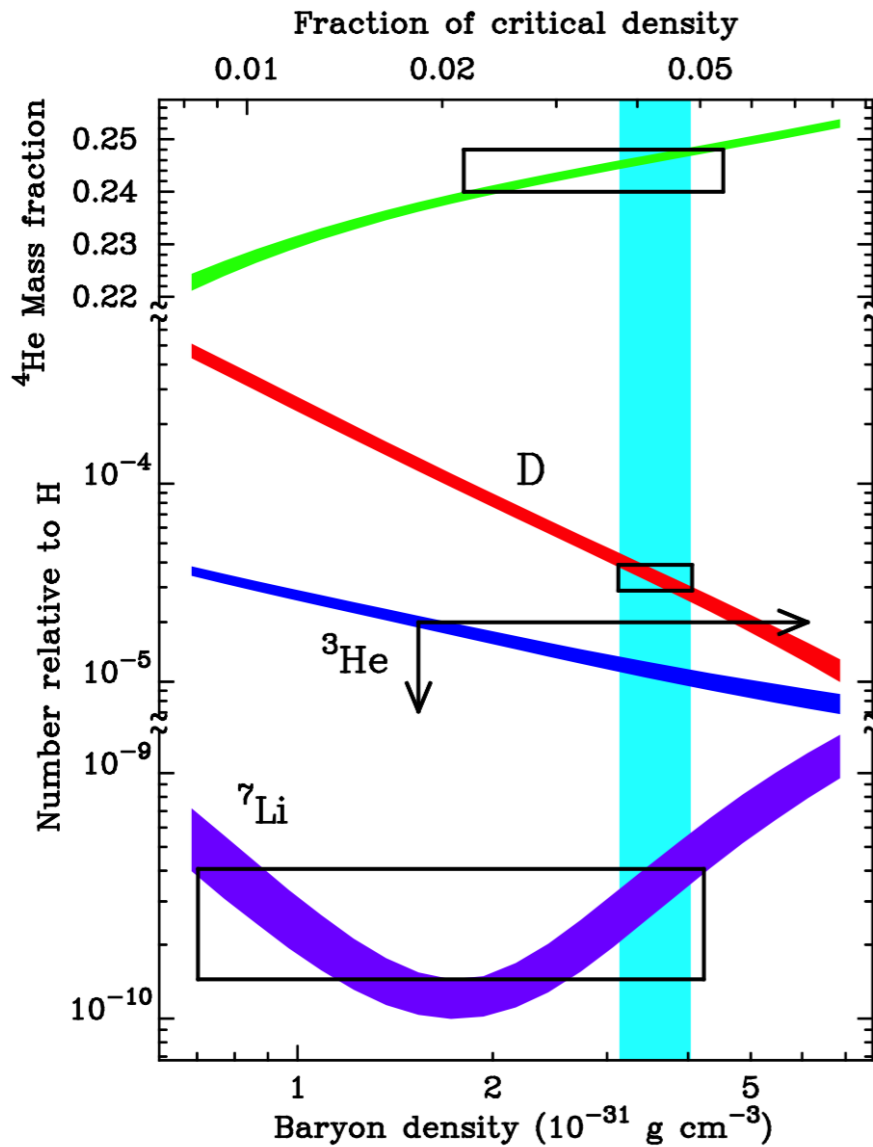


Figure 1.1: Constraint on the baryon density from Big Bang Nucleosynthesis, taken from [4]. Colored bands show the predictions for four light isotopes— ${}^4\text{He}$, deuterium, ${}^3\text{He}$, and lithium. Boxes (arrows) show the measured ranges (limits). Fixed by measurements of primordial deuterium, the cyan vertical band shows the baryon density is estimated to be $\sim 4 \times 10^{-31} \text{ g cm}^{-3}$, i.e. $\sim 4\%$ of critical density.

The concept of dark matter was first suggested by Zwicky in 1933 [5] by comparing the spread velocities of galaxies in clusters to that expected from the virial theorem and realizing the existence of unseen mass in the clusters. Rubin and Ford published in 1970 more precise measurements of the rotation curve of the galaxy M31, providing the first solid evidence of dark matter found in galaxies [6]. Figure 1.2 shows both the rotation curve in Rubin and Ford's paper and a more recent measurement for galaxy M33 [7]. The plateau on the curve at large radii clearly shows the contradiction with a contribution of only stellar disk and gas.

A number of large surveys of galaxies were performed in the last decades of the 20th century. The results of these surveys show large-scale structure in the universe. In the map of the universe as a result of the Sloan Digital Sky Survey (SDSS) [8], shown in Figure 1.3, galaxies are clearly not distributed randomly and smoothly, but are organized into galaxy clusters, superclusters, sheets, walls and filaments, which are separated by huge voids, forming the so called "cosmic web". To understand the formation of structure, we must push the standard cosmology into the next order. Dark matter plays a crucial role in structure formation, as it interacts essentially only by the gravitational force. This allows it to collapse into structures such as dark matter halos before baryonic matter, which is obstructed by repulsive pressure. Figure 1.4 shows the observed power spectrum of the distribution of galaxies is much harder than the prediction of a theory with only baryons and no dark matter.

More observational evidence for the existence of dark matter comes from more recent measurement of the anisotropy of the CMB, from gravitational lensing, etc. I will skip the discussion of these examples. Before concluding this section, there is another important ingredient of the energy in the universe worth raising. The measurement of the luminosity distance of type Ia supernovae and their redshifts [11] indicates that the universe does not only expand, but the expansion has also been accelerating. The most compelling explanation of an accelerating expansion is to add a cosmological constant term $\Lambda g_{\mu\nu}$ in Einstein's equation (Λ for cosmological constant and $g_{\mu\nu}$ for spacetime metric), which would effectively represent a new form of energy in the universe, known

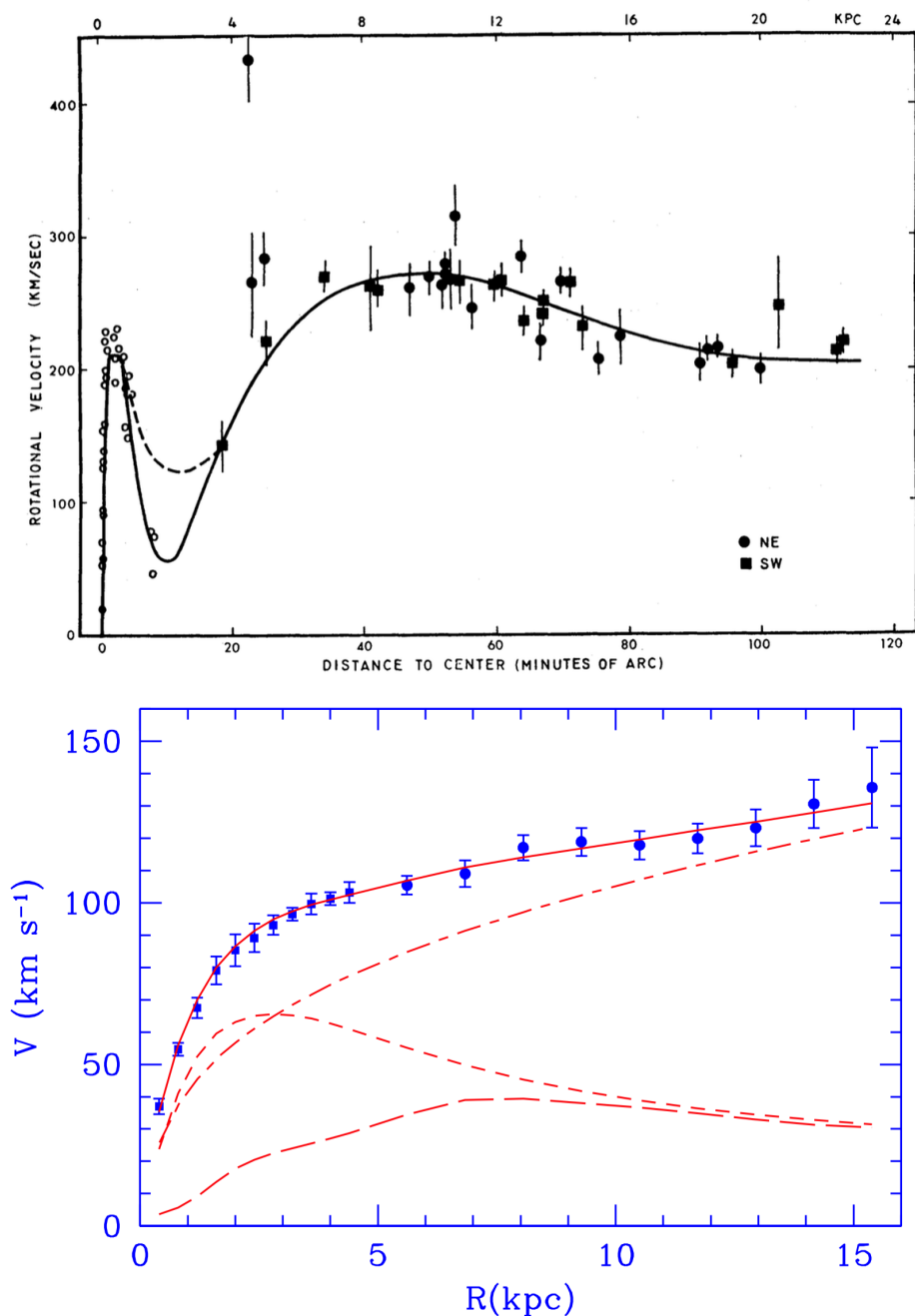


Figure 1.2: Rotation curves of galaxy M31 and galaxy M33. Plotted is the rotational velocity as a function of distance to the center of the galaxy. On the top is shown observed data and a polynomial fit for galaxy M31, taken from [6]. It implies a nearly flat rotation curve at large radii, which is not affordable by the gravitational force that can be generated by the luminous matter in the galaxy. On the bottom is shown the observed data and model predictions for galaxy M33, taken from [7]. Points and solid curve show the observation and the best fit, respectively. Also shown are the dark matter halo contribution (dashed-dotted line), the stellar disk contribution (short dashed line), and the gas contribution (long dashed line).

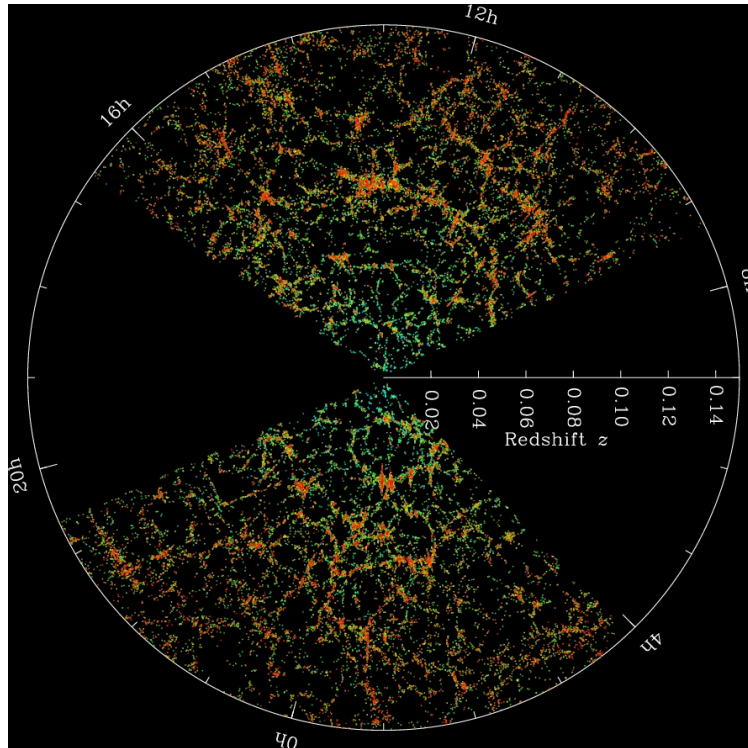


Figure 1.3: A slice through the Sloan Digital Sky Survey 3-dimensional map of the distribution of galaxies with the Earth at the center.

as dark energy, or vacuum energy. Dark energy has an equation of state $p = -\rho$, with which the second Friedmann equation Eq. (1.6) results in a positive \ddot{a} . The density of vacuum energy remains constant no matter how the scale factor a changes. Thus as the universe expands, and radiation and matter become diluted enough, the dark energy density starts to dominate the universe, and drive the expansion to accelerate. In addition, the baryonic, ordinary matter only contributes at most 5% of the critical density, as mentioned earlier. But, recent estimate of dark matter density takes 24% of the critical density. Therefore, in considering the “budgetary shortfall”, dark energy is needed as $\sim 71\%$ of the critical energy to ensure the universe is flat.

At present, the most compelling cosmology model is known as the Λ CDM model: a flat universe with a non-zero cosmological constant Λ and Cold (non-relativistic) Dark Matter (CDM). The dominant form of energy density, dark energy, is not well understood yet. And although there is a lot of evidence for dark matter on the side of cosmology and astronomy, we have not directly detected dark matter, and confirmed nothing about what dark matter is in the particle physics sense.

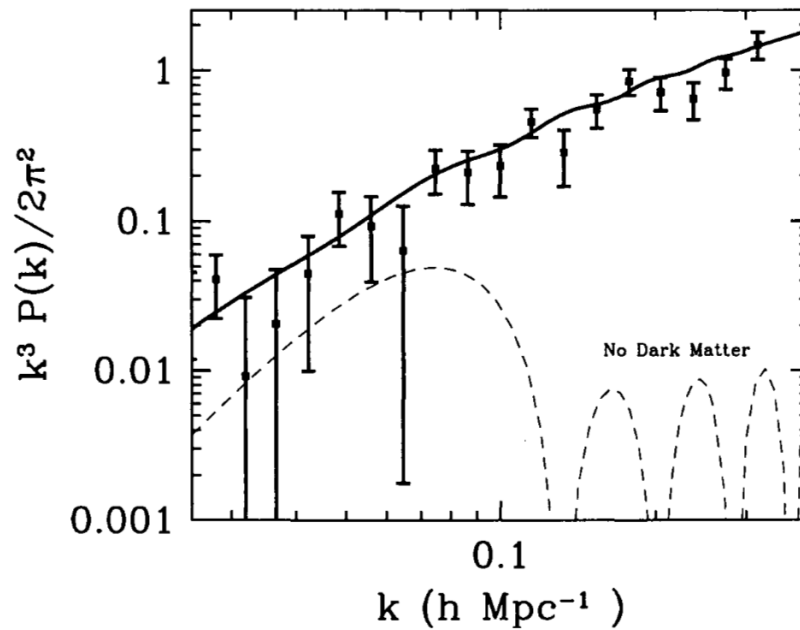


Figure 1.4: Power spectrum, i.e. the variance $\Delta^2 \equiv k^3 P(k) / 2\pi^2$ of the Fourier transform of the galaxy distribution as a function of scale wave number k . The figure is taken from [1], showing the analysis of data from the PSCz survey [9] by Hamilton and Tegmark (2001) [10]. On large scales (small k), the variance is smaller than unity, so the distribution is smooth. The solid line is the theoretical prediction from a model that contains dark matter and a cosmological constant. The dashed line is a theory that assumes matter with only baryons but no dark matter. The large amount of structure on small scales (large k) is in stark disagreement with the predictions of no dark matter.

1.2 Weakly Interacting Massive Particles

There are many candidate particles proposed in theory, including the axion [12], Kaluza-Klein particle [13], gravitino [14], etc. Currently the most compelling theory is a general class called Weakly Interacting Massive Particles [15], or WIMPs, which both satisfies the cosmological criteria of being cold, non-baryonic relic and meets the role in new physics for solving the hierarchy problem [16]. Most direct dark matter detection experiments are designed to discover WIMPs.

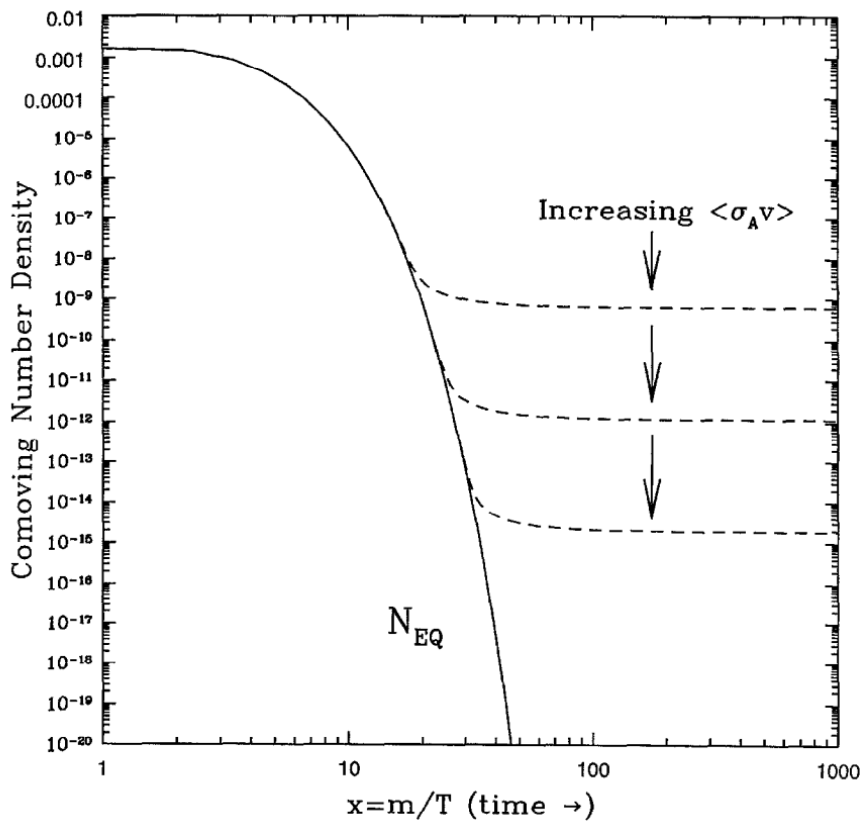


Figure 1.5: Comoving number density of WIMP dark matter in the early Universe, taken from [17]. The solid curve is the equilibrium abundance, while the dashed curves are the actual WIMP abundance resulting from three different values of thermal averaged pair annihilation cross section of WIMPs. Larger values of the annihilation cross section would leave smaller amounts of WIMP relics today.

In the generic WIMP scenario, two heavy particles (WIMPs) can annihilate to produce two light (or massless) particles, which are assumed to be very tightly coupled to the cosmic plasma. This process is reversible when the temperature is high enough for the process to produce the mass of the

WIMP, and the WIMPs are in equilibrium with the cosmic plasma. Its abundance is suppressed as $e^{-m/T}$ as temperature drops. When the temperature of the universe further drops below the mass of WIMP, they become so rare due to this suppression that they are not able to find each other fast enough to maintain the equilibrium abundance. In fact, WIMP particles begins to freeze out from the equilibrium, and its comoving density then becomes invariant. For non-relativistic particles, the dark matter density parameter when freeze-out occurs is [18]

$$\Omega_{\text{DM}} h^2 \approx \frac{3 \times 10^{-27}}{\langle \sigma_{\text{AV}} \rangle} \text{cm}^3/\text{s}, \quad (1.10)$$

where $\langle \sigma_{\text{AV}} \rangle$ is the thermal-averaged pair annihilation cross section of WIMPs, $h \equiv H_0/(100 \text{ km sec}^{-1} \text{ Mpc})$ is the dimensionless Hubble parameter, and Ω_{DM} is the fractional dark matter density. It is conventional to use the product as the parameter for dark matter density. The dark matter density is independent of the mass of the WIMP. Figure 1.5 shows the comoving number density of the dark matter in equilibrium drops exponentially as the temperature decreases; with three different annihilation cross sections, WIMP dark matter would freeze out from the equilibrium with different densities [17]. A larger dark matter annihilation cross section means that the WIMPs stay in equilibrium longer, and leave the density of the relic today lower.

New physics beyond the Standard Model is needed to solve the hierarchy problem in particle physics. If a new particle interacting with the electroweak scale exists, its annihilation cross section can be estimated to be $\langle \sigma_{\text{AV}} \rangle \sim \alpha^2 (100 \text{ GeV})^{-2} \sim 10^{-25} \text{ cm}^3 \text{ s}^{-1}$, for $\alpha \sim 10^{-2}$ [18]. It is close to the value needed to leave the right amount of dark matter in the universe. This striking coincidence has brought great motivation to assume the lightest stable particle at the electroweak scale to be the dark matter. The WIMP models have been studied with extensive theoretical work, and have led to a tremendous experimental effort in last two decades to detect these WIMPs [19–27].

1.3 Direct Dark Matter Detection

WIMP dark matter can potentially be detected by three complementary methods. WIMPs may be produced at high-energy accelerators such as the Large Hadron Collider (LHC) and detected indirectly by identifying the signal of missing energy [28]. Relic WIMPs may be detected indirectly when they gather more densely in massive celestial objects, increasing their annihilation rate enough and producing detectable signals [29]. Many indirect signals may have alternate astrophysical explanations, making these indirect detections ambiguous.

Relic WIMPs may be directly detected when they recoil off nuclei in terrestrial detectors [30, 31]. Direct dark matter detection is the most compelling method to test the WIMP hypothesis as compared with the other two methods, since it may find the most unambiguous signals. I will present in this section the generic characteristics of WIMP signals in direct detection, and briefly introduce implementations of these experiments, primarily following [32].

1.3.1 Spin-independent and Spin-dependent Cross Sections

Using Fermi's Golden Rule, the differential WIMP-nucleon cross section can be found dependent on the zero-momentum cross section independent of the momentum transfer, $\sigma_{0\text{WN}}$, and the form factor $F^2(q)$:

$$\frac{d\sigma_{\text{WN}}(q)}{dq^2} = \frac{1}{\pi v^2} |\mathcal{M}|^2 = \frac{\sigma_{0\text{WN}} F^2(q)}{4\mu_A^2 v^2}. \quad (1.11)$$

Here, v is the velocity of the WIMP in the lab frame, and the WIMP-nucleon reduced mass $\mu_A \equiv M_\chi M_A / (M_\chi + M_A)$ in terms of the WIMP mass M_χ and the mass M_A of a target nucleus of atomic mass A . The zero-momentum cross section for a non-relativistic WIMP of arbitrary spin

may be further written in terms of a spin-independent and a spin-dependent term:

$$\sigma_{\text{0WN}} = \frac{4\mu_A^2}{\pi} [Zf_p + (A - Z)f_n]^2 + \frac{32G_F^2\mu_A^2}{\pi} \frac{J+1}{J} (a_p \langle S_p \rangle + a_n \langle S_n \rangle)^2. \quad (1.12)$$

Here the two terms describe spin-independent and spin-dependent WIMP-nucleus cross section. f_p and f_n (a_p and a_n) are effective spin-independent (spin-dependent) couplings of the WIMP to the proton and neutrons, respectively. These couplings and the WIMP mass M_χ are the parameters that contain all the information of the particle physics models; the other parameters describe the target nuclei, i.e. the atomic number Z , mass number A , total nuclear spin J , and the expectation values of the proton and neutron spins within the nucleus $\langle S_{p,n} \rangle = \langle N | S_{p,n} | N \rangle$. For many models, $f_p \approx f_n$, then the atomic number Z cancels in the spin-independent WIMP-nucleus cross section

$$\sigma_{\text{0WN,SI}} \approx \frac{4\mu_A^2}{\pi} f_p^2 A^2 = \sigma_{\text{SI}} \frac{\mu_A^2}{\mu_n^2} A^2, \quad (1.13)$$

where μ_n is the reduced mass of the WIMP-nucleon system. In the last part of the equation, the spin-independent WIMP-nucleus cross section is rewritten by defining the spin-independent cross section of a WIMP interacting on a single nucleon

$$\sigma_{\text{SI}} \equiv \frac{4\mu_n^2 f_n^2}{\pi}. \quad (1.14)$$

This spin-independent WIMP-nucleon cross section σ_{SI} can be used to compare among different experiments and compare to models. A given model predicts a range in σ_{SI} and M_χ parameter space; experiments quote limits on σ_{SI} as functions of M_χ as their results, or would measure values of σ_{SI} and M_χ if making a discovery. The dependence on A^2 in Eq. (1.13) suggests the advantage of using target materials with heavy elements. For the spin-dependent interactions, contributions from proton and neutron couplings often cancel. The detection limits on the spin-dependent cross section should be quoted separately for neutrons and protons, each under the assumption that the other interaction is negligible. Also, the spin-dependent contributions of nucleons with opposite spins

cancel, so that the coherent spin-dependent cross section depends on the net spin of the nucleus. Nuclei with even numbers of protons (neutrons) have nearly no net proton (neutron) spins and hence no sensitivity to spin-dependent interactions on protons (neutrons). Argon is insensitive to spin-dependent interactions because of its even numbers of protons and neutrons for all significant isotopes. Many other materials used as WIMP targets, such as Ge, Si, Xe, have even numbers of protons, therefore are insensitive to spin-dependent interactions on protons. And only some isotopes of these targets, which results in a fraction of the detector's active mass, have sensitivity to spin-dependent interactions on neutrons. Typically, the target materials that are sensitive to spin-dependent interactions often result in worse backgrounds or background rejection and lower sensitivity to spin-independent interactions. Most models are more accessible experimentally via their spin-independent interactions than by their spin-dependent interaction.

1.3.2 The WIMP Recoil Energy Spectrum

Based on simple consideration of conservation of momentum and energy, the maximum recoil energy $max(E_R)$ for an elastic collision of a WIMP with kinetic energy E_χ on a nucleus satisfies

$$\frac{max(E_R)}{E_\chi} = \frac{4M_\chi M_A}{(M_\chi + M_A)^2} = \frac{4\mu_A^2}{M_\chi M_A} \equiv r. \quad (1.15)$$

The recoil energy E_R of each WIMP scatter would distribute randomly from zero to the maximum recoil energy $max(E_R)$, as the recoil angle varies. Here let's call this ratio r for convenience. The mean recoil energy is one half this amount. In typical models, a 100 GeV WIMP with a kinetic energy of ~ 40 keV would deposit ~ 20 keV in the lattice by recoiling off a 67 GeV germanium nucleus. By including the distribution of recoil energies with different $max(E_R)$ values, the general form for the recoil energy spectrum can be written into a falling exponential as a function of recoil

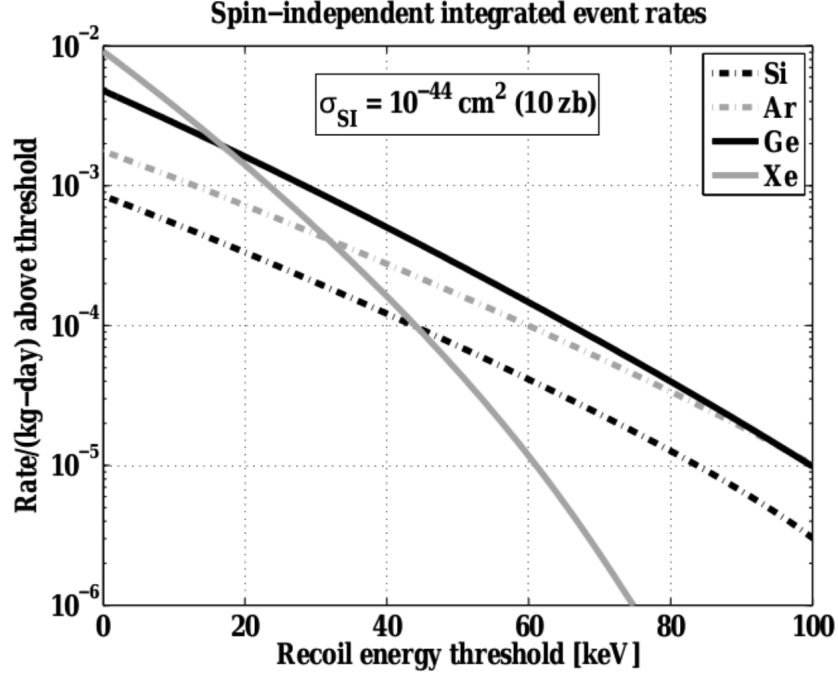


Figure 1.6: Expected spin-independent integrated event rates for a 100 GeV WIMP with cross section $\sigma_{\text{SI}} = 10^{-44} \text{ cm}^2$, taken from [34].

energy [33]:

$$\frac{dR}{dE_R}(E_R) = \frac{R_0}{E_0 r} e^{-E_R/E_0 r}, \quad (1.16)$$

where R_0 is the total WIMP-nucleus recoil event rate, E_0 is the most probable incident kinetic energy for a WIMP. A 50 GeV WIMP with a spin-independent WIMP-nucleon cross section $\sigma_{\text{SI}} \sim 10^{-6} \text{ pb}$ is expected to result in ~ 10 events/(kg day). Given that the energy spectrum is falling exponentially, a low energy threshold is critical for the detection of most of these events.

In many cases, the spectrum may be affected by the Galaxy's escape velocity. WIMPs with velocities above the Galaxy's escape velocity are likely to have already escaped. The finite escape velocity of the Milky Way Galaxy $\sim 540 \text{ km/s} \approx 2 \times 10^{-3} c$ [35] changes the recoil spectrum shape slightly. Figure 1.6 shows the expected WIMP recoil energy spectra for a 100 GeV WIMP scattering on different materials. A low energy threshold is critical to obtain a reasonable event rate.

1.3.3 Direct Detection Technologies

There are primarily three classes of technologies in use for WIMP direct detection experiments, distinguished with the way of collecting the deposited WIMP recoil energy, i.e. collecting energy via charge, light, or phonons/heat. Two types of target materials are mostly in use. Cryogenic semiconductor crystals were developed earlier, but the detectors using noble elements have demonstrated great advantages and have now published the strongest limits on spin-independent WIMP-nucleon cross sections above 10 GeV WIMP mass [36, 37].

Detectors using noble elements, with either single-phase (liquid) or dual-phase, generate signals by collecting scintillation light. A nuclear-recoil event in a noble liquid creates dimers in singlet states or triplet states, which de-excite in different characteristic times with emission of scintillation light. The nuclear recoils (induced by WIMPs or neutrons) and electron recoils (induced by gamma-rays or electrons) differ in the fraction of singlet states and triplet states, therefore result in dramatically different pulse shapes. With this property, noble liquid detectors reject gamma backgrounds with the technique called pulse shape discrimination (PSD). These experiments are usually designed with a fiducial volume, within which the events are accepted as candidates. The detector mass outside the fiducial volume is used as self-shielding against surface backgrounds. The examples of this type of experiment include MiniCLEAN [19, 20] and DEAP-3600 [21]. Some noble liquid detectors also apply an electrical field and collect both scintillation light and ionization charge. These experiments include LUX [22], XENON100 [23], Darkside [24].

Detectors using cryogenic semiconductors have excellent energy resolution to help identify the sources of the backgrounds from natural radioactivity in the experimental apparatus and environment. Many of these detectors, such as SuperCDMS [25] and EDELWEISS [26], collect both ionization charge and phonons. The ratio of energy from these two signal channels provide excellent discrimination against electron recoils. The CoGeNT experiment [27] uses p-type point contact (PPC) detectors with ionization charge readout only.

Although most of these experiments have demonstrated excellent discrimination between nuclear recoils and electron recoils, single-scattered neutron events cannot be distinguished from WIMP recoils. In the next chapter, I will further discuss neutron backgrounds and the strategies of dealing with neutron backgrounds for direct dark matter detection.

Chapter 2

Neutron Backgrounds

Neutrons can scatter off nuclei just like WIMPs do, resulting in a mimic of WIMP detection signals. The neutron-nucleus elastic scattering cross section is of course much higher than the expected WIMP-nucleus scattering cross section, so a neutron interaction with a detector would have a much higher chance to induce multiple scatters in the detector mass, which is a feature used to reject neutron background events. However, when neutrons produced single nuclear recoils, the events would be detected as truly indistinguishable background events, leaving the experimental results ambiguous. Therefore, it is crucial to accurately characterize and minimize neutron backgrounds.

Due to intrinsic contamination with ^{238}U , ^{235}U , and ^{232}Th in materials of the detector, shielding, and in lab cavern rock, radiogenic neutrons with kinetic energies up to several MeV are produced with (α, n) reactions and spontaneous fission (SF). See e.g. [38]. The radiogenic neutron backgrounds are described in Section 2.1. In addition, cosmogenic neutrons with energies extending to a few GeV are generated with the interactions of cosmic-ray muons with the rock surrounding the underground laboratory. As the overburden above the underground site increases, the flux of muons drops, but the average energy of muons increases. This makes the flux and energy spectrum of cosmogenic neutrons dependent on laboratory's depth. The cosmogenic neutron backgrounds are described in Section 2.2.

2.1 Radiogenic Neutrons

Radiogenic neutron backgrounds for direct WIMP search experiments are produced by (α, n) reactions with the α particles emitted primarily from uranium and thorium radioactive isotope decays in the materials surrounding or constituting the detector, and also produced by spontaneous fission of uranium and thorium. Usually, the (α, n) -produced neutrons dominate the total neutron-induced background for an underground experiment.

The general strategy to minimize radiogenic neutron background for underground experiments is to shield the detector with neutron moderators, which are hydrogen-rich materials. The neutron moderators most often used as shielding materials for dark matter experiments include water, high-density polyethylene (HDPE). As the hydrogen nucleus (a proton) has a mass very close to the mass of neutron, the elastic collision of a neutron onto a nearly static proton is very effective at reducing the speed of the incoming neutron. With a proper shield, the radiogenic background neutrons can be moderated to very low energies so that they are eventually captured in shielding materials, or reach the detector but are not energetic enough to induce nuclear recoils above the experiment's threshold energy.

Both for appropriately designing the shielding system and for analyzing the WIMP search data, the neutron induced background in the region of interest (ROI) must be evaluated in Monte Carlo simulations. Neutrons designated to start in the bulk or on the surface of all the materials of the detector, or surrounding the detector, need to be properly assigned with emission rates and energy spectra, which are crucial in determining the total background events in the ROI. Therefore, the radiogenic neutrons need to be understood very well in terms of their origin, transport, and interaction with different materials.

The neutron yield of the (α, n) reactions for various elements have been discussed by many authors [39–42]. The α particles produced from uranium and thorium decays in materials travel with energies in the MeV range. They interact with the nuclei in a thick target and generate neutrons.

The neutron yield is calculated by [41]

$$Y_i = \frac{N_A}{A_i} \int_0^{E_0} \frac{\sigma_i(E)}{S_i^m(E)} dE, \quad (2.1)$$

where E_0 is the initial energy of the α particle, S_i^m is the mass stopping power of element i , A_i is the atomic mass of element i , and N_A is Avogadro's constant. The neutron yields in the uranium and thorium decay chains can be determined by summing the individual yields induced by each α in the decay chain, with the weights based on the branching ratio for each element and the mass ratio in the host materials. The energy attenuation of the α particles is the dominant process in the host materials under the thick target hypothesis [43]. Assuming that the incoming α particle flux with energy E_j is invariant until the energy is attenuated to zero, the differential spectra of neutron yield can be derived as

$$\begin{aligned} Y_i(E_n) &= N_i \sum_j \Phi_\alpha(E_j) \int_0^{E_j} \frac{d\sigma(E_\alpha, E_n)}{dE_\alpha} dE_\alpha \\ &= \frac{N_A}{A_i} \sum_j \frac{R_\alpha(E_j)}{S_i^m(E)} \int_0^{E_j} \frac{d\sigma(E_\alpha, E_n)}{dE_\alpha} dE_\alpha, \end{aligned} \quad (2.2)$$

where N_i is the the total number of atoms for the element i in the host material, $\Phi_\alpha(E_j)$ is the incoming α particle flux with specific energy E_j , $R_\alpha(E_j)$ is the α particle production rate as a function of the energy E_j from the uranium or thorium decay chain. The cross sections used in Eq. (2.2) can either be calculated with simulation code, such as TALYS [44], or obtained from nuclear data bases, such as ENDF [45], or TENDL [46].

Many dark matter direct detection experiments use the SOURCES code [47] to calculate the neutron yield of (α, n) reactions. But the software is not open-source, so the lack of accessibility may prevent it from being easily modified with more and better data, which is strongly needed for the dark matter detection and the broader low-background counting community. C. Zhang, D.-M. Mei, and A. Hime performed an independent calculation of the (α, n) neutron yield for various materials, and developed the Radiogenic Neutron Generator (RNG), a web based generator

with data base [43]. The effort comparing the neutron yields and spectra calculated by the two softwares, and how the difference would result in the detectable neutron background in the dark matter ROI have been ongoing [48, 49].

2.2 Cosmogenic Neutrons

Direct dark matter detection experiments are placed and run at underground laboratories, as the overburden provides a natural shield against cosmic-ray muons and their induced particles. The remaining muons that traverse a detector and its surrounding material, but miss an external veto, serve as a background themselves. In addition, the interactions of muons with the surrounding materials and cavern rock can produce fast neutrons and activate radioactivities. The muon-induced neutrons are particularly important, as they become a source of neutron background in addition to the radiogenic neutrons. In general, the production rate of muon-induced neutrons at large depths is 2 to 3 orders of magnitude smaller than that of radiogenic neutrons. The latter typically have MeV neutron energies, and are hence relatively easy to shield. On the other hand, the cosmogenic muon-induced neutrons have a very hard energy spectrum, extending to several GeV. The high-energy muon-induced neutrons can easily penetrate the detector shielding materials. In addition, they may interact with the high-Z materials, such as lead and copper, which are commonly used as shielding materials against external gamma-rays, and generate multiple secondary neutrons in the MeV range. Figure 2.1 shows a MC simulation study in Ref. [50] with a typical shielding system for underground low-background counting experiments (designed for the MAJORANA Experiment [51] at that time), assuming 10 cm copper adjacent the target mass, followed by 40 cm lead, and an outer layer of 10 cm polyethylene. It is demonstrated that (α, n) neutrons from the cavern rock are efficiently attenuated by nearly 3 orders of magnitude at the energies below 10 MeV. The muon-induced neutrons are attenuated with the polyethylene shield by about an order of magnitude in the MeV range, but are essentially unaffected at higher energies. Note that after the layer of lead and copper the muon-induced MeV neutrons increase back to the level of, or even

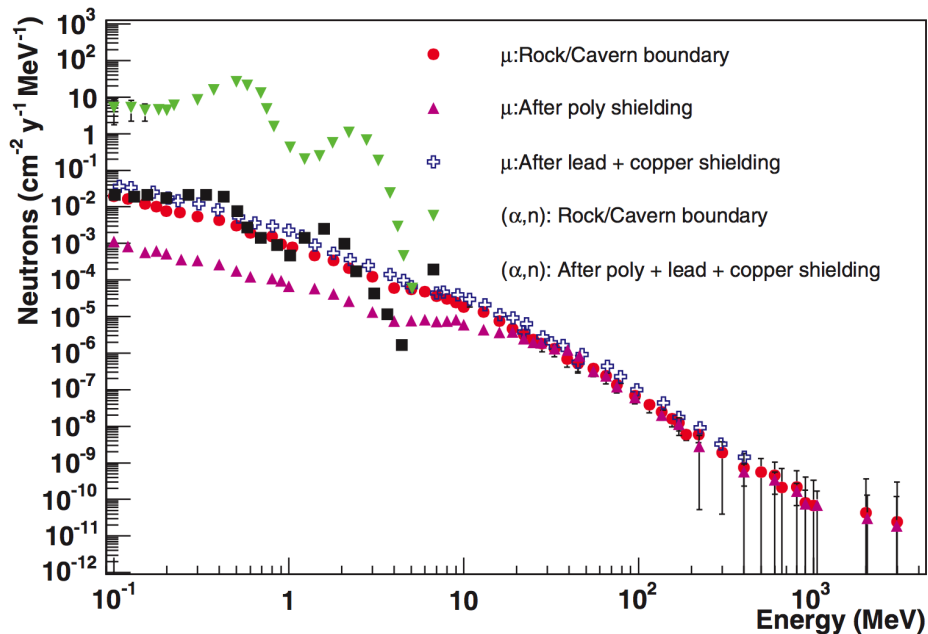


Figure 2.1: The energy spectrum for neutrons produced with (α, n) reactions in the cavern rock compared to those induced by muon interactions in the rock with and without shielding, taken from [50]. The lower energy neutrons (< 10 MeV) are quickly attenuated by polyethylene shielding, while the high-energy part of the muon-induced neutrons stay almost at the same level. The addition of lead and copper shielding adjacent to a detector serves as additional source of lower energy neutrons.

higher than, the muon-induced neutrons at the rock boundary. The inner lead and copper shield serves as an additional neutron production source with the spallation interactions induced by the high-energy neutrons. Therefore, although the total flux of muon-induced neutrons is far less than the radiogenic neutrons at deep underground sites, they are a potentially dangerous background for direct dark matter experiments, and they need to be characterized in detail.

There are two classes of fast neutrons that need to be distinguished—neutrons produced by the muons traversing the detector themselves, and neutrons created in the cavern rock by the muons missing the muon veto. The former can be rejected altogether with the primary muon by an external muon veto with sufficient coverage around the detector. The latter, however, are more difficult to shield or veto in coincidence with the primary muon due to the harder spectrum and long propagation range. Thus, the discussion is focused on fast neutrons produced by muon interactions in the cavern rock.

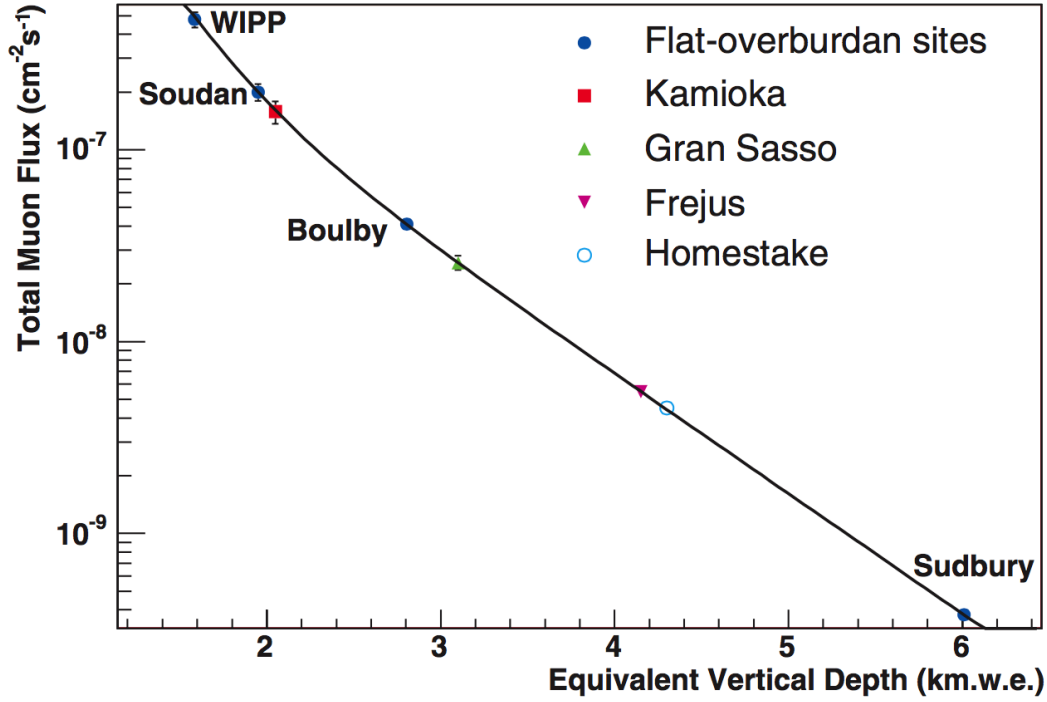


Figure 2.2: The total muon flux measured for the various underground laboratories, taken from [50]. The measured data are from [52–55].

The flux of cosmogenic fast neutrons strongly depends on the depth and composition of an underground laboratory. D.-M. Mei and A. Hime studied with Monte Carlo simulations the site/depth dependence for neutron yield and the flux of muon-induced neutrons [50]. The total muon flux has been measured at the various underground sites. Figure 2.2 shows the muon flux and depth relationship. The total muon flux decreases as the site goes deeper. However, the mean muon energy increases as the site goes deeper, because with more overburden only harder muons have larger probabilities to survive, leaving the softer muons already attenuated. The production of muon-induced neutrons at an underground site depends on both the total muon flux and neutron yield. The latter is positively related to mean muon energy. Mei and Hime obtained the simulated differential neutron flux at several sites, shown in Figure 2.3. Based on the differential flux at the various sites, they provided a convenient parametrization (now known as the Mei-Hime parametrization)

$$\frac{dN}{dE_n} = A_\mu \left(\frac{e^{-a_0 E_n}}{E_n} + B_\mu(E_\mu) e^{-a_1 E_n} \right) + a_2 E_n^{-a_3}, \quad (2.3)$$

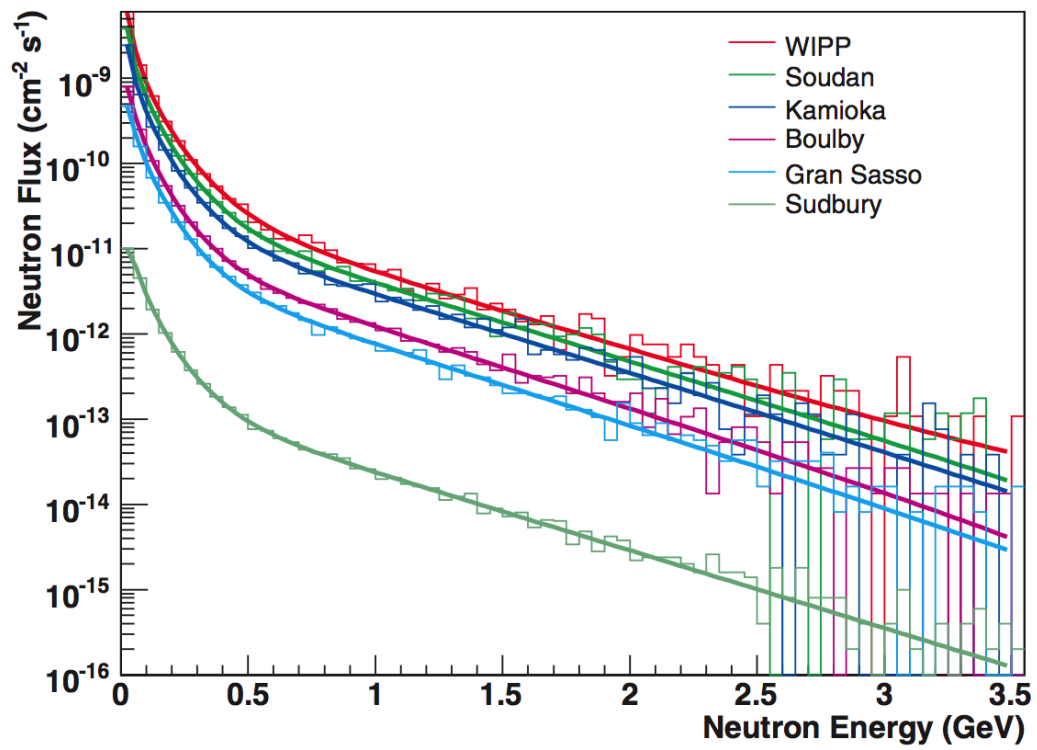


Figure 2.3: The differential energy spectrum for muon-induced neutrons at the various underground laboratories, taken from [50]. The bin width is 50 MeV.

where A_μ is a normalization constant, a_0 , a_1 , a_2 , and a_3 are fitted parameters, E_n is the neutron energy, and $B_\mu(E_\mu)$ is a function of muon energy E_μ in GeV,

$$B_\mu(E_\mu) = 0.324 - 0.641e^{-0.014E_\mu}. \quad (2.4)$$

In the paper, they also provided the fit parameters. The parametrization is valid for $E_n > 10\text{ MeV}$.

In recent years, there has been experimental effort to characterize the cosmogenic muon-induced neutrons at underground laboratories. The work in Ref. [56] measured the fast neutron flux at Soudan Mine with liquid scintillator, resulting in $2.3 \pm 0.52(\text{sta.}) \pm 0.99(\text{sys.}) \times 10^{-9} \text{ cm}^{-2} \text{ s}^{-1}$ for fast neutrons above 20 MeV, in a reasonable agreement with the model prediction discussed above. In a recent publication [57], an experiment called Muon-Induced Neutron Indirect Detection EXperiment (MINIDEX) has been run to measure neutrons induced by cosmic-ray muons in selected high-Z materials. The results from the first round of data have indicated a factor of 3 to 4 excess on the rate of muon-induced neutrons compared to Geant4 prediction. The neutrons measured by this experiment are not the same type of events that we are most interested in, since these events should be easy to tag with a muon veto. However, this experiment provides interesting results in benchmarking Monte Carlo predictions against data on cosmogenic neutron production.

In order to provide more useful data with which to benchmark simulations, the Neutron Multiplicity Meter (NMM) experiment [58] was built and at Soudan Mine. In the following chapters of this thesis, I will introduce the NMM detector, and present the Monte Carlo study and data analysis that I have done, in an effort to measure the cosmogenic neutron flux and benchmark neutron production with the Geant4 Monte Carlo simulations.

Chapter 3

The Neutron Multiplicity Meter at the Soudan Underground Laboratory

3.1 Motivation

Neutrons in underground laboratories are one of the most challenging backgrounds to direct dark matter detection experiments, as they cause nuclear recoils in detector mass to mimic WIMP signals. Proper design and operation of the dark matter experiment and correct analysis of the results rely on numerical Monte Carlo simulations to predict the background rate due to neutrons. At depths of 2000 meters of water equivalent (m.w.e.) and below, the neutron-induced background rate is correlated with the flux of high-energy neutrons (also called fast neutrons) produced by cosmic ray-muons interacting with cavern rock. The simulation of these processes is uncertain due to the lack of appropriate measurement of the fast neutron flux in underground laboratories for direct comparison.

The issue is intensified with neutron spallation processes induced by fast neutrons in high-Z shielding materials near the detector. To reduce the gamma background for WIMP direction experiments, high-Z materials such as lead are used to attenuate gammas from ambient U, Th, etc. While the high-Z materials are effective against gamma rays, the shield itself may become an

increased neutron source due to the neutron spallation process caused by unvetted muon-induced fast neutrons. These neutrons have energies above ~ 50 MeV, and thus low enough cross section on hydrogen that they can easily penetrate the shielding for moderating low-energy neutrons and reach the high-Z gamma shield. They tend to interact with the high-Z materials and cause spallation processes, which result in multiple secondary neutrons with energies below 10 MeV. These lower-energy neutrons, generated inside the neutron moderator, can easily reach the inner dark matter detector and mimic WIMP signals. The lack of knowledge on the fast neutrons induced spallation process and the lack of data on the fast neutron flux in underground laboratories together make the backgrounds due to the muon-induced neutrons a challenging issue for dark matter experiments.

The Neutron Multiplicity Meter (NMM) [58] was proposed and built to pin down the flux of the muon-induced fast neutrons to about 10% at the Soudan Underground Laboratory, at a depth of approximate 2000 m.w.e. Utilizing the high thermal-neutron capture cross section of gadolinium and using water serving both as a neutron moderator and a Cherenkov medium, the experiment has implemented a neutron multiplicity meter adjacent to a lead target, which is used as gamma shield in actual dark matter experiments, such as SuperCDMS [25]. When a high-energy neutron hits the lead target, the neutrons spallation, similar as it takes place in lead shielding of dark matter experiments, results in multiple neutrons with energies below 10 MeV. Most of these neutrons will be thermalized and captured by gadolinium nuclei and result in detectable light. The multiplicity of the secondary neutrons provides both a distinct signature of the fast neutron event and an indirect measurement of its initial energy. The data on the NMM not only measures the flux of the muon-induced high-energy neutrons at the Soudan Underground Laboratory, but also acquires information about the high-energy neutron spectrum and allow the underlying neutron production processes in Pb to be measured. Together, the flux and multiplicity distribution will help to benchmark the simulation codes and shed light on modeling the underlying processes. Being able to predict cosmogenic neutron background with greater reliability benefits the whole low background counting community, and helps improve extrapolations for the experiments aiming to operate in deeper sites, such as SuperCDMS SNOLAB. The successful operation of the NMM

at Soudan depth and results of the measurement demonstrates the feasibility of larger detectors with similar techniques that may be built and run for high-energy neutron benchmarking studies at greater depths.

3.2 Detection Technique

The main techniques of the Neutron Multiplicity Meter is utilizing the water-Cherenkov effect induced by the gamma rays from gadolinium neutron-captures to measure the rate of high-energy neutrons underground and the secondary neutron multiplicity of the spallation induced by the primary high-energy neutron in a lead target.

High-energy neutrons are difficult to stop. The idea of the design of the experiment is to convert a high-energy neutron into several secondary neutrons with lower energies. The major part of the detector is two moderate sized tanks filled with Gd-loaded water atop a lead stack as the detector target. A high-energy neutron induced by cosmic-ray muon in rock underground will mainly enter from above, penetrate the water, and cause neutron spallation in the Pb target. The disintegration of the Pb nucleus will release several neutrons with typical energy below 10 MeV emitted isotropically. Some of these neutrons leave the lead stack and enter the Gd-loaded water, where they are quickly moderated and thermalized by the protons in water. These thermal neutrons will travel in water until they find a gadolinium nucleus, which has a high thermal-neutron capture cross section, and most will be captured within a characteristic time of $\sim 10 \mu\text{s}$. The resulted excited nuclear state will decay and emit gamma rays of $\sim 8 \text{ MeV}$ after the capture. Then the consequent electromagnetic cascades will produce Cherenkov lights, which can be collected by the PMTs immersed in the water.

The captures of the thermal neutrons by the Gd nuclei in water take place as a Poisson process, and the rate of the captures decays exponentially since the first capture. This behavior makes advantage to the high-energy neutron detection: the neutrons released simultaneously in burst of several are spread out in time, and individually captured and counted. The characteristic timing

distribution of the neutron captures also provides a unique signature of pulse clustering which allows tagging of neutron multiplicity events as well as effective rejection of random gamma backgrounds.

The neutrons released via spallation induced by the primary high-energy neutron in Pb carry typical kinetic energy below 10 MeV. This fact features that the counting of the neutron multiplicity gives a rough indication of the primary neutron energy. Therefore the measured multiplicity distribution will provide extra information, other than the event rate only, for benchmarking the generation of the muon-induced neutrons underground, as well as the neutron spallation in Pb.

3.3 Detector Description

The Neutron Multiplicity Meter (NMM) ran and took data at the Soudan Underground Laboratory at a depth of 1.95 km.w.e. There are dark matter experiments SuperCDMS and CoGeNT at the Soudan lab sharing the same cavern with the NMM.

3.3.1 Main Components

Figure 3.1 is a cross-sectional view of the NMM. The detector consists of two optically separated water tanks, each containing 2 tons of water and holding two 20 inch KamLand photomultiplier tubes (PMTs) [59] with the surfaces immersed in water. Each tank is 96 inches long, 48 inches wide, and 30 inches high. Both tanks align on their longer sides, creating an essentially 96×96 inch square area, though there is a small gap between the two tanks due to the longer extents of their caps. The two water tanks sit atop 16 inches of stacked lead bricks, with a 84×80 inch footprint. The size of the lead footprint was chosen so the experiment would have a reasonable event rate: approximately 1 high-energy neutron candidate event per day. The water tanks extend past the lead stack to better cover the upward spallation neutrons emitted from Pb. The tank size is also motivated by the need for a high collection efficiency of the neutron-capture gammas: the water tanks need

to be large enough to catch most of capture gammas via Compton scattering. There are several cylindrical tubes embedded under the top layer of Pb stack, allowing calibration sources to be easily placed underneath each tank. One layer of 2 inch lead bricks are placed on top and three sides of each tank for background gamma shielding. The south tank is further elevated by an additional layer of lead bricks to make the gap between the two tanks smaller by letting the cap margins overlay. The

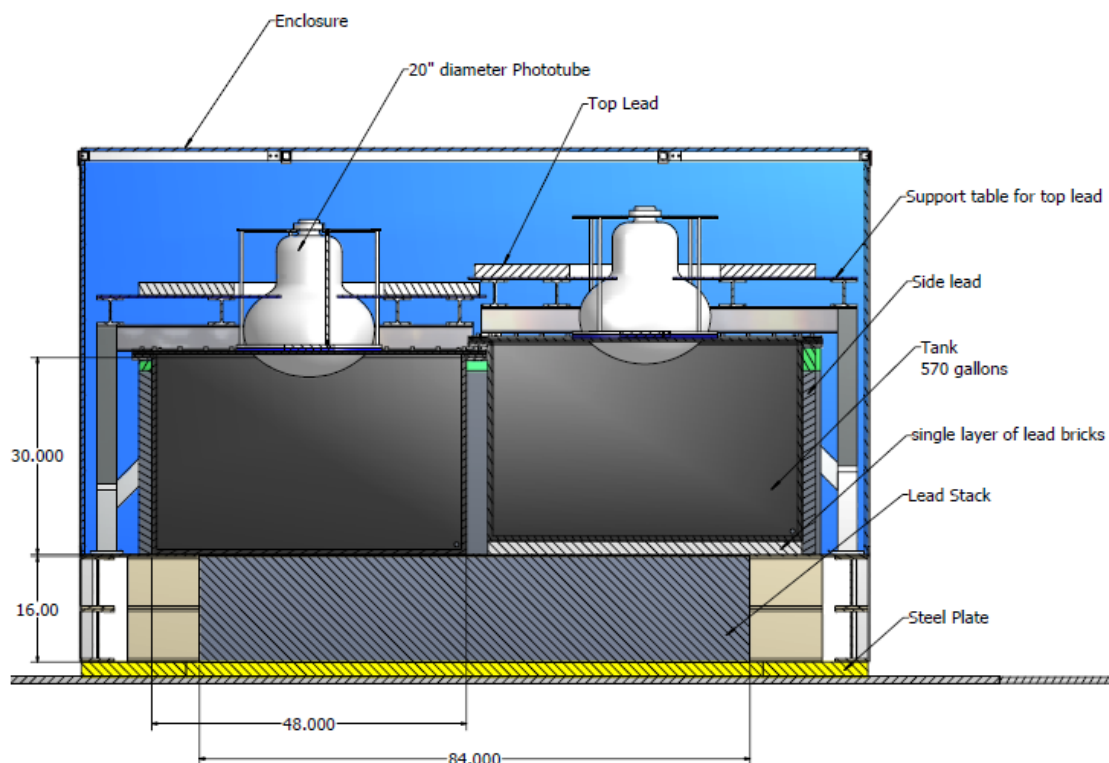


Figure 3.1: The profile drawing of the Neutron Multiplicity Meter (NMM). A stack of 16 inches high, 20 tonne lead serves as the target mass, with a footprint of 84×80 inches. Atop of the lead stack are two tanks of water, each 2 tons. On top of each water tank, there are two 20 inch KamLand PMTs, 4 in total, with the surfaces immersed in water. Both tanks aligning with the longer side of each other creates an essentially 96×96 inch square area, though there is a small gap in between two tanks due to the longer extents of their caps. One layer of 2 inch lead bricks are placed on top and three sides of each tank for background gamma shielding. The south tank is further elevated by an additional layer of lead bricks to make the gap between the two tanks smaller by letting the cap margins overlay.

water is Gd-loaded in forms of Gadolinium Trichloride. The two tanks have different concentrations of gadolinium: the south tank has 0.3% Gadolinium Trichloride, or effectively 0.2% Gd, and the north tank 0.7%, effectively 0.4% Gd. This will result in different capture times in the two tanks: the secondary neutrons are captured faster in the north tank than in the south tank. The water also

has approximately 1 ppm of Amino-G Salt, a water soluble wavelength shifter. The acrylic tanks are lined inside with highly reflective sintered Halon, with a diffuse reflectivity of approximately 94% [60].

3.3.2 Trigger, Electronics, and DAQ

The signal of the detector is based on the PMT collection of the photons emitted via Cherenkov effect by the Compton scattered high-speed electrons resulting from neutron-capture gammas. The detector trigger is designed based on the pulse multiplicity of the event in both tanks. The logical AND is defined for each tank as both PMTs firing a pulse above a 10 mV threshold within 160 ns of each other. The 160 ns coincidence time is set so to allow the photons resulting from the same neutron capture to reach both PMTs: the light may traverse the approximately 2 meter length of the water tank, and reflect on the order of ten times before hitting a PMT or being absorbed by the water. The requirement of coincident firing in both PMTs of each tank is set to suppress the false triggering by electronic noise and background gammas with very low energies. The multiplicity is defined as the number of logical ORs between the ANDs of the two tanks. Whether there is a single pair of coincident pulses in one tank, or a pair of coincident pulses in each tank taking place within 160 ns of each other to form a quadruple coincidence, the coincident pulses are counted as one in multiplicity. The trigger of an event is set on the total multiplicity within a given time window, e.g. triggering on multiplicity 5 in 60 μ s. It takes advantage of the characteristic timing distribution of the secondary neutron captures. The captures of the secondary neutrons and their resulting pulses are clustered in time toward the first one, while the background gamma-induced pulses spread evenly in time, therefore the setting of trigger on multiplicity for a given time interval will do a great job discriminating the gamma backgrounds. Once an event is triggered, a 100 μ s pre-trigger window and a 100 μ s post-trigger window from the trigger time are recorded. The DAQ system of the detector, constructed entirely from commercial modules, records digitized waveforms of each channel (PMT) over the 200 μ s window.

3.4 Data and Reduction

The digitized waveform of raw traces of events are reduced to data structures with amplitudes and times of coincident pulses of all four channels recorded on an event-by-event basis. The data are further processed to form the summed pulse amplitude from two PMTs in each tank, with averaged pulse time correspondingly. If all four channels fire above threshold with a timing so that the two averaged pulse times for tanks are in 160 ns of each other, namely a quadruple coincidence takes place, then the smaller summed pulse is removed, and the summed amplitude is added to the summed pulse in the other tank. The pulse time will be the average of the four. By this procedure, a neutron capture happening to fire all four PMTs at the same time will be counted as one multiplicity, instead of two. The summed pulse amplitudes with the treatment of quadruple coincidence, and the averaged pulse times are together recorded in a separate field called “quad” in the data structure, while the full information of the single channel pulses is kept as well.

3.4.1 Types of Events

It is worthwhile to consider several typical classes of detector events, to have a rough picture in mind before the description of analysis of the data.

Fast neutron event. This is the signal that the experiment is aimed to search. With the trigger construction discussed in the last section, the multiple pulses induced by the captures of secondary neutrons originated from the fast neutron interaction in Pb, taking place within a few tens of μs , would trigger a detector event of this type.

Multiple environmental gammas. The trigger for the fast neutron search guards strongly against environmental gammas triggering as a detector event, thanks to the clustering timing signature of the fast neutron events. However, there is still a fair chance to have multiple gammas firing pulses above threshold in the trigger time window, say 5 or more gamma-induced pulses in a

60 μ s trigger window. Instead of clustering toward the beginning of the trace as in the fast neutron events, they tend to spread out more evenly both in time and between tanks. They also have smaller pulse amplitudes in average. A likelihood analysis based on different pulse amplitude distributions of fast neutron events and multiple gamma events will be discussed in Chapter 5.

Muon event. Cosmic-ray muons can be considered as minimum ionizing particles when they pass through the detector water tanks, and the energy deposition in the detector is determined by the path length of the muon in water. Ideally, muons would fire a very large pulse in coincidence with both PMTs in a tank, or even in a quadruple coincidence, but the single multiplicity would not trigger an event. However, the extremely large pulses can cause the PMTs to fire multiple after-pulses. These fake pulses together with the initial large muon pulse may trigger the detector and be recorded as an event. In fact, more than 80% of the recorded events are muon events. In data analysis, typical muon events can be easily removed by setting a rejection cut on the pulse amplitude.

Clipping muon with spallation neutrons. If a muon passes through a water tank with a relatively small path, called “clipping”, and therefore deposits a smaller energy, its pulse may be too small to be identified as a muon based on its amplitude. Such a pulse is unlikely to cause after-pulsing. However, if the clipping muon hits the Pb target and causes neutron spallation, the resulting neutrons can be captured by Gd just as for a fast neutron. This type of event should not be confused with the fast neutron events. The neutron multiplicity of this type originates from the muon-induced spallation in Pb, and is an indirect measurement of the cosmic-ray muon energy, therefore it carries different information than that of a fast neutron event. The rate of these clipping events with initial pulse small enough to pass the muon rejection cut needs to be estimated as a background for the fast neutron events.

3.4.2 Useful Data Runs

With different trigger constructions and experimental setups, the detector can be set to run for different purposes. The types of resulting data sets are summarized below. Because the PMT gains were raised and rebalanced in April, 2011, during the data taking, each type of data run may fall into two periods of data-taking, low-gain runs and high-gain runs.

Cf-252 calibration runs. Having Cf-252 neutron source placed under each water tank, neutron calibration runs were taken with a multiplicity of 3 in 60 μ s trigger. The trigger on multiplicity was set to suppress random gamma triggers, but only on a moderate multiplicity threshold to allow Cf fission neutrons trigger efficiently. Both before and after the raising and rebalancing of the PMT gains, Cf-252 calibration runs were taken for each tank. In each run the tank was exposed for ~ 3 hours, resulting in $\sim 100,000$ events, including a few thousand events due to gamma background.

Co-60 calibration runs. The Co-60 gamma source was placed beneath each tank for a gamma calibration run. The trigger was set on multiplicity of 1 in 10 μ s. Each run has ~ 20 minute live time and $\sim 100,000$ events. Co-60 calibration runs were taken only with the low PMT gain.

U/Th background gamma exposures. Several data series were taken to sample the background gammas from ambient uranium and thorium, with a multiplicity of 3 in 60 μ s trigger, both before and after the raising and rebalancing of the PMT gains. In the further analysis of the data set, both rates and spectra of the U/Th background gammas are measured.

Fast-neutron search runs. The essential signal searches were taken with triggers on higher multiplicities to strongly suppress background gammas and efficiently trigger on fast-neutron events. There have been approximately 630 live days of fast-neutron search data collected in total, over low-gain and high-gain periods of running, with slightly different trigger settings.

- First fast-neutron search: multiplicity 5 in 60 μ s trigger, taken with the low PMT gains, collected data with ~ 158 days of live time.

- Second fast-neutron search: multiplicity 6 in $70\ \mu\text{s}$ trigger, taken with the high PMT gains, collected data with ~ 169 days of live times.
- Third fast-neutron search: multiplicity 4 in $50\ \mu\text{s}$ trigger, taken with the high PMT gains, collected data with ~ 303 days of live times.

The analysis of fast-neutron search data sets to measure the high-energy neutron flux and multiplicity distribution, as well as the usage of the calibration and background exposure data for helping the measurement, will be described in Chapter 5.

Chapter 4

Monte Carlo Study of the Neutron Multiplicity Meter

A Monte Carlo (MC) model based on Geant4 [61][62] has been created to simulate the NMM detector. The detector model includes all major components, except the steel support beams, the PMT mounts, and the non-immersed portion of the PMTs. An event in simulation begins with the emission of the primary particle, then the model simulates its propagation and interactions with the materials of detector. Subsequent Cherenkov lights emitted in the water tanks are treated as optical photons in Geant4. They propagate according to the parametrized optical properties of water, solute wavelength-shifter, wall reflector, etc., until reach the surface of PMTs and are recorded for offline processing. The reflectivity of the tank wall reflector, Halon in this case, is tuned to be 94% to best reproduce the asymmetry of the PMTs and the peak width in the parametrized muon simulation [60].

The MC package can be run with a detector-only setup to perform relatively fast simulations of calibration source runs, or it can be set up into the modeled Soudan cavern to carry out the simulations of cosmic muons and muon-induced high energy neutrons. The former type of simulations is used to calibrate the energy scale in the simulation processor to best reproduce the detector responses. The latter type of simulations includes rock surrounding the lab cavern. We may throw

only the Mei-Hime parametrized neutrons and simulate the detector responses as they are the signal we would detect with the NMM. However, a more comprehensive way is to throw cosmic muons on top of the rock layer. By doing so, the model simulates the interactions of the muons with rock and the generation of high-energy neutrons. Not only the high-energy neutrons, but also the primary muons and any secondaries may interact with the NMM detector. Thus this kind of simulation incorporates comprehensive information associated with the detection of the cosmogenic neutrons and rejection of backgrounds for the NMM.

4.1 Detector Responses and Energy Scale

Correct simulation of the event detection in the experiment requires accurate prediction of the detector responses to all involved particles. For neutron detection, the characteristic pulse amplitude spectrum comes from the smeared energy spectrum of the Gd neutron-capture gamma energy distribution. The smearing is primarily due to incomplete collection of the capture gammas in the water tanks and the uncertainty during the propagation and collection of the Cherenkov photons. The count of collected photons on the PMT surface is then converted to the pulse amplitude by multiplying an energy scale factor in mV/Photoelectron (PE). This conversion includes the information related to the amplifying process in the PMT dynode, and its uncertainty for the electron loss.

The Geant4-based MC model records the information of the PEs collected at the surfaces of PMTs when the simulation runs, and leaves the pulse height construction to the offline processor. The offline processor finds the photoelectrons clustered in time at a PMT to nominate a pulse with a pulse time and PE number and repeats the same procedure to find all pulses at each PMT. The PE number will be multiplied by the energy scale factor to convert to a pulse amplitude (or called pulse height) in mV, then added a random offset sampled from a gaussian function with a tuned width. For the two PMTs in the same tank, the processor determines if there are coincidence between the two

individual pulse traces according to the pulse times with a time window of 160 ns, and combines each pair of coincident individual pulses to form a summed pulse trace of the tank. The total pulse number from both tanks is the multiplicity of the event.

Accurate simulation of the pulse amplitudes will help correctly determine if there is a triggered coincidence when both PMTs collect a few photoelectrons, since the corresponding pulse heights may be close to the threshold. It helps predict event rate and pulse multiplicity. In addition, a muon rejection cut based on pulse height will be applied in the data analysis. Accurately simulating the pulse height distribution will help estimate the effectiveness of the cut for removing muon events and the efficiency to the high-energy neutron events.

4.1.1 Modeling Gadolinium Neutron Capture Gamma Emission

The energy scaling and spectrum smearing were tuned by M. Sweany by having the detector responses in simulations of ^{252}Cf neutron calibration, ^{60}Co gamma calibration, and a parametrized muon simulation reproduce the spectra in corresponding types of data [60]. The energy scale factor was tuned to 2.5 mV/PE, and the Gaussian convolution width to be

$$\sigma = 0.9\sqrt{\text{Pulse Height}}, \quad (4.1)$$

with pulse height in units of mV. The simulated responses made fair agreement with the corresponding spectra in data if (and only if) it was assumed that the lowest pulse height of most events is due to contamination from an accidental gamma. On the top of Figure 4.1 is a simulated ^{252}Cf neutron capture pulse height spectrum in M. Sweany's work compared with ^{252}Cf calibration data. The simulated spectrum makes fair agreement with multiplicity ≥ 3 events with the lowest pulse height in each event removed, but has obvious discrepancy with all pulse included multiplicity > 4 events. The interpretation is that the lowest pulse height in many events would be due to contamination from an accidental gamma.

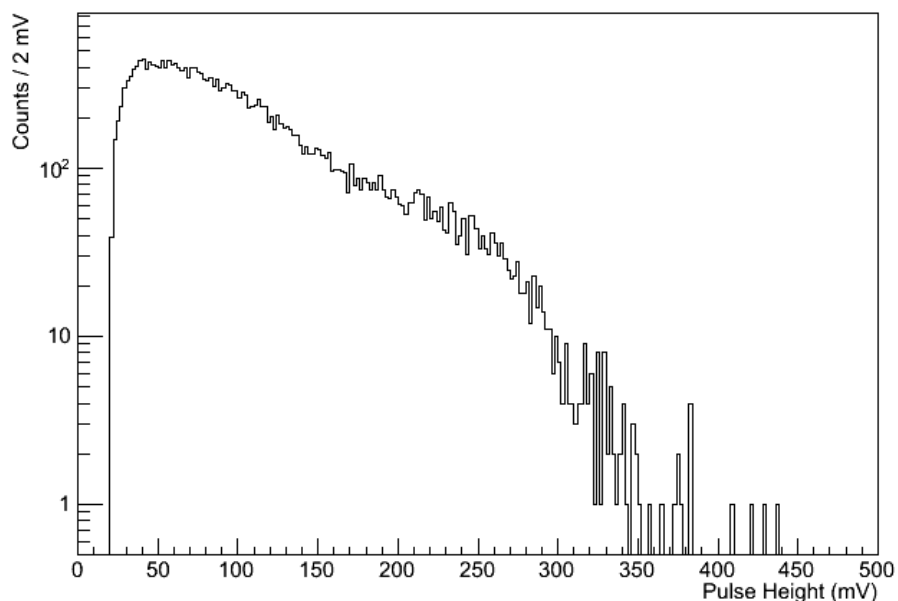
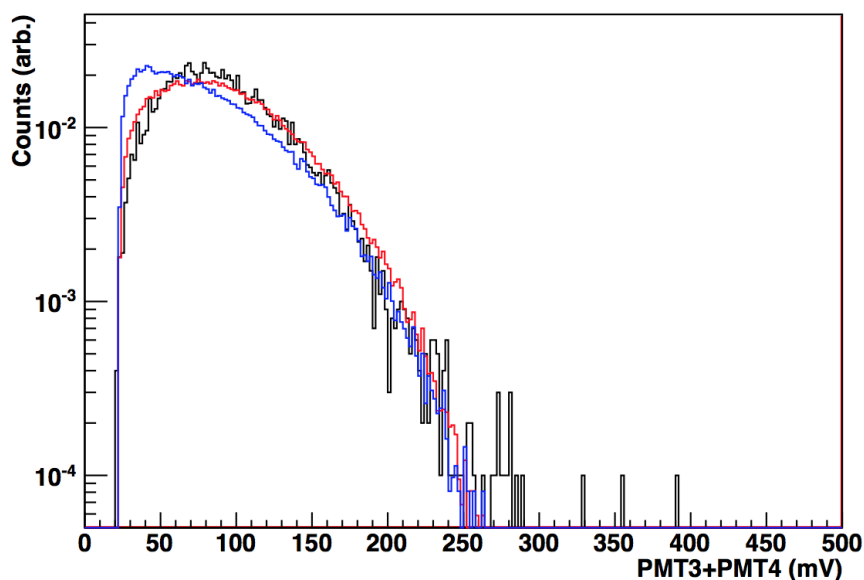


Figure 4.1: On the top is the tuned MC detector response compared with ^{252}Cf neutron calibration from M. Sweany's thesis. The black histogram is the summed response in simulation of a ^{252}Cf source placed beneath the center of a detector tank with Geant4.9.4.p04. The red histogram is ^{252}Cf calibration data, where only multiplicity ≥ 3 events are included but with the lowest pulse height in each event removed, and the blue histogram is all multiplicity = 4 events. On the bottom is the MC detector response in simulation of a ^{252}Cf source at the same location with Geant4.9.5.p01, using the same energy scale factor and smearing model as in M. Sweany's work. Note that agreement between data and old MC is fair only if lowest pulse-height is removed, but agreement is better with new GEANT MC at low pulse heights.

When M. Sweany tuned the energy scale and the convolution parameter, the MC software was built with Geant4.9.4.p04, which calculates the Gd neutron-capture gamma energies using the photon evaporation model [63]. As Geant4 updated to 9.5, the model associated with Gd neutron-capture gamma emission was changed to determine the capture gamma final state via the Geant4 Neutron Data Library (G4NDL) [64][65][45]. With the updated Geant4 neutron-capture gamma model but the same tuned parameters for pulse forming energy scaling and smearing, the simulation of ^{252}Cf neutron calibration results in a neutron capture pulse height spectrum shown in the bottom of Figure 4.1. The shape of this spectrum actually better resembles the low energy peak in the all-pulse included pulse height spectrum. The extra bump at relatively high energies implies that high-energy gammas may be simulated by the updated Geant4. If the bump does not appear on the ^{252}Cf neutron data, then the MC should need more smearing to obtain a smooth spectrum.

The updated model predicts a different individual gamma emission spectrum than that predicted by the photon evaporation model. The individual gamma emission spectrum better resembles the measured Gd neutron-capture gamma spectrum from literature [66], especially the high-energy gamma lines. Figure 4.2 shows the comparison of individual gamma energy spectra predicted by the two models, along with the measured gamma energy spectra of ^{155}Gd , ^{157}Gd [66], and natural Gd [67]. This explains the extra bump around relatively high energies in the simulated neutron spectrum with updated Geant4. More careful estimate of gamma background in the time of an event according to measured gamma rate shows that the probability of coincidence with a gamma pulse in a trigger neutron event is $\sim 0.07 \pm 0.003$, far less than the level of ~ 1 gamma per event. Thus the assumption that the lowest pulse height of each event is due to gamma contamination is not correct. The problem was with the old simulation; the pulse height spectrum predicted by the updated Geant4 is much more similar to the all-pulse included spectrum at low energies.

The energy scale and smearing parameter tuned with inaccurate capture gamma model therefore does not reflect correct properties of the detector. In addition, the PMTs have been rebalanced and tuned to a slightly higher gain since May, 2011. The data taken before and after the change

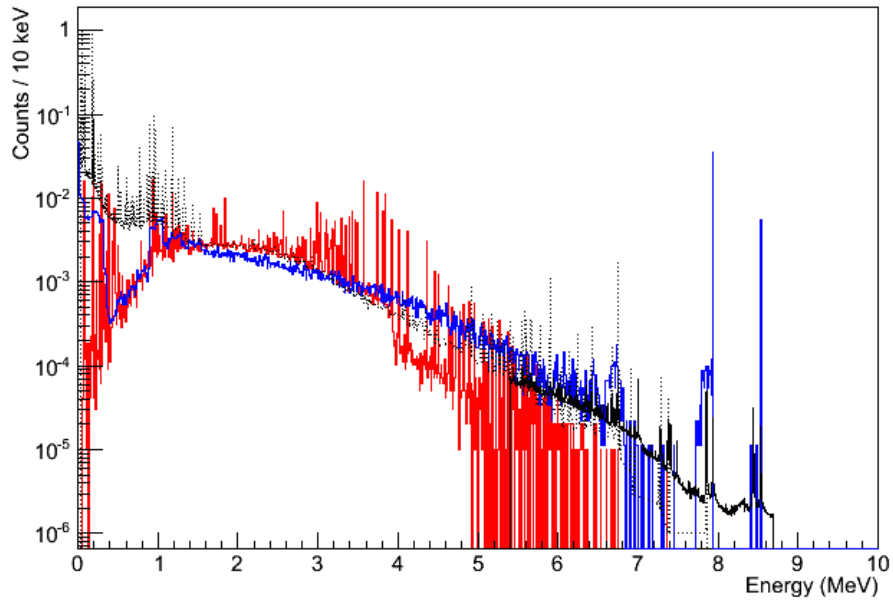


Figure 4.2: The comparison of individual gamma emission spectra of gadolinium neutron captures from Geant4 simulations and measurements. The simulated individual gamma emission spectrum from Geant4.9.4.p04 (photon evaporation model) is shown in red, and the individual gamma spectrum from Geant4.9.5.p01 (G4NDL) is shown in blue. The measured individual gamma spectrum from ^{155}Gd and ^{157}Gd together [66] is shown in black solid line, and the spectrum measured from natural Gd [67] is shown in black dashed line. G4NDL agrees with the measured spectra much better than photon evaporation model at high energy. At low energies, both models show discrepancy with the measured spectrum. But gammas at such low energies are likely below Cherenkov threshold and therefore less important.

should drive the MC offline processor into different sets of parameter values, and result in their MC detector responses accordingly. Therefore, the MC offline processor needed to be recalibrated with the updated Geant4 capture gamma model compared to the calibration data taken both before and after the PMT gain raise.

4.1.2 Recalibration of Energy Scale Factors

The updated capture gamma model features the high-energy gamma lines ~ 8 MeV, which cause an extra bump at relatively high pulse heights in the simulated detector response of ^{252}Cf calibration. The measured detector response in ^{252}Cf calibration runs don't carry an obvious bump feature. We modified the smearing model, and tried to fit the ^{252}Cf neutron response by varying the energy scale factor and smearing parameters. The attempt of fitting has shown that it is very difficult to wash out the bump feature in the MC detector response and have the MC response match the measured spectra. It could be due to some unknown deficiency on light collection or pulse measurement.

Although it is difficult to tune the energy scale and smearing parameters with ^{252}Cf neutron spectra, the energy scale may be tuned first using the pulse spectrum of muon events. A muon ionizes water molecules along the path when it penetrates the water tanks. The energy deposition of a muon is proportional to its path length in water, thus the shape of the muon spectrum is determined together by the size of water tanks and the angular distribution of the muon flux. The peak of the muon spectrum is at a much higher energy compared with neutron capture peak, thus the smearing effect at neutron capture energies becomes insignificant for the muon peak. In addition, the simulated muon spectrum is well known. Therefore, the energy scale factor as an overall conversion factor for all PMTs can be calibrated by fitting the muon spectrum in Monte Carlo and in real data assuming no smearing effect in the PMTs. If there are small unbalances among the four PMTs, it should be sensitive to the PMT asymmetry and may be tuned later along with smearing parameters using ^{252}Cf neutron calibration data.

We do not have dedicated data runs tuned for recording muon events, but we may extract muon events from the fast neutron search data. When a muon penetrates the water tanks and the lead stack, there is a high chance for the muon to cause neutron spallations in the lead stack. The spallation neutrons will then create a multiple neutron capture signature along with the initial high energy pulse indicating the primary muon. These events are picked up by the event trigger on multiplicity.

To simulate the same type of events, we sampled the primary muons from the data set generated by A. Reisetter using the MUSIC/MUSUN simulation package [68], based upon the geology and geometry of the rock overburden and observations of the muon energy, momentum, and angular distribution in the underground laboratory. In our simulation, the primary muons are initiated on top of a 4 m rock layer above the cavern ceiling, and a subset of them will hit the NMM detector then reproduce the reactions in the lead stack, thermalization and capture of neutrons, etc.

The energy of muon pulse is proportional to the muon's path length in the water tanks. And a muon with a longer path length in water generally has a longer path length in the lead stack, which results in a greater chance to cause spallations and produce more secondary neutrons. Therefore, the energy distribution of the selected muon events is not independent of the multiplicity of the events. To make a fair comparison, we should compare the muon events in MC and real data with the same multiplicity, or select the events with the same lower limit of multiplicity.

However, the multiplicity of the muon events in real data are skewed by afterpulsing. A large pulse such as a muon induced pulse tends to cause several fake pulses, and raises the multiplicity of the events. Many muons which did not create spallation neutrons would be still picked up by the multiplicity-5 trigger due to afterpulsing. C. Nedlik's study [69] has shown that afterpulses are clustered towards the initial muon pulse and there is almost no afterpulsing 50 μ s after the initial pulse. Here we use a time window of 50–100 μ s since the initial large (> 1 V) pulse for event selection. Events of MC and real neutron search data with two or more pulses in this time window are selected, and the pulse height spectra are made of their initial large pulses. If the first pulse of an event is not large enough (> 1 V), then ignore it but check the next pulses until find a large pulse.

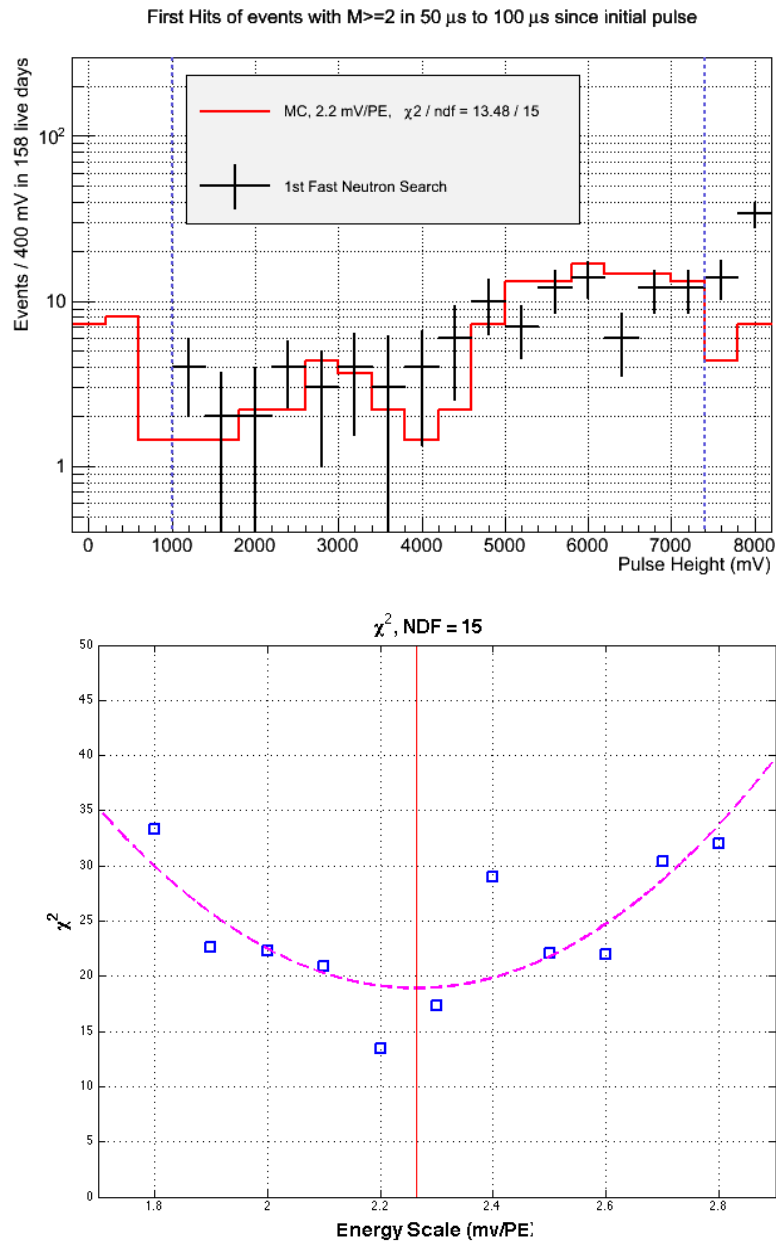


Figure 4.3: Fit of muon pulse height spectrum in MC with the measured muon pulse height spectrum from low-gain data set for tuning the low-gain energy scale factor in MC offline processor. On the top is a comparison of muon pulse spectrum from the 1st neutron search run (black with error bars) and the simulated muon spectrum with an energy scale factor of 2.2 mV/PE close to best fit (red histogram). The χ^2 for the fit is calculated in the range of 1 V–7.4 V. The range is chosen so to select muon pulses, instead of neutron capture pulses, and also to exclude the PMT gain saturation near 8 V. On the bottom is the χ^2 s of the fits for several trial values of energy scale (blue squares), and a quadratic function to fit with the distributions of the χ^2 s (magenta dashed line). The best-fit value of energy scale for the low PMT gain, marked with a red vertical line, is found to be 2.26 mV/PE at the minimum of the quadratic function. The p -value of the best fit is 0.21.

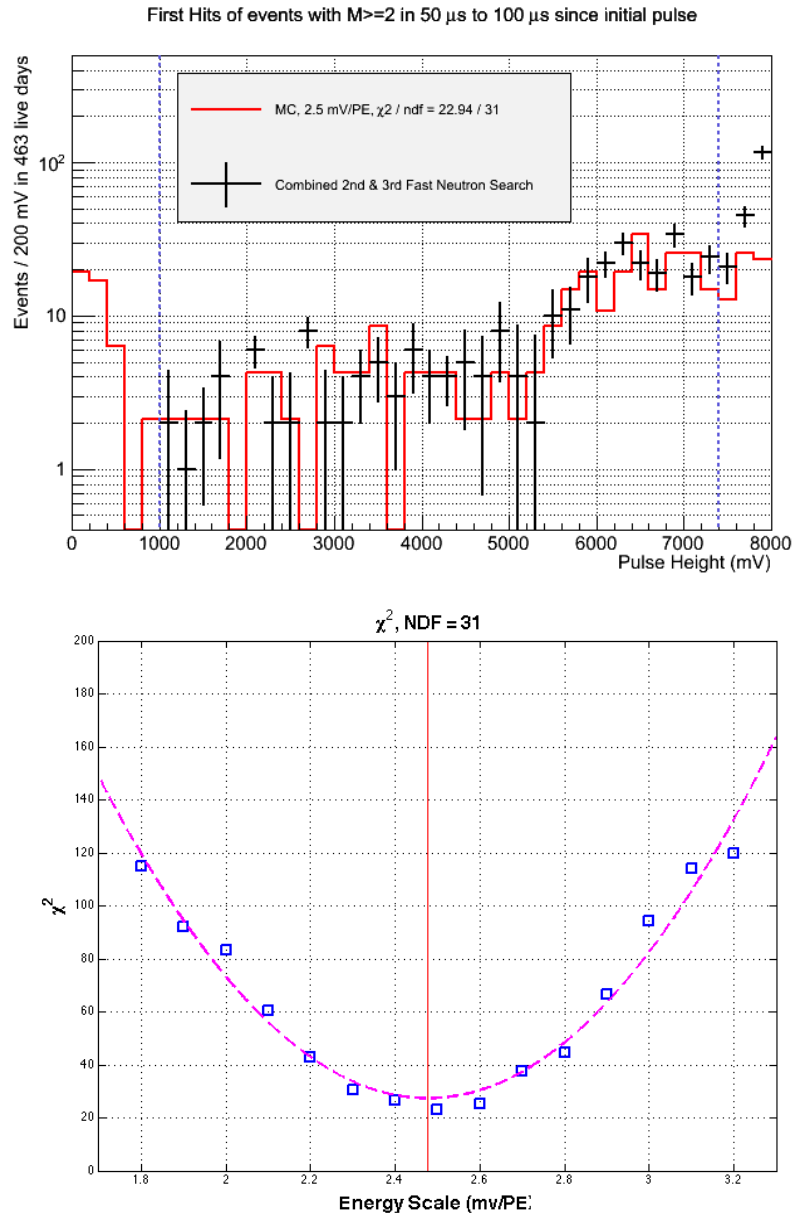


Figure 4.4: Fit of muon pulse height spectrum in MC with the measured muon pulse height spectrum from high-gain data set for tuning the high-gain energy scale factor in MC offline processor. On the top is a comparison of muon pulse spectrum combined from the 2nd & 3rd neutron search runs (black with error bars) and the simulated muon spectrum with an energy scale factor of 2.5 mV/PE close to best fit (red histogram). The χ^2 for the fit is calculated in the range of 1 V–7.4 V. The range is chosen so to select muon pulses, instead of neutron capture pulses, and also to exclude the PMT gain saturation near 8 V. On the bottom is the χ^2 s of the fits for several trial values of energy scale (blue squares), and a quadratic function to fit with the distributions of the χ^2 s (magenta dashed line). The best-fit value of energy scale for the high PMT gain, marked with a red vertical line, is found to be 2.48 mV/PE at the minimum of the quadratic function. The p -value of the best fit is 0.88.

We do this to avoid missing the muon pulse of the events in which an accidental background gamma is recorded before the muon pulse. We also apply a pulse height likelihood cut (will be discussed in Chapter 5) to real data that the neutron likelihood parameter $L > 0.99$ to reject afterpulsing and background gammas. With this method, we can make a fair comparison of muon spectra of MC and real neutron search data.

We fit the pulse spectrum in MC with that in data by running the MC offline processor with different energy scale factors and calculate the χ^2 s for the data-MC comparisons. Then the χ^2 as a function of the energy scale is fit with a quadratic function to determine the best fit energy scale factor with the minimum of χ^2 . The results are shown in Figure 4.3 for the low-gain energy scale and Figure 4.4 for the high-gain energy scale. On the top of both figures are the comparisons of muon pulse spectrum in neutron search data and simulated muon spectrum with the energy scale close to the best fit. On the bottom of both are the χ^2 s for several trial values of energy scale, and quadratic functions to fit with the distributions of the χ^2 s. The low-gain fit, limited by the amount of the data, is not very constraining. The values of energy scales at the minima of quadratic functions are taken as the best fits, which is 2.26 mV/PE for low PMT gain, and 2.48 mV/PE for high PMT gain.

4.1.3 Recalibration of Smearing Parameters

Once the overall energy scale has been tuned to provide the best fit with the muon pulse spectrum, we apply it to process ^{252}Cf simulation data. The comparison of MC and ^{252}Cf calibration data can provide information on the smearing parameters.

The ^{252}Cf calibrations were performed by putting the ^{252}Cf source under the top lead plate beneath the center of the water tank for the calibration of the response in that tank and setting the trigger on multiplicity of 3 in 60 μs . Calibrations for both the south tank and the north tank were taken during the 1st fast neutron search (with relatively low PMT gains). After the PMT gains were

raised and rebalanced, both calibrations were taken again with the high PMT gains, which were used for the 2nd and 3rd fast neutron searches.

Each simulation of a ^{252}Cf calibration is performed with the same setup of the source location as the run of each tank. Then the overall energy scale factor tuned with muon pulse spectra for low gain and high gain is applied in the MC offline processor to produce the detector response in MC for low gain and high gain, respectively. Besides the overall energy scale factor, this time we can add a random shift to the pulse height of each event to smear the pulse height spectrum, and comparing the resulting spectrum to the calibration data, we should be able to find the values of parameters that can well model the smearing effect in PMTs.

The previous model of the Gaussian width for the smearing effect, which is described in equation (4.1), is over-simplified. The electronic noise in the DAQ can cause intrinsic smearing on the pulse height no matter how many PEs the pulse includes. We modify the model of the Gaussian width as

$$\sigma = \sqrt{s_0^2 + s_1^2 \cdot [\text{Pulse Height}]}, \quad (4.2)$$

with pulse height in unit of mV. Here s_0 is the statistical uncertainty due to electronic noise, measured as 2.3 mV for every single PMT, and s_1 is a free parameter that needs to be tuned by fitting the MC with ^{252}Cf calibration data.

We select events with multiplicity $3 \leq M \leq 6$ and collect the pulses in the pre-trigger time $-60-0 \mu\text{s}$ to form the pulse height spectrum. Then the measured U/Th gamma background spectrum is subtracted from the raw ^{252}Cf pulse spectrum with appropriate normalization. By tuning the smearing parameter s_1 in the simulated detector responses of ^{252}Cf neutron captures, we found that the good fits would never be made with the overall energy scale factor tuned by muon spectrum fitting. However, we may use the PMT asymmetry as the handle to find out the value of s_1 best

describing the smearing effect in PMTs. The PMT asymmetry is defined as

$$\text{Asymmetry} = \frac{[\text{East PMT Pulse}] - [\text{West PMT Pulse}]}{[\text{East PMT Pulse}] + [\text{West PMT Pulse}]}, \quad (4.3)$$

for a pair of coincident pulses from the two PMTs of a water tank. The larger the value of s_1 in the offline MC processor, the wider the distribution of PMT asymmetries.

Small unbalances between east and west PMTs are known to exist. By fitting the channel asymmetry, the energy scale factor should also be tuned slightly around the fit value with muon spectrum comparison. I do this by adding and subtracting the same value on the energy scale factors of east and west PMTs, called East-West Adjustment, respectively, and vary this small adjustment to find the best fit with the asymmetry distribution, shown in Figure. 4.5, 4.6, 4.7, and 4.8. Table 4.1 summarizes the resulting best-fit East-West Adjustment values.

Once the best fit of the East-West Adjustment is found, we use it as a tuned parameter and vary the smearing parameter s_1 . It is reasonable to assume all the PMTs have the same smearing for a certain gain setting. We sum the χ^2 s for south tank and north tank at the same value of s_1 , and do a combined quadratic least-square fit to find the best fit value of s_1 for a certain gain setting. An example of PMT asymmetry comparison between MC and ^{252}Cf neutron data for the south tank with low PMT gain is shown on the top of Figure 4.9, and the plot on the bottom of the same figure shows the distribution of χ^2 against the value of s_1 for the PMT asymmetry comparisons with both tanks combined. The best-fit value of s_1 is chosen at the minimum of quadratic fit of the χ^2 s. The same plots for high PMT gain calibration is shown in Figure 4.10.

The best fit values of the parameters of MC energy scale and smearing are summarized in Table 4.1, including the adjusted energy scale factors of each single PMT, calculated by adding and subtracting the East-West Adjustment on the overall energy scale factors.

The best fit of energy scales with proper adjustment between east and west PMTs and tuned smearing parameters still result in the simulated ^{252}Cf neutron spectra with the feature of a bump

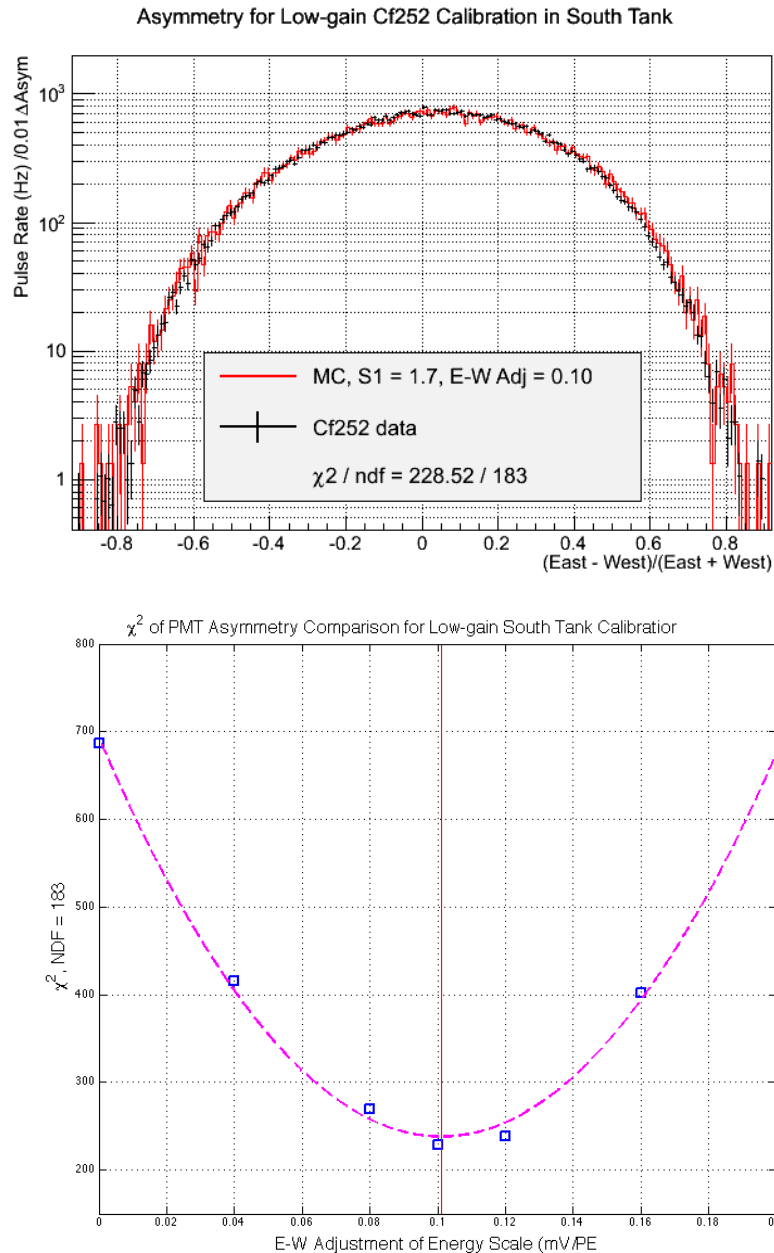


Figure 4.5: Fit of the PMT asymmetry distribution from ^{252}Cf neutron simulation with that from ^{252}Cf calibration run during the time of low PMT gain for the south tank to tune the East-West Adjustment on PMT energy factors. On the top is a comparison of the PMT asymmetry distribution from low-gain ^{252}Cf calibration data for the south tank (black with error bars) and the PMT asymmetry distribution from simulation with $s_1 = 1.7$ as a trial value and East-West Adjustment = 0.10 close to the best fit (red with error bars). On the bottom is the χ^2 s of the fits for the south tank for several trial values of East-West Adjustment (blue squares), and a quadratic function to fit with the distributions of the χ^2 s (magenta dashed line). The best-fit value of East-West Adjustment for the south tank with the low PMT gain, marked with the red vertical line, is found to be 0.101 at the minimum of the quadratic function.

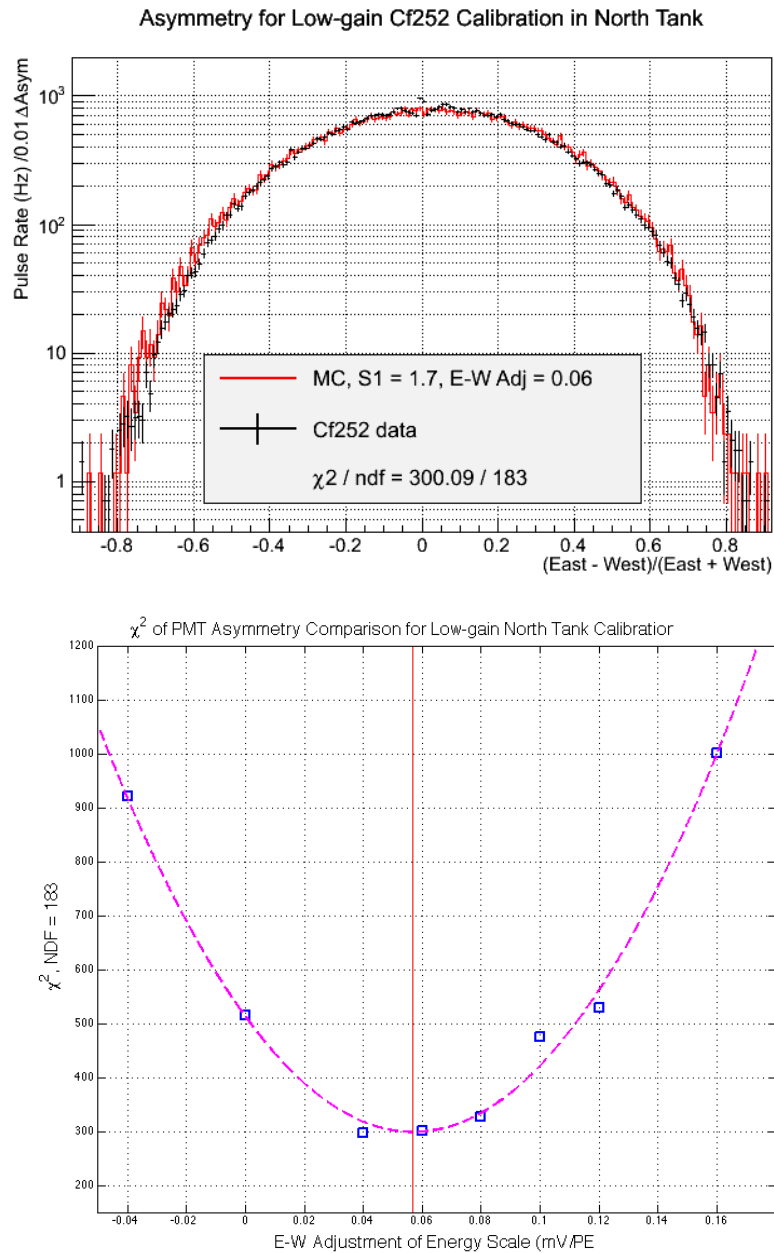


Figure 4.6: Fit of the PMT asymmetry distribution from ^{252}Cf neutron simulation with that from ^{252}Cf calibration run during the time of low PMT gain for the north tank to tune the East-West Adjustment on PMT energy factors. On the top is a comparison of the PMT asymmetry distribution from low-gain ^{252}Cf calibration data for the north tank (black with error bars) and the PMT asymmetry distribution from simulation with $s_1 = 1.7$ as a trial value and East-West Adjustment = 0.06 close to the best fit (red with error bars). On the bottom is the χ^2 s of the fits for the north tank for several trial values of East-West Adjustment (blue squares), and a quadratic function to fit with the distributions of the χ^2 s (magenta dashed line). The best-fit value of East-West Adjustment for the north tank with the low PMT gain, marked with the red vertical line, is found to be 0.057 at the minimum of the quadratic function.

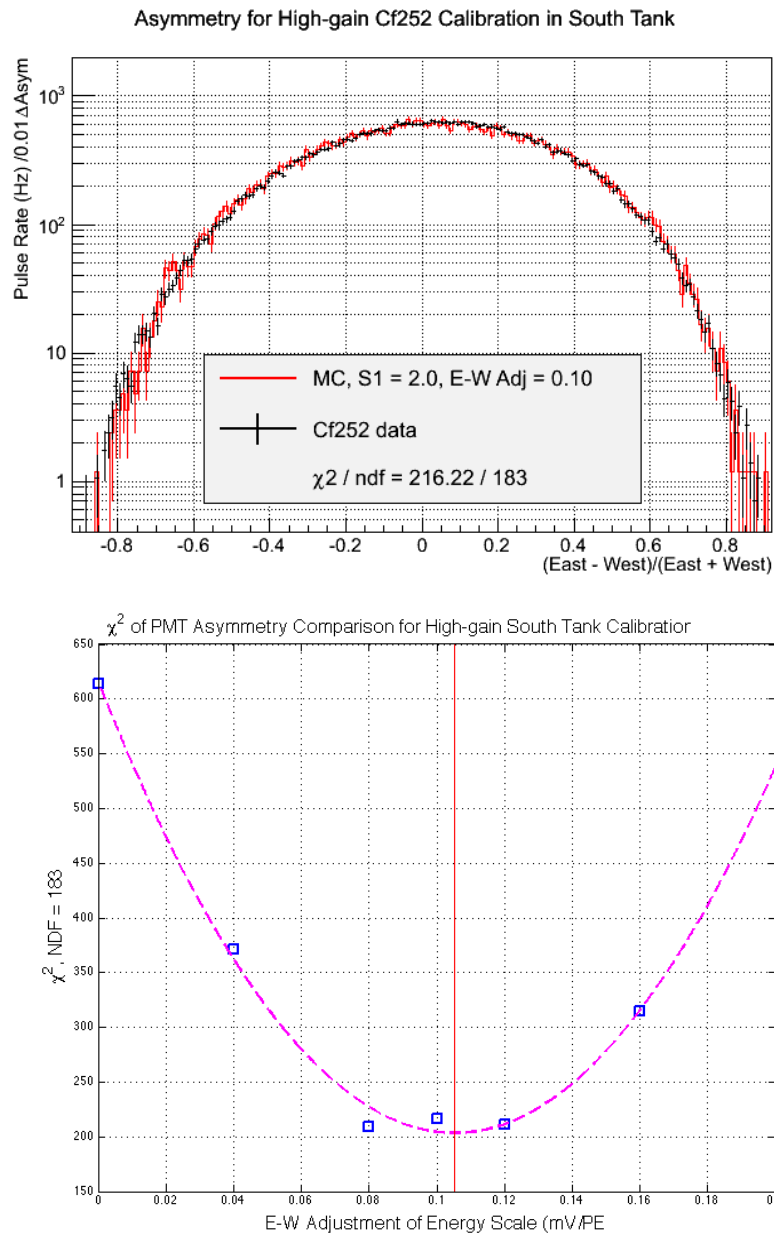


Figure 4.7: Fit of the PMT asymmetry distribution from ^{252}Cf neutron simulation with that from ^{252}Cf calibration run during the time of high PMT gain for the south tank to tune the East-West Adjustment on PMT energy factors. On the top is a comparison of the PMT asymmetry distribution from high-gain ^{252}Cf calibration data for the south tank (black with error bars) and the PMT asymmetry distribution from simulation with $s_1 = 2.0$ as a trial value and East-West Adjustment = 0.10 close to the best fit (red with error bars). On the bottom is the χ^2 s of the fits for the south tank for several trial values of East-West Adjustment (blue squares), and a quadratic function to fit with the distributions of the χ^2 s (magenta dashed line). The best-fit value of East-West Adjustment for the south tank with the high PMT gain, marked with the red vertical line, is found to be 0.105 at the minimum of the quadratic function.

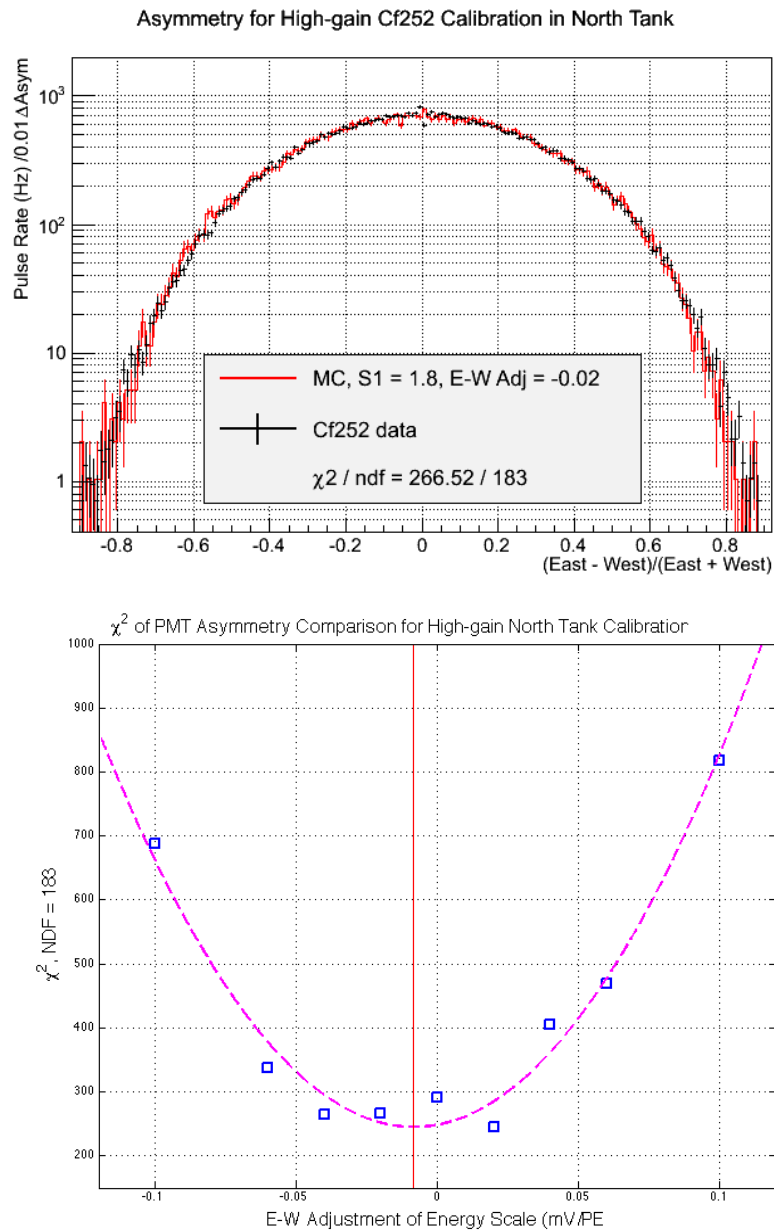


Figure 4.8: Fit of the PMT asymmetry distribution from ^{252}Cf neutron simulation with that from ^{252}Cf calibration run during the time of high PMT gain for the north tank to tune the East-West Adjustment on PMT energy factors. On the top is a comparison of the PMT asymmetry distribution from high-gain ^{252}Cf calibration data for the north tank (black with error bars) and the PMT asymmetry distribution from simulation with $s_1 = 1.8$ as a trial value and the East-West Adjustment = -0.02 close to the best fit (red with error bars). On the bottom is the χ^2 s of the fits for the north tank for several trial values of East-West Adjustment (blue squares), and a quadratic function to fit with the distributions of the χ^2 s (magenta dashed line). The best-fit value of East-West Adjustment for the north tank with the high PMT gain, marked with the red vertical line, is found to be -0.008 at the minimum of the quadratic function.

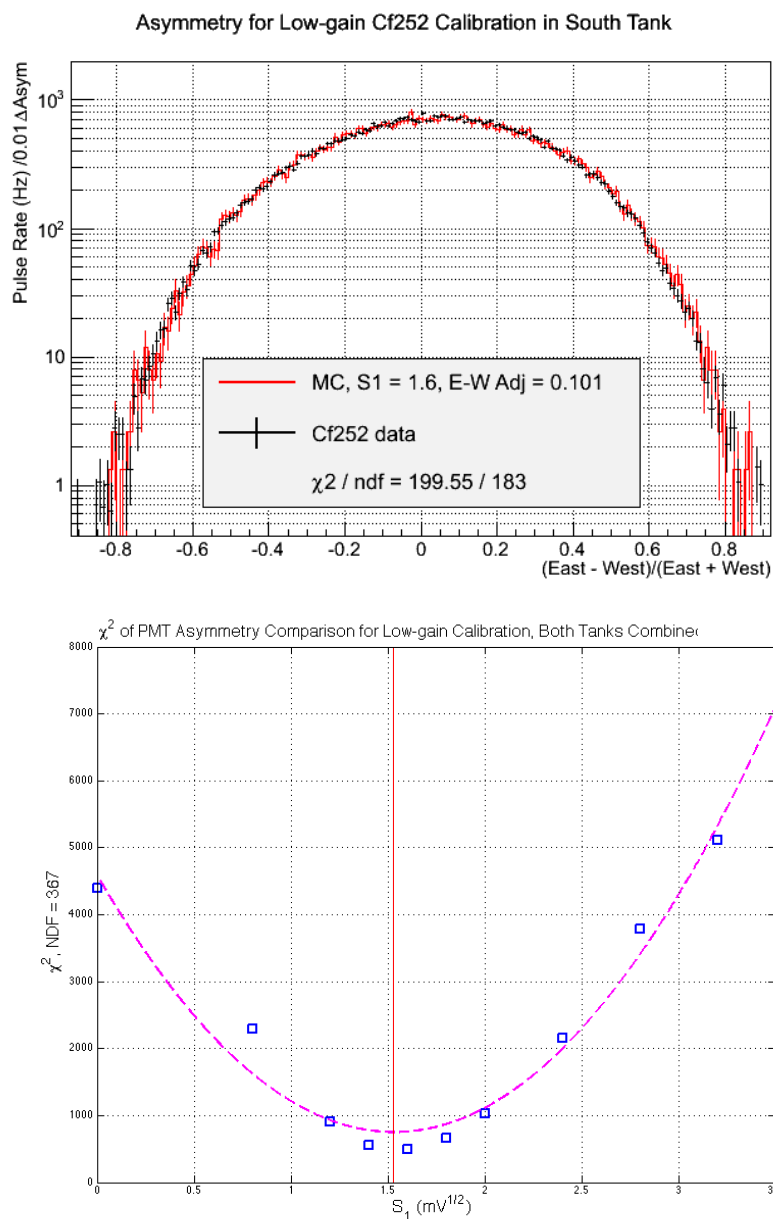


Figure 4.9: Fit of the PMT asymmetry distribution from ^{252}Cf neutron simulation with that from ^{252}Cf calibration run during the time of low PMT gain for tuning the smearing parameter s_1 . On the top is a comparison of the PMT asymmetry distribution from low-gain ^{252}Cf calibration data for the south tank (black with error bars) and the PMT asymmetry distribution from simulation with tuned E-W adjustment and $s_1 = 1.6$ value close to the best fit (red with error bars). On the bottom is the χ^2 s of the fits summed over south tank and north tank for several trial values of s_1 (blue squares), and a quadratic function to fit with the distributions of the χ^2 s (magenta dashed line). The best-fit value of s_1 for the low PMT gain, marked with red vertical line, is found to be $1.53 \text{ mV}^{1/2}$ at the minimum of the quadratic function.

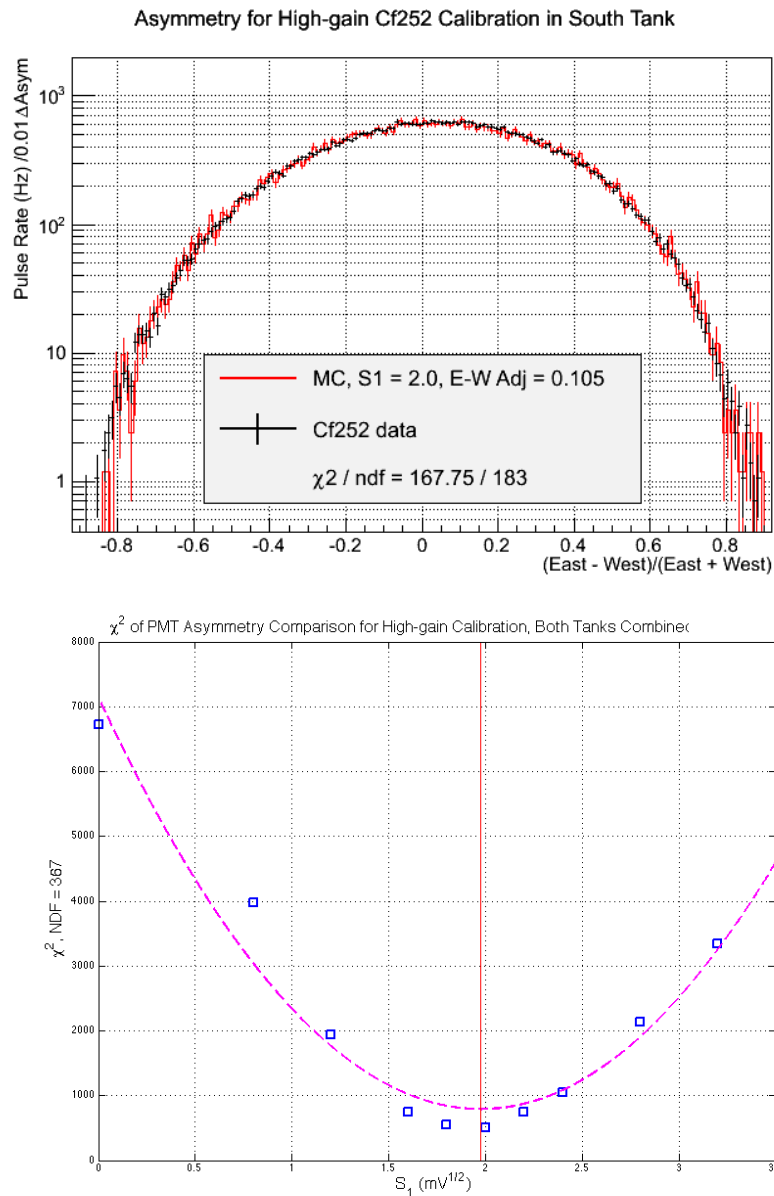


Figure 4.10: Fit of the PMT asymmetry distribution from ^{252}Cf neutron simulation with that from ^{252}Cf calibration run during the time of high PMT gain for tuning the smearing parameter s_1 . On the top is a comparison of the PMT asymmetry distribution from high-gain ^{252}Cf calibration data for the south tank (black with error bars) and the PMT asymmetry distribution from simulation with tuned E-W adjustment and $s_1 = 2.0$ value close to the best fit (red with error bars). On the bottom is the χ^2 s of the fits summed over south tank and north tank for several trial values of s_1 (blue squares), and a quadratic function to fit with the distributions of the χ^2 s (magenta dashed line). The best-fit value of s_1 for the high PMT gain, marked with red vertical line, is found to be $1.97 \text{ mV}^{1/2}$ at the minimum of the quadratic function.

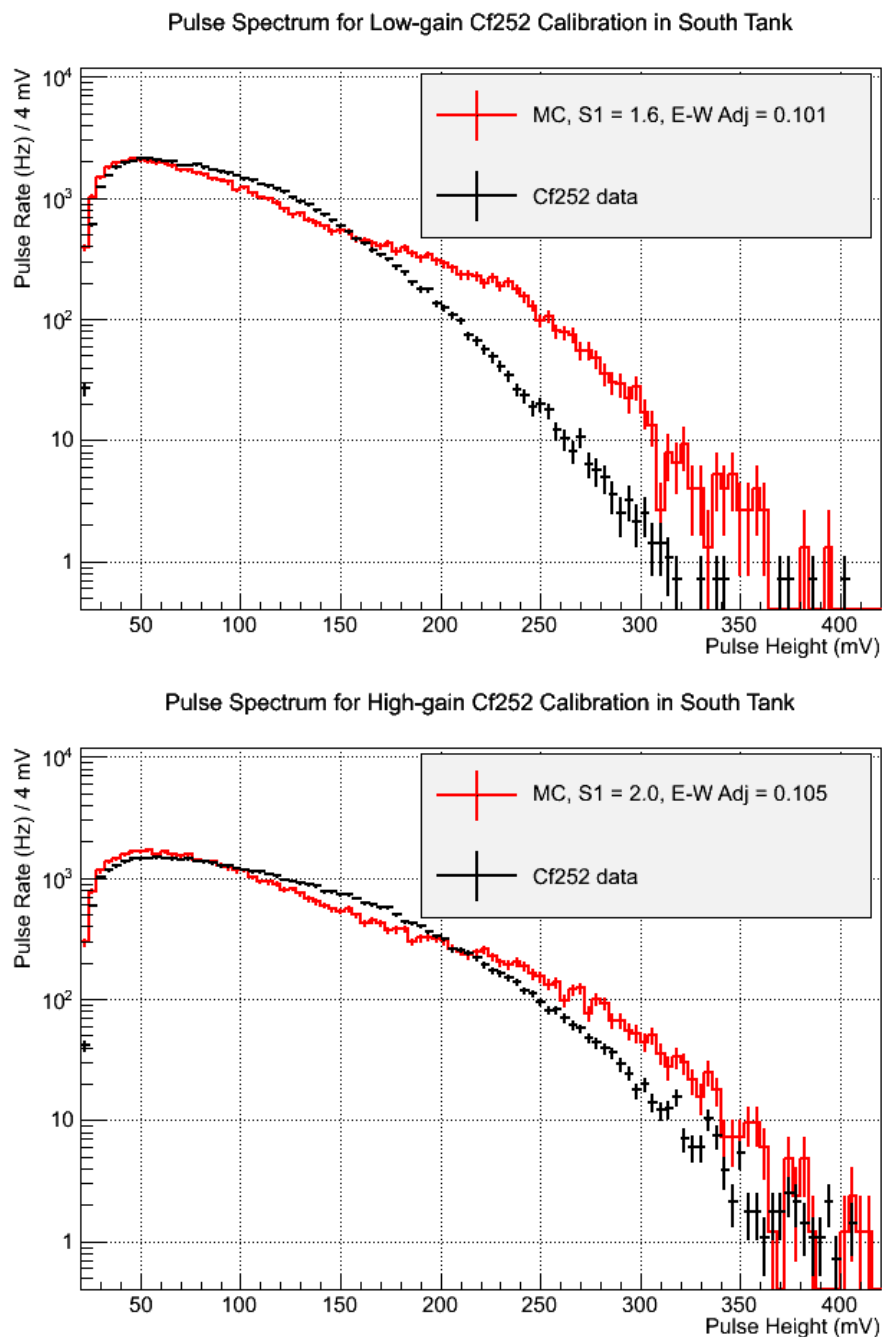


Figure 4.11: The comparison of ^{252}Cf neutron pulse height spectra from simulations with tuned PMT energy scale and smearing parameters in this work (red) and the pulse height spectra measured in ^{252}Cf neutron data (black). On the top is the comparison for low PMT gain using south tank data. On the bottom is the comparison for high PMT gain using south tank data.

Table 4.1: Summary of best-fit values of energy scales and smearing parameters in the MC offline processor. The values of overall energy scale result from the fits shown in Figure 4.3 and 4.4. The East-West Adjustment is the value added to the east PMT and subtracted from the west PMT of the best fit energy scale factor for a PMT gain setting, to fine-tune the energy scale factors for the single PMTs. The fits of East-West Adjustment are shown in Figure 4.5, 4.6, 4.7, and 4.8. Smearing parameters s_1 is defined with Eq. (4.2) and the fits for the values are shown in Figure 4.9 and 4.10.

	Overall Energy Scale (mV/PE)	East-West Adjustment (mV/PE)		Single PMT Energy Scale (mV/PE)				Smearing Parameter s_1 (mV ^{1/2})
		South	North	SE	SW	NE	NW	
Low-gain	2.26	0.101	0.057	2.361	2.159	2.317	2.203	1.53
High-gain	2.48	0.105	-0.008	2.585	2.375	2.472	2.488	1.97

around ~ 250 mV, as shown in Figure 4.11 for south tank data of both low and high PMT gains. This is definitely not a perfect reproduction of the detector response. The reason for this remaining discrepancy is likely from the optical part of simulation. An all-included muon simulation resulting in a large amount of data was performed with the updated version of Geant4 but the optical parameters had been tuned with older version of Geant4. Thus to study the results of the all-included muon simulation, we could only tune the parameters in the offline processor. However, the spectra show good agreement at pulse heights less than ~ 60 mV, at which the trigger rate in MC is sensitive to the energy scale and smearing. The MC parameters tuned in this work would be able to minimize the systematic errors of the event rate in the simulation. The pulse height distributions of neutron captures are used to construct a pulse height likelihood function and a neutron-selection cut. But the function and cut are built with the measured spectra and applied to real neutron search data. On the other hand, the background leakage of the cut should be estimated with simulated muon events and sampled with U/Th gamma PDF. Therefore the disagreement at higher pulse heights will not be crucial to the neutron search data analysis.

4.2 A Comprehensive Simulation of Cosmic Muons and Muon-induced Neutrons

In order to understand the muon background, as well as the production and detection of the high-energy neutrons, instead of simulating the detector response of muon background and parametrized high-energy neutrons separately, we have performed a comprehensive muon simulation. The idea is to propagate cosmic-ray muons on top of a rock layer and directly simulate the interaction of muons in the cavern rock. The simulation includes the process of muon-induced hadronic showers and the initiation of the high-energy neutrons, which is the signal we are searching for in this experiment. It naturally incorporates the correlation between the high-energy neutron and the initial muon, i.e., help study the rate of a clean neutron-capture signal and the rate of a neutron-capture event accompanied by a direct hit of the initial muon on the detector.

The study of this simulation will serve two purposes. It can help the analysis of the fast neutron search data. It may reveal informative MC truth, which is useful for improving the data selection cuts, and the understanding of the content of detected events. Another purpose is to provide a simulated multiplicity spectrum, and use it to benchmark the measured multiplicity distribution. This comparison is one of the fundamental goals of the Neutron Multiplicity Meter experiment.

4.2.1 Simulation Setup

In the MC software, the detector model is placed in the cavern at the location of the NMM in the Soudan cavern. The cavern is $32\text{ m} \times 14.5\text{ m}$ large and 11 m high. The cavern model is surrounded by rock with 4 m thickness on its six sides, making a $40\text{ m} \times 22.5\text{ m}$ large and 19 m high “world” in the Geant4 MC software. In the comprehensive simulation, muons are initiated on the top surface and four sides of the “world”. Before propagating into the cavern, the muon may cause a hadronic shower and/or spallations in the 4 m thick ceiling and side wall rock, and the high-energy neutrons

generated by these processes in the rock surrounding the cavern are naturally included in the MC. The initial energy and incident angle of each muon is sampled from results of a simulation with cosmic-ray muons propagating from ground surface to the depth of the Soudan mine (2090 m.w.e.) using the MUSIC/MUSUN package [68]. The energy spectrum and angular distribution of the primary muons are shown in Figure 4.12. The energy spectrum and the angular distribution shown here are correlated, as muons at greater angles (smaller $\cos \theta$) are less likely to reach the depth, but those that do reach the depth are more likely to carry higher energies.

There are 3.384×10^7 primary muons simulated in this work, which covers the top surface as well as the four sides of the MC world. Of these, there are 2.159×10^7 primary muons started on the top surface. A flux through a horizontal surface should be used to compare with the measured muon flux at the Soudan site, $(2.0 \pm 0.2) \times 10^{-7} \text{ cm}^{-2} \text{ s}^{-1}$ [53]. Therefore, the live time of the comprehensive muon simulation is estimated as

$$\frac{2.159 \times 10^7}{2.0 \times 10^{-7} \text{ cm}^{-2} \text{ s}^{-1} \times (40 \text{ m} \times 22.5 \text{ m})} = 1.20 \times 10^7 \text{ s} \approx 138.8 \text{ days}. \quad (4.4)$$

Here the horizontal dimension of the MC world is used.

The MC software records not only the optical photons that hit the surface of PMTs as the raw data of detector response, but also the relevant MC truth, including position and momentum of any particle that is traversing the surfaces of water tank, lead stack, or cavern wall, as well as the positions and times of neutron captures.

4.2.2 Data Processing

The simulation records the times when optical photons hit the PMT surfaces relative to the beginning of each event. The first step of data processing is to find pulses from the raw simulated data of optical photon timing. The recorded photons are randomly selected with a probability based on the quantum efficiency of the PMT as a function of the photon wavelengths. The selected photons are

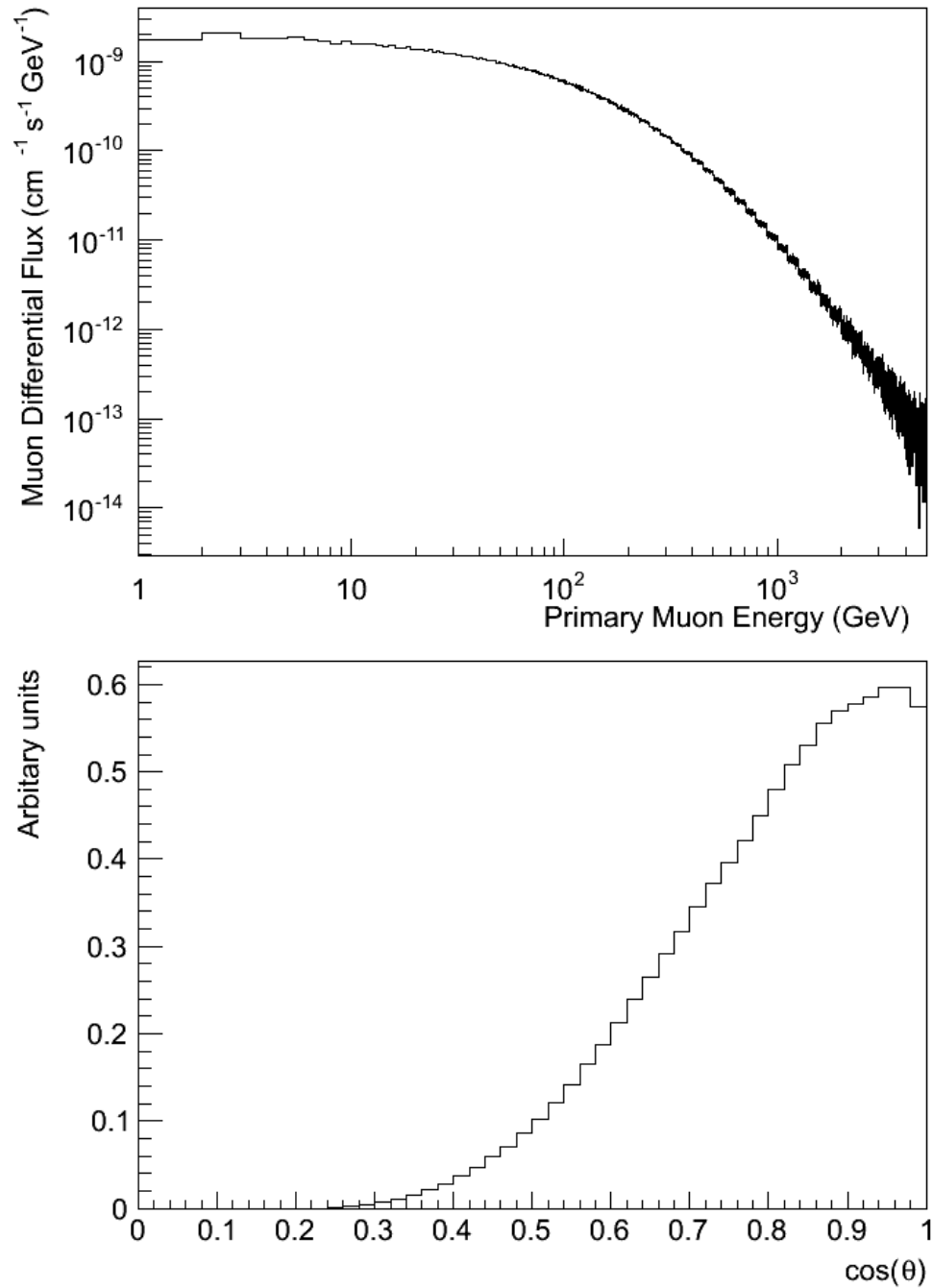


Figure 4.12: Primary muons in the comprehensive simulation. On the top is the energy spectrum of the primary muons used in this simulation. On the bottom is the angular distribution of the primary muons shown in cosine of the zenith angle, $\cos \theta$. The initial states of the muons are sampled from the results of a MUSIC/MUSUN simulation with cosmic-ray muons propagating from ground surface to the depth of the Soudan mine.

further recorded as photoelectrons. The processor then goes over the sequence of the photoelectron times in each PMT. When it finds a photoelectron, it groups all the later photoelectrons within 250 ns of the leading photoelectron as a pulse and counts as number of PEs in the pulse. Then it repeats the same way of combining PEs into pulses for the rest of the event. This forms a trace of pulses counted in PEs. The time of a pulse is calculated as the average time of all the photoelectrons within the pulse.

The pulses in real data are measured in volts. To be able to compare with data, the PE counts of simulated pulses need to be converted to mV by multiplying by an energy scale factor and applying a Gaussian random offset with a width controlled by smearing parameters. The energy scale factors and smearing parameters have been discussed in Section 4.1, and the tuned parameters shown in Table 4.1 are used to process the comprehensive muon simulation data.

For any single PMT channel, there is a 10 mV threshold for the pulse trigger in the detector DAQ settings. In the MC, pulses are therefore required to be at least 10 mV to “trigger”—to be further recorded. According to the parameters in Table 4.1, this is equivalent to triggering on ~ 5 PEs.

The triggered single PMT pulses are matched with the pulse trace in the other PMT of the same water tank to find coincidences in timing. If two pulses from both PMTs are within 250 ns of each other, we say that they are coincident pulses. The average pulse time of the two coincident pulses is called the coincident pulse time. All the coincident pulse times for the two PTMs form the coincident pulse trace of the water tank. The pulse of an individual PMT not coincident with any pulse in the other PMT will not be recorded in the coincident pulse trace. The pulse height sums over the coincident pulse pairs form a trace of summed pulse heights for the water tank.

The processor merges the coincident pulse traces of the two tanks into one pulse trace in chronological order for both coincident pulse times and summed pulse heights. There is a special circumstance that two coincident pulses in one tank are also coincident in time with the two coincident pulses in the other tank. We call it a quadruple coincidence. A set of quadruple coincident

pulses are usually caused by the same particle interaction. For quadruple coincident pulses, the pulse heights are added up again to form a single summed pulse height, and the pulse times are taken as the average over the two tanks.

With the procedure described above, the raw data of PMT photon hits are reduced to vectors (or traces) of coincident pulse timings and summed pulse heights. They are stored, along with the individual PMT pulse traces of timing and pulse heights from all four PMTs, to form the data structure of the event.

4.2.3 Monte Carlo Truth Analysis

It is important to link the pulse with its source recorded in Monte Carlo truth—the interaction in the detector that caused the pulse. For instance, a neutron capture in a water tank would illuminate the tank with Cherenkov light induced by capture gamma emission and fire the PMTs. Charged particles may ionize water or emit Cherenkov light when they pass through the water tanks, but instead of directly recording the interactions, particles are recorded when they traverse the boundaries of the water tanks, bottom lead, and cavern. All the available MC truth can be used to determine the sources of pulses.

PULSE-TAGGING ALGORITHM

The algorithm of tagging the pulse with its source is based on matching their timing. Figure 4.13 shows the distribution of time difference from a pulse back to the closest MC truth “event”, i.e. either a neutron capture in water tanks or a charged particle crossing the boundary of water tanks. The distribution of the time differences shows that the source events cause the resulting pulses in ~ 300 ns. Thus 300 ns is a proper time window for finding the coincidence between a pulse and its source. Any interaction recorded in MC truth taking place earlier than the 300 ns time window may be considered uncorrelated with the pulse.

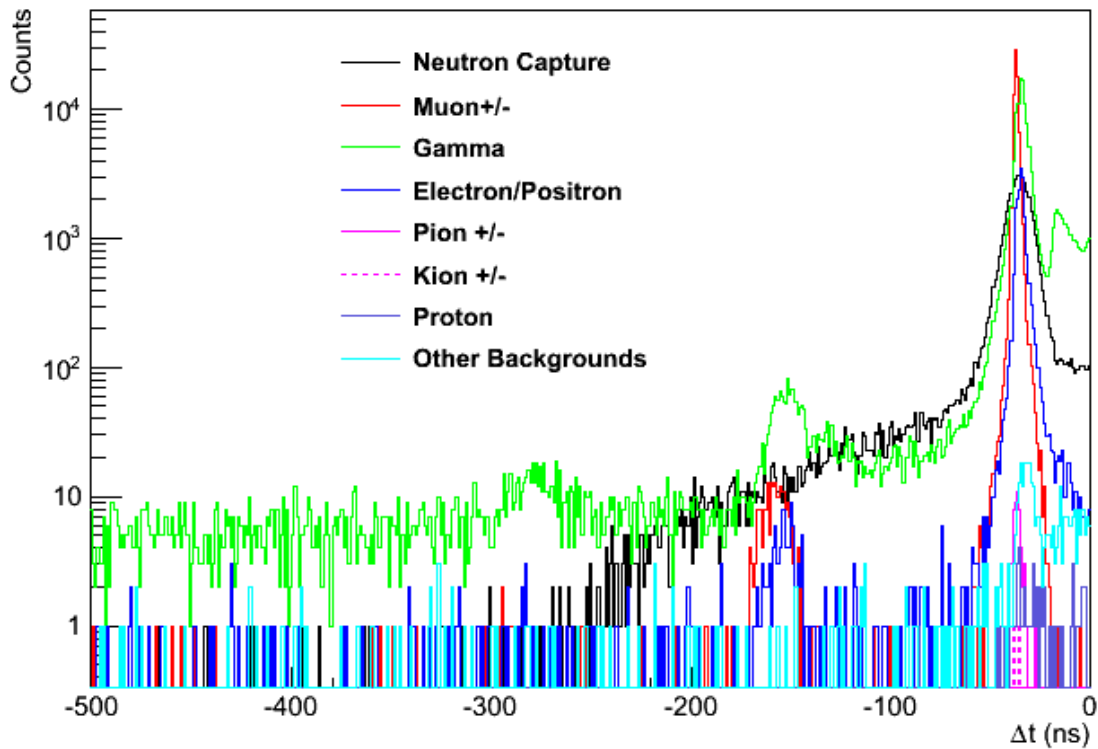


Figure 4.13: The difference in time between a pulse and the MC truth “event” taking place right before the pulse time. The MC truth “event” can be a neutron capture (in black), or any charged particle crossing the boundary of water tanks (in colors). In the plot, the timing difference is taken relative to the time of the pulse. The peaks in the time difference distributions show the correlation between an MC truth “event” and the pulse. The timing difference at the major peak is related to the size of the water tanks. The neutron captures take place within ~ 300 ns prior to the pulse. The flat tails for all types of MC truth “event” show the cases that the pulses are unrelated to the MC truth. The reason of the multiple peaks for charged particles is unclear.

The procedure is as follows.

1. First check in the 300 ns time window prior to the pulse to see if there is any neutron capture in the water tanks. If a neutron capture in the water tanks is found, the pulse is tagged as a neutron capture pulse.
2. If no neutron capture is found, then check if there is any charged particle traversing the boundary and flying into the water tanks. Label the pulse as “muon pulse” if the charged particles found in the 300 ns pre-time window include a muon. Tag the pulse as a “secondary charged particle pulse” if one or more charged particles, but no muons, are found. A muon pulse should be considered differently from the secondary charged particles induced by the muon.
3. If neither a neutron capture, nor any incident charge particle is found, which happens in rare cases, then consider the pulse as caused by a neutron capture in the acrylic wall of the water tanks. That is because only neutron captures taking place in water were recorded when the simulation was running, but the wall of the water tanks made of acrylic can also capture neutrons with the hydrogen nuclei. In the simulation, the logical boundary of the water tanks was set as the outer boundary of the acrylic tank wall. Given this fact, it is reasonable to tag a pulse associated without any recorded source in 300 ns pre-time window in MC as a neutron capture pulse with the capture happened in acrylic tank wall.

TYPES OF EVENTS

Given the pulses tagged with their sources as neutron capture, muon, or secondary charged particles, the detector events can be divided into different types according to the composition of pulses.

1. **Fast neutron events.** When an event consists only of neutron capture pulses, it is a detection of the secondary neutrons liberated by the incident fast neutron into the lead target. It is so identified as a fast neutron event, which is what we ideally search for in the NMM experiment.

2. **Muon events.** If an event consists only of muon pulses, or of any muon pulse plus secondary background pulses, it is considered as a muon event.
3. **Secondary charged particle events.** If an event consists only of secondary charged particle pulses, it is called a secondary charged particle event. When the muon travels in cavern rock, it creates many secondary particles. These particles may have chance to scatter and travel into the water tanks, even when the muon itself misses.
4. **Muons accompanied with neutron captures.** A muon that left a pulse means it penetrates one or both water tank(s). In the meantime, the muon is very likely to hit the lead stack as well. If an event is found as a muon pulse with multiple neutron capture pulses, the secondary neutrons are very likely released directly by the muon striking the lead target. These neutron captures are not a detection of a fast neutron, and this type of event is not considered as signal. If it happens that the muon passes one of the water tanks by a small corner with a path length short enough, to fire a pulse small enough to pass the muon rejection cut, then the subset of this type may mimic the signal type of real fast neutrons. In this case, we call it a clipping muon.
5. **Skewed fast neutrons.** If an event consists of mostly neutron capture pulses, but also one or two secondary background pulses, in contrast to the last type, the lead target is almost certainly not hit by the muon, thus the detection of multiple neutron captures is indeed the signal of a fast neutron, but with one or two background pulses that skews the counting of the multiplicity.

RESULTS

With the classification of events discussed above, the MC truth of each type of events can be studied to help understand the real data taken in the NMM experiment.

In Figure 4.14 the multiplicity spectrum of each event type discussed above is shown in a

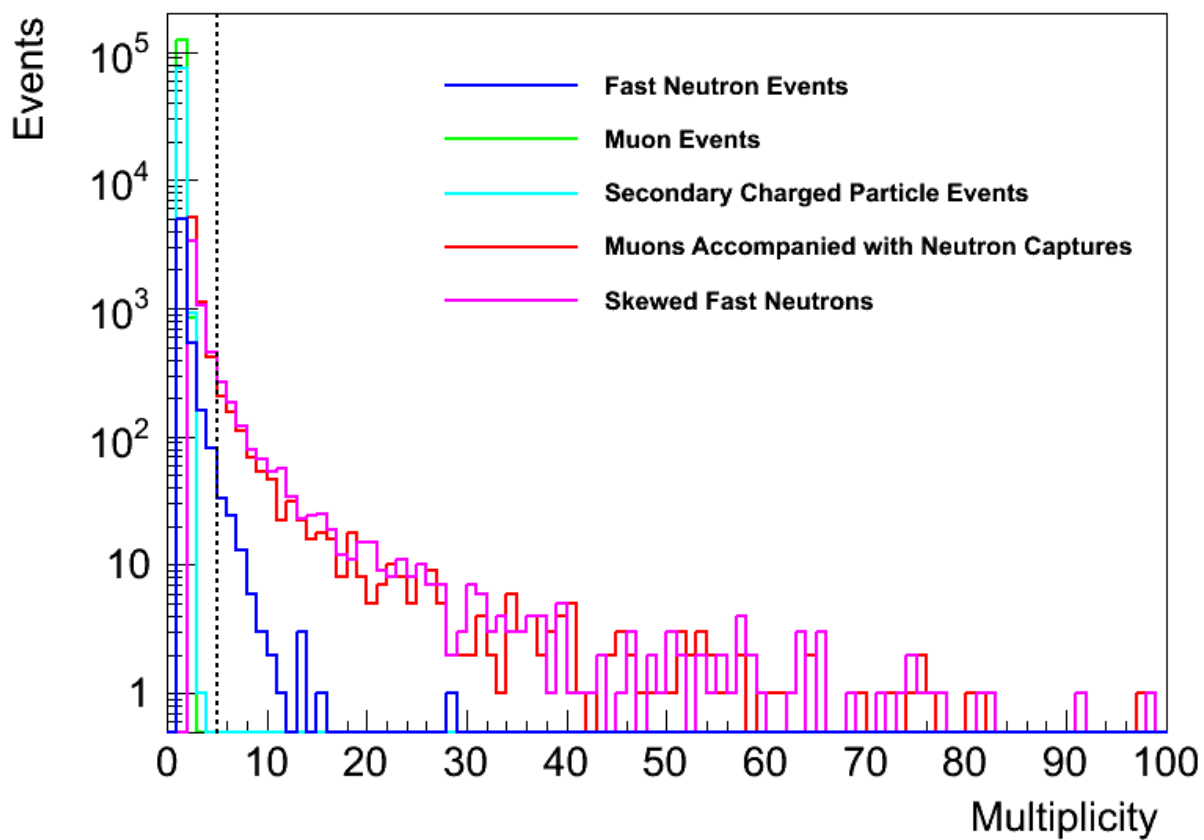


Figure 4.14: Pulse multiplicity spectra of the events in different types based on MC truth. All the types of events in MC truth are shown in colors described in the legend. A dashed black vertical line shows the trigger threshold on pulse multiplicity at 5. The scales in Y-axis of all spectra are based on their original counts in the MC.

color histogram for the comprehensive muon simulation results, processed with lower PMT gain parameters. The detector trigger on multiplicity at threshold 5 is indicated with the dashed black line in the figure. Two major types of backgrounds, muon events and secondary charged particle events, which mostly fire one or two pulses, are completely suppressed by the threshold on multiplicity. Note in the real data of the experiment, an initial pulse due to a muon or other charge particles may be energetic enough to cause severe afterpulsing, so the multiplicity may exceed 5 and trigger an event.

Spectra of the maximum pulse of each event are plotted for all five types of events in Figure 4.15. On the top the maximum pulse spectra are shown up to 10 V. The muon peaks are clearly shown in the muon events and muons accompanied with neutron captures (in green and red). The events involved with secondary charged particle show a different shape of high energy peaks compared with the muon peaks (in cyan and magenta). Some high energy pulses shown in the fast neutron events, which are too large for Gd neutron capture emissions, are likely due to mis-tagging to the pulses. For example, a large pulse induced by a muon or a high-energy charged particle happens to be closer to a neutron capture in timing than the real source would be mis-tagged as a neutron capture pulse. But the mis-tagged pulses are rare compared with correctly tagged capture pulses. On the bottom the pulse spectra are shown up to 500 mV for a better look at low energies. The maximum pulse spectrum of fast neutron events is consistent with the detector responses measured and simulated in ^{252}Cf calibration runs. The skewed fast neutrons are less populated in the low energy pulse region than fast neutron events as the maximum pulses of the skewed fast neutrons are mostly from high-energy charged particles, but the spectrum is relatively similar to neutron captures. Muons accompanied with neutron captures have a small population at the low energy region. With a muon rejection cut at 300 mV or even smaller volt, most of muons accompanied with neutrons captures will be removed from the candidate set.

It is useful to check the distribution of pulse timing in the events. The pulse timings of neutron capture pulses and muon pulses since the beginning of each event are plotted in Figure 4.16 for

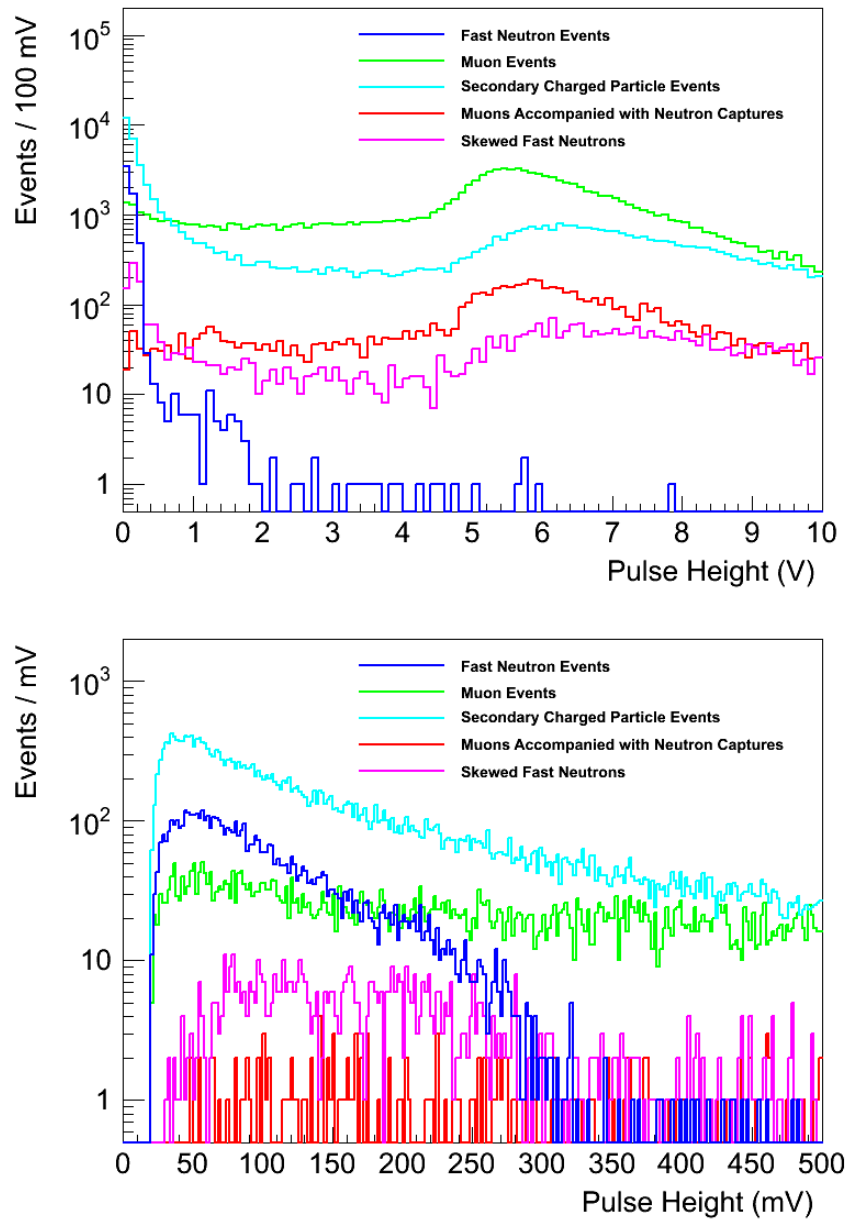


Figure 4.15: Pulse spectra of the maximum pulse in each event for different event types (in colors as described in legends). On the top is shown in the pulse height scale up to 10 V and binned per 100 mV. On the bottom is shown in the scale up to 500 mV and binned per mV. The scales on Y-axis of all spectra are based on their original counts in the MC. Note that gigh-energy muons are minimum ionizing particles, therefore the peak of muon pulses at ~ 5.4 V corresponds to the height of the water tanks, 76.2 cm, which is the path length of most muons traversing the water tanks, and the corresponding energy deposition is estimated to be ~ 152 MeV, based on the minimum stopping power of muon in water, $1.992 \text{ MeVcm}^2/\text{g}$ [70]. The peaks of charged particles are similar to those of muons, but the shape is slightly different. The large pulses in fast neutron events are likely due to mis-tagged muons or high-energy charged particles.

different types of events except for secondary charged particle events. Neutron capture pulses (in solid lines) feature a rising time of $\sim 5 \mu\text{s}$, which originates from the time delay from the initiation of interactions to the first capture of secondary neutrons, and an exponential fall time, which describes the process of every moderated neutron in the water tank finding a gadolinium nucleus and being captured. The neutron capture timing distributions in different event types are identical, providing a sanity check that the tagging of neutron capture pulses is correct. Muon pulses (in dashed lines) appear only in a very prompt time window, $0 - \sim 0.5 \mu\text{s}$. In fact, the cosmic muons are very penetrating and never back-scatter into the detector. It is also confirmed in the MC that the muon pulse takes only the first position of the event, and no interactions of any other particle with the detector ever take place earlier than the muon in the event.

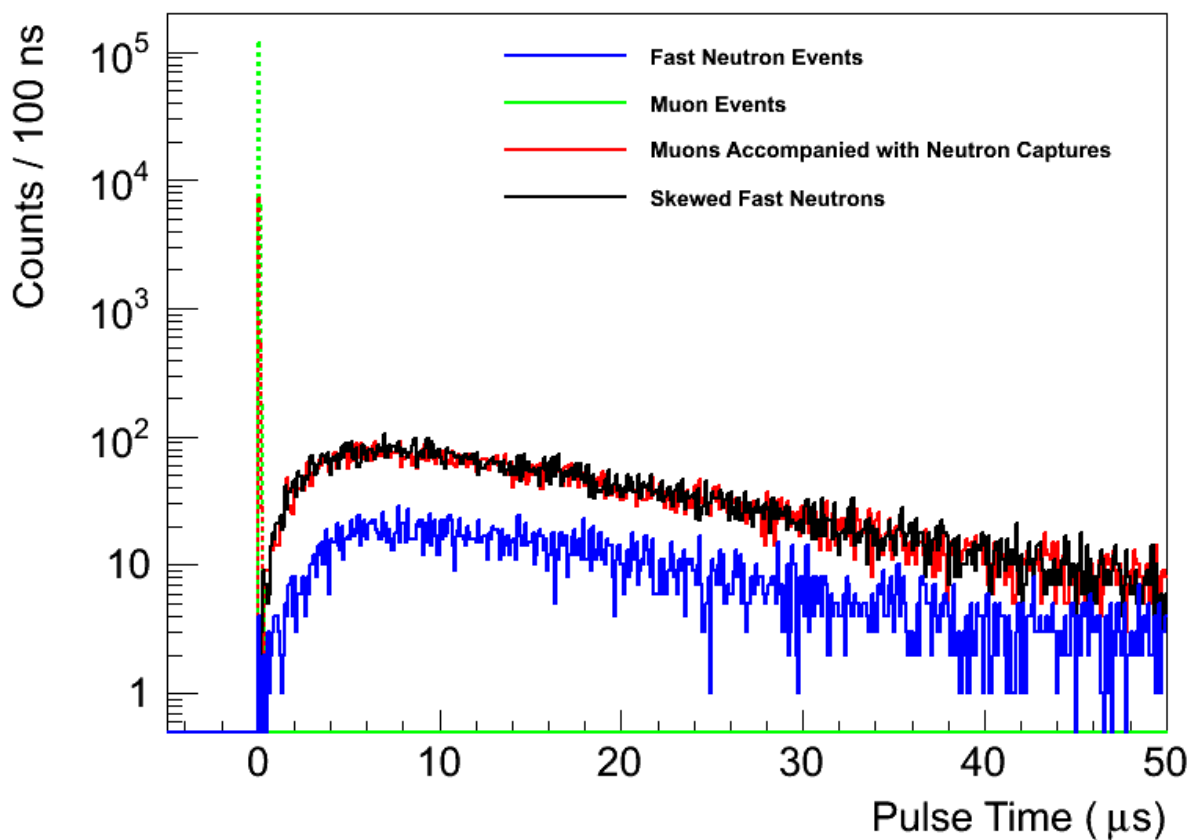


Figure 4.16: Pulse time (relative to the beginning of an event) distributions of neutron capture pulses and muon pulses in different types of events. The pulse times in MC are binned into histograms for neutron capture pulses (in solid) and muon pulses (in dashed), with colors showing event types as described in legend. Since the type of “secondary charged particle events” has neither neutron capture pulses nor muon pulses, it is not shown in this figure. The muon pulses are always prompt (within $\sim 1 \mu\text{s}$ since the beginning of the event). The non-prompt curves for the three types of neutron related events feature the neutron capture timing distribution, i.e. with a rise time about several μs for most neutrons to be thermalized, and an exponential fall time for the neutrons to be captured by Gd.

4.2.4 Muon Rejection Cut Study

The facts found in the comprehensive muon simulation may help improve the muon rejection cut. The previous design of the muon rejection cut was to require that the maximum pulse height of any pulse in the event be smaller than 300 mV. It is relatively inefficient to remove muon events by cutting on all pulses in the event. The analysis of the comprehensive muon simulation confirms that the detector response of the muon is prompt in time and always fires as the first pulse in any muon-involved event in the MC. A smarter way to remove muon events is to set the cut only on the first pulse of the event. This way of cutting can avoid removing neutron capture events in which there is any non-prompt pulse greater than the cut threshold, and focus better on the muon pulse. In the real data analysis, however, there is a non-negligible chance to record a pulse induced by a background gamma ahead of the muon pulse, making the muon pulse the second pulse of the event. The rate of n gammas to be coincident ahead of a muon can be estimated as

$$R(n\gamma + \mu) = \frac{(r_\gamma \cdot 100\mu\text{s})^n e^{-r_\gamma \cdot 100\mu\text{s}}}{n!} \cdot r_\mu, \quad (4.5)$$

which is the Poisson probability for n gamma pulses with the gamma pulse rate r_γ occurring in 100 μs time interval, multiplying by the muon pulse rate r_μ . Muon events usually trigger at the 4th coincident after-pulse after the primary muon pulse, but the trigger time is very close to the time of the muon pulse, so it is reasonable to approximate pre-trigger time with 100 μs . The gamma pulse rate for two tanks together is approximately 700 Hz for the low PMT gain and 850 Hz for the high PMT gain; muon pulse rate is estimated using fast neutron search data to be 4.7 mHz for the low-gain, and 8.0 mHz for the high-gain. Then the estimated $1\gamma + \mu$ rate is 3×10^{-4} Hz for the low-gain and 6×10^{-4} Hz for the high-gain; the estimated rate of $2\gamma + \mu$ events is 1×10^{-5} Hz for the low-gain and 3×10^{-5} Hz for the high-gain. Thus it is necessary to set the cut on the first two pulses of the event. With this style of cutting, the cut threshold may be tightened to remove muon events more efficiently without losing efficiency on neutron capture events. This change is

especially important for higher-multiplicity events.

To quantify the performance of both styles of muon cuts, the efficiency of the muon cut on passing neutron capture events is calculated by Monte Carlo simulation. For a given value of multiplicity M , M pulses are sampled according to the pulse height distribution measured in ^{252}Cf calibration data to form an event. The efficiency of each case is calculated by applying the cut to 10^6 sampled events to count the pass fraction of neutron capture events. The efficiencies as a function of cut position on pulse height are shown in Figure 4.17 and Figure 4.18 for low PMT gain and high PMT gain, respectively. In each figure, the left column shows the efficiencies of the muon cut on the maximum pulse of the event, and the right column shows the efficiencies of the muon cut on the first two pulses of the event. The calculation (in red curve) is compared with the measurement from ^{252}Cf calibration data (in data points and error bars). The comparisons are shown for multiplicity 3, 4, 5, and 6. Efficiencies for higher multiplicities are calculated but not measured (and not shown here) since there is not large enough statistics from the events with higher multiplicities in ^{252}Cf calibration data. The measurements and calculations agree well on high pulse heights ($> 200\text{ mV}$), but show discrepancies at low pulse heights. The discrepancies are presumably due to background gamma pulses. The expected background gamma distribution has been subtracted from the pulse height distribution measured in calibration data. The background-subtracted pulse height distribution is used in calculation and neutron likelihood construction. But when the cut efficiencies are measured in ^{252}Cf data, the cut applies to neutron capture events mixed with background gamma events. Background gamma pulses have significantly lower pulse heights, and therefore have a higher pass fraction. The mixture of the background gamma population in the testing events makes the measured pass efficiencies higher than the calculations.

The cut efficiency on neutron capture events decreases as the cut is tightened, set to a lower pulse height. The efficiencies of the cut on the maximum pulse drop faster than the cut on the first two pulses as the cut position decreases, and drop more drastically as the multiplicity increases, while the efficiency of the cut on the first two pulses is not sensitive to multiplicity. In the case of

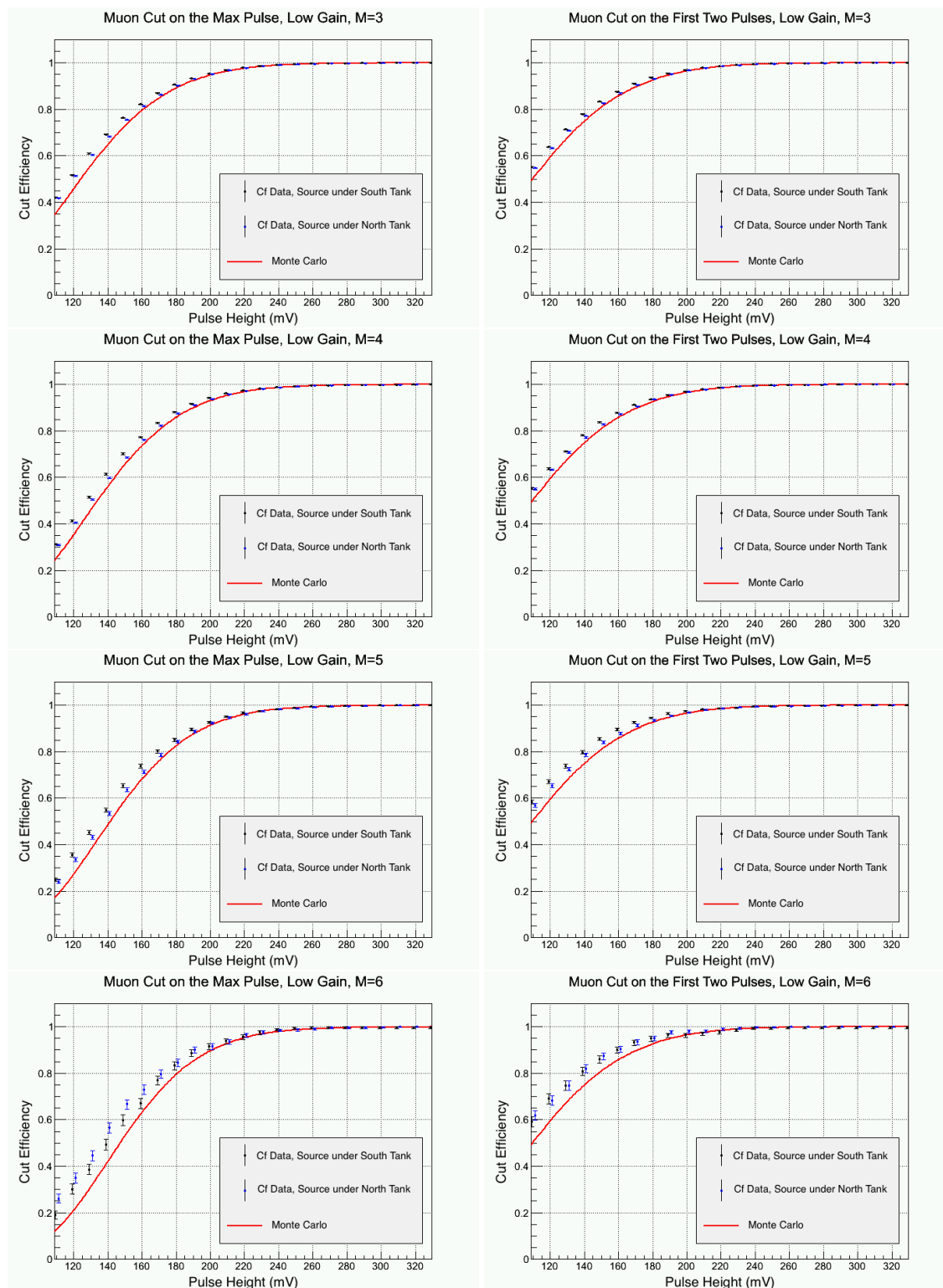


Figure 4.17: Efficiencies of muon cut for neutron capture events with low PMT gain as a function of the cut pulse height, compared for both cut-on-maximum style (left column) and cut-on-first-two style (right column), shown for events of multiplicity 3, 4, 5, and 6 (in each row from top to bottom). The calculated efficiencies from MC sampling are shown in the red curves, while the efficiencies measured with Cf neutron data are shown in black (source under source tank) and blue (source under north tank) data points.

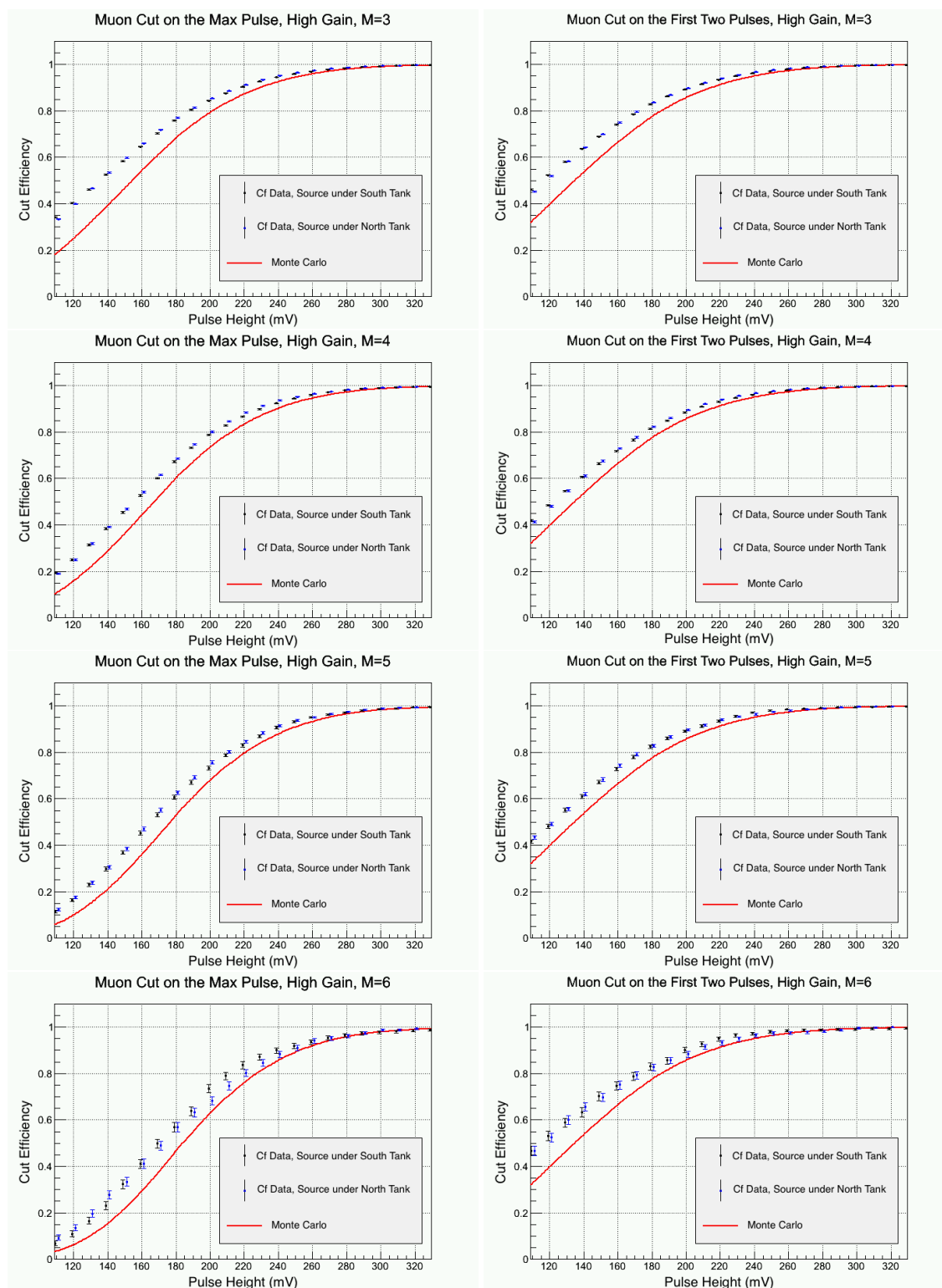


Figure 4.18: Efficiencies of muon cut for neutron capture events with high PMT gain as a function of the cut pulse height, compared for both cut-on-maximum style (left column) and cut-on-first-two style (right column), shown for events of multiplicity 3, 4, 5, and 6 (in each row from top to bottom). The calculated efficiencies from MC sampling are shown in the red curves, while the efficiencies measured with Cf neutron data are shown in black (source under source tank) and blue (source under north tank) data points.

low PMT gain, if the muon cut is tightened to 200 mV, the cut on the maximum pulse will have the efficiency dropped to $\sim 90\%$ for events of multiplicity 5, and even lower for events of higher multiplicities, while the cut on the first two pulses will drop the efficiency only to $\sim 96.7\%$, and it is not sensitive to multiplicity. Therefore, redesigning the cut style as applying on the first two pulses and tightening to 200 mV is affordable in the sense of not losing much efficiency on neutron capture events. In the case of high PMT gain, the cut position is tuned to 250 mV to get the same efficiency. According to the calculation earlier in this section, the chance for the muon pulse to occur at the third place, i.e. as a $2\gamma + \mu$ event, is much smaller than at the second place, but it still results in, say, ~ 137 events in the 158 live days of the 1st fast neutron data. We add a cut at 300 mV on the third pulse to remove this type of events. Neutron pulses are below 300 mV, so adding the cut on the third pulse does not affect the estimation of the cut efficiency.

As discussed in subsection 4.2.3, the basic muon events do not survive the multiplicity trigger requirement in the MC. In addition to removing the muon events that triggered in the real data due to afterpulsing, the main role of the muon rejection cut is to remove the events of low pulse height muons accompanied by neutron captures, known as clipping muons. The pulse spectrum of simulated muon pulses is shown in Figure 4.19 for all muons accompanied with neutron captures (in blue) and the same type of events but surviving multiplicity trigger requirement (in red). The left column of plots show the spectra for low PMT gain, while the right column of plots show the spectra for high PMT gain. The top plots, which show the spectra with scale up to 10 V, indicate that the shapes of the spectra before and after the multiplicity trigger applied are nearly identical. From the bottom plots, which focuses on the low pulse height end, it is shown that, in case of low PMT gain, there are only 7 clipping muon events surviving both multiplicity trigger and a muon rejection cut at 200 mV in the comprehensive muon simulation with 138.8 days of live time. In the case of high PMT gain, 8 clipping muons survive the muon rejection cut at 250 mV. The muon spectra of the events before applying the trigger requirement (the blue histograms) can be used to estimate how much the clipping muon rate can be reduced by tightening the cut in the real data analysis. Tightening the muon cut from 300 mV to 200 mV is expected to remove $\sim 25\%$ of the

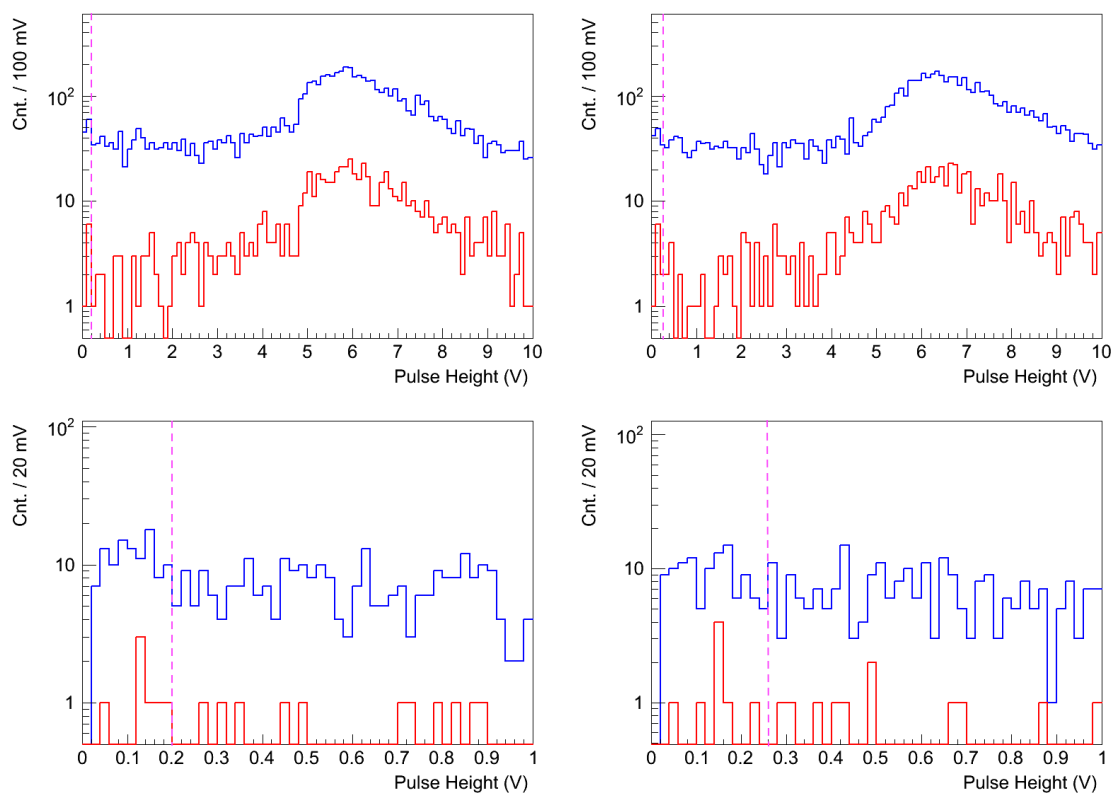


Figure 4.19: Muon pulse spectrum from the events of muons accompanied by neutron captures. The spectrum of all events from this type is shown in the blue histogram, and that of the events triggered with at least multiplicity-5 is shown in the red histogram. The two plots in the left column show the spectra for the low PMT gain, and the two on the right column show the spectra for the high PMT gain. On the top are plots with a pulse height scale up to 10 V with 100 mV bin width, while on the bottom are plots showing low pulse heights with 20 mV bin width. Muon rejection cut is set at 200 mV for the low PMT gain, and at 250 mV for the high PMT gain, marked with the magenta vertical lines.

previously surviving clipping muons for low PMT gain data, and tightening the cut to 250 mV is expected to remove $\sim 14\%$ previously surviving clipping muons for high PMT gain data.

Another muon problem in real data is the muons followed by afterpulses. Afterpulsing is led by an initial pulse large enough to ionize the gas impurities significantly. A relative small pulse (down to the neutron capture pulse region) is usually not expected to cause afterpulsing with 5 or more coincident pulses to trigger. A tightened muon cut at 200 mV for low PMT gain data or 250 mV for high PMT gain data would further secure the region of interest with few or no muon events falsely selected.

4.2.5 Multiplicity Spectrum

With the multiplicity trigger threshold and the improved muon rejection cut applied, the selection of candidate events can be determined. The MC truth analysis can help reveal how well the event selection criteria work to include the expected signals, and how often backgrounds are falsely included in the candidate set, which cannot be directly viewed in real data analysis. Table 4.2 summarizes the statistics of all types of events in MC truth on each selection requirement for both the low PMT gain and the high PMT gain analyses. The first columns, “Hit”, show the number of events making any PMT detected hit in the detector, the second columns, “M5”, list the number of events having 5 or more pulses to meet the multiplicity trigger requirement, and the third columns, “Selected”, list the number of events both having triggered and passed the muon rejection cut, which requires the first two pulses be smaller than 200 mV for low PMT gain and 250 mV for high PMT gain to make their efficiencies on neutron capture events both estimated as $\sim 96.7\%$. The numbers of Hit and M5 events for low and high PMT gains are close within statistical uncertainty, while the numbers of Selected events in types of fast neutrons and skewed fast neutrons for high PMT gain are slightly greater than those for low PMT gain. The ratio of the Selected to the M5 events appears much lower than 96.7%, which is due to the mis-tagging of the pulses from muons or high-energy charge particles as neutron capture pulses. So the fast neutron events in M5 falsely

include some muons accompanied with neutron captures or skewed fast neutrons with a high-energy pulse, but these events can be removed by the muon cut. The higher event rate for high PMT gain is presumably because the higher PMT gain tends to result in more pulses over the single pulse threshold thus triggering more events. The selected fast neutrons and skewed fast neutrons are both taken into account as fast neutron signals, while the number of the selected muons accompanied with neutron captures, or known as clipping muons, can be considered as a background. But the number and multiplicity distribution of the selected events from all the three types together can be compared with the measured numbers of events in the same analysis scheme to benchmark between Geant4 MC and measurement. The results from both the high-gain and the low-gain are based on the same 3.384×10^7 simulated events, but with different values of energy scale and smearing factor to process the raw data.

Table 4.2: Event numbers in each MC event type with each selection requirement found in the comprehensive muon simulation with 138.8 days of live time.

	Low PMT gain			High PMT gain		
	Hit	M5	Selected	Hit	M5	Selected
Fast neutron events	5811	87	59	5868	87	67
Muon events	123762	0	0	123601	0	0
Secondary charged particle events	74902	0	0	75254	0	0
Muons accompanied with neutron captures	7668	950	7	7906	959	8
Skewed fast neutrons	6040	1174	70	6030	1166	77

The multiplicity distribution of the selected events is shown in Figure 4.20 for the low PMT gain results on the top and the high PMT gain results on the bottom. There is no significant difference between the expected distributions at low gain and those at high gain. For both low and high PMT gains, the skewed fast neutron spectrum is slightly harder than the spectrum of the pure fast neutrons. Since a skewed fast neutron event consists of neutron capture pulses from a fast neutron plus one or two secondary charged particle pulses, the spectrum of the skewed fast neutrons can be interpreted as a spectrum of another group of fast neutrons but being shifted by charged particle hits. This fact suggests that there are a significant fraction of high-energy neutrons that are strongly correlated

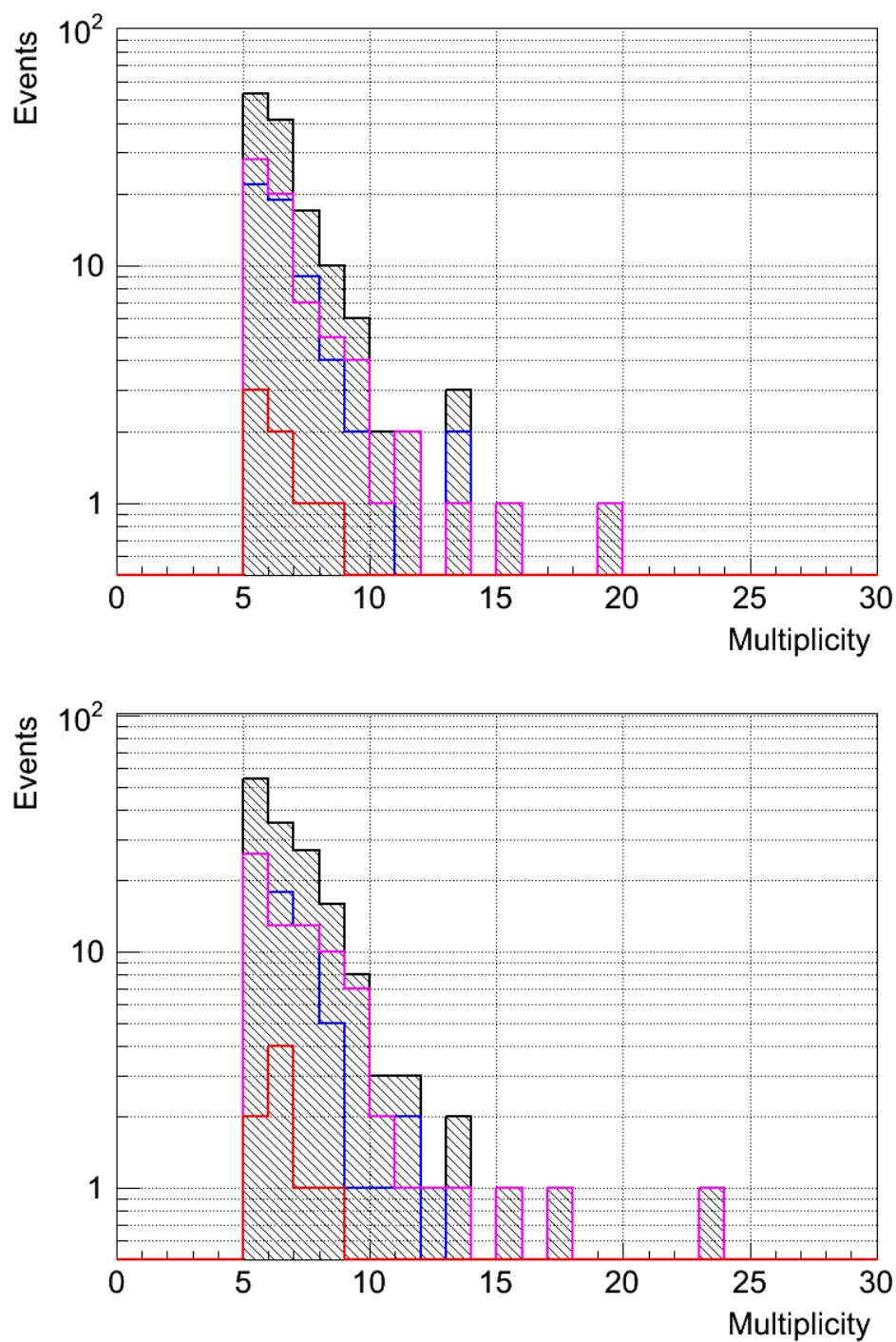


Figure 4.20: Multiplicity distributions of the events selected for the fast neutron search in the comprehensive muon simulation. On the top is shown the multiplicity distribution resulting from low PMT gain analysis, and on the bottom from high PMT gain analysis. The plots show the multiplicity spectra contributed by fast neutron events in blue, skewed fast neutron events in magenta, clipping muon events in red, and the overall distribution of all selected events in black with shaded area.

with the primary muon between their incident angles, because many of the secondary particles are from the muon emitted shower. The clipping muons are considered as an indistinguishable background, which is $\sim 5\%$ of the selected events. The MC truth study has helped us understand the content of the signals. However, since it is impossible to distinguish the three types of events with measurement, the overall multiplicity distribution will be used to benchmark with the measured multiplicity spectrum.

4.2.6 Neutron Flux Reconstruction

In addition to the results discussed above, an analysis on neutron flux may be performed to explore the possibility of reconstructing the fast neutron flux from the measured event count and multiplicity distribution.

Previous MC studies by M. Sweany [60] have indicated that the multiplicity has little dependence on the energy of the incoming fast neutron, which is washed out by moderation and spallation in the water. However, the trigger threshold at multiplicity 5 does play a role of energy threshold at $\sim 40 - 50\text{MeV}$ (shown in Figure 4.23 in [60]). Note that many incoming neutrons with energies greater than 50MeV may not trigger, but the triggered events have to be from the fast neutrons above the effective energy threshold $\sim 40 - 50\text{MeV}$. To reconstruct the flux of the fast neutrons above threshold, it is necessary to investigate how the detected event count is related to the incoming fast neutron flux.

Neutron flux is determined as the count of neutrons having passed a horizontal surface within a unit of time and a unit of area. The neutron tracks recorded at the cavern ceiling, the top of the water tanks, and the top of the bottom lead can be extracted to calculate the neutron fluxes accordingly. The total count on each surface divided by the area of that surface and the live time of the simulation is then the flux on that surface. In Figure 4.21, the differential fluxes of neutrons exiting the cavern ceiling, through the top surfaces of the water tanks, and through the top surface of the bottom lead

as functions of neutron kinetic energy are plotted together. The fluxes through the tops of the tanks and the bottom lead are only from counting the same neutrons recorded on the cavern ceiling and walls. As expected, the fluxes at the cavern ceiling and the tops of the water tanks are close to each other, except that the recording surface for the water tanks is under the top shielding lead, so that the neutrons recorded are slightly attenuated by scattering and captures in the top lead. However, the flux recorded through the top of the bottom lead is largely reduced compared with the flux through the tops of the tanks for energies above 50 MeV, while the neutrons under 50 MeV have been hugely increased. Moderation in the water causes the neutron energy to be reduced as it hits the lead, and spallations in the water release low energy secondary neutrons. The flux through the tops of water tanks will be used to study the detector acceptance.

In Figure 4.22, the spectrum of the primary neutron energies of the accepted events is normalized by dividing by the live time and the area of the tops of the tanks to make an effective “detected flux” (in solid line for overall events and colored lines for the three types of events) to be compared with the incoming flux through the top surfaces of the water tanks (in dashed line). There is no significant difference between the results from the low and the high PMT gain analyses shown in the Figure. Besides the true high-energy neutrons (above 50 MeV), there are many low-energy neutrons accepted in the analysis results.

A way to reveal more details is to plot 2-dimensional histograms of events with multiplicity vs. neutron energy. Figure 4.23 plots these 2-dimensional histograms for fast neutron events on the top, skewed fast neutron events in the middle, and clipping muon events on the bottom, with the left column showing the results from low PMT gain and the right column from high PMT gain. The histograms include only the events that pass muon cut, but keep the events with multiplicities below 5. The events above multiplicity 5 are clearly distributed in two separate populations. For the real high-energy neutrons, the multiplicity-5 trigger does make an effective energy threshold at approximately 50 MeV, which is consistent with M. Sweany’s study. Another totally different group of events that have multiplicities greater than 5 populate at very low energies, mostly below

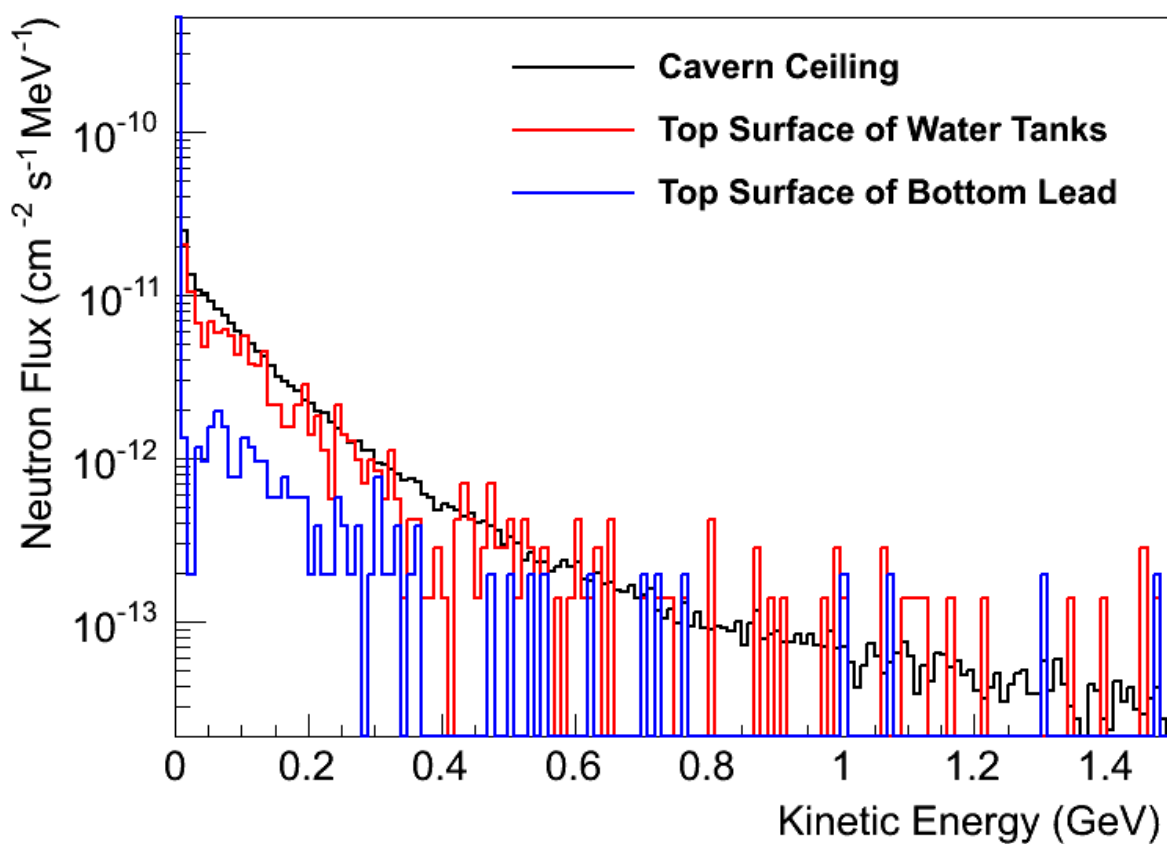


Figure 4.21: Muon-induced neutron flux through three surfaces in the comprehensive muon simulation. In the black histogram is shown the neutron flux from the cavern ceiling, in the red histogram the flux through the top surface of the water tanks, and in the blue histogram the flux through the top surface of the bottom lead. Only the neutrons directly incoming from cavern rock are included for counting the fluxes through the tank top and the bottom lead top.

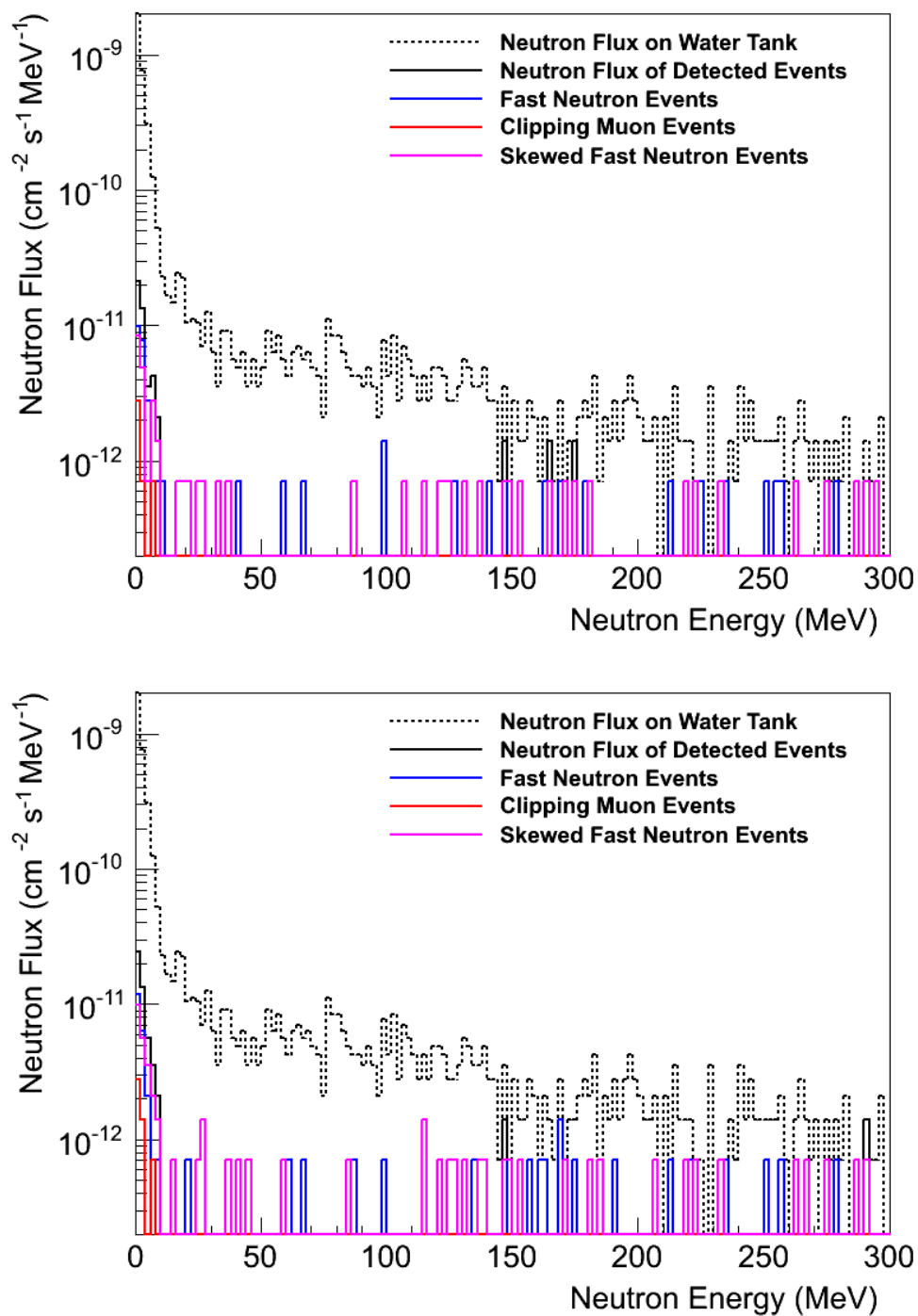


Figure 4.22: Primary neutron energy spectrum of the accepted events, normalized with the tank top surface area and MC live time, shown in black solid line for overall events and color lines for three types of events. The total neutron flux through the top surface of the water tanks is shown in a dashed line to be compared with the detected flux. The results for low and high PMT gains are shown on the top and bottom, respectively. For an event with more than one neutron hitting the top surface of the tanks, only the neutron with the highest energy is counted in the histograms.

10 MeV. The reason these events can trigger is that they are multiple low energy neutrons incident into the water tanks from the cavern rock in the same event. We may call these events “low-energy neutron bundles”. These events are definitely not included in M. Sweany’s MC, in which only mono-energetic neutron beams were shot into the north tank with one primary neutron per event. For the clipping muon events, the main reason that the events can trigger is the muon-induced neutrons in the lead stack, but the histograms show the energy of the primary neutron that happened to fly from the cavern rock into the tanks. They are distributed at very low energy as well. The low-energy neutron bundles emitted in rock and clipping muon events are both considered as backgrounds for the detection of high-energy neutrons. The multiplicities of events with primary neutron energies greater than and less than 50 MeV are compared in Figure 4.24. The real high-energy neutrons do show a few events extending to higher multiplicities, but the difference between the two multiplicity distributions is not significant enough to separate the two groups. We can extract a fraction for neutrons above 50 MeV out of the overall accepted events. This fraction is estimated to be $(43 \pm 7) \%$ for low PMT gain and $(45 \pm 7) \%$ for high PMT gain. Note there are a handful of high-multiplicity events in Figure 4.24 but not in Figure 4.23. In these events, the energies of the primary neutrons are above 300 MeV.

Finally, to reconstruct a flux measurement of fast neutrons above 50 MeV, we can define the gathering power of the detector as the quotient of the accepted event rate over the real high-energy (> 50 MeV) neutron flux,

$$\mathcal{G} = \frac{\mathcal{R}_{\text{acc}}}{\mathcal{F}}. \quad (4.6)$$

This definition of gathering power is different from M. Sweany’s, but directly connects the measured event rate of high-energy neutrons to the horizontal flux on the top of water tanks. According to the statistics in Figure 4.22, the gathering power is estimated as $(4.3 \pm 0.6) \times 10^3 \text{ cm}^2$ for low PMT gain and $(5.0 \pm 0.6) \times 10^3 \text{ cm}^2$ for high PMT gain. When analyzing real data, we can use the estimated fraction of real high-energy neutrons first, then use the gathering power, to reconstruct a flux measurement.

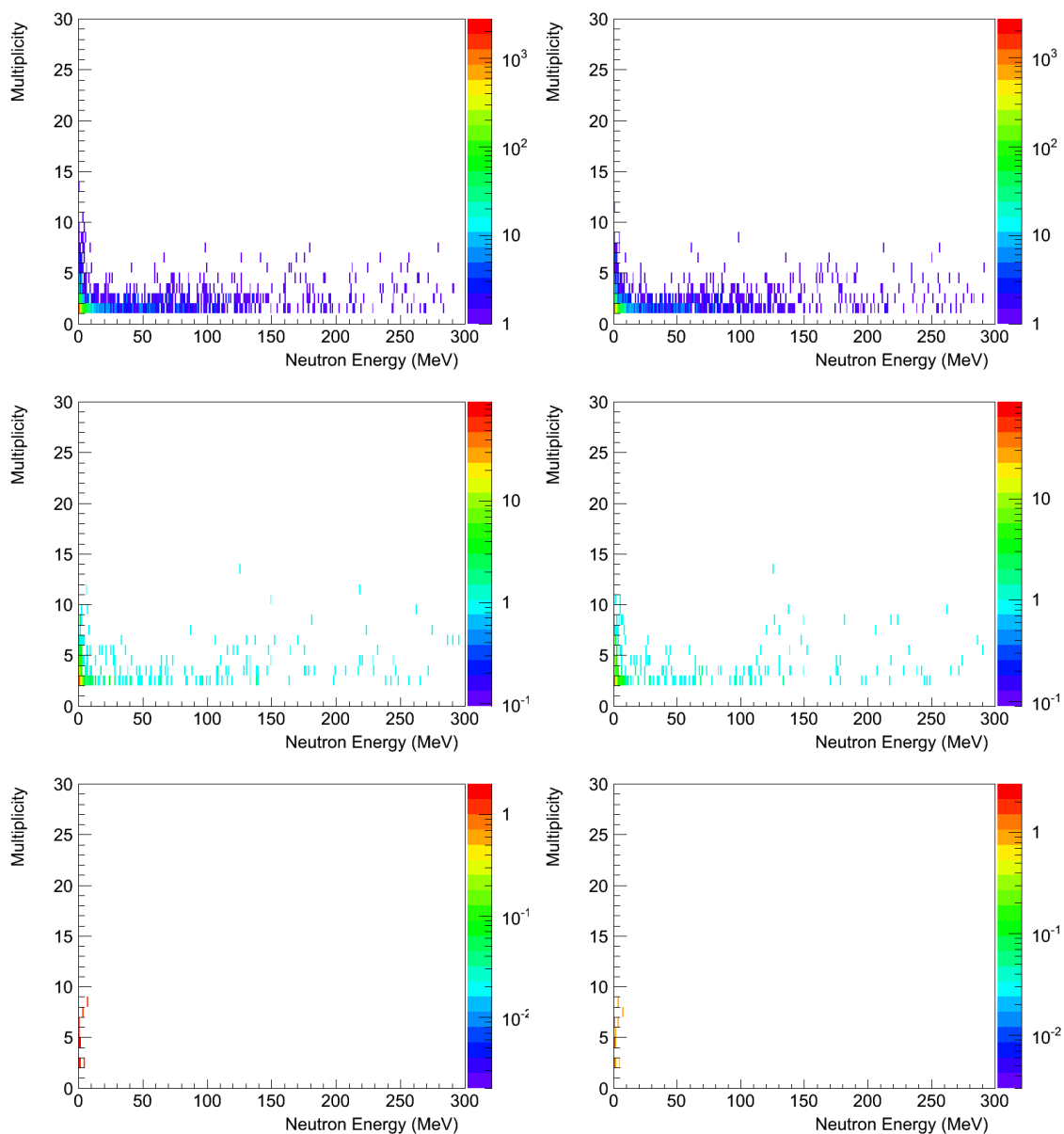


Figure 4.23: 2-dimensiona histograms of event multiplicity vs. primary neutron energy. The figure is arranged with fast neutron events on the top, skewed fast neutron events in the middle, and clipping muon events on the bottom, with the left column showing the results from low PMT gain and the right column from high PMT gain. The events above multiplicity 5 are distributed in two separate populations. The events with the primary neutrons above ~ 50 MeV, including those with even higher energies than 300 MeV and out of the range of the plots, are real high-energy neutrons. The events mostly below ~ 10 MeV, called “low-energy neutron bundles”, are accompanied by multiple other MeV neutrons triggering by the captures of the primary MeV neutrons.

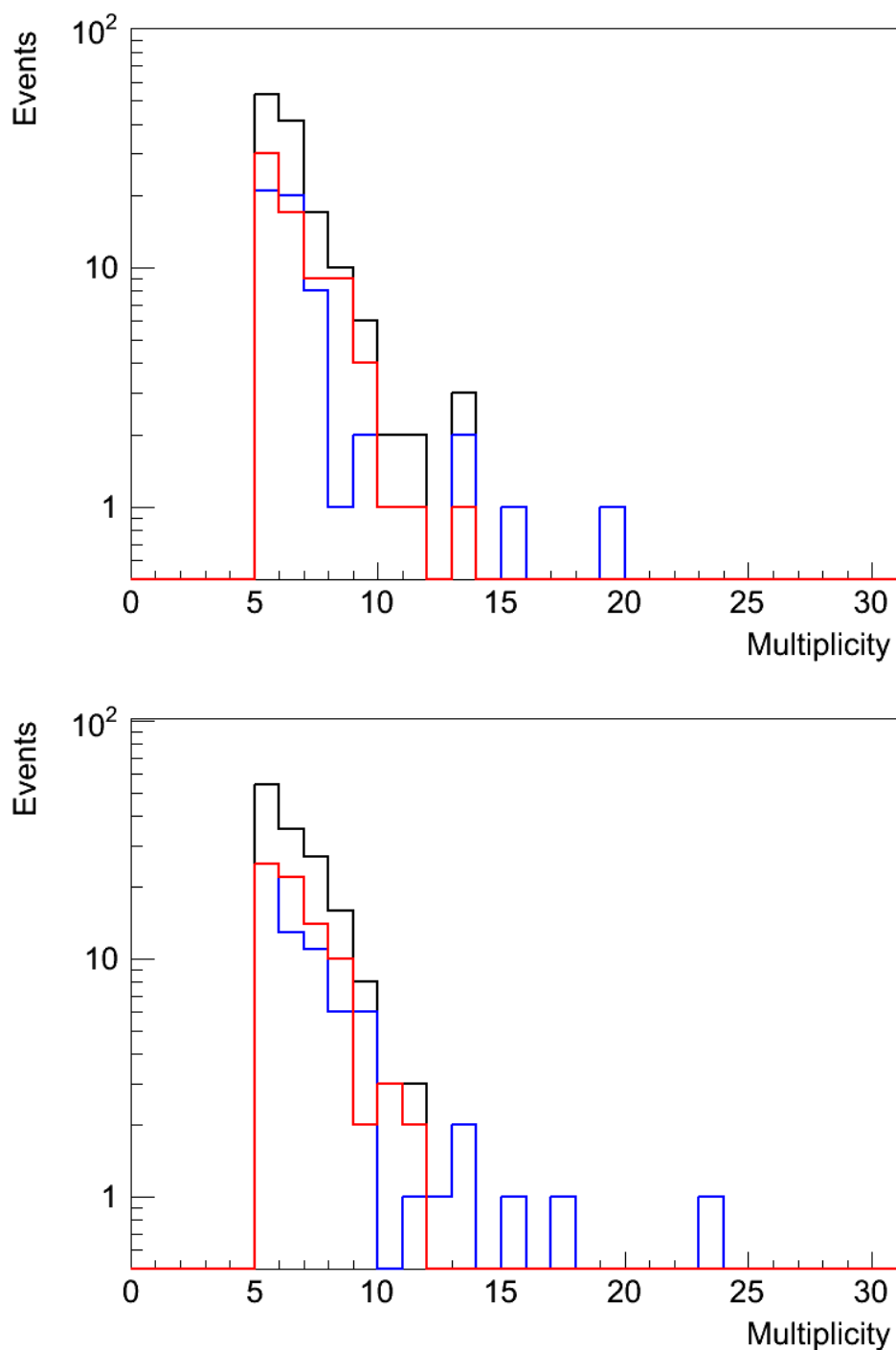


Figure 4.24: The multiplicity distributions of the accepted events, split into the events of real high-energy neutrons (in blue) and the events of neutron bundles (in red), with the overall distribution (in black) plotted together. The real high-energy neutrons are selected as the incoming neutron energy greater than 50 MeV, and the neutron bundles as the highest neutron energy of the event less than 50 MeV. The distributions for low PMT gain is shown on the top plot, and the distributions for high PMT gain is on the bottom.

Chapter 5

Fast Neutron Search Analysis for the Neutron Multiplicity Meter Experiment

As mentioned in Chapter 3, there have been three periods of running for the fast neutron search, with slightly different multiplicity trigger settings. The first fast neutron search run was taken with a lower PMT gain, but the later two runs were taken after the PMT gain was raised and balanced. The first fast neutron search run collected 158.2 live days of data, while the amount of data in the second and third runs counts 169.2 days and 302.8 days of live time, respectively, making the total 630.2 days of live time. With the help of the better understood detector mechanism revealed in the MC study in Chapter 4, the three data sets of fast neutron search have been analyzed to measure the high-energy neutron flux at the Soudan Underground Laboratory, at a depth of ~ 2000 m.w.e, and the high-energy neutron multiplicity spectrum, benchmarking the Geant4 MC.

In this chapter I present the analysis of the fast neutron search data. In addition to the muons and muon-induced background particles, which are well understood in the Geant4 MC study, there are gamma rays emitted by U/Th decays from ambient materials and the cavern rock. Most of the gamma rays cannot trigger the detector since the trigger requires at least five coincident pulses in the trigger window, but there is still a chance that five or more gammas are accidentally coincident in the detector in a short time window. There are also pulses induced by electronic noise in the

neutron search data, which can affect the analysis and have not been studied in MC. In the analysis of the neutron search data, a method based on the pulse height likelihood distribution has been developed to discriminate gamma backgrounds, and data quality cuts were created to remove the events with noise pulses. Finally, the multiplicity spectrum is extracted to compare with the result from the Geant4 MC, and the data are also analyzed to make a measurement of the high-energy neutron flux at the Soudan mine.

5.1 Pulse Height Likelihood Analysis

The types of events expected in the NMM have been introduced in Section 3.4.1. With muon events and clipping muon with spallation neutrons well understood in the comprehensive MC study and shown to be suppressed by the multiplicity trigger setting and muon rejection cut, the major remaining background is the environmental gamma rays that accidentally fire the detector with multiple coincident pulses in the trigger time window.

The rate of the multiple gamma events is determined mainly by the rate that gamma rays arrive in coincidence. This gamma rate is measured with the U/Th background gamma exposure data, which resulted in (330 ± 3) Hz in the south tank and (367 ± 3) Hz in the north tank in the low-PMT-gain running period, and (412 ± 4) Hz in the south tank and (433 ± 4) Hz in the north tank in the high-PMT-gain running period. The probability to have k coincident gamma pulses in any trigger time window t_{Tr} conforms with the Poisson distribution, as

$$P(k; r t_{Tr}) = \frac{(r t_{Tr})^k \cdot e^{-r t_{Tr}}}{k!}, \quad (5.1)$$

with r the summed coincident gamma pulse rate in both tanks. To derive the rate of the gamma events with a give multiplicity k , consider the occurrence of $k - 1$ gamma pulses in duration of time

t_{Tr} followed by one gamma pulse in time dt . The probability of an event defined as so is

$$\begin{aligned} I_k dt &= P(k-1; rt_{\text{Tr}}) \cdot r dt \\ &= \frac{(rt_{\text{Tr}})^{k-1} \cdot e^{-rt_{\text{Tr}}}}{(k-1)!} r dt, \end{aligned} \quad (5.2)$$

which gives the rate of gamma events with k gamma pulses,

$$I_k = \frac{(rt_{\text{Tr}})^{k-1} \cdot e^{-rt_{\text{Tr}}}}{(k-1)!} r. \quad (5.3)$$

Taking the trigger time of the 1st fast neutron search run, $t_{\text{Tr}} = 60 \mu\text{s}$, and the gamma rate to be the sum over the two tanks measured for the low PMT period, $r \approx 697 \text{ Hz}$, the rate of multiple gamma events may be estimated for each multiplicity, namely the number of gamma pulses, k . It is enlightening to compare the background gamma event rate with the estimated fast neutron rate with respect to multiplicity. In Figure 5.1, the neutron multiplicity spectrum from the result of the comprehensive muon simulation for low PMT gain is normalized with the live time of the simulation to show the event rate of high-energy neutrons, plotted in the black histogram. The estimated multiple gamma rate is plotted in red. It is clear that the background gamma events are dominant over the high-energy neutrons for low multiplicities, but the gamma rate plunges fast as multiplicity increases. An event trigger set at 5 on multiplicity, indicated by the dashed magenta line, can strongly suppress background gammas, though may still leave more multiple gamma events than, or comparable with, the high-energy neutron events at multiplicity 5 and 6.

5.1.1 Pulse Height Likelihood Cut

A technique based on pulse height distributions has been developed to further separate the remaining multiple gamma events from high-energy neutrons. The spectrum of pulse heights (or ‘‘pulse amplitudes’’) of high-energy neutrons and that of background gammas form different distributions. The high-energy neutron signal consists of multiple neutron capture pulses, which are directly

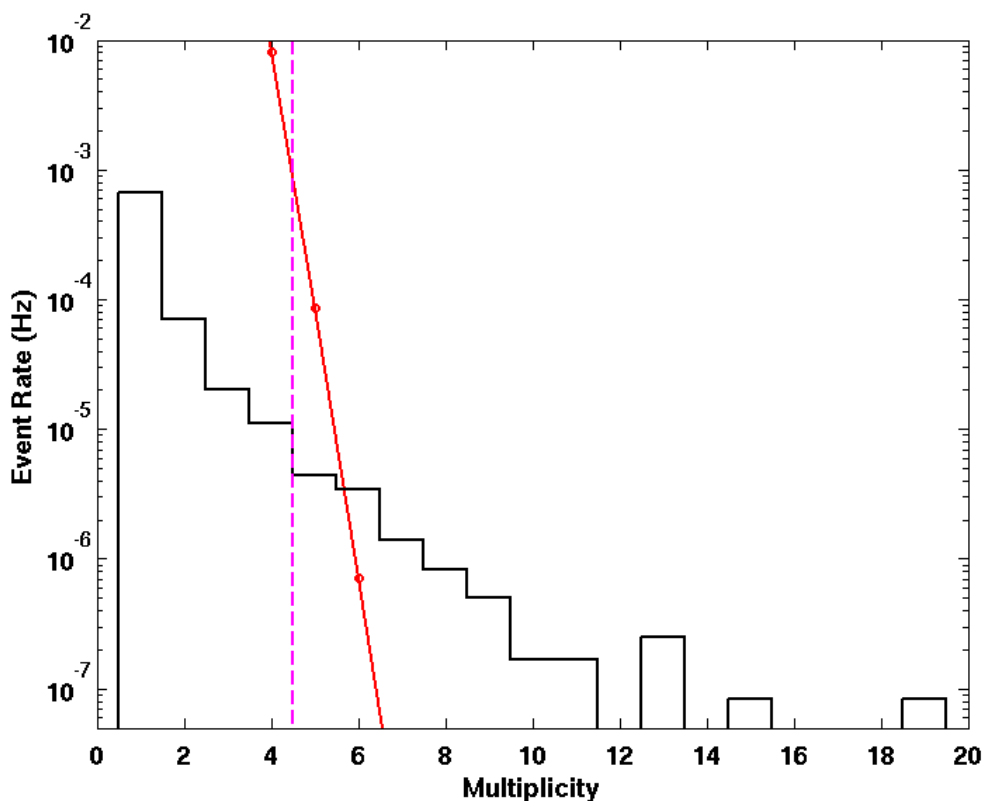


Figure 5.1: Comparison of background gammas and high-energy neutrons in event rate with respect to multiplicity. The rate of multiple gamma events, in red circles and line, is estimated according to Poisson distribution with the input of measured single gamma rate in low PMT gain U/Th gamma exposure runs. The rate of high-energy neutrons as a function of multiplicity, in black histogram, is based on the results of the comprehensive muon simulation processed with low PMT gain parameters. The background gammas are dominant over the high-energy neutron events at low multiplicities up to 5, but plunge fast as multiplicity increases. A trigger on multiplicity at 5 in the fast neutron search runs, labeled with the magenta dashed line, efficiently suppresses most of background gammas. Removing the remaining multiple gammas above the trigger threshold is a major task of the analysis in this chapter.

from ~ 8 MeV gamma cascades of the deexcitation of the capture products, while the background gammas are from U/Th decays of energy spectrum with end point 2.6 MeV. The energy resolution of the NMM detector is limited as shown in Section 4.1.3 with strong smearing over the features of the original energy spectra. However, the detected pulse spectra of high-energy neutrons and background gammas are still distinctive enough to develop a likelihood analysis. The comparison of the pulse spectra of neutron captures and background gammas is shown in Figure 5.2, using the neutron capture pulse spectrum (in blue) measured with the ^{252}Cf calibration data and gamma pulse spectrum (in red) measured with the U/Th background gamma exposure data (taken with multiplicity-1 in $10\ \mu\text{s}$ trigger). Gamma background (about 1-2% of the rate) was subtracted from the pulse spectrum of the ^{252}Cf calibration data to form the the neutron capture pulse spectrum. The background gamma pulse spectrum peaks at ~ 0.03 V, and falls quickly, while the neutron capture pulse spectrum peaks at ~ 0.05 V, and extends in a relative hard spectrum up to ~ 0.28 V.

By averaging the pulse height spectra of the south and north tanks, probability density functions (PDFs) of neutron capture pulse height $P_n(A)$ and background gamma pulse height $P_g(A)$ can be established for both low gain and high gain data, as functions of pulse height A . For an event of M pulses with pulse heights A_1, A_2, \dots, A_M in fast neutron search data, the likelihood [71] that the event is induced by a high-energy neutron (through neutron captures) is

$$n \equiv \prod_{i=1}^M P_n(A_i), \quad (5.4)$$

while the likelihood for the event to be caused by M gammas is

$$g \equiv \prod_{i=1}^M P_g(A_i). \quad (5.5)$$

n and g for an event may be compared to each other to indicate how likely the event is a fast neutron or from background gammas. Previously, it was standard in this experiment to define a pulse height

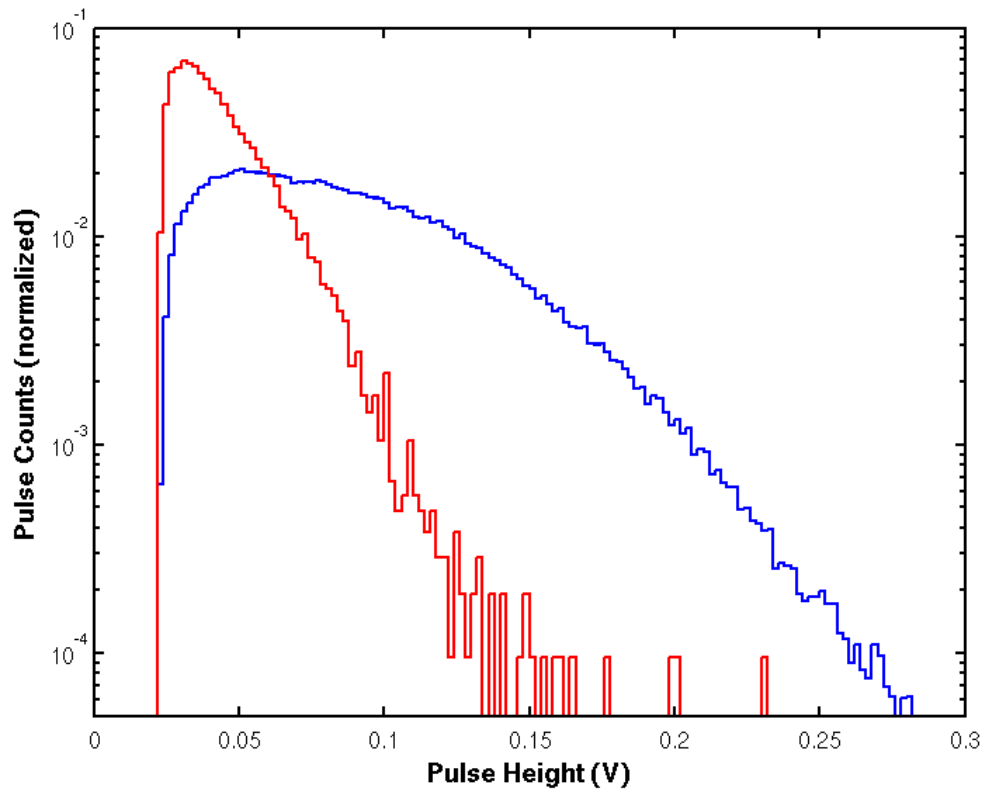


Figure 5.2: Comparison of the pulse spectra of neutron captures and background gammas. The neutron capture pulse spectrum (blue histogram) is measured with the ^{252}Cf calibration data. Gamma pulse spectrum (red histogram) is measured with the U/Th background gamma exposure data. The background gamma pulse spectrum peaks at ~ 0.03 V, and falls quickly, while the neutron capture pulse spectrum peaks at ~ 0.05 V, and extends in a relative hard spectrum up to ~ 0.28 V.

likelihood fraction function

$$L \equiv \frac{n}{n+g}, \quad (5.6)$$

which can serve as a single estimator to tell how likely it is that an event is from a fast neutron or from background gammas.

A demonstration of the distribution of L is shown in the gray histogram in Figure 5.3 for the multiplicity 5 events from the 1st fast neutron search data. The greater and closer to 1 the value of L , the more likely the event originated from a high-energy neutron. An L distribution of only high-energy neutrons (in blue) and an L distribution of only multiple gamma events (in magenta) can be drawn by MC sampling of fake neutron events from the fast neutron PDF n and the multiple gamma PDF g , respectively. A preliminary method to separate the high-energy neutrons and the background gammas is to set a cut on L , say $L > 0.99$, labelled by the red vertical line. A χ^2 fit with the sum of the two components (in black) shows that the sum of the two components provides a good fit to the data ($\chi^2/\text{ndf} = 82.8/94$). The MC sampling predicts that the $L > 0.99$ cut would accept $\sim 68\%$ high-energy neutron events, with ~ 0.4 expected background gamma events, for the event set of multiplicity 5.

5.1.2 Pulse Height Log-Likelihood Ratio (LLR) Fit

An analysis by setting a cut on L and estimating its efficiency would lead to extracting the original number of signal events. Eventually, it is equivalent to just fitting the L distribution in data with the modeled components of signal and background.

In addition, representing the data with L has its shortcomings. The most signal-like data, which convey the most interesting information, are distributed around the high L region, particularly the last bin in Figure 5.3. With these most informative data sorted in a single bin, a lot of important information is lost. A better way of representing the likelihood is using a log-likelihood ratio

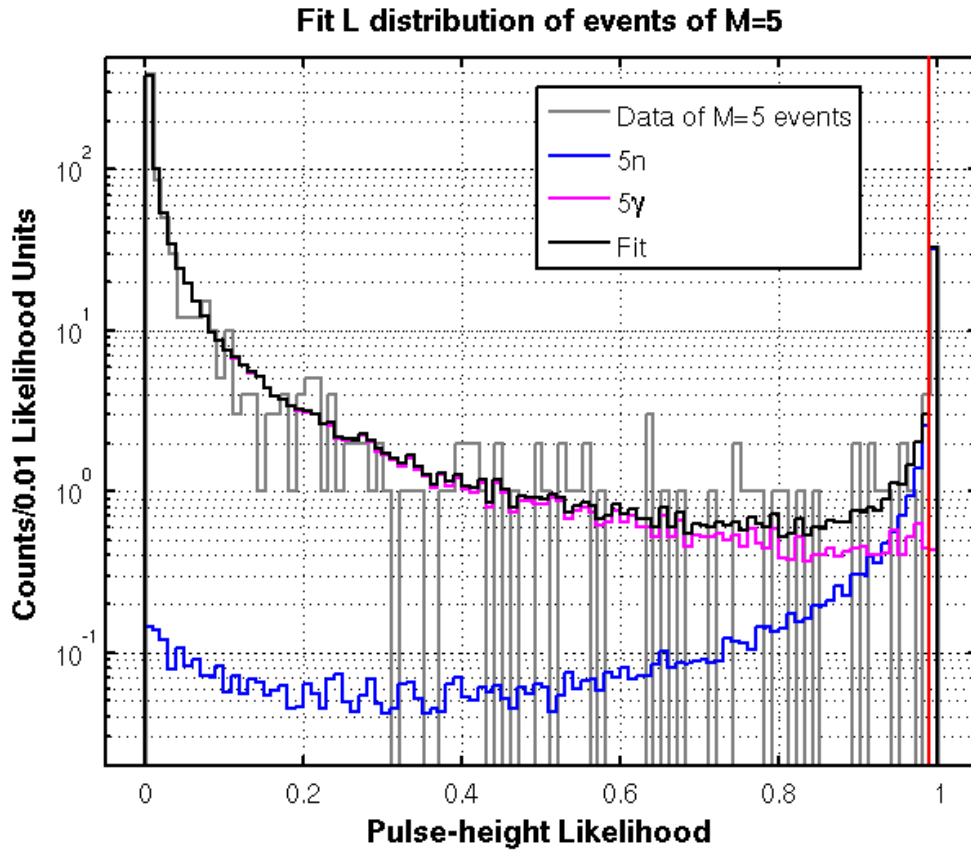


Figure 5.3: Distribution of “pulse-height likelihood” estimator $L \equiv \frac{n}{n+g}$ for the multiplicity 5 events from the 1st fast neutron search data. The greater and closer to 1 the value of L , the more likely the event is induced by a high-energy neutron. The less and closer to 0 the value of L , the more likely the event is caused by background gammas. The expected distribution of L for high-energy neutrons only is shown in the blue histogram, and the expected distribution of L for multiple gammas only is shown in magenta histogram. These expected distributions are generated by MC sampling of fake events from the neutron pulse height PDF $P_n(A)$ and gamma pulse height PDF $P_g(A)$ with 5 pulses per event and calculating the L value from Eq. (5.7). The distributions are normalized by finding the best fit of their sum (black histogram) to the data (gray histogram). The fit indicates that a cut of $L > 0.99$, labeled by the red vertical line, would accept $\sim 68\%$ high-energy neutron events, with ~ 0.4 expected background gamma events, from the multiplicity-5 data. The goodness-of-fit is $\chi^2/ndf = 82.8/94$, with $p = 0.79$.

(LLR) (with base 10 for a convenient correspondence to L) of the neutron likelihood to the gamma likelihood

$$\text{LLR} \equiv \log_{10} \left(\frac{n}{g} \right). \quad (5.7)$$

This representation will show the highly signal-like data in more detail, better revealing whether the model provides a good fit. The LLR distribution of the multiplicity 5 events from the 1st fast neutron search data is shown in Figure 5.4. Similar to the L distribution, the greater the value, the more likely that an event is from a high-energy neutron. But an LLR value 2 approximately corresponds to $L = 0.99$. The events in the last bin, from $0.99 - 1$, of the L histogram have been extended to a distribution with $\text{LLR} > 2$. The high peak around -2 represents the population of gamma-like events.

5.1.3 Component Modeling for the LLR Fit

As discussed above, the components of the LLR distribution of the candidate events from fast neutron search data include real fast neutron events as the signal and background gammas. For a particular multiplicity M , they are the events with M neutron capture pulses and the events with M gamma pulses. Naively speaking, there could also be the components for $(M - 1)$ neutrons with 1 gamma, $(M - 2)$ neutrons with 2 gammas, ..., and 1 neutron with $(M - 1)$ gammas in the LLR distribution. To fit the LLR distribution, firstly, the component representing each case has to be modeled. A pulse height induced by either a neutron capture or a background gamma is expected to conform with the PDF of neutron captures, $P_n(A)$, or the PDF of background gammas, $P_g(A)$, accordingly. Pulse heights can be sampled from the PDFs $P_n(A)$ and $P_g(A)$ with a Monte Carlo method to form a pulse train for each of many events simulated, for each case of pulse compositions. Then the LLR value may be calculated for all the sampled events of a given pulse composition to form the LLR distribution of each case of pulse compositions. The pulse height PDFs for low and

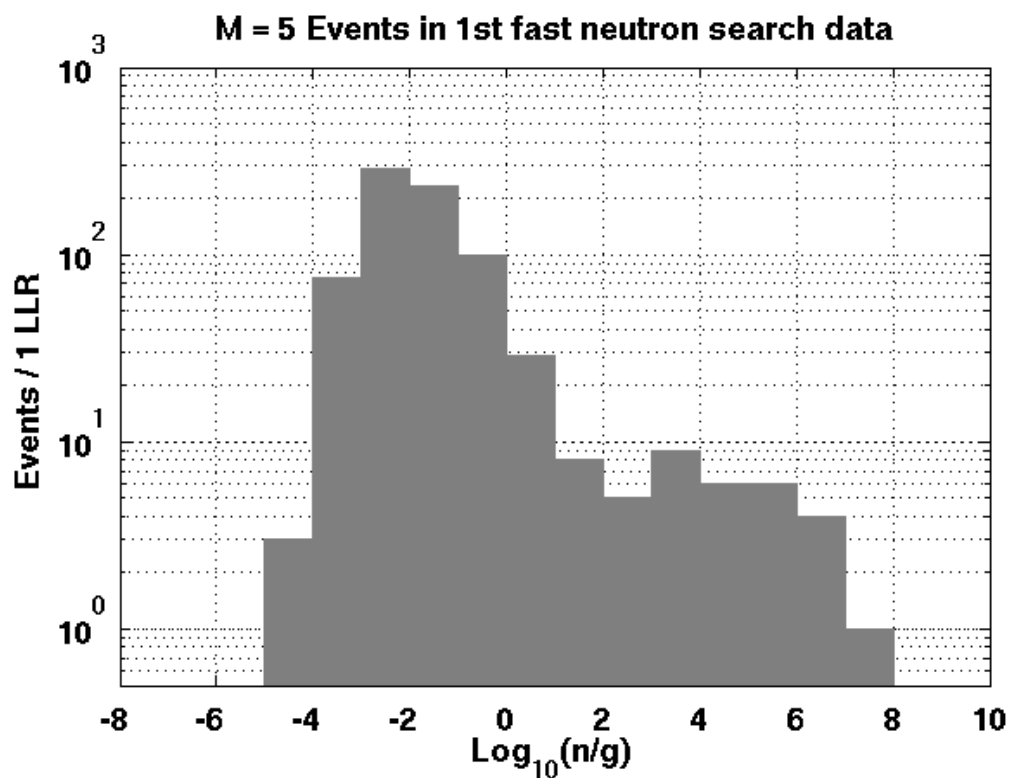


Figure 5.4: Representation of neutron likelihood in log-likelihood ratio (LLR) $\log_{10}\left(\frac{n}{g}\right)$ for the multiplicity-5 candidate events in the 1st fast neutron search data, with 1 LLR value difference per bin. The greater the LLR value, the more likely that an event is induced by a high-energy neutron. The large population with a peak around -2 is formed by background gammas, while the events with $\text{LLR} > 2$ are mostly high-energy neutron events. The cut $L > 0.99$ is approximately equivalent to cutting on LLR at 2.

high PMT gains are slightly different, so this process was done differently for the two gain settings and applied appropriately to the different fast neutron search data sets, i.e. the model based on the low PMT gain was used for the 1st fast neutron search, and the model based on high PMT gain was used for the 2nd and 3rd fast neutron searches. Figure 5.5 shows the LLR component distributions of multiplicity 5 for each case of pulse components, with the low gain distributions on the top and the high gain on the bottom.

Given the Poisson distribution of the gamma pulse multiplicity with the measured gamma rate, the rate of these coincidence with neutron capture and several gammas should be small. For a fast neutron event with multiplicity $(M - 1)$, namely $(M - 1)$ neutron capture pulses in the $200 \mu\text{s}$ event recording time, the rate of the fast neutron event being coincident with 1 gamma, in the 1st fast neutron search data for example, is

$$\begin{aligned} R_{(M-1)n;1g} &= R_{(M-1)n} \cdot P(1; 697 \text{ Hz} \cdot 200 \mu\text{s}) \\ &\approx R_{(M-1)n} \cdot 0.121, \end{aligned} \quad (5.8)$$

with the notation $P(k; r \cdot t) = e^{-rt} (rt)^k / k!$ the Poisson distribution. In the 1st fast neutron search data with 158 live days, the number of multiplicity 4 events is estimated by the comprehensive muon simulation as 137 ± 12 , which would result in ~ 17 as the estimate of events with 4 neutrons and 1 gamma. This number is somewhat smaller than the simulation's estimated multiplicity-5 events in the 1st fast neutron search data, 62 ± 8 . Then, the rate of $(M - 2)$ neutron captures being coincident with 2 gammas can be estimated as

$$\begin{aligned} R_{(M-2)n;2g} &= R_{(M-2)n} \cdot P(2; 697 \text{ Hz} \cdot 200 \mu\text{s}) \\ &\approx R_{(M-2)n} \cdot 0.00845. \end{aligned} \quad (5.9)$$

With the number of multiplicity 3 events in the 1st fast neutron search data estimated as 273 ± 15 , the number of events with 3 neutrons and 2 gammas is estimated as ~ 2.3 , which is smaller than the uncertainty of estimated multiplicity 5 events and may be ignored. And the components of $(M - 3)$

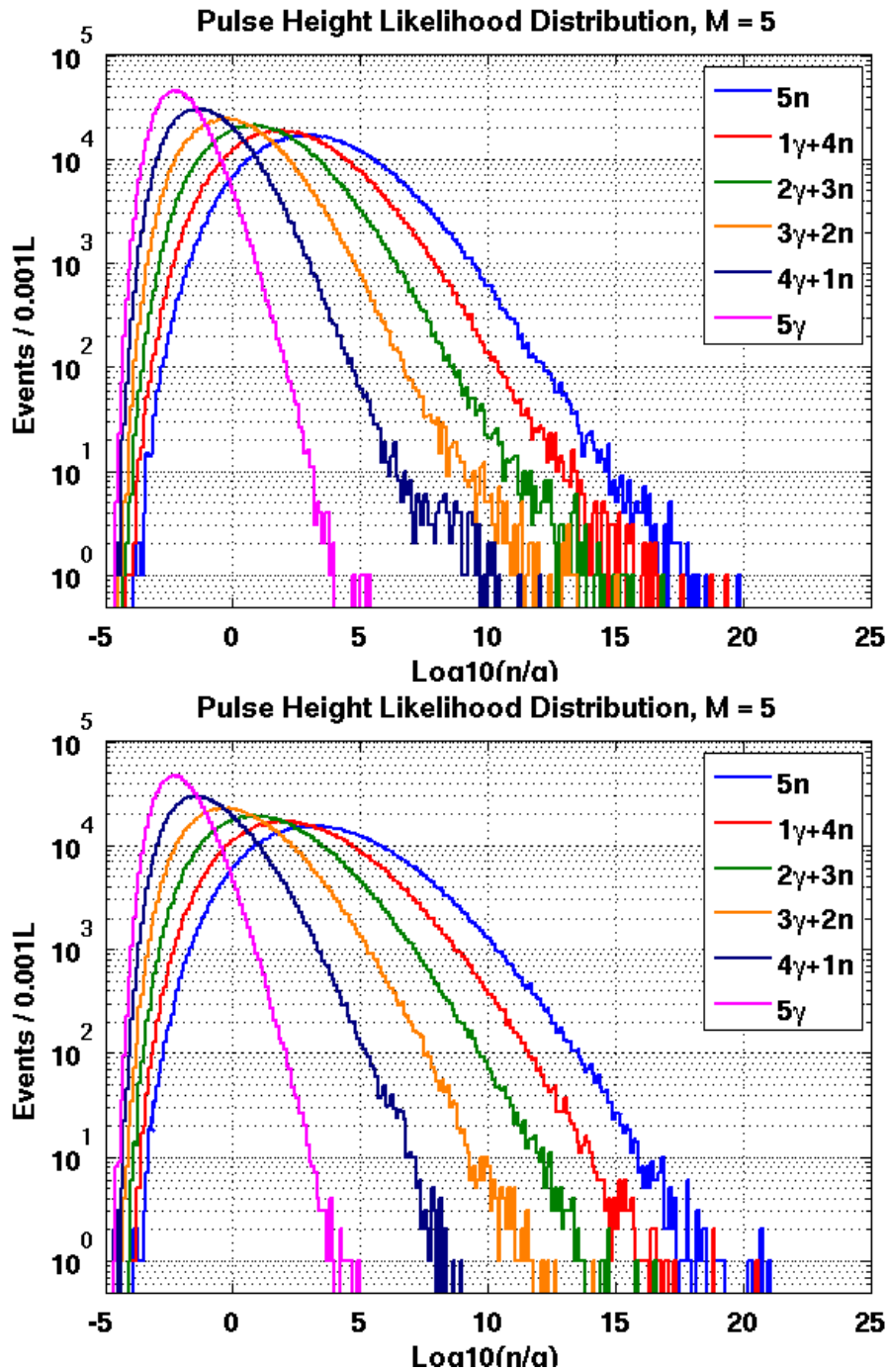


Figure 5.5: LLR component distribution of multiplicity 5 for each combination of neutron captures and gamma pulses, with the low-gain distributions on the top and the high-gain distributions on the bottom. The component distributions include “5n”, standing for the events of 5 neutron captures, “1 γ +4n”, standing for 4 neutrons coincident with 1 gamma, “2 γ +3n”, “3 γ +2n”, “4 γ +1n”, and “5 γ ”. They are plotted in colors as shown in the legends. The different component distributions are generated by sampling fake events based on neutron capture pulse PDF $P_n(A)$ and background gamma pulse PDF $P_g(A)$ with the appropriate pulse combination, then calculating the LLR values. The component distributions for high PMT gain are slightly more extended towards larger LLR values than their counterparts for low PMT gain.

neutrons plus 3 gammas, etc. would be even smaller.

In summary, the model for the LLR fit includes the component of M neutron captures, the component of $(M - 1)$ neutron captures with 1 gamma, and the component of M gammas, but ignoring the other possible pulse combinations, to fit the LLR distribution of multiplicity M events.

Furthermore, we may find the dependence of the $(M - 1)n+1g$ component on the Mn component, and therefore constrain the fit further. The comprehensive muon simulation, although not necessarily predicting the absolute multiplicity spectrum of high-energy neutrons accurately, should give a reasonable estimation of the ratio of the event rates between two multiplicities. Thus, we can assume

$$\frac{\mathcal{A}_{(M-1)n}}{\mathcal{A}_{Mn}} = \frac{\mathcal{N}_{(M-1)n}^{\text{MC}}}{\mathcal{N}_{Mn}^{\text{MC}}}, \quad (5.10)$$

where \mathcal{A}_{Mn} denotes the amplitude of the M -neutron component in the LLR fit for the fast neutron search data, and $\mathcal{N}_{Mn}^{\text{MC}}$ denotes the number of M neutron events predicted by the MC. In the fast neutron search data, some of the events with $(M - 1)$ neutron captures would be coincident with 1 gamma pulse and appear as multiplicity- M events. The probability of the coincidence is the Poisson probability P_{1g} of 1 gamma being present in $200 \mu\text{s}$. Then we have

$$\mathcal{A}_{(M-1)n+1g} = \mathcal{A}_{(M-1)n} \cdot P_{1g}. \quad (5.11)$$

Combining the above two equations gives the dependence of the $(M - 1)n+1g$ amplitude on the Mn amplitude,

$$\mathcal{A}_{(M-1)n+1g} = P_{1g} \cdot \frac{\mathcal{N}_{(M-1)n}^{\text{MC}}}{\mathcal{N}_{Mn}^{\text{MC}}} \cdot \mathcal{A}_{Mn}. \quad (5.12)$$

Therefore, the fit for the LLR distribution of multiplicity M events includes three components, M neutrons, $(M - 1)$ neutrons with 1 gamma, and M gammas. But only the amplitude of M neutrons, \mathcal{A}_{Mn} , and the amplitude of M gammas, \mathcal{A}_{Mg} , are independent parameters.

The $(M - 1)n+1g$ events should be considered as signal, since most of the pulses are neutron captures, signaling detection of fast neutrons. But their multiplicities are shifted by one, and the estimates of these events should be counted as multiplicity $(M - 1)$ when reconstructing the multiplicity spectrum.

5.2 Data Quality Cuts

The LLR fit of the fast neutron search data at first often resulted in rather bad fits for some multiplicities. The gamma peak often shows discrepancy between the LLR distribution of fast neutron data and the multi-gamma component in the model. Especially at the intermediate LLR values (about $-1 \leq M \leq 2$), the excess of events in the fast neutron search data over the model may drive the amplitude of signal components up, and result in an overestimate of high-energy neutrons. This issue is particularly severe in the 3rd fast neutron search data.

Unphysical events, such as those induced by electronic noise, are a common problem in particle detection experiments, and are known to exist in the NMM as well. These noise pulse events may compromise the LLR distribution, since they are neither neutron capture pulses nor background gamma pulses. The afterpulsing induced by the muon events potentially leaking into the candidate event set may also result in abnormal LLR values. Therefore, it is necessary to examine the data quality over all the data sets of the fast neutron search, and develop data quality cuts to remove unphysical events.

5.2.1 Muon Pulse and Afterpulsing with Mis-coincidence

In an examination of event waveforms among high-multiplicity fast neutron candidate events, some dangerous events were spotted. They look like typical muon events with a large leading pulse and many after-pulses, which should have been removed by the muon rejection cut. An example is shown

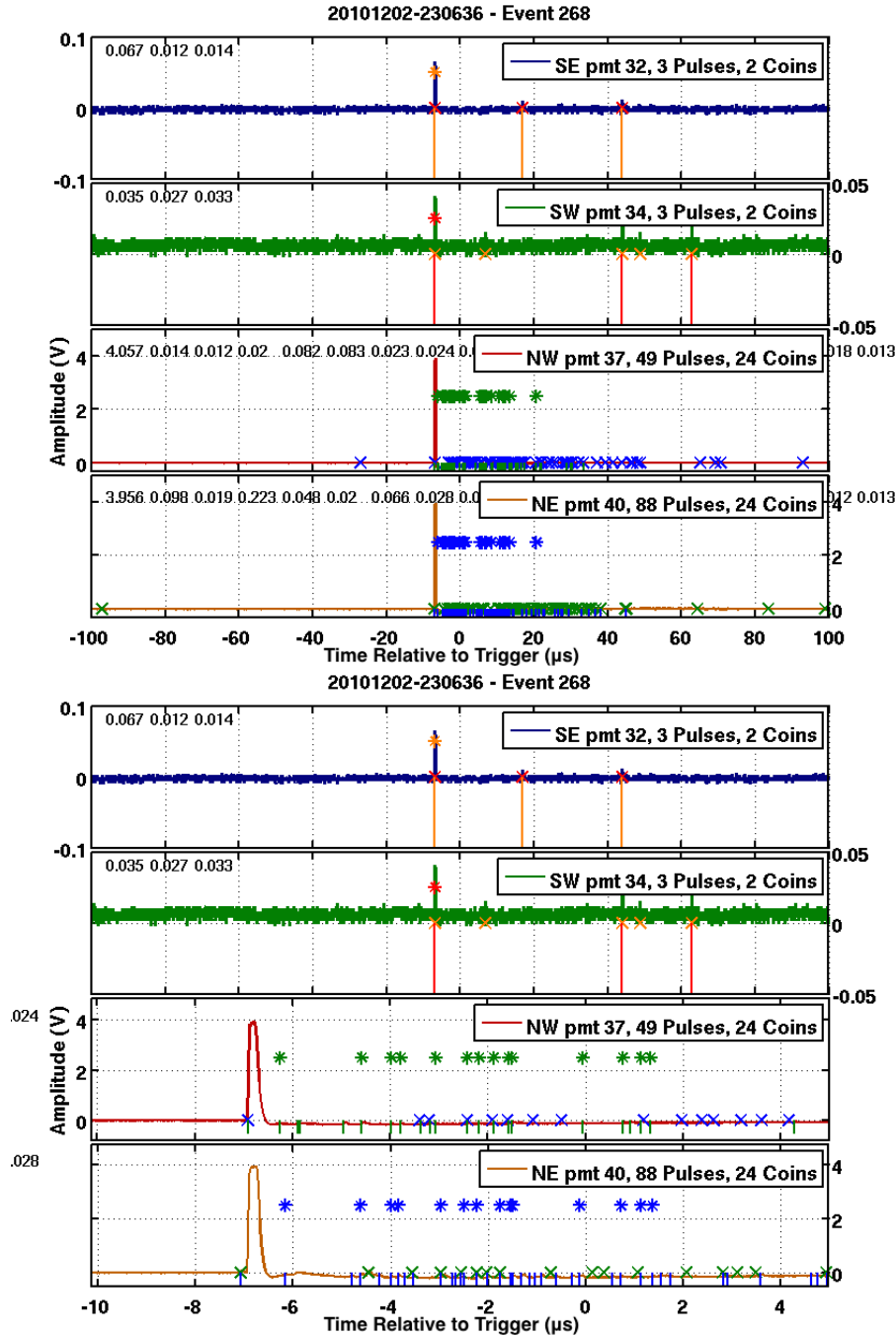


Figure 5.6: An example of mis-coincident muon event with afterpulsing, shown with waveforms in the four PMT channels. On the top is the overall look, while on the bottom the two channels of the north tank are zoomed in from $-10 \mu\text{s}$ to $5 \mu\text{s}$ in time relative to trigger. The cross marks along the baseline of the waveforms label the individual triggered pulses in a single PMT, and the star marks at a higher level label the coincident pulses between the two channels identified by DAQ software. The times of the two individual muon pulses in the north tank channels are measured to separate just farther than 160 ns , the time window for identifying coincident pulses. It causes the DAQ to miss the huge muon pulse from triggering and recording. Therefore the event cannot be screened by the muon rejection cut and leaves a falsely large multiplicity originated from accidentally coincident after-pulses.

in Figure 5.6, with the overall look on the top and zoomed-in on the bottom. In the waveform plots, the crosses along the baseline of the waveform mark the individual triggered pulses, while the stars at a higher level label the identified coincident pulses. A closer look shows that the muon pulses in the two north tank channels are not identified as a coincidence because their digitized pulse times are just far enough to be out of the time window for identifying channel coincidence. Since the leading large muon pulse is therefore not formally triggered and recorded, the event can sneak into the candidate set without being caught by the muon cut on the first two pulses at 0.2 V or 0.25 V. The remaining after-pulses make a very large number of coincident pulses just by accident, such as 24 in the example, potentially giving a very dangerous high-multiplicity false signal.

However, these sneaky mis-coincidence muon events are easy to remove. A cut on the individual PMT pulses at 1 V works perfectly to clear this issue. This cut is high enough to avoid killing any normal event of neutron captures, thus the efficiency can be considered 100%. This cut is included as part of the muon cut for these data.

5.2.2 Removing Noise Pulses: Integral-Amplitude Ratio Cut

The electronic noise usually does not trigger pulses when the pulse threshold is properly set. But there is still a chance for relatively large electronic noise to trigger and be recorded as pulses. The shapes of the electronic noise pulses are usually very different than the normal photoelectron pulses and appear much messier. Since the noise-triggered events are not physical, the noise pulses in the two PMTs in a tank may only make coincident pulse pairs by accident, requiring the individual pulse numbers in both channels to be much greater than the number of coincident pulse pairs. An example of electronic noise event is shown in Figure 5.7, with the whole waveforms of four channels on the top and zoomed-in at $-20\ \mu\text{s}$ to $20\ \mu\text{s}$ on the bottom. In this event, the noise pulses happen in the two PMTs of the north tank. The overall waveform on the top shows that there are many individual noise pulses in the NW channel that cannot find counterparts in the NE channel to form coincident pulses. So the 16 individual pulses in the NW and the 9 individual pulses in the NE give

only 5 coincident pulses for the north tank. With the zoomed-in waveforms shown on the bottom, the pulses around $0\ \mu\text{s}$ have very messy shapes, and the major pulse at $\sim -1\ \mu\text{s}$ is much wider than normal pulses, such as the pulse at $\sim -5\ \mu\text{s}$.

Based on the characteristics of the electronically noisy events discussed above, there may be two major ways to remove them. One is to cut on the number of triggered pulses of individual channels relative to the coincident pulse number. This method is found to be not very efficient at keeping good events while cutting enough noisy events.

Another way is to exploit the characteristics of the pulse shapes of the noisy events. As shown in the example event in Figure 5.7, the noisy events usually have some pulses with irregular shapes and extra large widths. In reduced data format, there are both pulse amplitudes (pulse heights) and pulse integrals recorded, though only amplitudes are used for the high-level analysis. The ratio of pulse integral to pulse amplitude is proportional to pulse width, therefore may be used as an indicator to tell if the pulse is induced by large electronic noise. To label an event, I choose to use the maximum Integral-Amplitude Ratio (IAR) among all pulses of the event, and this quantity should form a certain distribution among the normal events.

The ^{252}Cf calibration data were taken to detect relatively intense neutron captures in short period of time, so the probability for electronic noise events to happen in calibration data should be very low. The IAR distributions of ^{252}Cf calibration data for multiplicity 5 to 8 are shown as scatter plots of IAR vs pulse height in Figure 5.8 for low-gain calibration and both Figures 5.9 and 5.10, with blue dots for south tank events and orange dots for north tank events. The calibration events distribute within a horizontal band which is wider for small pulse heights and narrower for large pulse heights, and centered along $\text{IAR} \approx 0.12$. They are seldom found with IAR values greater than 2. For a comparison, the fast neutron search data are also plotted (with black dots) in Figure 5.8 for the 1st fast neutron search, Figure 5.9 for the 2nd, and Figure 5.10 for the 3rd. The PMT gains of each fast neutron search data set corresponds to that of the ^{252}Cf calibration data in each figure. The events of the fast neutron search data in the figures have already passed the muon rejection cut.

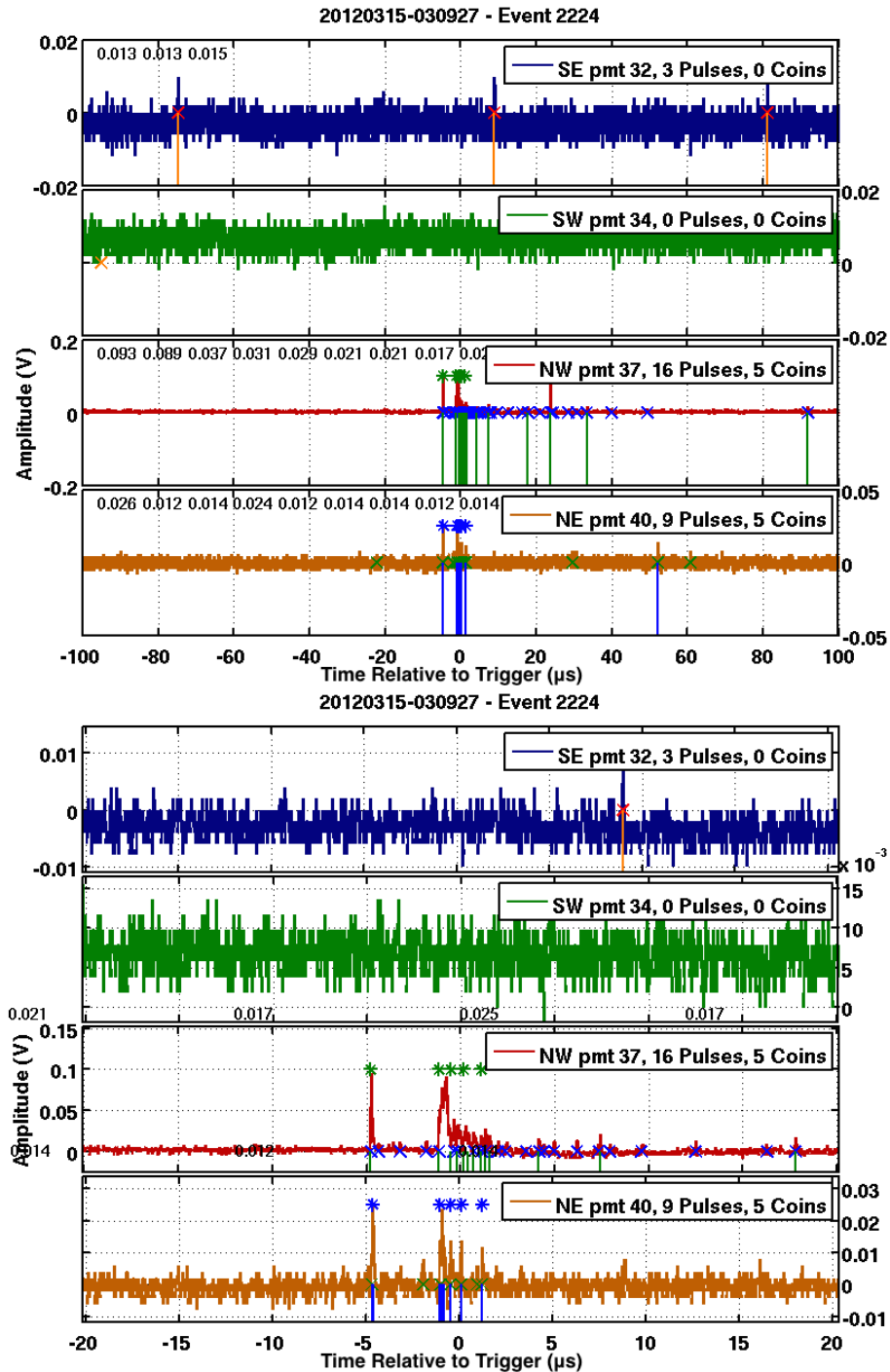


Figure 5.7: An example of an electronic noise event, shown with waveforms in the four PMT channels. On the top is the overall look, while on the bottom the two channels of the north tank are zoomed in from $-20\ \mu\text{s}$ to $20\ \mu\text{s}$ in time relative to trigger. The noisy pulses appear in the north tank channels. The individual pulse numbers in the two channels of the north tank appear very unbalanced and there are relatively few coincident pulses, shown in the overall waveform on the top figure. One of the major pulses has a messy shape that is wider than usual, shown on the bottom zoomed-in waveform.

Most of these candidate events distribute in the band that aligns with the ^{252}Cf neutron captures in the 1st and 2nd fast neutron search data. A few outliers with large IAR values are considered as electronic noise events. The 3rd fast neutron search seems to contain much more noise events, and the distribution in Figure 5.10 indeed shows a vast distribution of high IAR events standing out of the normal event band.

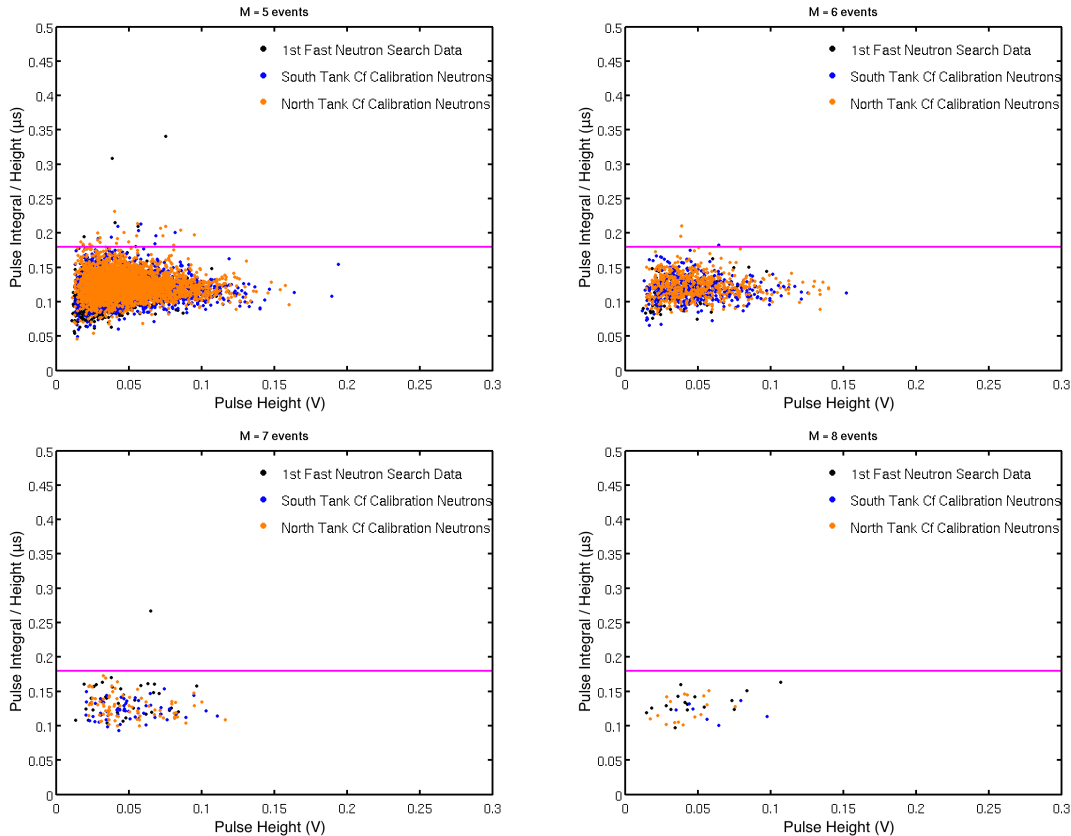


Figure 5.8: The scatter plots of pulse integral to amplitude ratio (IAR) vs pulse height of the 1st fast neutron search data and the low-gain run of ^{252}Cf calibration. The IAR value for the event is that of the pulse with the maximum IAR in the event. The four plots show the data groups of multiplicity 5, 6, 7, and 8, respectively, as labeled on the top of each plot. The events of the 1st fast neutron search data, in black dots, are already applied with another data quality cut and muon rejection cut. The events of ^{252}Cf calibration data are shown in blue dots for the south tank and orange dots for the north tank. The major population of fast neutron search events aligned well with the ^{252}Cf calibration events in a band around $\text{IAR} \approx 0.12$ are considered as normal events, while a few events from the multiplicity 5 and 7 groups in fast neutron search found with high IAR values are considered as electronic noise events. A cut of $\text{IAR} < 0.18$, labeled with magenta lines, would just remove the noise events, without losing many good events.

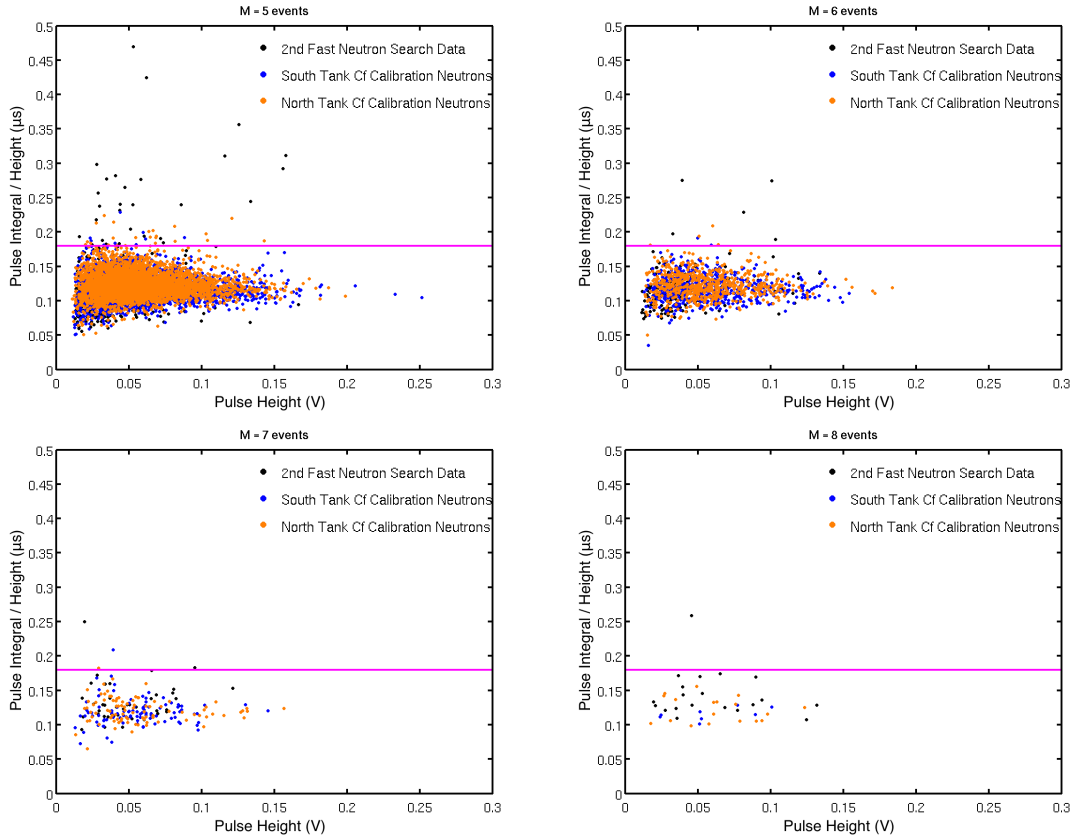


Figure 5.9: The scatter plots of pulse integral to amplitude ratio (IAR) vs pulse height of the 2nd fast neutron search data and the high-gain run of ^{252}Cf calibration. The IAR value for the event is that of the pulse with the maximum IAR in the event. The four plots show the data groups of multiplicity 5, 6, 7, and 8, respectively, as labeled on the top of each plot. The events of the 2nd fast neutron search data, in black dots, are already applied with another data quality cut and muon rejection cut. The events of ^{252}Cf calibration data are shown in blue dots for the south tank and orange dots for the north tank. The major population of fast neutron search events aligned well with the ^{252}Cf calibration events in a band around $\text{IAR} \approx 0.12$ are considered as normal events, while a few events from all multiplicity groups in fast neutron search found with high IAR values are considered as electronic noise events. A cut of $\text{IAR} < 0.18$, labeled with magenta lines, would just remove the noise events, without losing many good events.

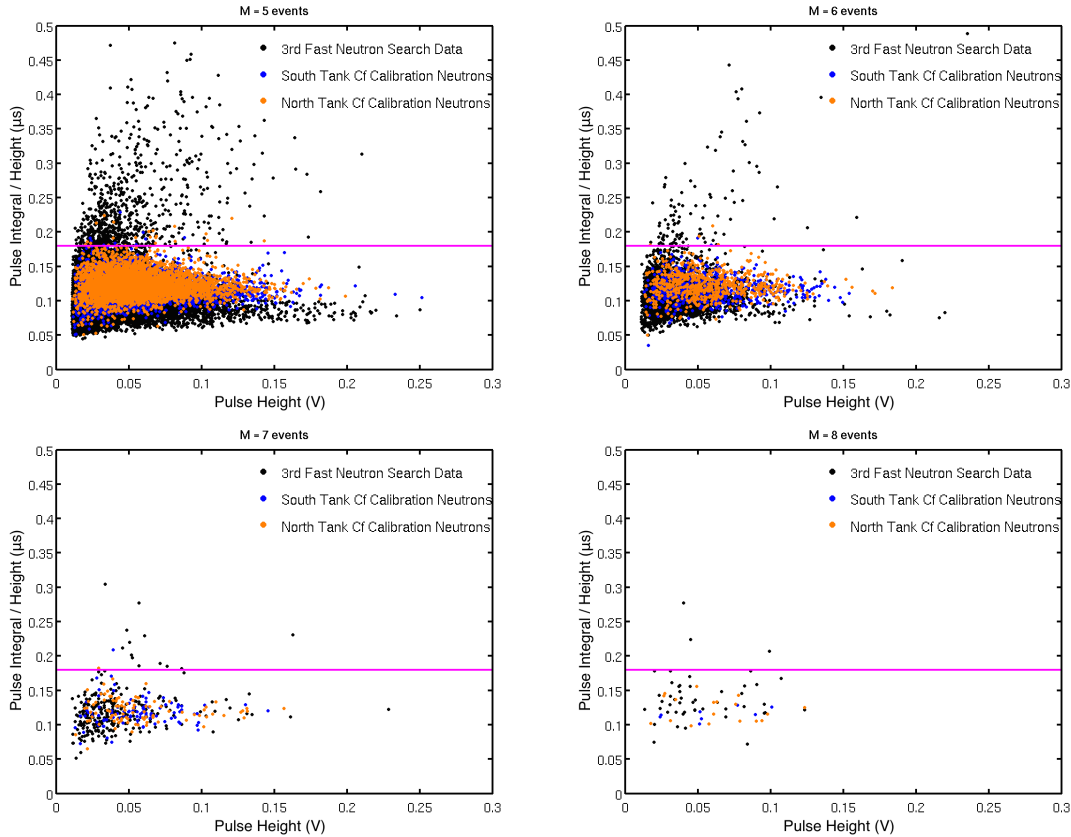


Figure 5.10: The scatter plots of pulse integral to amplitude ratio (IAR) vs pulse height of the 3rd fast neutron search data and the high-gain run of ^{252}Cf calibration. The IAR value for the event is that of the pulse with the maximum IAR in the event. The four plots show the data groups of multiplicity 5, 6, 7, and 8, respectively, as labeled on the top of each plot. The events of the 3rd fast neutron search data, in black dots, are already applied with another data quality cut and muon rejection cut. The events of ^{252}Cf calibration data are shown in blue dots for the south tank and orange dots for the north tank. The major population of fast neutron search events aligned closely with the ^{252}Cf calibration events in a band around $\text{IAR} \approx 0.12$ are considered as normal events, while a large number of events from the multiplicity 5 and 6 groups, and a few from the multiplicity 7 and 8 groups in fast neutron search found with high IAR values are considered as electronic noise events. A cut of $\text{IAR} < 0.18$, labeled with magenta lines, would just remove the noise events, without losing many good events.

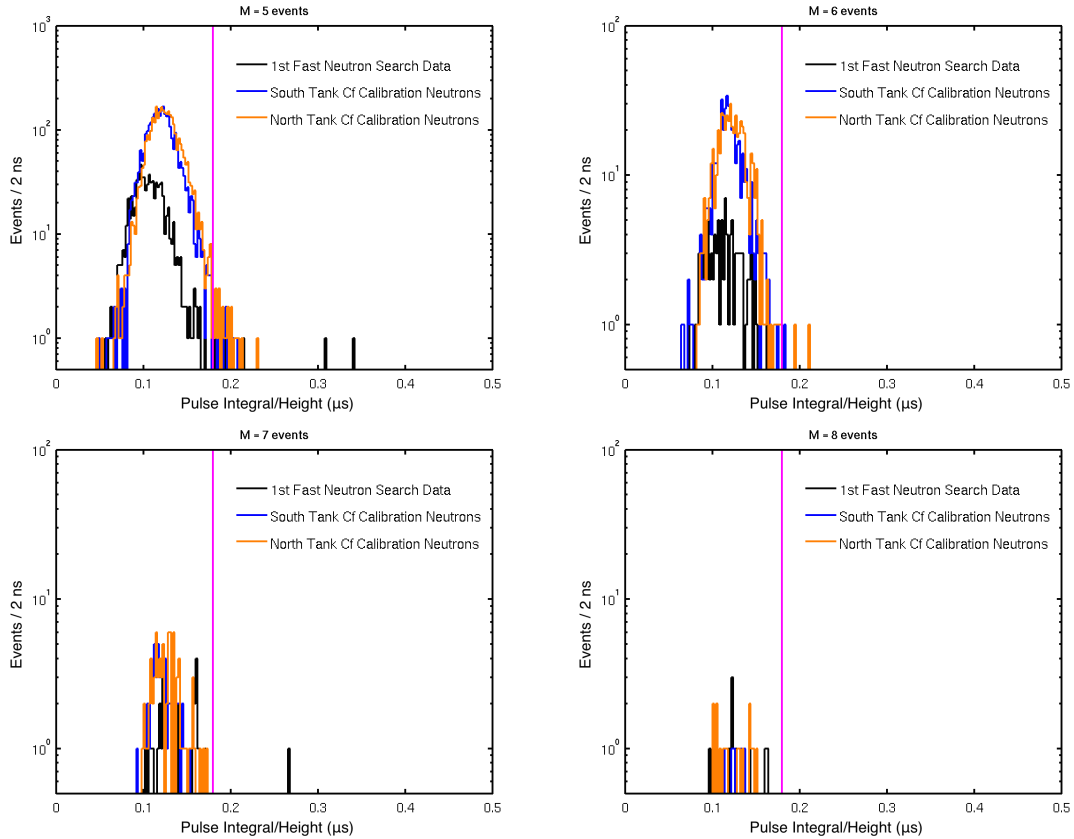


Figure 5.11: The histograms of pulse integral to amplitude ratio (IAR) for the 1st fast neutron search data and the low-gain run of ^{252}Cf calibration. The IAR value for the event is that of the pulse with the maximum IAR in the event. The four plots show the data groups of multiplicity 5, 6, 7, and 8, respectively, as labeled on the top of each plot. The events of the 1st fast neutron search data, in black histograms, are already applied with another data quality cut and muon rejection cut. The events of ^{252}Cf calibration data are shown in blue histograms for the south tank and orange histograms for the north tank. The majority of fast neutron search events populated closely with the ^{252}Cf calibration events are considered as normal events, while a few events in fast neutron search found with high IAR values are considered as electronic noise events. The population of normal events in fast neutron search slightly move towards high IAR values as multiplicity increases, since the IAR ratio of the event is selected as the maximum IAR value from more pulses. A cut of $\text{IAR} < 0.18$, labeled with magenta lines, would just remove the noise events, without losing many good events.

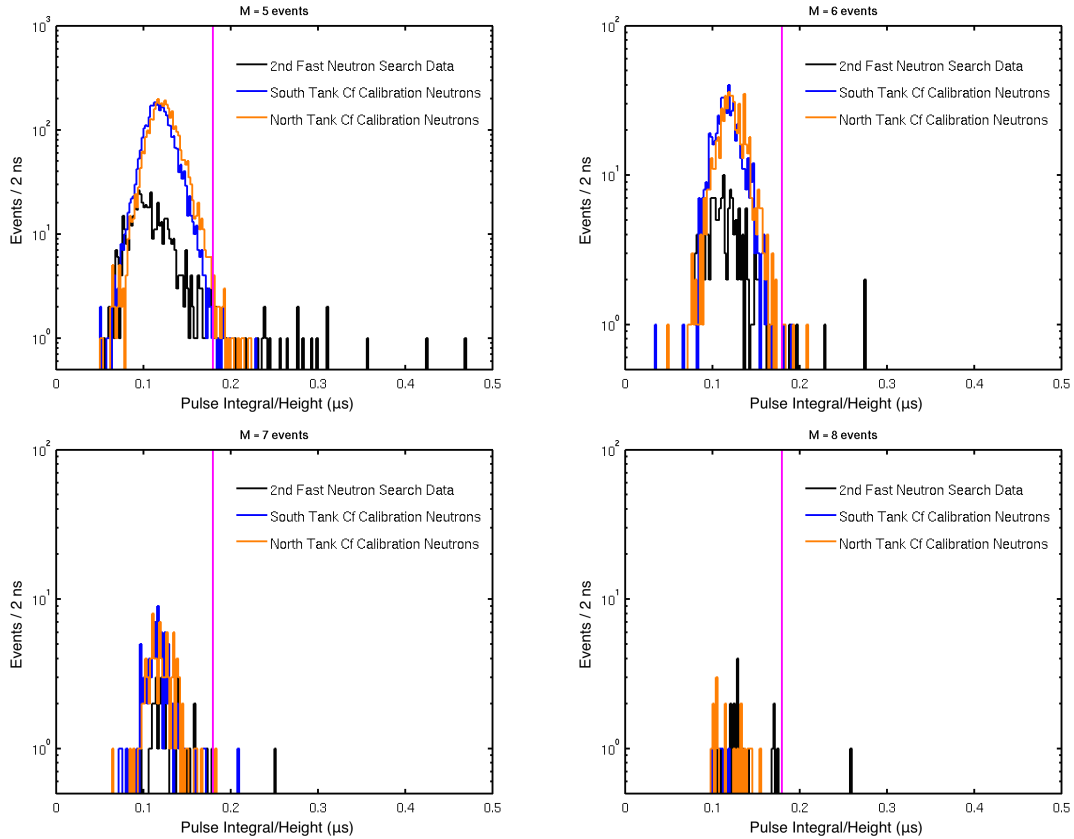


Figure 5.12: The histograms of pulse integral to amplitude ratio (IAR) for the 2nd fast neutron search data and the high-gain run of ^{252}Cf calibration. The IAR value for the event is that of the pulse with the maximum IAR in the event. The four plots show the data groups of multiplicity 5, 6, 7, and 8, respectively, as labeled on the top of each plot. The events of the 2nd fast neutron search data, in black histograms, are already applied with another data quality cut and muon rejection cut. The events of ^{252}Cf calibration data are shown in blue histograms for the south tank and orange histograms for the north tank. The majority of fast neutron search events populated closely with the ^{252}Cf calibration events are considered as normal events, while a few events in fast neutron search found with high IAR values are considered as electronic noise events. The population of normal events in fast neutron search slightly move towards high IAR values as multiplicity increases, since the IAR ratio of the event is selected as the maximum IAR value from more pulses. A cut of $\text{IAR} < 0.18$, labeled with magenta lines, would just remove the noise events, without losing many good events.

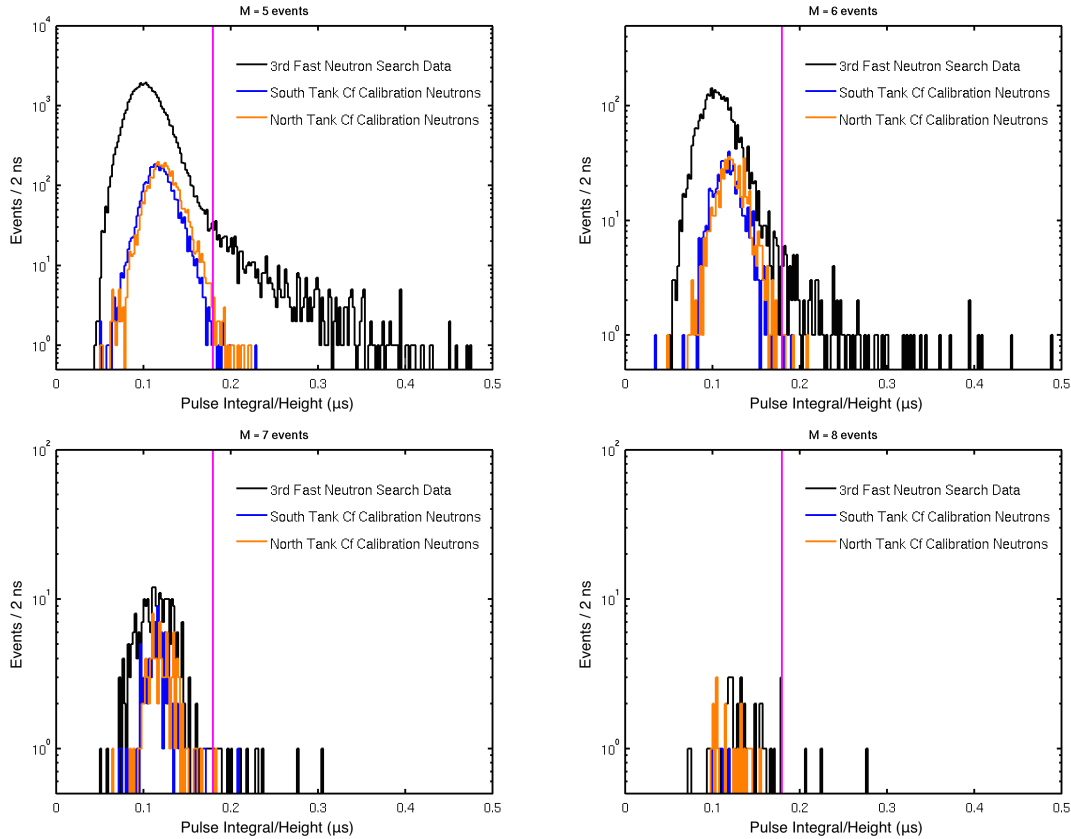


Figure 5.13: The histograms of pulse integral to amplitude ratio (IAR) for the 3rd fast neutron search data and the high-gain run of ^{252}Cf calibration. The IAR value for the event is that of the pulse with the maximum IAR in the event. The four plots show the data groups of multiplicity 5, 6, 7, and 8, respectively, as labeled on the top of each plot. The events of the 3rd fast neutron search data, in black histograms, are already applied with another data quality cut and muon rejection cut. The events of ^{252}Cf calibration data are shown in blue histograms for the south tank and orange histograms for the north tank. The majority of fast neutron search events populated closely with the ^{252}Cf calibration events are considered as normal events, while many events in fast neutron search found with high IAR values are considered as electronic noise events, especially for multiplicity 5 and 6 groups with long tails at the large value end. The population of normal events in fast neutron search slightly move towards high IAR values as multiplicity increases, since the IAR ratio of the event is selected as the maximum IAR value from more pulses. A cut of $\text{IAR} < 0.18$, labeled with magenta lines, would just remove the noise events, without losing many good events.

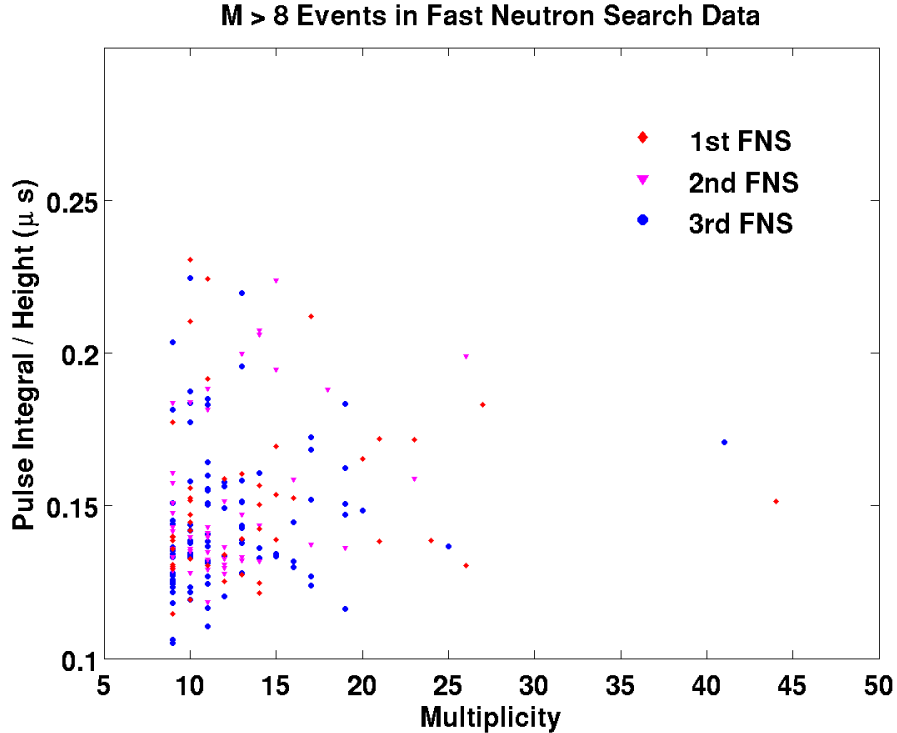


Figure 5.14: Scatter plot of the IAR against multiplicity for the events of multiplicity 9 or greater having passed the muon rejection cut from all the three fast neutron searches. The IAR distribution is consistent with the good ^{252}Cf data.

To demonstrate the distribution of the IAR more clearly, the same comparisons are plotted as histograms of IAR in Figures 5.11, 5.12, and 5.13 for the 1st, 2nd, and 3rd fast neutron search data, respectively. It is found that the peak of the IAR of fast neutron candidate events sits at some slightly smaller values than that of the calibration data for multiplicity 5, but moves towards higher values as multiplicity increases. It is understandable. The IAR of an event is selected from the pulse with the maximum IAR of the event. As multiplicity gets larger, the IAR is selected among more pulses. Thus it is a natural tendency that IAR of fast neutron candidate events moves towards higher values as multiplicity increases. It would not be wise to set too tight a cut, as it could falsely remove too many good events for high multiplicities. A cut of $\text{IAR} < 0.18$ is tight enough to remove all the noisy events that are clearly outliers in the long tails of the distributions, but not so tight that it reduces efficiency appreciably for the main peak of good events. Given the tendency of the peak of good events to move towards higher values for larger multiplicities, it is better not to apply the

cut to events of 9 and more multiplicities. To check if there are non-physical events of multiplicity 9 or greater, the IAR distribution of these events were examined. Figure 5.14 is a scatter plot of the IAR against multiplicity for the events of multiplicity 9 or greater having passed the muon rejection cut from all fast neutron search data. It is clear shown that the IAR distribution of these high-multiplicity events is consistent with the good ^{252}Cf data. I also checked the raw-waveform traces of these events, and found no peculiar events.

Although the calibration data may not perfectly represent the distribution of IAR for high-energy neutrons, they are still the best sample we can trust, without significant conatamination of noise events and background gammas. Therefore, we use the ^{252}Cf neutron calibration data to measure the efficiency of the IAR cut. Assuming all ^{252}Cf events are physical events, with the cut of $\text{IAR} < 0.18$, the measured efficiency, i.e. the acceptance of good neutron capture events, is shown in Figure 5.15 at multiplicity 5 to 8. The efficiency for low-gain data is shown on the top, while for high-gain data is on the bottom. The measurements based on the south tank events are plotted in blue circle and error bar, while the measurements based on the north tank events are in red. In black is shown the measurement using data over both tanks for each multiplicity. As the efficiency approximate keeps constant through these multiplicities, it is good enough to quote a constant cut efficiency. The efficiency of the IAR cut is then measured with the multiplicity 5 through 8 ^{252}Cf , to be $0.9959^{+0.0008}_{-0.0009}$ for low-gain data and $0.9952^{+0.0008}_{-0.0009}$ for high-gain data, shown in Figure 5.15.

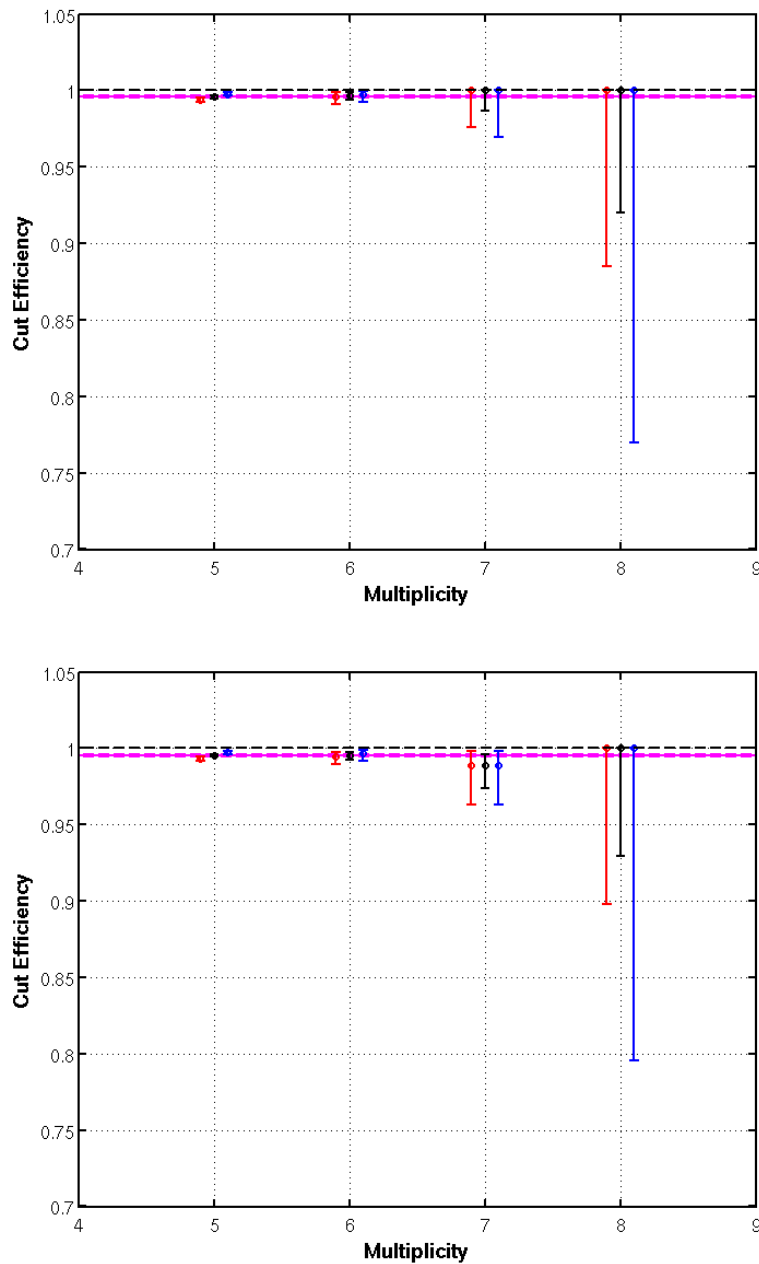


Figure 5.15: The efficiency of the data quality cut of $IAR < 0.18$, defined as the acceptance fraction for good ^{252}Cf calibration events. On the top is measured with the low-gain ^{252}Cf calibration run, and on the bottom is measured with the high-gain ^{252}Cf calibration run. The circles with error bars show the efficiencies measured with multiplicity 5 to 8 individually, with blue for south tank data, red for north tank data, and black for the overall measurement combining both tanks. The change in efficiency as multiplicity increases is not significant, so it is reasonable to treat the efficiency as a constant over multiplicity 5 to 8. The measurements using the overall data including multiplicity 5 to 8 suggest the efficiency to be $0.9959^{+0.0008}_{-0.0009}$ for low-gain data and $0.9952^{+0.0008}_{-0.0009}$ for high-gain data, marked with magenta solid lines, with error bars, almost directly on top of the average, in magenta dashed lines. The black dashed line marks one.

5.3 Results of Log-Likelihood-Ratio (LLR) Fit

Based on the model of three components discussed in section 5.1, χ^2 fits are performed for data collection of each multiplicity in each fast neutron search data set, with the muon and IAR data quality cuts discussed in section 5.2 applied. In this section, I present the results of the LLR fit for each multiplicity case for all the fast neutron search data sets, in Figures 5.16 through 5.32. As described in Section 5.1.3, each fit has only two free parameters: the number of photon events, and the the number of all-neutron events, with the number of 1g events given by Eq. (5.12). In each plot, the LLR distribution of the fast neutron search data is in the gray shaded histogram; for the events of multiplicity M , the signal component Mn is shown in blue histogram, the signal component $(M - 1)n+1g$ in orange, the background component Mg in red, and the fit function, i.e. the sum of above three, is black. The LLR value range for the fit is shown as in between two dashed magenta lines.

With the data quality cuts added to the analysis, the candidate events give LLR distributions more consistent with the model distributions in most cases. But for multiplicity 5 events in the 1st fast neutron search (Figure 5.16), and multiplicity 5 and 6 events in the 3rd fast neutron search (Figure 5.27 and Figure 5.28), the intermediate LLR distribution still shows a large excess over the fit model. Tighter cuts, or the cuts based on pulse numbers on individual channels do not preferentially remove events in this regions, suggesting that these events are not unphysical, noise events. Another possible explanation of the excess is that the true LLR distribution of gamma events has a harder spectrum than expected at the intermediate values, as may occur if the pulse-height distribution of gammas is harder than indicated by U/Th calibration runs. There were only a few calibration runs and U/Th gamma exposure runs, not covering the whole period of fast neutron searches. It is possible that the background gamma pulse spectrum drifted due to PMT gain changing or other unknown reasons, so the likelihood model does not reflect the exact distribution. Given the circumstance, the best we can do is to keep using the current data quality cuts, and do the LLR fit

in a partial range, with which the fit performs well, but avoid the intermediate region. The partial range fits of the LLR distribution are performed for multiplicity 5 and 6 events in the 1st and the 3rd fast neutron search data, shown in Figure 5.16, Figure 5.17, Figure 5.27, and Figure 5.28. The fit ranges are marked with the dashed magenta lines, with the active value ranges for fitting between the first and second lines, and also between the third and fourth lines. With this treatment, the fits are in good agreement with the data in the gamma peak region and the most signal-like region. The total numbers of events estimated by the fit function show reasonably close to the total number in data. The signal components, Mn and $(M - 1)n+1g$ should then give good estimates of the number of fast neutron events.

Beyond multiplicity 6 in the fast neutron search data, the statistics in each multiplicity appears too low to bin into every 1 LLR difference and still get a meaningful distribution. For the multiplicity 7 to 10, we choose to use bins of 3 LLR difference. In the 2nd fast neutron search, the events of multiplicity 6 may be binned with 1 LLR difference bins, but with 3 LLR difference bins it is easier to see the agreement by eye with the statistical fluctuation being smeared. So I use the wider bins for this case as well. Note that there is no multiplicity 5 data set in the 2nd fast neutron search data, since the 2nd fast neutron search was run with trigger at multiplicity 6 in 70 μ s.

For the choice of fitting range, it is generally good to include all candidate events. Usually it does not matter whether to include one more bin with zero counts. For some cases, it is crucial to include the zero-count bin, where the LLR values are the typical values that background gammas occupy. One instance is multiplicity 8 in the 1st fast neutron search, shown in Figure 5.19. If the -6 to -3 bin with zero counts were not included in the fit, the background gamma component in the -3 to 0 bin would rise up to match the data, making gamma component in the -6 to -3 bin falsely high. This would give a poor estimate of total background gamma rate, and might potentially be harmful for signal rate extraction as well.

As the multiplicity increases, the chance to include background gamma events in the candidate set goes extremely low, as for multiplicity 8 to 10 in the 1st and 2nd fast neutron search data, or it

becomes very obvious to separate the signals and backgrounds even if a single background gamma event happens to be included in the candidate events, as for multiplicity 9 and 10 in the 3rd fast neutron search data. So the LLR fits are less necessary for these cases. In addition, for the events of multiplicity 10 in all three fast neutron search data, the fits significantly underestimate the total number of signal events, which is more obvious to know directly by counting. In these cases, the relation shown in Eq. (5.12) is directly applied to the original counts of signal-like events to estimate the Mn component and the $(M - 1)n+1g$ component.

As the analysis runs into the multiplicities beyond 10, the statistics becomes very scarce. It is reasonable to use wider bins of multiplicities, say multiplicity 11 to 15, 16 to 20, etc., and the counts divided by 5 to represent the amplitudes comparable with the previous multiplicity bins. As the multiplicity “smeared” into wider bins and the probability to mix any background gamma even smaller, it becomes unnecessary to separate the Mn component and $(M - 1)n+1g$ component. Therefore, in the analysis of the multiplicity 11 and larger, the way is to simply bin the events into multiplicity bins of width 5, and divide the counts by 5 to normalize. As an example, Figure 5.33 shows the LLR distribution for the group of multiplicity 11 to 16 on the top, and the group of multiplicity 16 to 20 on the bottom, in the 3rd fast neutron search. The LLR values of these events show a solid confidence of being inferred as fast neutrons.

With the extracted signal event numbers, of two components if applicable, in all relevant multiplicities, the multiplicity spectrum can then be constructed, and compared to the simulated one. In addition, the extracted signal event numbers will allow a measurement of the high-energy neutron flux.

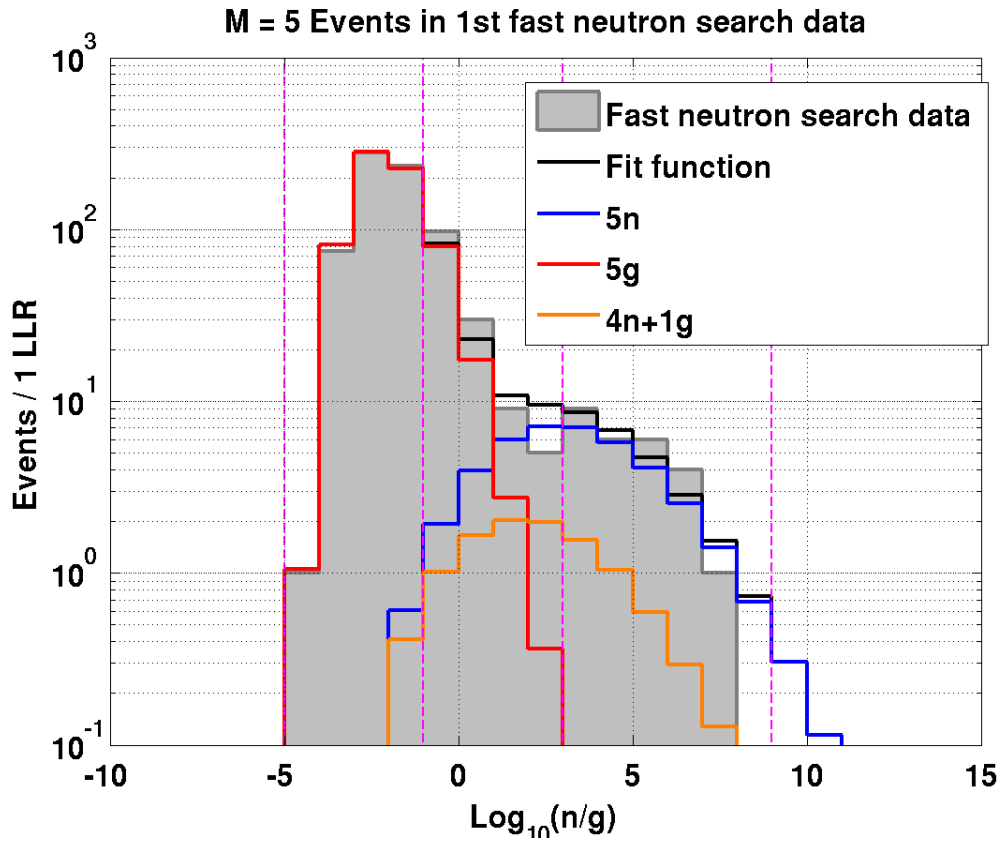


Figure 5.16: Least-squares fit of the LLR distribution for the multiplicity 5 events in the 1st fast neutron search data with a model composed of signal components $5n$ (blue), multiplicity-shifted signal component $4n+1g$ (orange), and background gamma component $5g$ (red). The candidate events, shown in the gray histogram, are binned per 1 LLR difference. The fit is performed in a partial range, from -5 to -1, and from 3 to 9, labeled as in between the first two magenta lines and in between the third and fourth magenta lines, respectively. The resulted fit function, shown in the black histogram, is the sum of the three components, with amplitudes of $5n$ and $5g$ as the two free parameters, while the amplitude of the $4n+1g$ component dependent on that of $5n$ according to Eq. (5.12). The goodness-of-fit is tested to be $\chi^2/ndf = 2.36/8$, with $p = 0.97$.

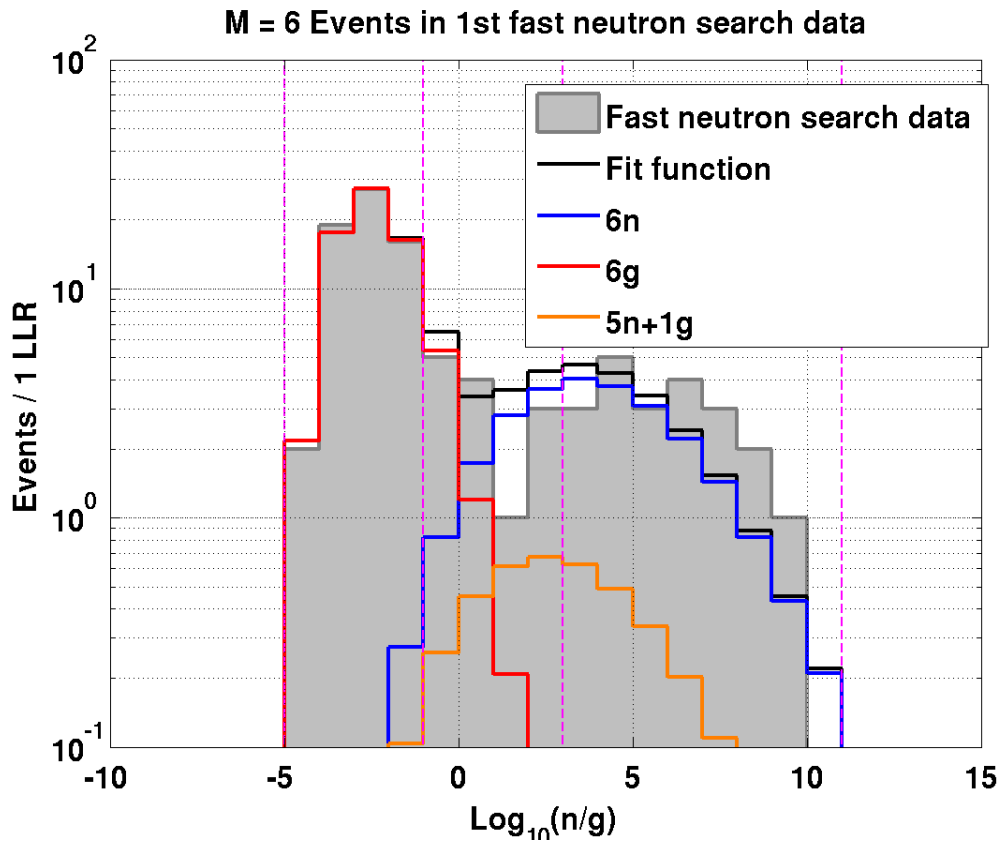


Figure 5.17: Least-squares fit of the LLR distribution for the multiplicity 6 events in the 1st fast neutron search data with a model composed of signal components $6n$ (blue), multiplicity-shifted signal component $5n+1g$ (orange), and background gamma component $6g$ (red). The candidate events, shown in the gray histogram, are binned per 1 LLR difference. The fit is performed in a partial range, from -5 to -1, and from 3 to 11, labeled as in between the first two magenta lines and in between the third and fourth magenta lines, respectively. The resulted fit function, shown in the black histogram, is the sum of the three components, with amplitudes of $6n$ and $6g$ as the two free parameters, while the amplitude of the $5n+1g$ component dependent on that of $6n$ according to Eq. (5.12). The goodness-of-fit is tested to be $\chi^2/ndf = 3.55/10$, with $p = 0.97$.

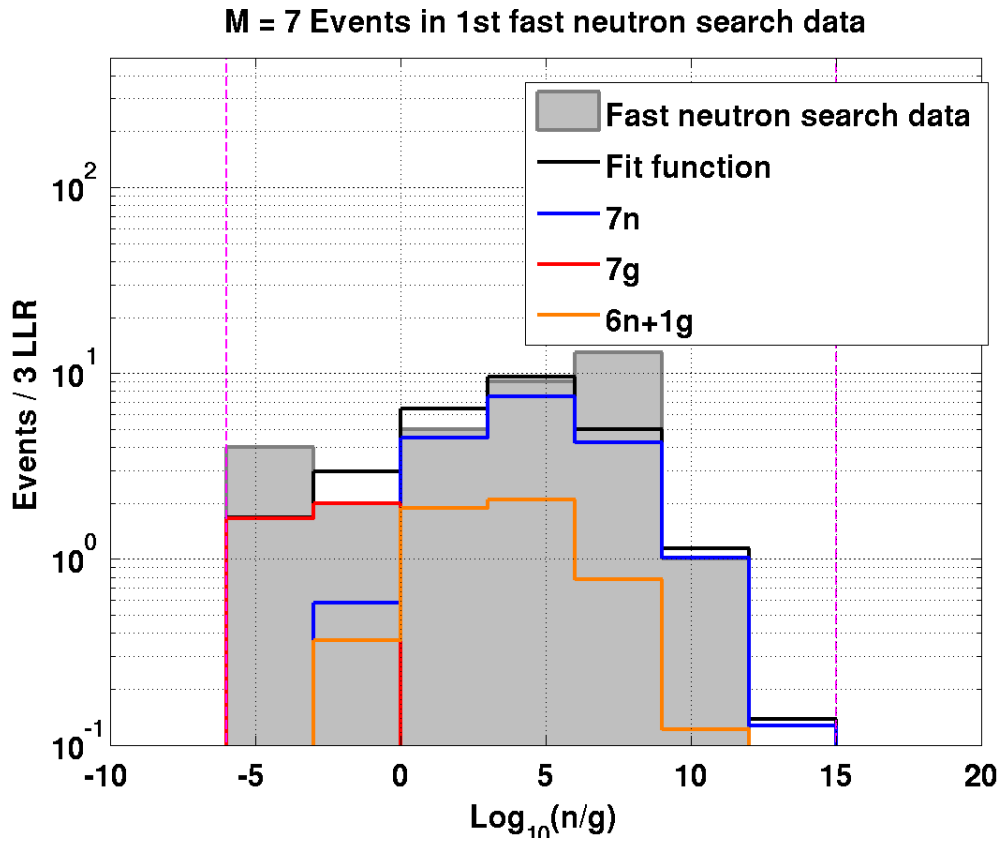


Figure 5.18: Least-squares fit of the LLR distribution for the multiplicity 7 events in the 1st fast neutron search data with a model composed of signal components $7n$ (blue), multiplicity-shifted signal component $6n+1g$ (orange), and background gamma component $7g$ (red). The candidate events, shown in the gray histogram, are binned per 3 LLR difference. The fit is performed from -6 to 15, labeled as in between the two magenta lines. The resulted fit function, shown in the black histogram, is the sum of the three components, with amplitudes of $7n$ and $7g$ as the two free parameters, while the amplitude of the $6n+1g$ component dependent on that of $7n$ according to Eq. (5.12). The goodness-of-fit is tested to be $\chi^2/ndf = 7.23/5$, with $p = 0.21$.

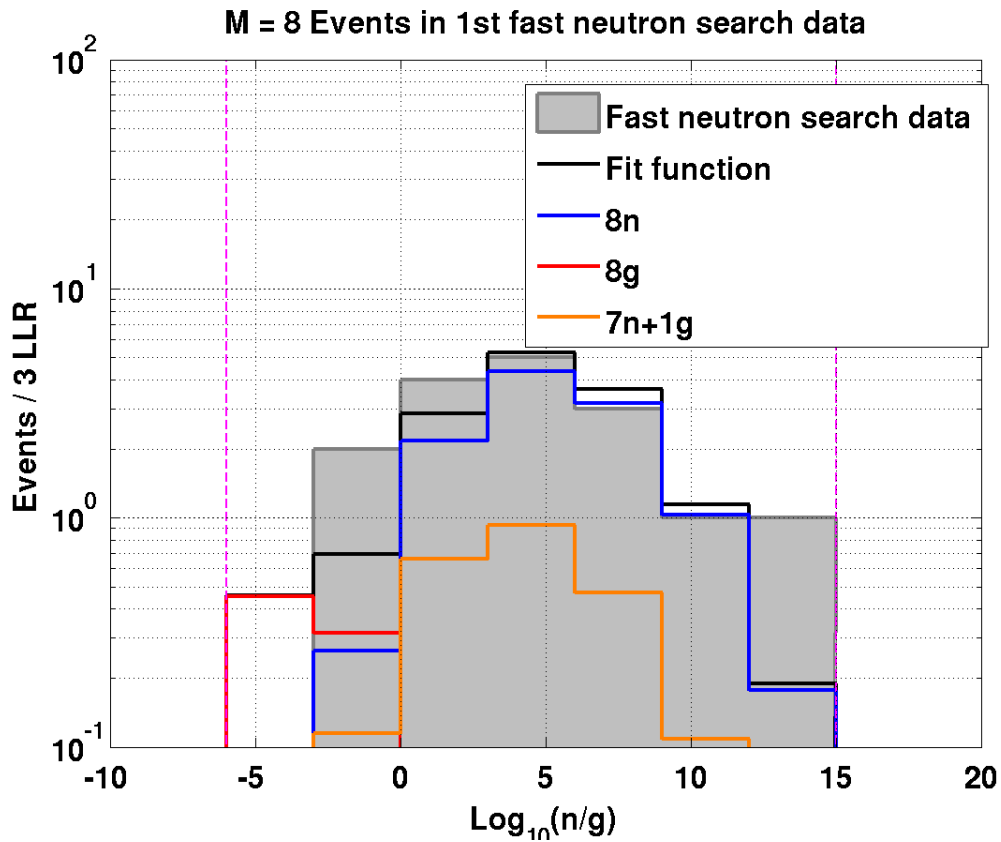


Figure 5.19: Least-squares fit of the LLR distribution for the multiplicity 8 events in the 1st fast neutron search data with a model composed of signal components $8n$ (blue), multiplicity-shifted signal component $7n+1g$ (orange), and background gamma component $8g$ (red). The candidate events, shown in the gray histogram, are binned per 3 LLR difference. The fit is performed from -6 to 15, labeled as in between the two magenta lines. The first empty bin is necessary to be included to constrain $8g$ component. The resulted fit function, shown in the black histogram, is the sum of the three components, with amplitudes of $8n$ and $8g$ as the two free parameters, while the amplitude of the $7n+1g$ component dependent on that of $8n$ according to Eq. (5.12). The goodness-of-fit is tested to be $\chi^2/ndf = 2.22/5$, with $p = 0.82$.

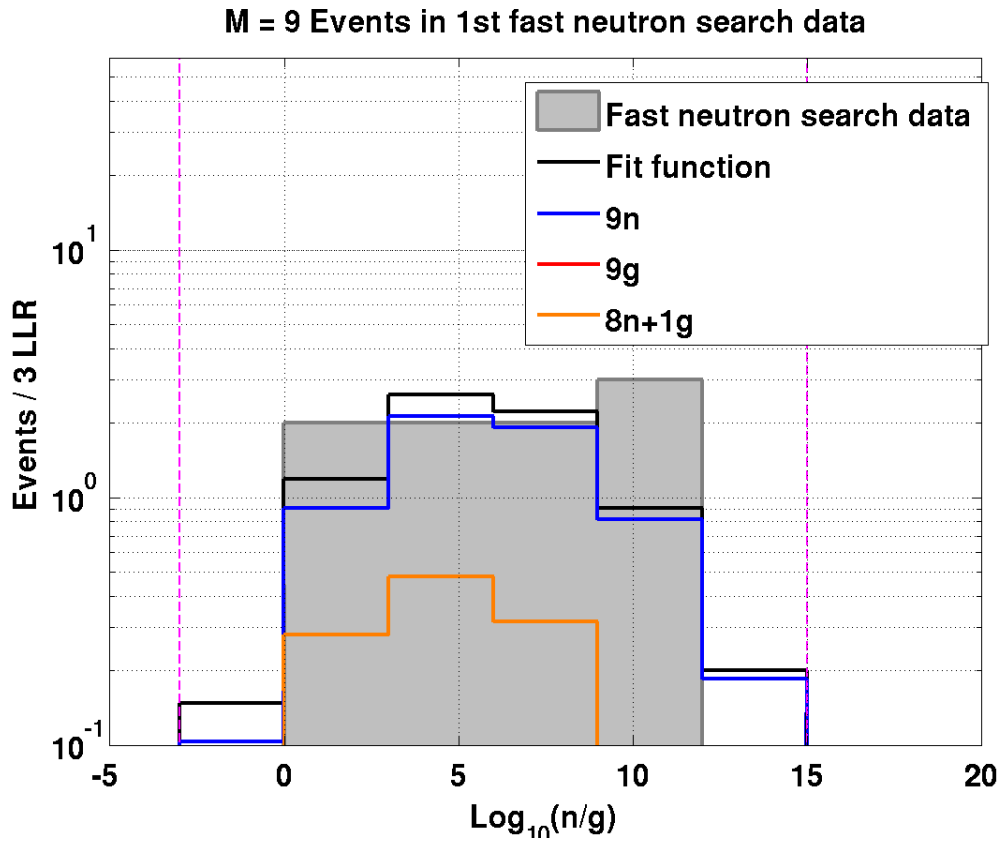


Figure 5.20: Least-squares fit of the LLR distribution for the multiplicity 9 events in the 1st fast neutron search data with a model composed of signal components $9n$ (blue), multiplicity-shifted signal component $8n+1g$ (orange), and background gamma component $9g$ (red). The candidate events, shown in the gray histogram, are binned per 3 LLR difference. The fit is performed from -3 to 15, labeled as in between the two magenta lines. The first empty bin is necessary to be included to constrain $9g$ component. The resulted fit function, shown in the black histogram, is the sum of the three components, with amplitudes of $9n$ and $9g$ as the two free parameters, while the amplitude of the $8n+1g$ component dependent on that of $9n$ according to Eq. (5.12). The goodness-of-fit is tested to be $\chi^2/ndf = 2.06/4$, with $p = 0.72$.

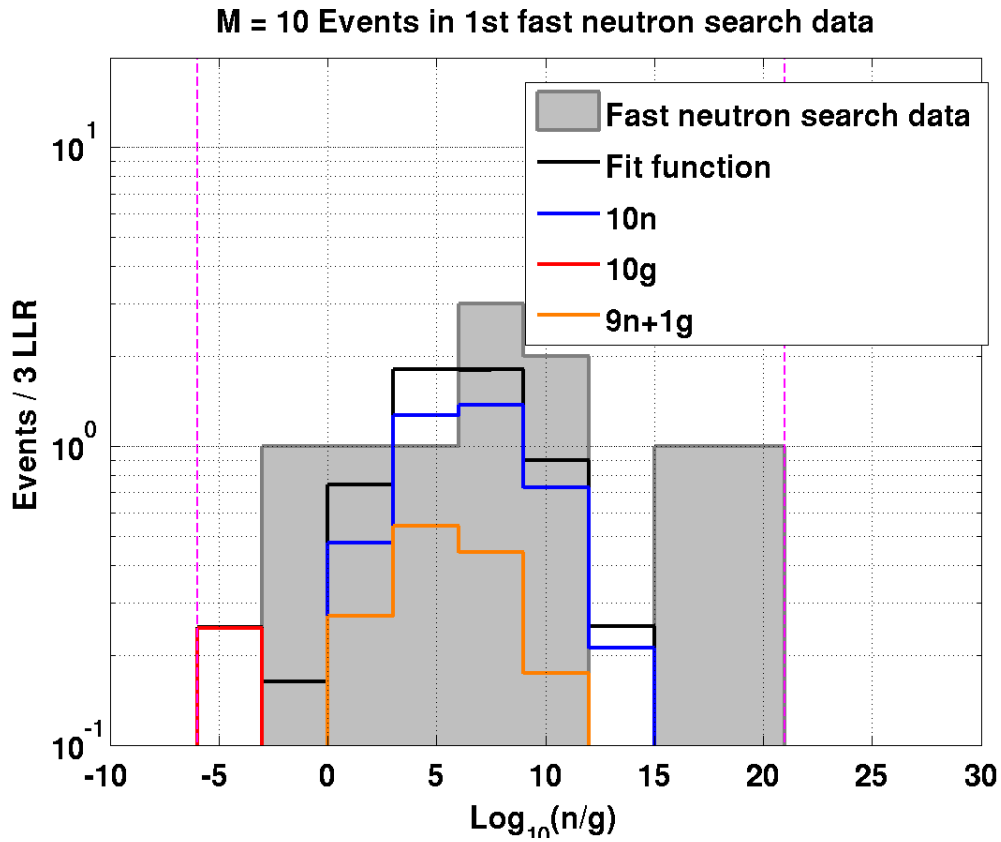


Figure 5.21: Least-squares fit of the LLR distribution for the multiplicity 10 events in the 1st fast neutron search data with a model composed of signal components 10n (blue), multiplicity-shifted signal component 9n+1g (orange), and background gamma component 10g (red). The candidate events, shown in the gray histogram, are binned per 3 LLR difference. The fit is performed from -6 to 20, labeled as in between the two magenta lines. The first empty bin is necessary to be included to constrain 9g component. The resulted fit function, shown in the black histogram, is the sum of the three components, with amplitudes of 10n and 10g as the two free parameters, while the amplitude of the 9n+1g component dependent on that of 10n according to Eq. (5.12). The goodness-of-fit is tested to be $\chi^2/ndf = 4.52/7$, with $p = 0.72$.

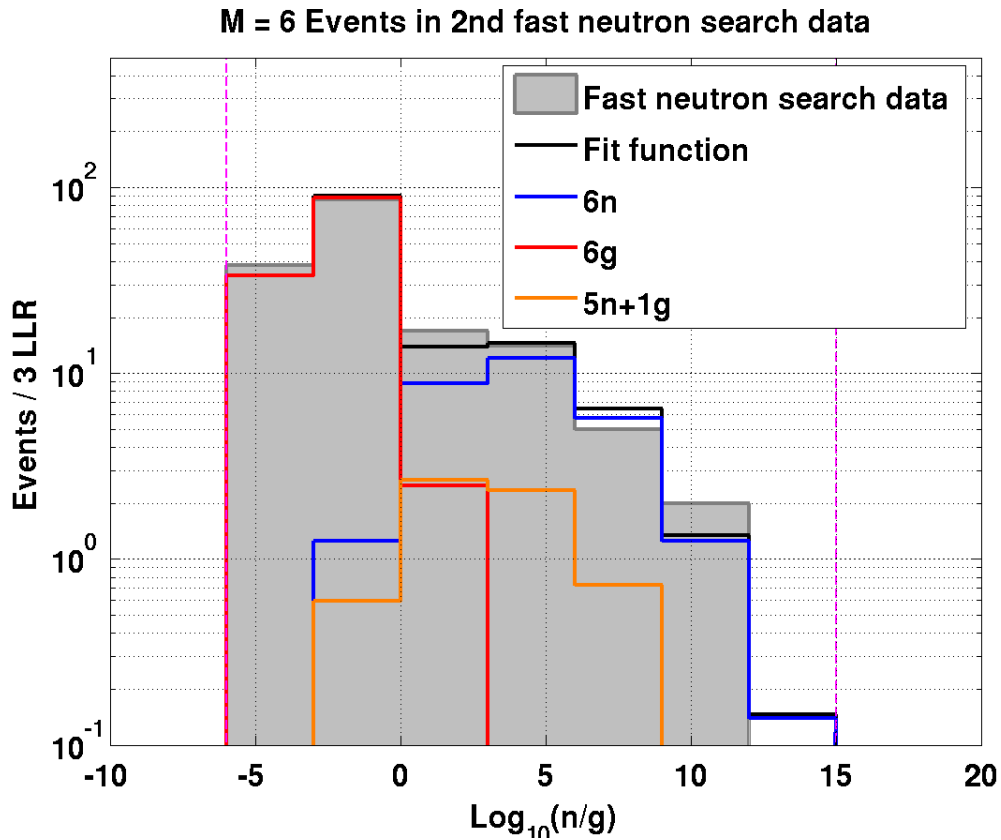


Figure 5.22: Least-squares fit of the LLR distribution for the multiplicity 6 events in the 2nd fast neutron search data with a model composed of signal components $6n$ (blue), multiplicity-shifted signal component $5n+1g$ (orange), and background gamma component $6g$ (red). The candidate events, shown in the gray histogram, are binned per 3 LLR difference. The fit is performed from -6 to 15, labeled as in between the first two magenta lines. The resulted fit function, shown in the black histogram, is the sum of the three components, with amplitudes of $6n$ and $6g$ as the two free parameters, while the amplitude of the $5n+1g$ component dependent on that of $6n$ according to Eq. (5.12). The goodness-of-fit is tested to be $\chi^2/ndf = 1.98/5$, with $p = 0.85$.

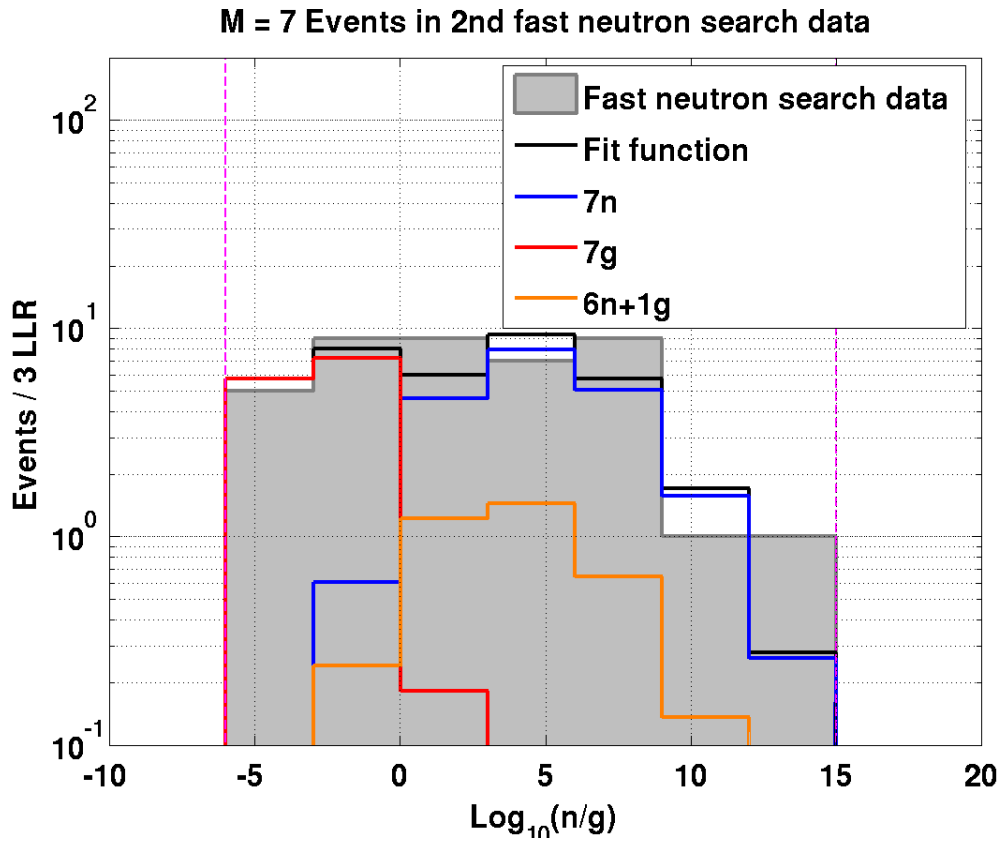


Figure 5.23: Least-squares fit of the LLR distribution for the multiplicity 7 events in the 2nd fast neutron search data with a model composed of signal components $7n$ (blue), multiplicity-shifted signal component $6n+1g$ (orange), and background gamma component $7g$ (red). The candidate events, shown in the gray histogram, are binned per 3 LLR difference. The fit is performed from -6 to 15, labeled as in between the first two magenta lines. The resulted fit function, shown in the black histogram, is the sum of the three components, with amplitudes of $7n$ and $7g$ as the two free parameters, while the amplitude of the $6n+1g$ component dependent on that of $7n$ according to Eq. (5.12). The goodness-of-fit is tested to be $\chi^2/ndf = 4.21/5$, with $p = 0.52$.

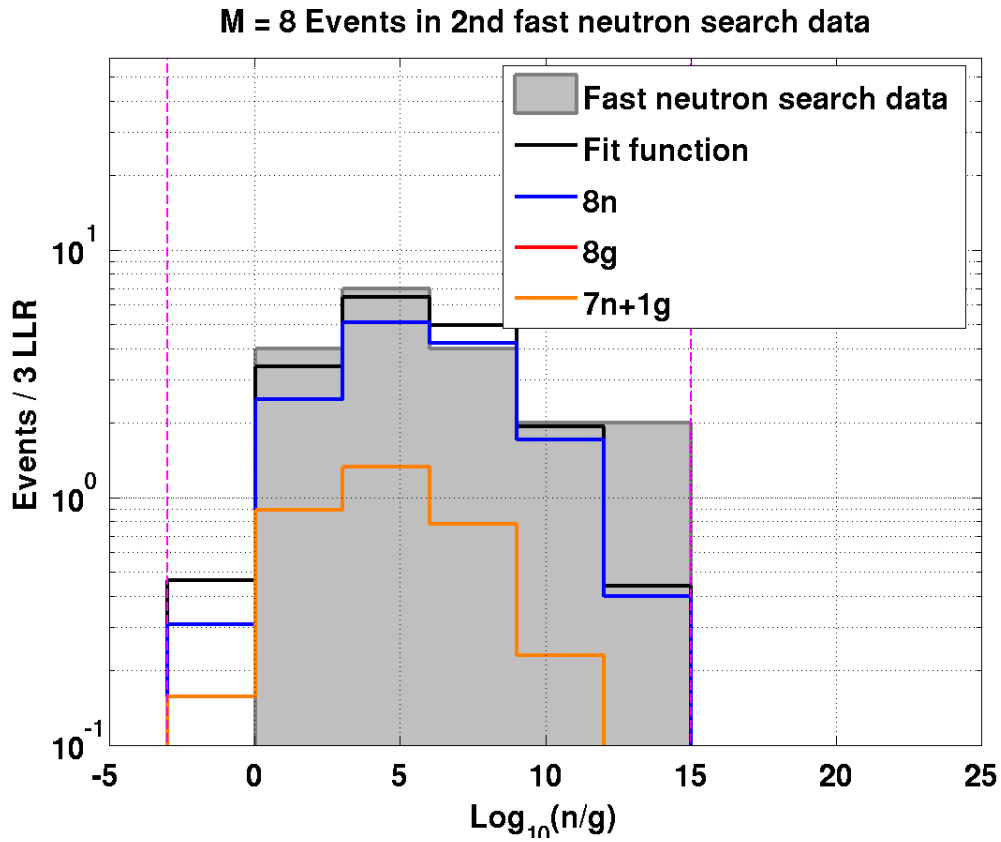


Figure 5.24: Least-squares fit of the LLR distribution for the multiplicity 8 events in the 2nd fast neutron search data with a model composed of signal components $8n$ (blue), multiplicity-shifted signal component $7n+1g$ (orange), and background gamma component $8g$ (red). The candidate events, shown in the gray histogram, are binned per 3 LLR difference. The fit is performed from -3 to 15, labeled as in between the two magenta lines. The first empty bin is necessary to be included to constrain $8g$ component. The resulted fit function, shown in the black histogram, is the sum of the three components, with amplitudes of $8n$ and $8g$ as the two free parameters, while the amplitude of the $7n+1g$ component dependent on that of $8n$ according to Eq. (5.12). The goodness-of-fit is tested to be $\chi^2/ndf = 1.82/4$, with $p = 0.77$.

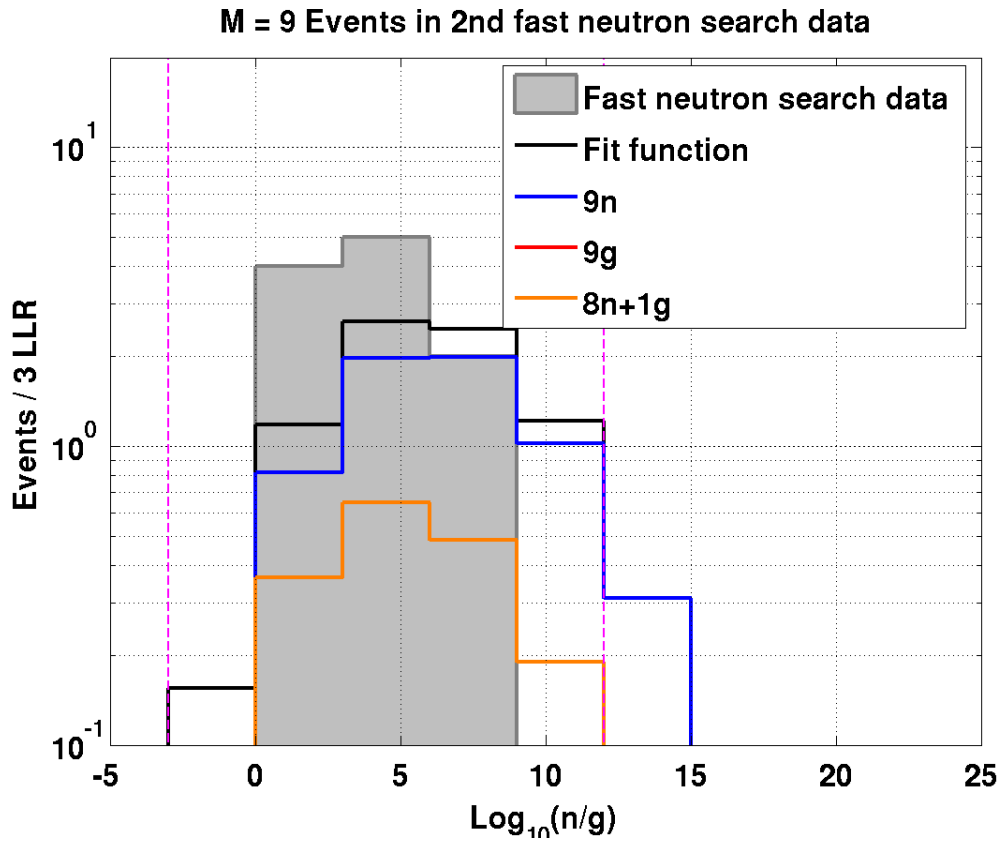


Figure 5.25: Least-squares fit of the LLR distribution for the multiplicity 9 events in the 2nd fast neutron search data with a model composed of signal components $9n$ (blue), multiplicity-shifted signal component $8n+1g$ (orange), and background gamma component $9g$ (red). The candidate events, shown in the gray histogram, are binned per 3 LLR difference. The fit is performed from -3 to 15, labeled as in between the two magenta lines. The first empty bin is necessary to be included to constrain $9g$ component. The resulted fit function, shown in the black histogram, is the sum of the three components, with amplitudes of $9n$ and $9g$ as the two free parameters, while the amplitude of the $8n+1g$ component dependent on that of $9n$ according to Eq. (5.12). The goodness-of-fit is tested to be $\chi^2/ndf = 4.73/3$, with $p = 0.19$.

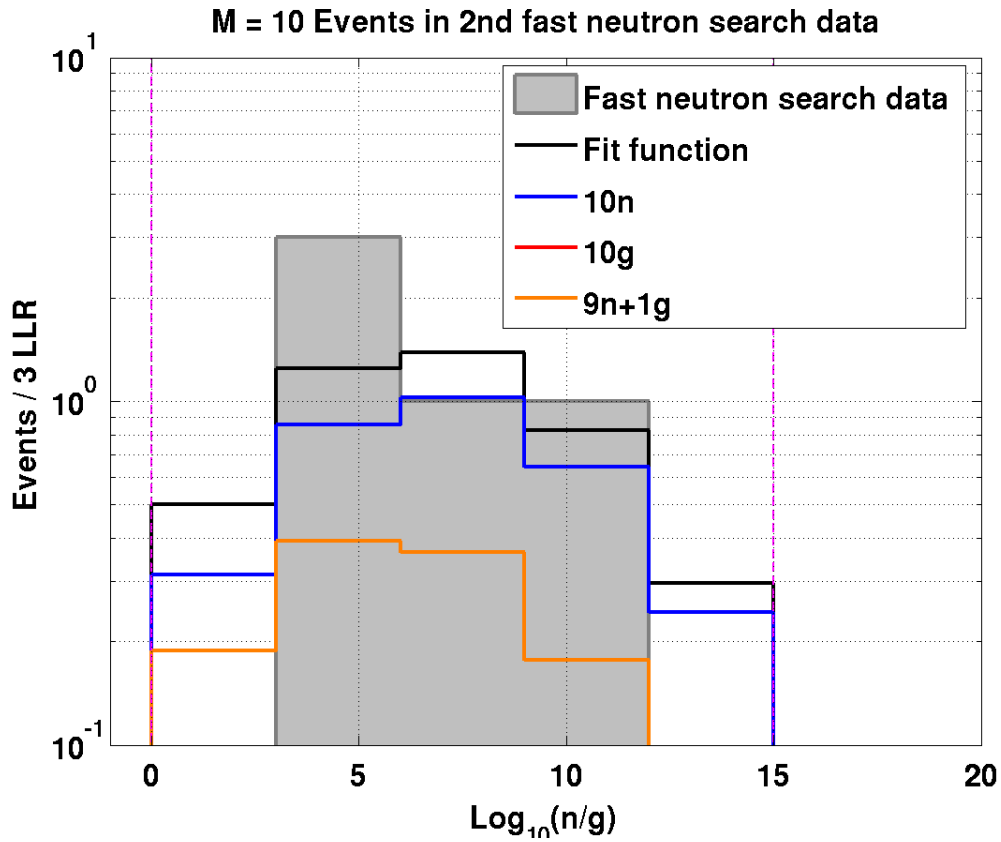


Figure 5.26: Least-squares fit of the LLR distribution for the multiplicity 10 events in the 2nd fast neutron search data with a model composed of signal components 10n (blue), multiplicity-shifted signal component 9n+1g (orange), and background gamma component 10g (red). The candidate events, shown in the gray histogram, are binned per 3 LLR difference. The fit is performed from 0 to 15, labeled as in between the two magenta lines. The first empty bin is necessary to be included to constrain 10g component. The resulted fit function, shown in the black histogram, is the sum of the three components, with amplitudes of 10n and 10g as the two free parameters, while the amplitude of the 9n+1g component dependent on that of 10n according to Eq. (5.12). The goodness-of-fit is tested to be $\chi^2/ndf = 1.54/3$, with $p = 0.67$.

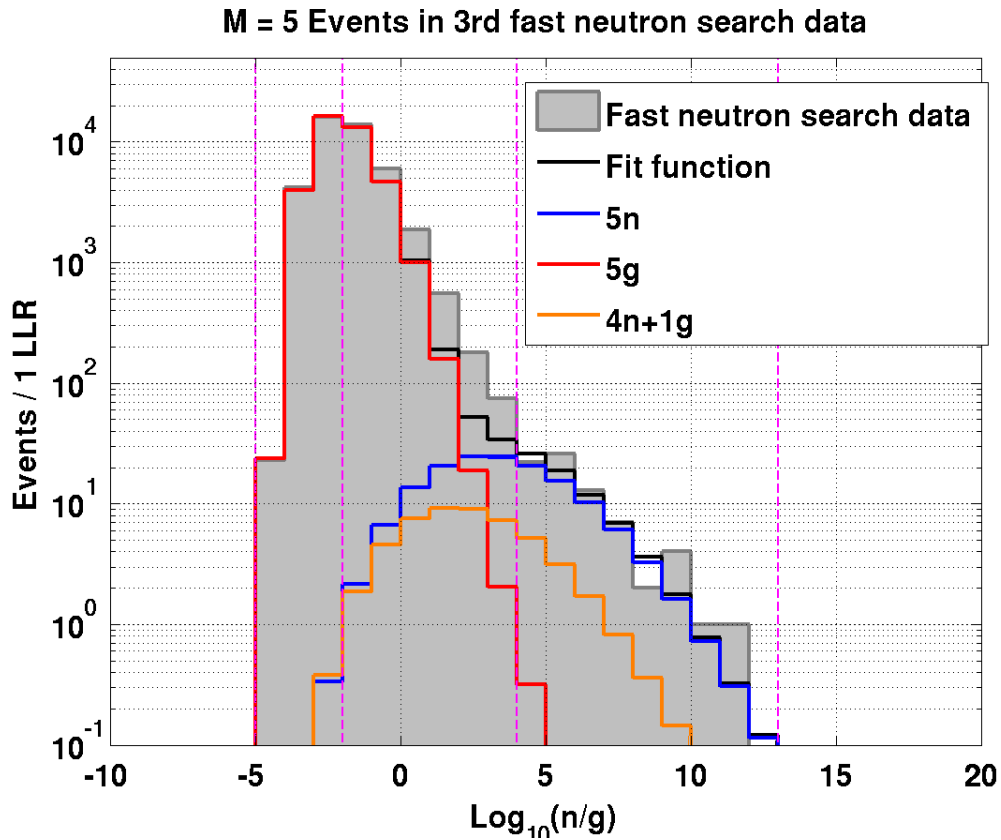


Figure 5.27: Least-squares fit of the LLR distribution for the multiplicity 5 events in the 3rd fast neutron search data with a model composed of signal components $5n$ (blue), multiplicity-shifted signal component $4n+1g$ (orange), and background gamma component $5g$ (red). The candidate events, shown in the gray histogram, are binned per 1 LLR difference. The fit is performed in a partial range, from -5 to -2, and from 4 to 13, labeled as in between the first two magents lines and in between the third and fourth magenta lines, respectively. Including one more fitting bin at -2 to -3 would essentially make no change for estimating the signal amplitudes, but only increase χ^2 dramatically. The resulted fit function, shown in the black histogram, is the sum of the three components, with amplitudes of $5n$ and $5g$ as the two free parameters, while the amplitude of the $4n+1g$ component dependent on that of $5n$ according to Eq. (5.12). The goodness-of-fit is tested to be $\chi^2/ndf = 14.09/10$, with $p = 0.17$.

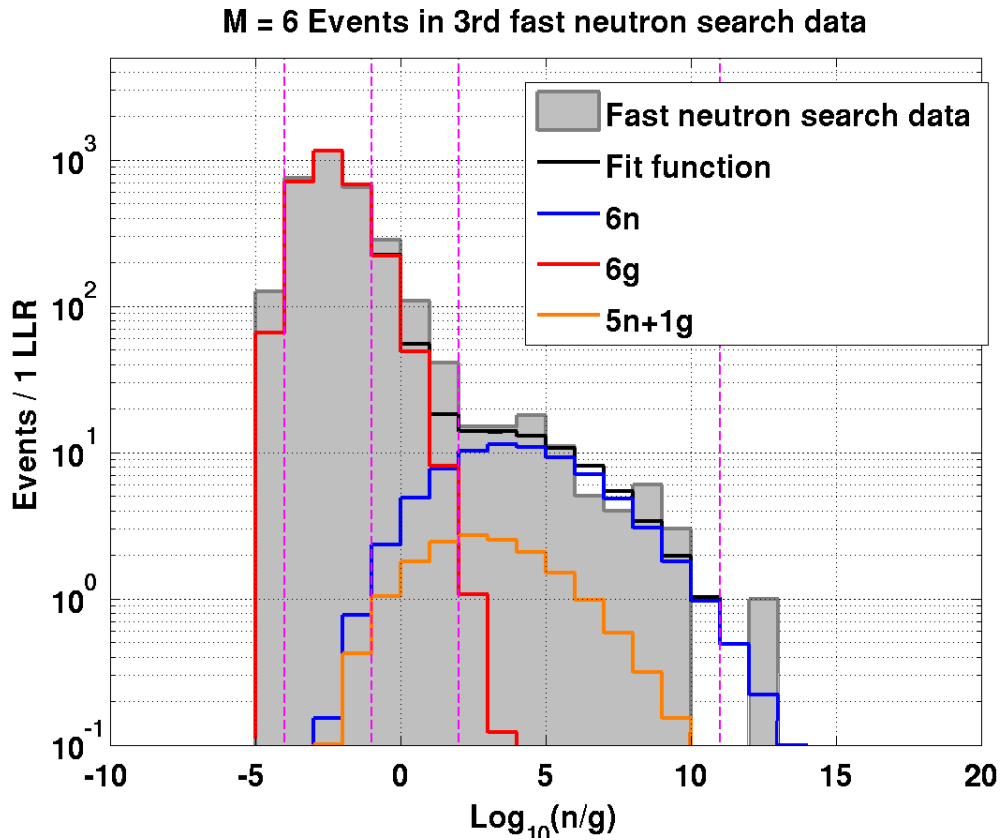


Figure 5.28: Least-squares fit of the LLR distribution for the multiplicity 6 events in the 3rd fast neutron search data with a model composed of signal components $6n$ (blue), multiplicity-shifted signal component $5n+1g$ (orange), and background gamma component $6g$ (red). The candidate events, shown in the gray histogram, are binned per 1 LLR difference. The fit is performed in a partial range, from -4 to -1, and from 2 to 11, labeled as in between the first two magents lines and in between the third and fourth magenta lines, respectively. Including one more fitting bin at -5 to -4 would essentially make no change for estimating the signal amplitudes, but only increase χ^2 dramatically. The resulted fit function, shown in the black histogram, is the sum of the three components, with amplitudes of $6n$ and $6g$ as the two free parameters, while the amplitude of the $5n+1g$ component dependent on that of $6n$ according to Eq. (5.12). The goodness-of-fit is tested to be $\chi^2/ndf = 10.39/10$, with $p = 0.41$.

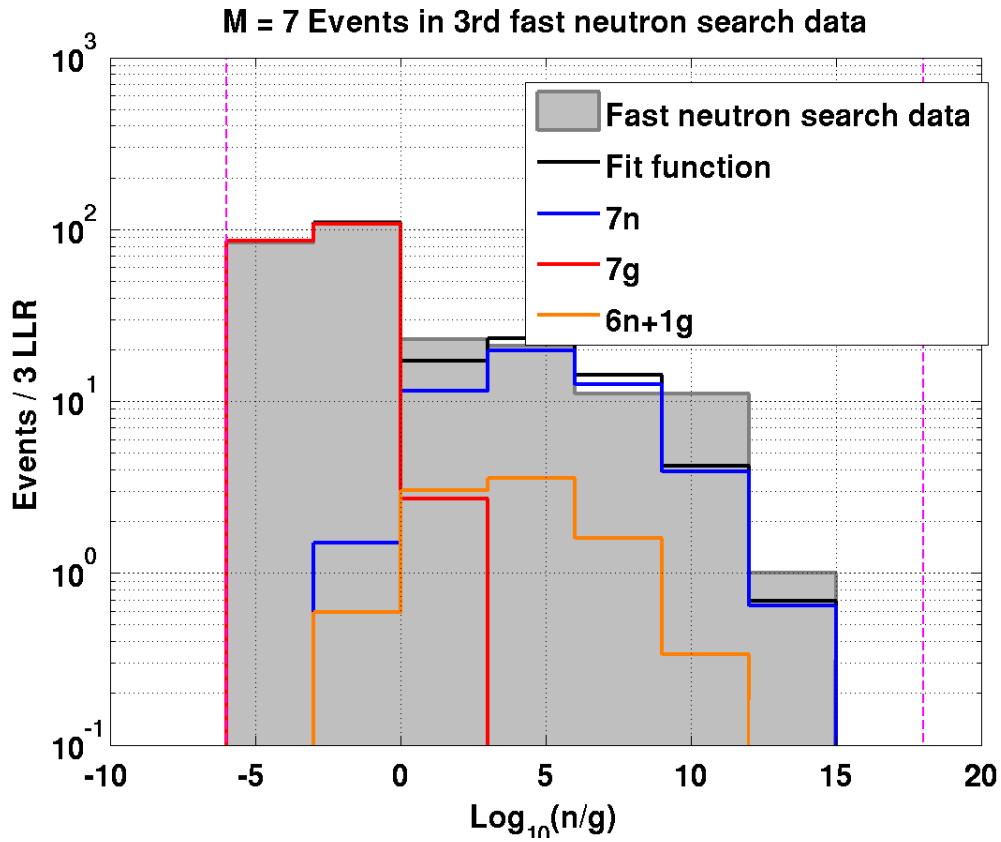


Figure 5.29: Least-squares fit of the LLR distribution for the multiplicity 7 events in the 3rd fast neutron search data with a model composed of signal components $7n$ (blue), multiplicity-shifted signal component $6n+1g$ (orange), and background gamma component $7g$ (red). The candidate events, shown in the gray histogram, are binned per 3 LLR difference. The fit is performed from -6 to 18, labeled as in between the first two magenta lines. The resulted fit function, shown in the black histogram, is the sum of the three components, with amplitudes of $7n$ and $7g$ as the two free parameters, while the amplitude of the $6n+1g$ component dependent on that of $7n$ according to Eq. (5.12). The goodness-of-fit is tested to be $\chi^2/ndf = 6.96/6$, with $p = 0.32$.

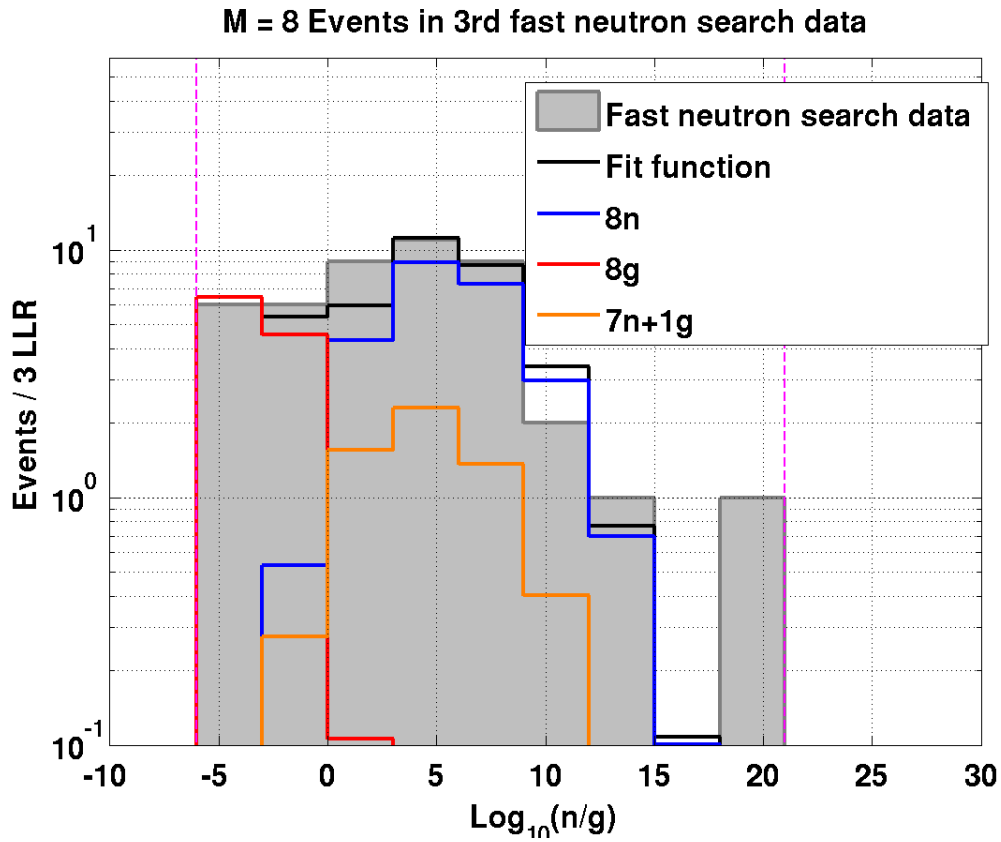


Figure 5.30: Least-squares fit of the LLR distribution for the multiplicity 8 events in the 3rd fast neutron search data with a model composed of signal components $8n$ (blue), multiplicity-shifted signal component $7n+1g$ (orange), and background gamma component $8g$ (red). The candidate events, shown in the gray histogram, are binned per 3 LLR difference. The fit is performed from -6 to 21, labeled as in between the first two magenta lines. The resulted fit function, shown in the black histogram, is the sum of the three components, with amplitudes of $8n$ and $8g$ as the two free parameters, while the amplitude of the $7n+1g$ component dependent on that of $8n$ according to Eq. (5.12). The goodness-of-fit is tested to be $\chi^2/ndf = 3.12/7$, with $p = 0.87$.

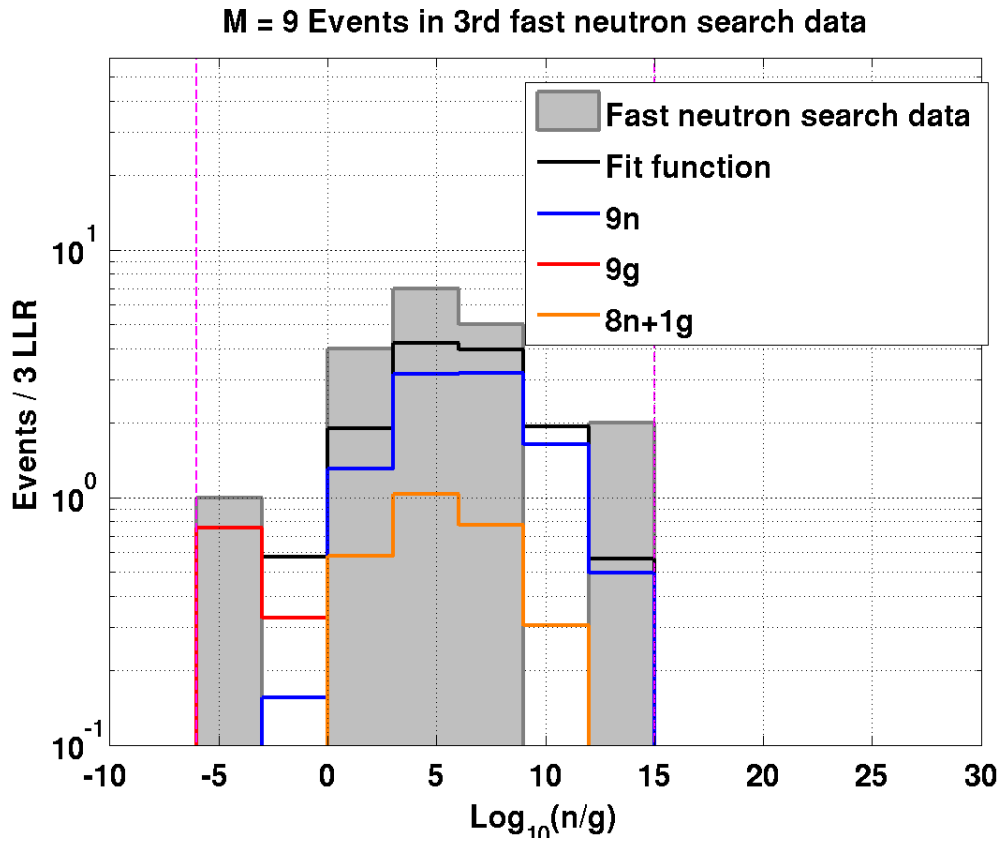


Figure 5.31: Least-squares fit of the LLR distribution for the multiplicity 9 events in the 3rd fast neutron search data with a model composed of signal components $9n$ (blue), multiplicity-shifted signal component $8n+1g$ (orange), and background gamma component $9g$ (red). The candidate events, shown in the gray histogram, are binned per 3 LLR difference. The fit is performed from -6 to 15, labeled as in between the first two magenta lines. The resulted fit function, shown in the black histogram, is the sum of the three components, with amplitudes of $9n$ and $9g$ as the two free parameters, while the amplitude of the $8n+1g$ component dependent on that of $9n$ according to Eq. (5.12). The goodness-of-fit is tested to be $\chi^2/ndf = 7.64/5$, with $p = 0.18$.

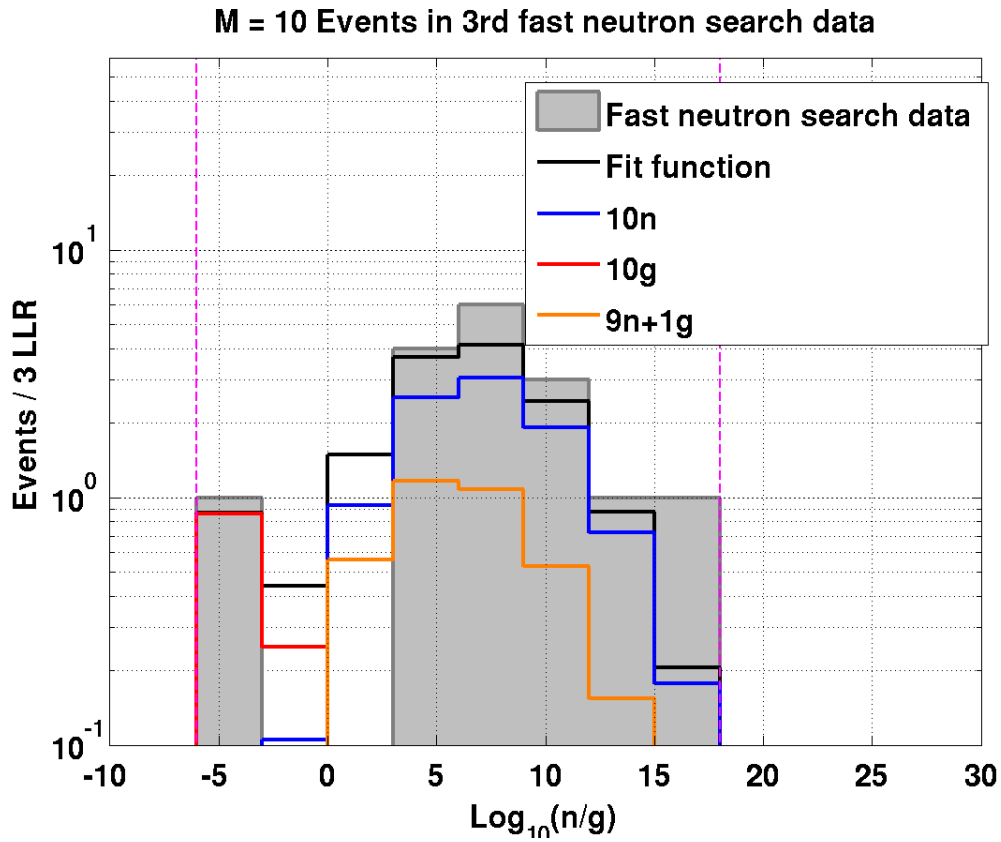


Figure 5.32: Least-squares fit of the LLR distribution for the multiplicity 10 events in the 3rd fast neutron search data with a model composed of signal components $10n$ (blue), multiplicity-shifted signal component $8n+1g$ (orange), and background gamma component $10g$ (red). The candidate events, shown in the gray histogram, are binned per 3 LLR difference. The fit is performed from -6 to 18, labeled as in between the first two magenta lines. The resulted fit function, shown in the black histogram, is the sum of the three components, with amplitudes of $10n$ and $10g$ as the two free parameters, while the amplitude of the $8n+1g$ component dependent on that of $10n$ according to Eq. (5.12). The goodness-of-fit is tested to be $\chi^2/ndf = 3.79/6$, with $p = 0.71$.

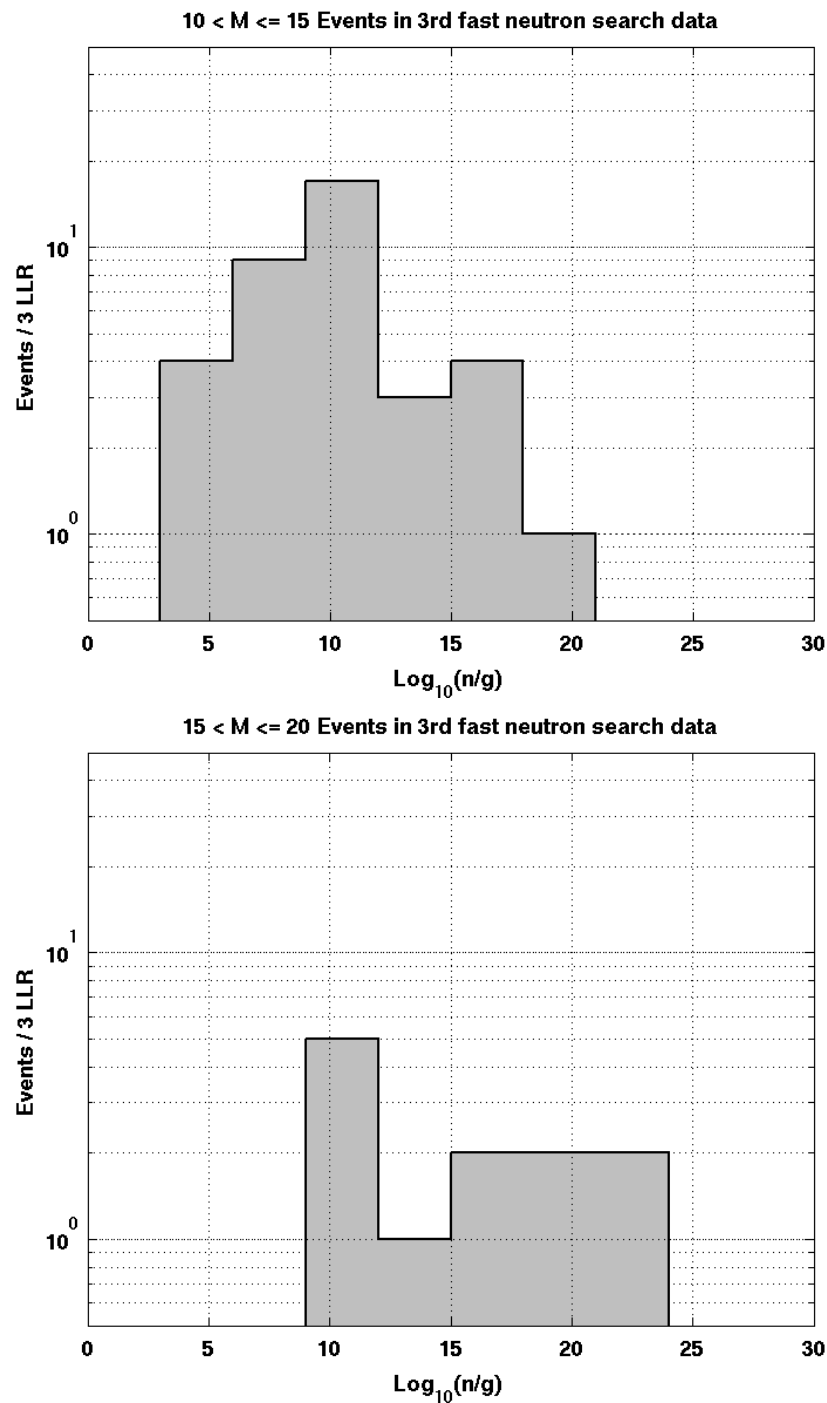


Figure 5.33: The LLR distribution of two data groups with multiplicity greater than 10 in 3rd fast neutron search data. On the top is the data group with multiplicity from 11 to 15, and on the bottom is the data group with multiplicity from 16 to 20. In both multiplicity groups, the LLR values are so high that it is of great confidence to think there are no gamma background events but only high-energy neutrons. As multiplicity goes higher, the LLR of the events in the group of 16 to 20 distributes at larger values. With the grouping of events per 5 multiplicity, the difference between Mn and $(M - 1)n + 1g$ becomes no importance.

5.4 Benchmark of High-energy Neutron Multiplicity Spectrum

Based on the model discussed in section 5.1, the $(M - 1)n+1g$ component in the model should be treated as signal-like events, but their true multiplicity is less by one than the multiplicity of the same data group. Thus when constructing the multiplicity spectrum, they should be added to the event group of one multiplicity less. For example, by fitting the group of multiplicity 6, we extract both the number of $6n$ events and the number of $5n+1g$ events, but the number of $5n+1g$ events should be added to number of $5n$ events that are extracted by fitting the multiplicity 5 group. This unfolding procedure is a necessary step to eliminate the the effect of background gammas on the multiplicity spectrum. Note this effect of background gammas is not included in the comprehensive muon simulation, and should not be confused with the effect of muon or secondary charged particle shifting the multiplicity of the fast neutron events, revealed in the simulation. After applying the unfolding procedure, the results should bring a fair comparison between the multiplicity spectra of data and MC.

The least squares fits of the LLR distribution with the model in last section follow the standard method of least squares (LS) [72][71] to estimate parameters, which in our case are the amplitudes of signals and backgrounds, by minimizing the sum of squares

$$\chi^2(\boldsymbol{\theta}) = \sum_{i=1}^N \frac{(y_i - \mu(x_i; \boldsymbol{\theta}))^2}{\sigma_i^2}, \quad (5.13)$$

where $\boldsymbol{\theta}$ is the vector of the parameters in model, i.e. $(\mathcal{A}_{Mn}, \mathcal{A}_{Mg})$ for multiplicity M events, x_i represents the LLR value, y_i represents the event counts in the LLR bin of x_i , and μ is the expected counts in the bin predicted by the model. Equation (5.13) can also be written in the form of a vector and a matrix, as

$$\chi^2(\boldsymbol{\theta}) = (\mathbf{y} - \boldsymbol{\mu}(\boldsymbol{\theta}))^T V^{-1} (\mathbf{y} - \boldsymbol{\mu}(\boldsymbol{\theta})), \quad (5.14)$$

where V is the covariance matrix of \mathbf{y} . For independent variables, V is a diagonal matrix, and the terms are just σ_i^2 . Our model is that the signal components plus the background component form the overall LLR distribution. Thus $\mu(x_i; \boldsymbol{\theta})$ is a linear function of the parameters, i.e.,

$$\mu(x_i; \boldsymbol{\theta}) = \sum_{j=1}^m \theta_j h_j(x_i). \quad (5.15)$$

Or,

$$\boldsymbol{\mu}(\boldsymbol{\theta}) = H\boldsymbol{\theta}, \quad (5.16)$$

in matrix form. $h_j(x_i)$ represents the component function of the LLR distribution, obtained by sampling fake events from their PDFs. Then the goal is to minimize

$$\chi^2(\boldsymbol{\theta}) = (\mathbf{y} - H\boldsymbol{\theta})^T V^{-1} (\mathbf{y} - H\boldsymbol{\theta}). \quad (5.17)$$

The solution can be reached when

$$\frac{\partial}{\partial \theta_j} (\chi^2) = 0, \quad (5.18)$$

which leads to

$$\hat{\boldsymbol{\theta}} = (H^T V^{-1} H)^{-1} H^T V^{-1} \mathbf{y}. \quad (5.19)$$

The covariance matrix for the parameters $U_{ij} = \text{Cov}[\hat{\theta}_i, \hat{\theta}_j]$ is given by

$$U = (H^T V^{-1} H)^{-1}. \quad (5.20)$$

Finally, the uncertainties of the estimated parameters \mathcal{A}_{Mn} and \mathcal{A}_{Mg} are given by

$$\begin{aligned}\sigma_{\mathcal{A}_{Mn}} &= \sqrt{U_{11}}, \\ \sigma_{\mathcal{A}_{Mg}} &= \sqrt{U_{22}}.\end{aligned}\tag{5.21}$$

Then, since the amplitude of $(M-1)n+1g$ component is not independent, its uncertainty $\sigma_{\mathcal{A}_{(M-1)n+1g}}$ is calculated with error propagation rules based on the dependence given by Eq. (5.12).

With the uncertainties of signal components calculated from the covariance matrices, the uncertainty of the event rate at each multiplicity M is given by summing in quadrature from the results of the fits to multiplicities M and $M+1$,

$$\sigma_{\mathcal{A}_M} = \sqrt{\sigma_{\mathcal{A}_{Mn}}^2 + \sigma_{\mathcal{A}_{Mn+1g}}^2}.\tag{5.22}$$

Gathering all the unfolded amplitudes of fast neutron signals and their uncertainties allows the measured multiplicity spectra of all three fast neutron search data sets to be constructed, shown in Figures 5.34, 5.35, and 5.36, in red circles with error bars. The horizontal error bars for multiplicity greater than 10 represent the bin widths, 5. The uncertainties in these bins are simply the square root of the bin counts divided by 5. All the amplitudes in the multiplicity spectrum represent the best estimates of the numbers of high-energy neutrons detected by the NMM during the live times of each fast neutron search run, which is $T_1 = 158.2$ days in the 1st fast neutron search, $T_2 = 169.2$ in the 2nd, and $T_3 = 302.8$ in the 3rd.

The measured multiplicity spectrum is compared to the Geant4 MC result, which corresponds to 138.8 live days. The MC multiplicity spectrum processed with low PMT gain parameters is used to compare with the spectrum of 1st fast neutron search, with the amplitudes and uncertainties normalized to the live time of 158.2 days; the spectrum processed with high PMT gain parameters is used to compare with the spectra of the 2nd and 3rd fast neutron search data, normalized to 169.2 days and 302.8 days, respectively. The multiplicity spectra from the Geant4 MC are shown in black

circles with error bars in the three figures.

In comparing the 1st fast neutron data and low-gain MC, shown in Figure 5.34, the measured and simulated multiplicity spectra agree well at multiplicity 7 to 9, while the measured rate shows a modest deficit at multiplicity 5 and 6 and an excess at multiplicity 10 to ~ 25 . In comparing the 2nd fast neutron search data and high-gain MC, shown in Figure 5.35, the measured and simulated multiplicity spectra agree at multiplicity 6 to 10, though the MC rates are slightly higher at multiplicity 6 and 7, similar to the 1st fast neutron search data. There is again an excess in the measured spectrum at multiplicity 10 to ~ 20 . In comparing the 3rd fast neutron data and high-gain MC, shown in Figure 5.36, the measured and simulated multiplicity spectra agree well at multiplicity 6 to 9, while the measured rate is higher than the MC at multiplicity 5 and multiplicity 10 to ~ 20 .

Finally, the spectra from the three data sets can be combined together to make a more precise measurement of the multiplicity spectrum. For most multiplicities, the amplitudes of the three runs can just be added together, and the uncertainties combine as the square root of the quadrature sum. A special care should be taken for multiplicity 5, since there is no multiplicity 5 in the 2nd fast neutron search. The amplitudes of the 1st and the 3rd runs should be summed first, then scaled by a factor of $(T_1 + T_2 + T_3)/(T_1 + T_3)$ so that the combined amplitude of multiplicity 5 represents the same total live time. Also, the combined uncertainty is scaled in the same way.

To combine the low-gain and high-gain results in the MC, the amplitudes in each should be scaled to the total live time of the corresponding neutron search runs. The scaling factors for MC results processed with the low and high PMT gains are considered as

$$s_L = \frac{T_1}{T_{MC}} = \frac{158.2}{138.8}, \tag{5.23}$$

$$s_H = \frac{T_2 + T_3}{T_{MC}} = \frac{169.2 + 302.8}{138.8}.$$

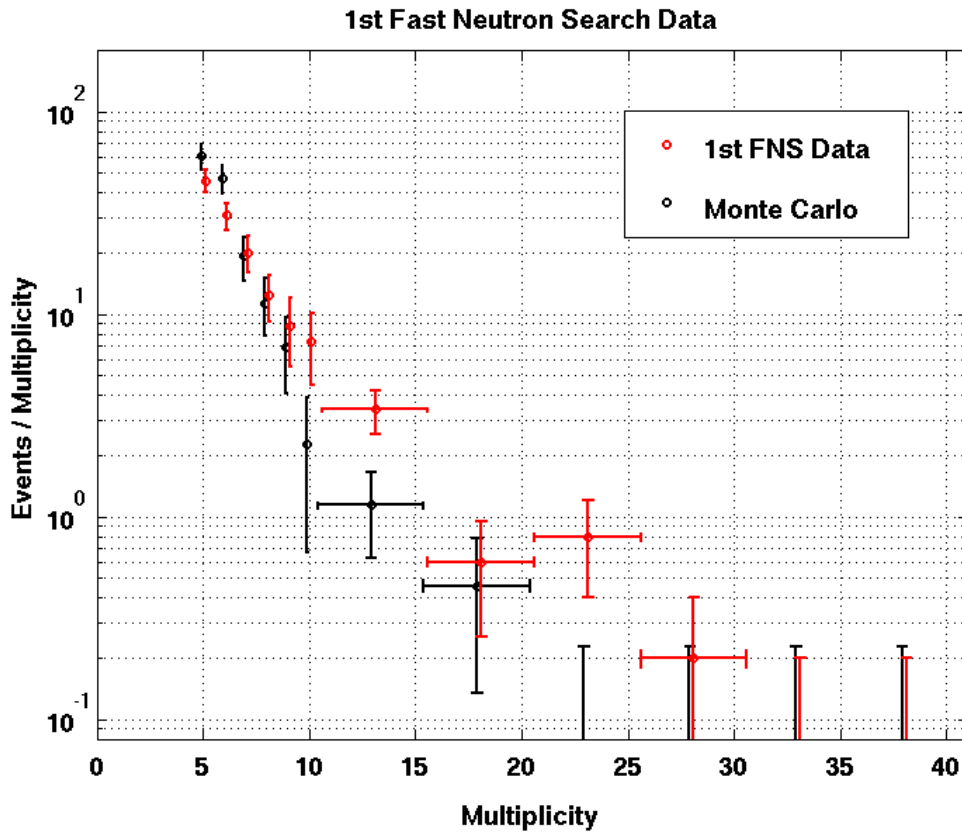


Figure 5.34: Multiplicity spectrum of the 1st fast neutron search data (red circles and error bars), compared with the multiplicity spectrum of the low-PMT-gain MC (black circles and error bars). Y-axis represents the estimated event counts per multiplicity in 158.2 live days, and the spectrum of the MC has been scaled to the same live time. Due to lower statistics, events are binned per 5 multiplicities for multiplicities greater than 10, with the amplitudes and error bars scaled by 1/5. The measured and simulated multiplicity spectra agree well at multiplicity 7 to 9, while with modest excesses at 5 and 6 by the MC and excess on measured spectrum at 10 to ~ 25 .

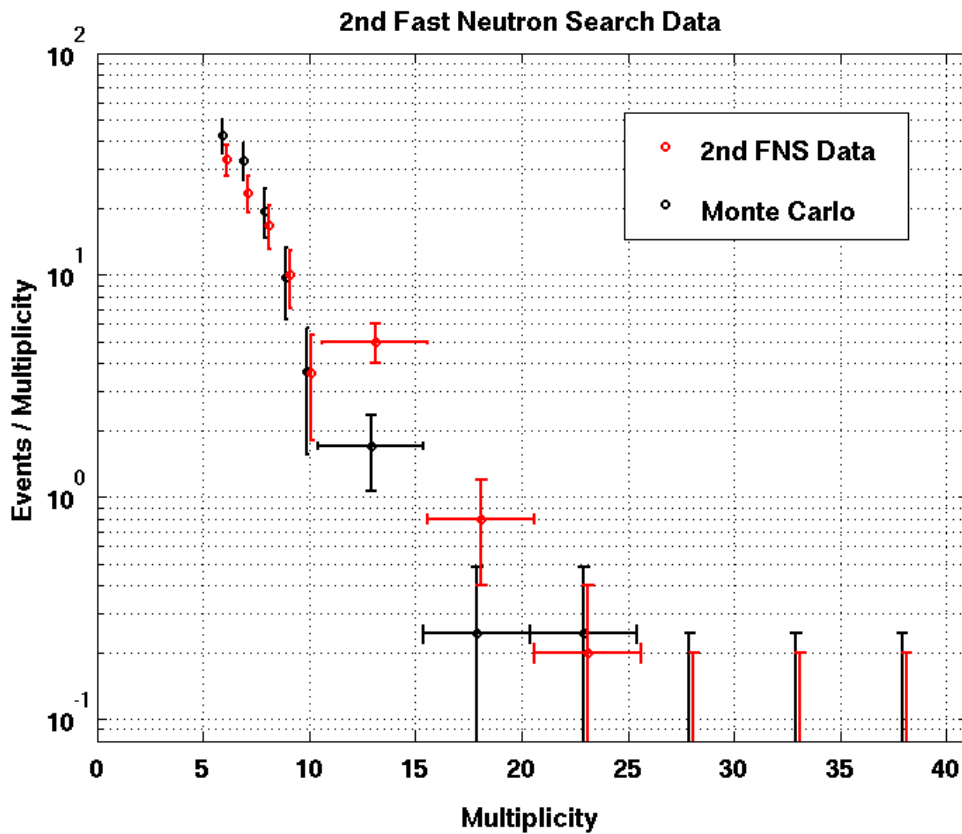


Figure 5.35: Multiplicity spectrum of the 2nd fast neutron search data (red circles and error bars), compared with the multiplicity spectrum of the high-PMT-gain MC (black circles and error bars). Y-axis represents the estimated event counts per multiplicity in 169.2 live days, and the spectrum of the MC has been scaled to the same live time. The spectrum is started with multiplicity 6, since the 2nd fast neutron search were run with multiplicity 6 in $70\ \mu\text{s}$ trigger, instead of trigger at multiplicity 5. Due to lower statistics, events are binned per 5 multiplicities for multiplicities greater than 10, with the amplitudes and error bars scaled by $1/5$. The measured and simulated multiplicity spectra agree generally well at multiplicity 6 to 10, though there is modest excesses at 6 and 7 by the MC similar to the 1st fast neutron search data. There is excess on measured spectrum at 10 to ~ 20 .

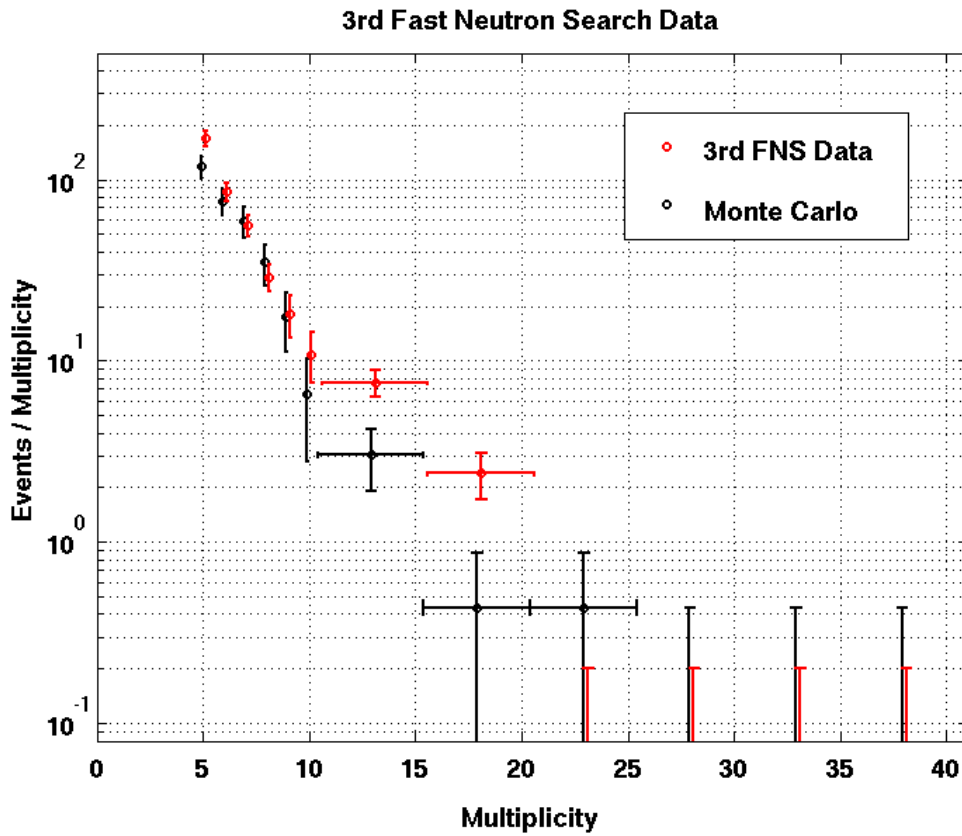


Figure 5.36: Multiplicity spectrum of the 3rd fast neutron search data (red circles and error bars), compared with the multiplicity spectrum of the high-PMT-gain MC (black circles and error bars). Y-axis represents the estimated event counts per multiplicity in 302.8 live days, and the spectrum of the MC has been scaled to stand for the same live time. Due to lower statistics, events are binned per 5 multiplicities for multiplicities greater than 10, with the amplitudes and error bars scaled by 1/5. The measured and simulated multiplicity spectra agree well at multiplicity 6 to 9, while excess on measured spectrum shows up at multiplicity 5 and multiplicity 10 to ~ 20 .

Then the amplitudes of low-gain spectrum $A_L(M)$ and high-gain spectrum $A_H(M)$ combine as

$$A_C = s_L \cdot A_L + s_H \cdot A_H . \quad (5.24)$$

Note when combining the uncertainties, the two spectra $A_L(M)$ and $A_H(M)$ are not independent. They are both from the same simulation with the same live time, 138.2 days, although processed with different PMT gain parameters and with independent random numbers for accepting photoelectrons. The two spectra do convey some different information due to the different PMT gains. For example, different fractions of real high-energy neutrons out of all accepted events and different gathering powers result from the different PMT gains, and they could finally reflect on the difference of the two multiplicity spectra. That is why the two spectra should be summed up with the proper weights, instead of just using one of them. However, most of their uncertainties are from the same MC. Therefore, the correct way of combining their uncertainty, in a conservative manner, is to sum directly with weights,

$$\sigma_C = s_L \cdot \sigma_L + s_H \cdot \sigma_H . \quad (5.25)$$

Figure 5.37 shows the multiplicity spectrum of high-energy neutrons with all the three fast neutron search data sets combined compared against the spectrum simulated with the Geant4 based comprehensive muon simulation. The spectrum represents the best estimate of the event numbers of high-energy neutrons detected by the NMM as a function of multiplicity, in a total live time of 630.2 days. The combined spectrum cancels the discrepancies at multiplicities 5 to 7 appearing in each data set in different ways, making the measurement and MC agree better at these multiplicities. The measured event number at multiplicity 5 still slightly exceeds the prediction by the MC, but within their error bars. The measured and simulated multiplicity spectra continue to agree up to multiplicity 9. Then starting at multiplicity 10, the excess in the measured spectrum over MC approximately with a factor of 3 is confirmed in the 630.2 days of live time combined results. The

excess exists with clear evidence up to multiplicity ~ 20 . For higher multiplicities, both measured and MC spectra are limited by statistics, leaving the conclusion in this region ambiguous. However, the higher expected event number of the measured spectrum than the MC spectrum in the 21-25 bin, and the non-zero counts in 26-30 bin of the measurement, both hint of a possible continuation of the excess of measured spectrum over MC.

The Neutron Multiplicity Meter was proposed to measure the multiplicity as an approximation or indication of the original energy of the high-energy (50 MeV) neutron. However, according to the analysis of the comprehensive muon simulation in Chapter 4, the accepted events include both high-energy (50 MeV) neutrons and low-energy multiple neutrons. It is impossible to extract a pure multiplicity spectrum for just a high-energy neutrons. However, including the low-energy multiple neutrons is expected to happen in both the real experimental run and the comprehensive muon simulation. This makes a fair comparison between the the measured and simulated spectra.

As shown in Figure 4.23 and 4.24 in Chapter 4, the MC indicates that $\sim 2/3$ of events of multiplicity 10 or greater are detections of the neutrons with energies above 50 MeV. Therefore, the excess in the measured spectrum at multiplicities 10 and greater may potentially suggest that the energy spectrum of high-energy neutrons underground is harder than what is predicted by the Geant4 MC. At this point, we are unable to prove this supposition with the data of the NMM. In principle, it is possible that the underestimation of high-multiplicity events in the MC is from underestimating the rate of low-energy multiple neutrons, instead of underestimating the rate of high-energy neutrons. The former supposition could be linked to the neutron spallation cross section in cavern rock, while the latter could be related to the cross sections for muons to interact with cavern rock and generate high-energy neutrons. In other words, either the muon-induced neutrons cause more spallations in cavern rock and thus result in more low-energy neutrons, or the cosmic-ray muons themselves induce more high-energy neutrons, than the prediction of Geant4. It is also possible that the excess is caused by both. In either case, it is all about muon-induced neutrons.

For the underground dark matter direct detection experiments, if the excess of neutron back-

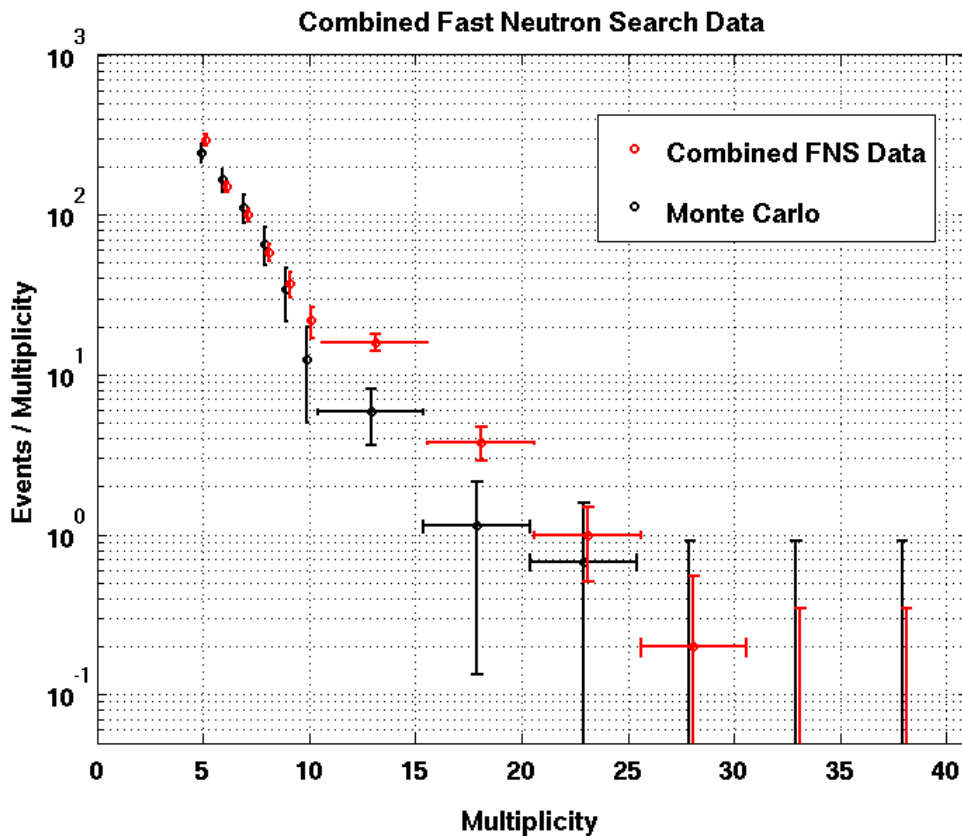


Figure 5.37: Multiplicity spectrum of the combined fast neutron search (FNS) data, compared with the MC multiplicity spectrum. The multiplicity spectrum in red circles and error bars is measured with all fast neutron search data of 630.2 days of live time. This result is obtained by combining all three spectra above measured with fast neutron search data sets, with appropriate weights based on their live times. The spectrum in black circles and error bars is resulted from the comprehensive muon simulation of 138.8 live days discussed in Chapter 4. Both spectra processed with the low-gain and high-gain parameters are combined with the weights based on the live times of low-gain and high-gain running in fast neutron search. The uncertainties of low-gain and high-gain MC spectra are not independent, thus uncertainties of overall MC spectrum are combined as direct summation of the two with weights. Y-axis represents the estimated event counts per multiplicity in 630.2 live days, and the spectrum of MC has been scaled to stand for the same live time. Due to lower statistics, events are binned per 5 multiplicities for multiplicities greater than 10, with the amplitudes and error bars scaled by 1/5. The measured and simulated multiplicity spectra agree well at multiplicity 5 to 9, with the previous discrepancies at multiplicity 5 and 6 cleared after all data sets combined. The combined results confirm the excess on measured spectrum over MC approximately with a factor of 3, starting at multiplicity 10 and existing up to ~ 20 , or potentially to even higher multiplicities.

grounds is from low-energy (most likely below 10 MeV) multiple neutrons, the problem can be easily solved by properly shielding with neutron moderating materials, such as water and high-density polyethylene; if the excess is caused by more high-energy (above 50 MeV) cosmogenic neutrons, then the neutron moderators are not able to stop them, also the inner gamma shielding with high-Z materials, such as Pb and Cu, could help make the detector in danger of the multiple secondary neutrons induced by the high-energy neutrons. In the latter case, the importance of developing and building a neutron veto for the dark matter detector is raised.

To further study the source of the excess and narrow down the uncertainty of benchmarking, it is worthwhile building and running experiments similar with the NMM at other underground laboratories, with sufficient neutron moderator as shielding. The experiments can then exclude the detection of low-energy neutrons, and test whether the excess of neutrons is due to a harder spectrum of high-energy neutrons. These experiments would also result in more neutron flux data at more underground sites, which is important to improve our understanding of cosmogenic neutron backgrounds underground.

5.5 Measurement of the High-energy Neutron Flux at the Soudan Underground Laboratory

The results of the LLR fits can also be used to measure the absolute flux of high-energy neutrons with energies above 50 MeV detected by the NMM. This calculation needs the fraction of true high-energy ($> 50\text{ MeV}$) neutrons out of the overall accepted events and the gathering power found in the comprehensive muon simulation in Chapter 4. The event rates in the low-gain run and the high-gain runs should be treated separately with their own gathering powers.

Starting from the multiplicity spectrum of each fast neutron search run, the 1st run is during low PMT gain, while the 2nd and 3rd runs are both during high PMT gain and their multiplicity spectra may be combined. Let's denote the multiplicity spectrum of the low-gain run with $A_m^L \pm \sigma_m^L$, and

the multiplicity spectrum of the high-gain run with $A_m^H \pm \sigma_m^H$, where the superscripts L and H for low-gain and high-gain, respectively. The estimated total numbers of fast neutron events in low-gain and high-gain runs are the sums of the series,

$$\begin{aligned} N_L &= \sum_m A_m^L, \\ N_H &= \sum_m A_m^H, \end{aligned} \tag{5.26}$$

with the variances of the total event numbers of the two sets obtained by

$$\begin{aligned} \sigma_L^2 &= \sum_m (\sigma_m^L)^2, \\ \sigma_H^2 &= \sum_m (\sigma_m^H)^2. \end{aligned} \tag{5.27}$$

Using the multiplicity spectra of the three fast neutron search data sets resulted from the analysis in Section 5.4, Eq. (5.26) and (5.27) give the estimated number of accepted events to be 150.4 ± 11.3 in ~ 158.2 live days of the 1st fast neutron search data (in low-gain), and 628.8 ± 31.8 in ~ 472.0 live days of the 2nd and 3rd fast neutron search data together (in high-gain). The relative uncertainties of the two measurements are 7.5% and 5.1%, respectively.

According to Eq. (4.6), the definition of gathering power is the rate of accepted real high-energy ($> 50\text{MeV}$) neutron events divided by the flux of high-energy neutrons above 50 MeV. But the real high-energy ($> 50\text{MeV}$) neutron events are only a part of all accepted events. Here denote the fraction of the real high-energy neutrons out of all accepted events as f_L for low-gain run and f_H for high-gain run. They are estimated to be $f_L = (43 \pm 7)\%$ and $f_H = (45 \pm 7)\%$ with the MC truth study in Chapter 4. Then the gathering power may further be written as

$$\mathcal{G} = \frac{f \cdot N/T}{\mathcal{F}}, \tag{5.28}$$

where N stands for the total number of accepted events in the data set and T for the live time of the

data set. It is equivalent to

$$\mathcal{F} \cdot T = \frac{f \cdot N}{\mathcal{G}}, \quad (5.29)$$

which can be understood as the total number of high-energy ($> 50 \text{ MeV}$) neutrons traversing in a unit horizontal area during a run. Then given these quantities of the low-gain run and the high-gain run, the flux of high-energy ($> 50 \text{ MeV}$) neutrons averaged over the two data sets is

$$\begin{aligned} \mathcal{F} &= \frac{\mathcal{F}_L \cdot T_L + \mathcal{F}_H \cdot T_H}{T_L + T_H}, \\ &= \frac{f_L \cdot N_L / \mathcal{G}_L + f_H \cdot N_H / \mathcal{G}_H}{T_{\text{tot}}}. \end{aligned} \quad (5.30)$$

And the uncertainty of the averaged flux can be calculated with

$$\sigma_{\mathcal{F}} = \frac{1}{T_{\text{tot}}} \sqrt{\left(\frac{\sigma_{f_L}^2}{f_L^2} + \frac{\sigma_{N_L}^2}{N_L^2} + \frac{\sigma_{\mathcal{G}_L}^2}{\mathcal{G}_L^2} \right) \cdot \left(\frac{f_L N_L}{\mathcal{G}_L} \right)^2 + \left(\frac{\sigma_{f_H}^2}{f_H^2} + \frac{\sigma_{N_H}^2}{N_H^2} + \frac{\sigma_{\mathcal{G}_H}^2}{\mathcal{G}_H^2} \right) \cdot \left(\frac{f_H N_H}{\mathcal{G}_H} \right)^2}. \quad (5.31)$$

The gathering power is estimated as $(4.28 \pm 0.56) \times 10^3 \text{ cm}^2$ for the low-gain run and $(5.02 \pm 0.61) \times 10^3 \text{ cm}^2$ for the high-gain run with the MC in Chapter 4. The total live time of all three fast neutron searches is 630.2 days (with actual precision up to 0.1 s used in the calculation). By plugging the values of gathering powers and estimated event numbers in the two data sets from the early part of this section in the Eq. (5.30) and (5.31), the flux of high-energy ($> 50 \text{ MeV}$) neutrons at the Soudan Underground Laboratory is measured to be

$$(1.3 \pm 0.2) \times 10^{-9} \text{ cm}^{-2} \text{ s}^{-1}.$$

The relative uncertainty is about 15%.

As mentioned earlier in this section, the relative uncertainties of the event counts or rate

measurements in low-gain and high-gain runs are only 7.5% and 5.1%, respectively. The dominant uncertainty in the flux measurement is from the fractions of neutrons above 50 MeV out of all accepted events and the gathering powers, which are limited by the statistics of the comprehensive muon simulation. The relative uncertainties of these quantities decrease as $\sim \sqrt{1/N_{\text{MC}}}$, as the total event number of MC N_{MC} increases. It is estimated that if we had run the comprehensive muon simulation of ~ 400 days of live time, namely costing almost a factor of 3 of the CPU hours we had for the MC, we could achieve a 10% measurement of the high-energy neutron flux, with the same amount of data taken in the experiment.

D. Mei and A. Hime have given an MC estimation of the cosmogenic neutron flux for several sites with different threshold energies with FLUKA [50]. Their simulated flux at the Soudan Underground Laboratory is $4.73 \times 10^{-9} \text{ cm}^{-2}\text{s}^{-1}$ above a threshold of 10 MeV, and $1.073 \times 10^{-9} \text{ cm}^{-2}\text{s}^{-1}$ above 100 MeV. The measurement in this work is consistent with the range between the two values.

Chapter 6

Active Neutron Veto for SuperCDMS

Experiment at SNOLAB

An active neutron veto is vital for minimizing background level and achieving the desired sensitivity for next-generation direct dark matter detection experiments. In this chapter, I present the design, evaluation, and prototyping of the active neutron veto for SuperCDMS SNOLAB.

6.1 Passive Shielding for SuperCDMS SNOLAB

The next phase of the SuperCDMS experiment will be built and run at SNOLAB, with a depth of 6,800 feet (6010 meter of water equivalent), reducing both cosmic-ray muons and cosmogenic neutrons by more than two orders of magnitude.

The detectors will be surrounded by a layered shielding system, consisting of ultra-pure copper, high-density polyethylene (HDPE) passive shielding layer, lead, and a combination of HDPE and water tanks. Figure 6.1 shows the schematic layout with profile view and 3-dimensional view of the cryostat and shielding layers. The goal of this shield is to reduce the flux of external gamma rays and neutrons to a level that allows the detectors to achieve nearly background-free sensitivity. The copper shielding is provided by the walls of the SNOBOX, which are multiple layers of ultra-pure copper,

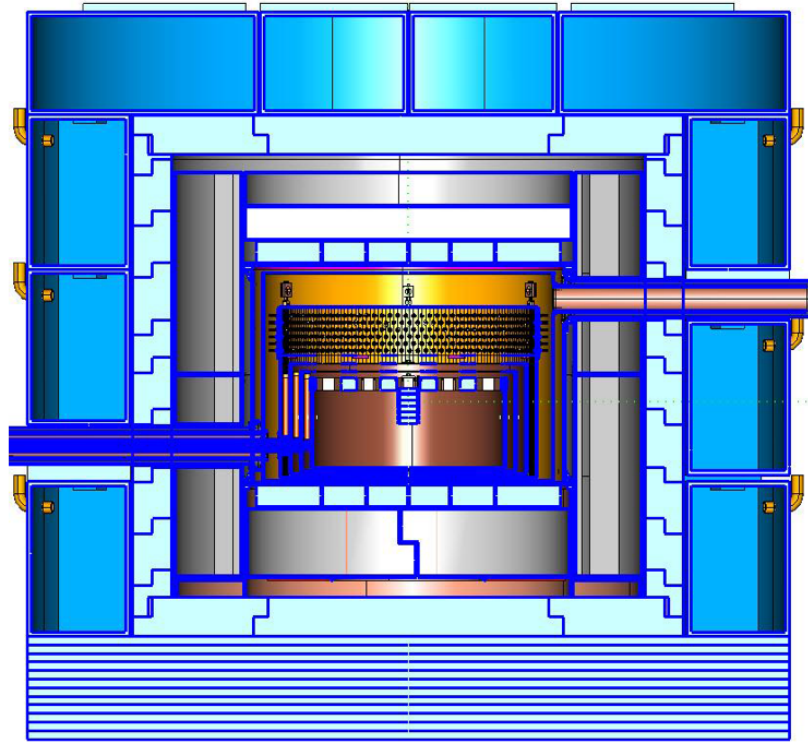
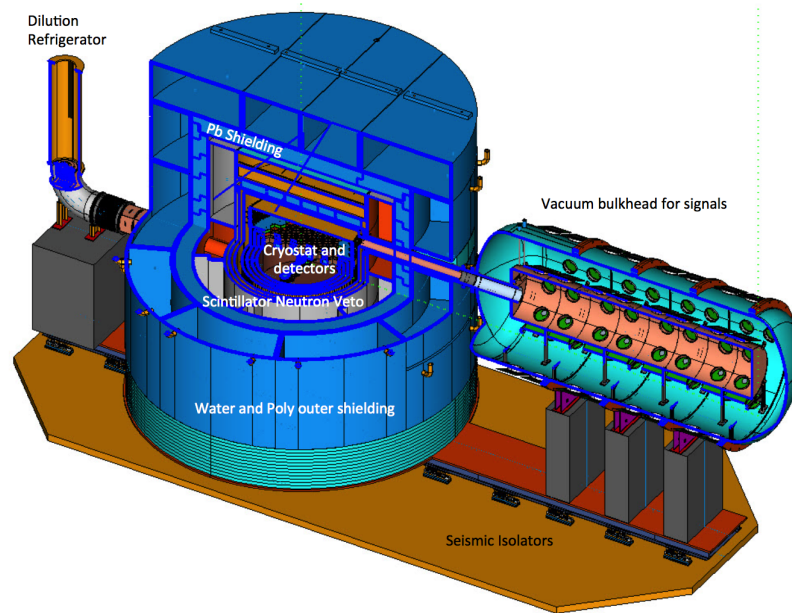


Figure 6.1: Conceptual design of the SuperCDMS SNOLAB cryogenic and shielding system. On the top is shown the 3-dimensional view. The dilution refrigerator on the left side of the diagram provides the cooling for the thermal cans surrounding the detectors (center). A vacuum bulkhead and heat sinking vessel (E-tank) is shown on the right. On the bottom is shown the profile view. A passive polyethylene neutron shield, or an active neutron veto detector (gray), lies inside the lead shielding (light cyan), which is surrounded by a massive polyethylene (bottom light cyan) and water shield (blue).

each 3/8"-1/2" thick. The iZIP detectors are located in the innermost can. The copper cans shield the detectors from the particles emitted by radioactive contaminants in the environment. Copper is the most radiopure material available with the mechanical properties that allow construction of such large cans.

In the current baseline design, the second layer outward in the shielding system is a 40 cm layer of HDPE. The thickness of this layer is more than necessary for passive shielding against the external neutron flux, but it is to preserve space for a potential upgrade with an active neutron veto.

Surrounding the HDPE or active neutron veto is a ~ 23 cm thick layer of lead. The lead will be from known sources that have low uranium and thorium contamination. The purpose of this layer is to reduce the flux of external gamma rays.

Next to the lead shield is a thin metal sheet impervious to radon diffusion. The space within this metal sheet will be constantly purged with dry nitrogen to prevent radon daughter deposition on the surfaces that can result in radioactive contaminants near the detectors.

The outermost shielding is a 60 cm layer consisting of water tanks and a HDPE base. This layer will reduce the neutron flux from the external environment. HDPE is commonly used for neutron shielding, as it is efficient at neutron moderation and it provides mechanical support. But water shielding is more economical for the top and sides of the layer.

Note there are two layers for neutron shielding. It is necessary to have both the outermost layer and a layer adjacent the copper cans serving as neutron shielding. The outer water tanks and HDPE is needed for reducing the neutron flux that can hit the lead layer. Then, as discussed in Chapter 2, when high-energy neutrons hit the lead shielding, the lead itself may become an extra source of neutrons, and it is pretty close to the detector. So within the lead layer, it is necessary to place a HDPE shielding to reduce the additional neutron flux, or scintillator layer, as an active veto shield, to tag neutron background events.

6.2 Active Neutron Veto

Although our current best estimate of the neutron background event rate at SNOLAB indicates that SuperCDMS can run nearly background-free with only passive shielding for several years of running [73], it is impractical to exhaustively screen every component of the detector system to ensure the most optimistic radiopurity levels are achieved. It is advantageous to build an active veto with a high efficiency for tagging neutron-induced events from the events that are detected by the iZIP detectors. When a neutron causes a single-scattering nuclear recoil in the detector mass, there is a high chance that the neutron would also induce a detectable signal in the active veto shield within a designated time window relative to the iZIP event. This coincidence of iZIP event and veto detector signal would trigger a veto to reject the neutron induced event. An active veto will not only directly reduce the neutron background rate, but also provide an *in situ* measurement of the coincident neutron rate and serve as a neutron monitor to estimate the residual neutron background more precisely.

6.2.1 Design

The design for the veto consists of 40 cm thick modular tanks filled with liquid scintillator. The layer will be constituted with 6 cylindrical wedge tanks around the sides of the cryostat and cylindrical end caps on the top and bottom, as demonstrated in Figure 6.2. The tank walls will be made of 1/2" thick acrylic to minimize radioactive contamination. To maximize light collection, the inner walls of the tanks will be lined with a highly reflective material, such as specially-treated Tyvek. The veto modular tanks will be filled with liquid scintillator, which will be based on linear alkylbenzene (LAB) solvent loaded with 2 g/L PPO of diphenyloxazole (PPO), as the primary fluor, and 6.5 mg/L bis-MSB, as the wavelength shifting (WLS) fluor. The LAB scintillator will also be loaded with a high neutron-capture cross section element, which will significantly decrease the capture time of thermal neutrons. This would help reduce the necessary size and time window of the neutron

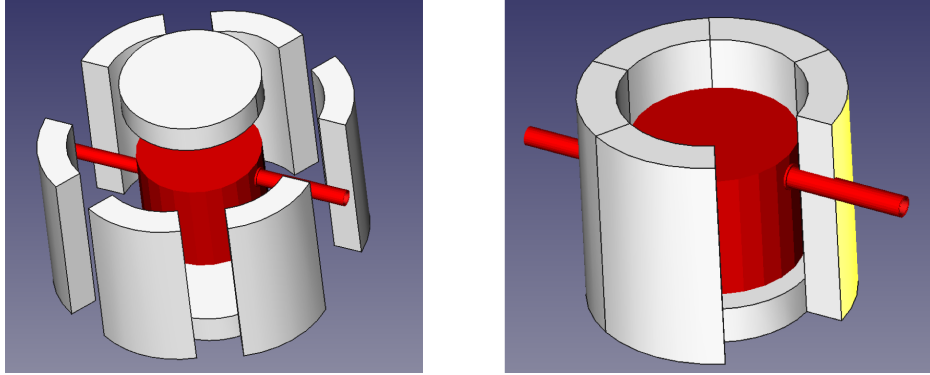
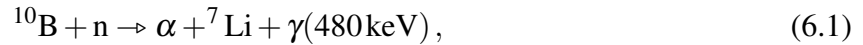


Figure 6.2: Schematic graphs for the layout of the active neutron veto modules. The white wedges and cylindrical ends represent the modules, and the red parts represent the cryostat copper cans and the pipes used for electronics stem and cryogenic system. On the left all the modules are shown with their locations separated away from the actual locations for installation. On the right are shown with their actual locations for installation, without the top cap and one of the side wedges.

veto detector [74]. The current plan is to load LAB with 30% w/w trimethyl borate (TMB), which will result in $\sim 3\%$ boron by weight. Boron has a high cross section to capture thermal neutrons, leading to a reaction:



with 94% branching. The reaction results in a distinct peak at the energy corresponding to $\sim 60\text{keV}$ electron equivalent (60keV_{ee}) [75]. The gamma may either escape from the scintillation detector, or be detected via Compton scattering to form a continuous spectrum. The choice of the boron concentration is for the sake of a sufficient neutron capture rate without significantly affecting the scintillator light output. This will be further discussed in 6.2.2.

To detect the scintillation light, we will use silicon photomultipliers (SiPMs), also known as multi-pixel photon counters (MPPCs). SiPMs are much more compact than PMTs, and yet much more radiopure. Each scintillator module will be installed with the order of 100 SiPMs. To achieve efficient light collection, an array of wavelength shifting (WLS) fibers will be fed into the veto modular tanks before the liquid scintillator is filled, and attached to the surfaces of SiPMs. The fibers can concentrate the emitted light onto the small sensor area of the SiPMs. The SiPMs will be

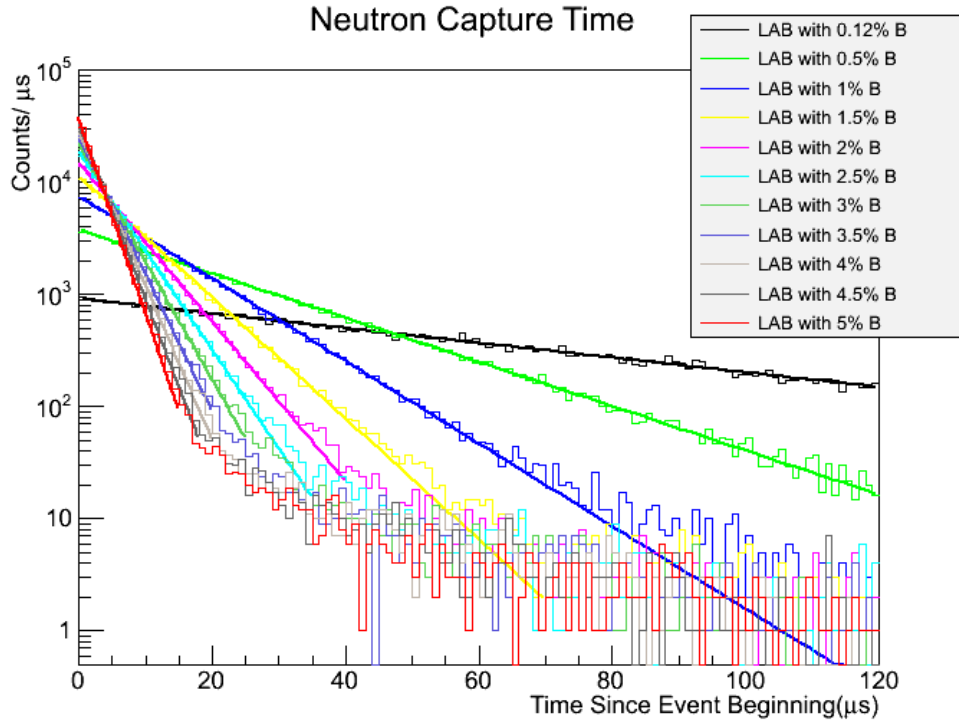


Figure 6.3: Neutron capture times in the active neutron veto with different boron concentrations. The distributions are fit with exponential functions to estimate the characteristic times.

cooled to $-20\text{ }^{\circ}\text{C}$ to reduce the dark count rate to a level below a few MHz total per module.

6.2.2 Monte Carlo Evaluation

In order to evaluate the efficiency of the active neutron veto for tagging single-scatter neutrons, I performed Monte Carlo simulations using a Geant4 based package, named supersim.

As mentioned in the last subsection, the boron concentration is set to be $\sim 3\%$. This value was determined with the following Monte Carlo study. To explore the effect of changing the boron concentration, I ran simulations with different values of the boron concentration, i.e. 0.12%, 0.5%, 1.0%, ..., 5% (from 0.5% to 5% with 0.5% increment between every two simulations), among which 0.12% and 5% are the two values found in other experiments [75, 76]. 10^5 primary neutrons in each simulation were generated randomly in the liquid scintillator bulk, with a typical (α, n) neutron spectrum up to $\sim 8\text{ MeV}$. From the resulting data in each simulation, the efficiency for successful

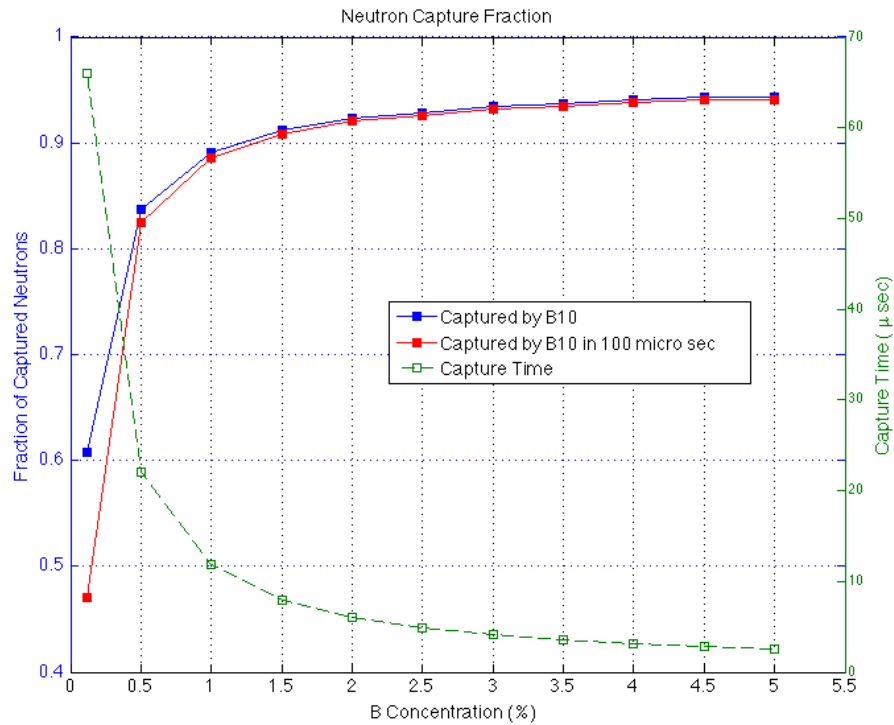


Figure 6.4: Estimated neutron tagging efficiency, plotted together with capture time, both as functions of boron concentration. The tagging efficiency with infinite time is in the blue box and solid line, and the tagging efficiency with a 100 μs veto time window is in the red box and solid line, with both labeled by the left-hand Y-axis. The neutron capture time is in the green empty box and dashed line, labeled by the right-hand Y-axis. The tagging efficiency (capture time) increases (decreases) dramatically as boron concentration increases at low values, while the changes of both slow down with respect to the change of boron concentration at higher values.

tagging of the single-scatter neutron events in iZIPs was calculated, and the times of captures since the event beginning were collected to histograms. Figure 6.3 shows the capture time distribution for different boron concentrations. Fit with exponential functions is performed for each distribution to obtain the characteristic time of capture (or simply called capture time). In Figure 6.4, the tagging efficiencies (called Fraction of Captured Neutrons in the Y-axis label) are plotted together with capture times, with the left-hand side of the Y-axis representing the tagging efficiency and the right-hand side of the Y-axis representing capture time. As boron concentration increases from 0.12% to 1.5%, the tagging efficiency dramatically increases above 0.9, and the capture time goes below $10\ \mu\text{s}$; as boron concentration continues to increase, both the increase of tagging efficiency and dropping of capture time slow down. The plot clearly indicates that any value beyond 3% would not significantly improve tagging efficiency. Given that a 3% boron concentration already requires a load of 30% TMB, too much doping can dramatically hurt the light transparency and result in bad light collection. Therefore, we believe that a 3% boron concentration is a reasonable choice. In the figure, a comparison is also made between the tagging efficiencies with infinite time and with a time window of $100\ \mu\text{s}$. It is shown that the efficiency with $100\ \mu\text{s}$ veto time would not be significantly lower than that with infinite time. In realistic experimental running, the order of $100\ \mu\text{s}$ for the event time is a reasonable setting.

Another Monte Carlo simulation study was performed to test the veto time window and veto threshold. 10^5 primary neutrons were initiated from the outermost layer of the copper cans, the “outer vessel can” (OVC), and the data were analyzed with different settings of veto time windows. The results, shown in Figure 6.5, are veto efficiency as a function of veto threshold in keV_{ee} (keV electron-equivalent energy) for different values of the veto time window. With a $50\ \text{keV}_{ee}$ threshold and $100\ \mu\text{s}$ veto time window, the veto efficiency is estimated to be $(92.2 \pm 0.9)\%$ for single-scatter neutron-induced nuclear recoil events in iZIP detectors.

From the other simulations of radioactive contaminations in the shield and veto materials, the rate of background events in the veto detector above $50\ \text{keV}_{ee}$ threshold is estimated to be less than

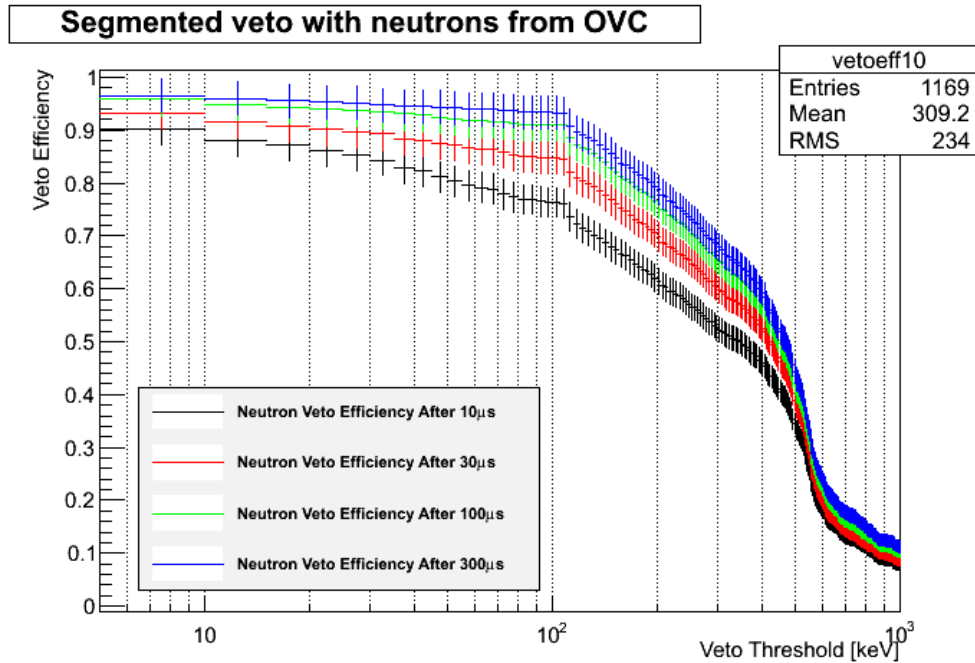


Figure 6.5: Veto efficiency for tagging single-scatter neutron-induced iZIP events as a function of threshold energy in keV_{ee} , for veto time window $10\ \mu\text{s}$ (black), $30\ \mu\text{s}$ (red), $100\ \mu\text{s}$ (green), and $300\ \mu\text{s}$ (blue). A higher threshold energy or a shorter veto time window results in a lower veto efficiency. The parameters chosen in the current design are a threshold of $50\ \text{keV}_{ee}$ and $100\ \mu\text{s}$, which are demonstrated to be able to achieve a veto efficiency of 92-93%.

200 Hz, resulting in $< 2\%$ veto-induced live-time loss with a $100\ \mu\text{s}$ window. We therefore believe that this design of active neutron veto will meet the goal of 90% veto efficiency without significant negative impact on dark matter search efficiency. In addition, the rate of the neutrons tagged by the active neutron veto can be used to estimate the rate of the residual neutron backgrounds, helping the neutron veto serve as a more precise neutron monitor.

6.3 Prototyping of the Neutron Veto

The design requirement of the active neutron veto, i.e. using $100\ \mu\text{s}$ window, triggering events at a $50\ \text{keV}_{\text{ee}}$ threshold, and tagging single-scatter neutron events with 90% efficiency, will be achieved by focusing on two aspects: maximization of the amount of energy deposited in the veto by neutron-induced events, and ensuring sufficient light is produced, collected, and detected in the veto system. The simulation evaluation that was done was based on a simplified geometry, and tallying with energy deposition without optical simulations. All the information on a more detailed geometry and the parameters associated with optical components needed to be explored and collected to further develop the veto. It was wise and necessary to start with a prototype detector.

6.3.1 The Quarter-Scale Prototype

We designed and constructed a neutron-detector prototype with approximately one quarter the size of a single full size module. A box shape was used instead of the curved wedge module geometry to simplify construction and assembly. The prototype dimensions were $23 \times 12 \times 3.75$ inches, assembled out of 0.5 inch thick clear acrylic. To maximize the light collection efficiency, the inner surface of the acrylic vessel were lined with Lumirror reflector, as can be seen in Figure 6.6 left. The prototype was strung with 16 1.5 mm diameter Kuraray Y-11 WLS fibers through holes drilled through the acrylic and sealed with 5-minute epoxy. Each fiber was 28 inches long and was bundled into groups of four at each end. The fiber readout was accomplished using 8 Hamamatsu S12572-100C 3 mm

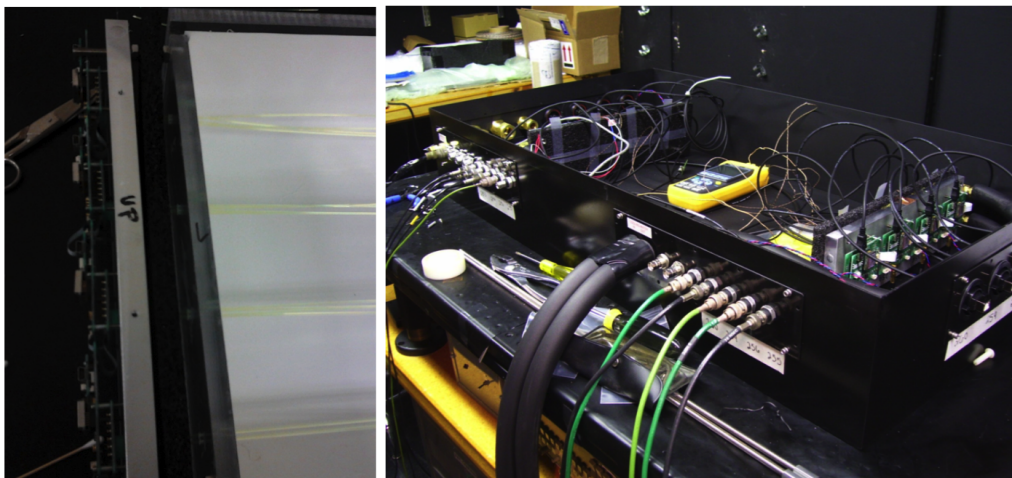


Figure 6.6: The photographs of the quarter-scale neutron-veto prototype. On the left in shown one end of the liquid scintillator prototype before it was sealed. The SiPMs are mounted to the Al cooling plate and are coupled to the fibers that are fed through the holes on the ends of the acrylic vessel into the liquid scintillator. On the right is shown the dark box after the SiPMs were installed but before the acrylic vessel was inserted. The measurements were conducted in the dark box that was held under nitrogen purge.

SiPMs, one for each end of the 4-fiber bundle. Custom mounts were constructed to mount the fiber ends over the face of the SiPM. The SiPMs were mounted on a cooling plate in order to reduce the dark rate.

The entire assembly was housed in a dark box, as shown in Figure 6.6 right, under a fume hood for safety. The atmosphere in the dark box was held under a nitrogen purge to reduce the flammability hazard of the TMB and to prevent condensation from forming on the SiPMs.

6.3.2 Monte Carlo Model

The Geant4 Monte Carlo package supersim works in tallying energy deposition, but does not perform an optical simulation. The MC performed to evaluate the overall design of the neutron veto hence does not provide the information on optimizing the light collection. An integrated method of simulation including both the process of particle interaction and transportation, and the process of optical simulation, would be rather time consuming, and inefficient for understanding the optical

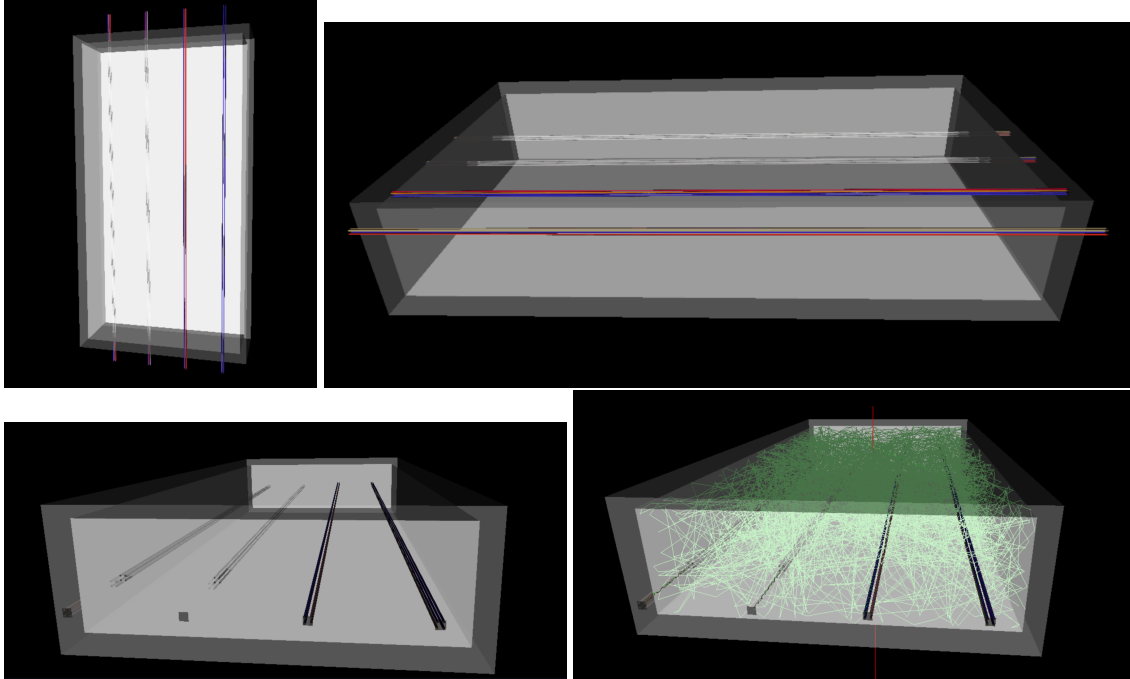


Figure 6.7: Screenshots of a 3D visualization for the veto prototype geometry. The top two and the bottom left are 3 different views of the detector geometry. The white and transparent face and boundary show the acrylic walls, and blue/red strings are the four bundles of fibers, 16 in total. The inner wall of the acrylic tank is modeled with an optical surface with the reflectivity curve of Lumirror. The bottom right is a demonstration of an event with a muon (red track) traversing the detector from top down and inducing optical photons (green tracks).

part specifically. Given the demand for a dedicated optical Monte Carlo model, I developed a Geant4 Monte Carlo package, modeling the quarter-scale neutron-veto prototype. In the MC package, I fully modeled the geometry of the acrylic tank, including the four bundles of WLS fibers, but ignored the steel dark box and the shelf for fixing the electronics readout, etc. The SiPMs were only modeled as surfaces attached to the ends of fibers. Figure 6.7 shows screenshots of a 3D visualization of the detector geometry and an event demonstration.

To run an optical simulation properly, it's necessary to configure optical properties to our best knowledge for each component associated with photon transport in the system. We use wavelength dependent parameters whenever we can measure them or find data in the literature. A trial value of the intrinsic light yield of liquid scintillator is set to be 11,500 photons/MeV, approximately as suggested in Ref. [77]. For the modeling of the physics in the scintillator, the future plan is to use

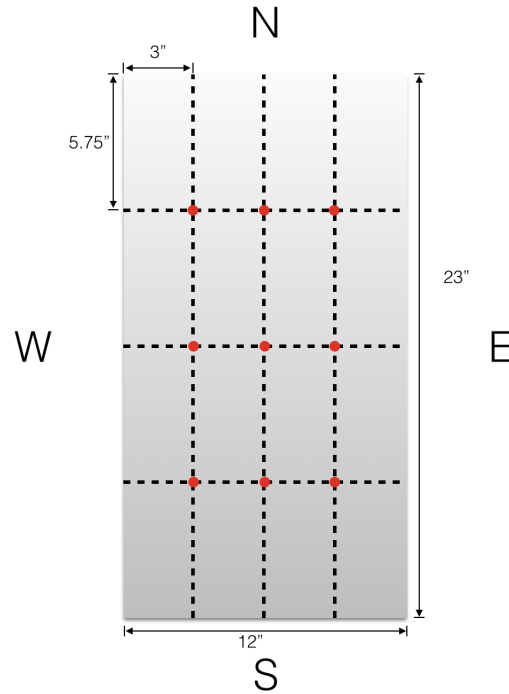


Figure 6.8: The 9 locations of radioactive sources for calibration. The rectangle shows the range of the liquid scintillator, and the red dots at the crossings of dash lines show the 9 locations of the source. The dash lines divide the rectangle by four equal parts in both dimensions.

the emission spectrum for LAB with 2 g/L PPO as the primary emission, and the measured emission spectrum for 6.5 mg/L bis-MSB as the WLS reemission. For bulk absorption, we plan to use the absorption length measured for LAB/PPO mixture as the primary absorption length, and the one measured for LAB/PPO/bis-MSB mixture as the WLS absorption length. This is for modeling the first phase of characterization (without TMB), then substituting all data for LAB with the those measured for LAB + 30% TMB (also with proper concentrations of PPO and bis-MSB) when modeling the liquid scintillator solution with TMB. To a first approximation, we use the emission spectrum measured with LAB/PPO/bis-MSB mixture, without the WLS process in the scintillator.

The reflector is treated as a skin surface of the logical volume of the Lumirror thin layer. The reflection of Lumirror is neither quite Lambertian nor diffuse. The angular distribution of its reflection is recently measured and built in Geant4 as a look-up table model [78].

We characterize the neutron veto prototype with various radiative sources including Ba133,

Cs137, Co60, Cf125 etc., and with cosmic ray mode. In radiative source runs, the sources are set in 9 fixed locations on the top of the steel dark box, as shown in Figure 6.8. The idea for determining the unknown optical parameters is to run the same radioactive sources with the same array of locations in the simulations. For each location use the PE spectra obtained in the 8 channels to fit the measured PE distributions. While tuning the parameters and running the simulation again and again, the parameters would be trained to best fit the simulated PE spectra with the measured ones. In this section, I only present a primary simulation that demonstrates the MC model for the prototype.

In this demonstrative MC study, ^{137}Cs are set collimated at East, Center, and West source locations. There are 10^5 primary gammas simulated in each case, conforming to the ^{137}Cs spectrum. The deposited energy spectrum and photoelectron spectrum are shown in Figure 6.9, for the three source locations. In order to measure light yield and energy resolution, we fit the PE spectrum with the deposited energy distribution convoluted with a gaussian function with the standard deviation

$$\sigma = \sqrt{A \cdot \text{PE}}, \quad (6.2)$$

where A is a dimensionless constant and $\text{PE} = (\text{LightYield}) \cdot E_{\text{dep}}$. In the fit info box of the plots, p_0 is a normalization factor that scales the amplitude, p_1 is the Light Yield in PE/MeV, and p_2 is the constant A . According to the fit results, the light yield is about 0.36 PE/keV, so that a 50 keV threshold is equivalent to ~ 18 PE. The energy resolution near the threshold is about 24-25%.

Figure 6.10 shows the fraction of individual channel PE over the total PE (in the left column), and the PE spectra in individual channels, for the different source locations. As can be seen, the channels that are closer to the source get harder spectra. The distribution of the individual channel response is sensitive to the source location, and can be used to tune the unknown optical parameters in the model with a large batch of simulations.

Since the active neutron veto was not funded in the baseline development of SuperCDMS SNOLAB, the prototyping work has stopped. If the collaboration continues the neutron-veto

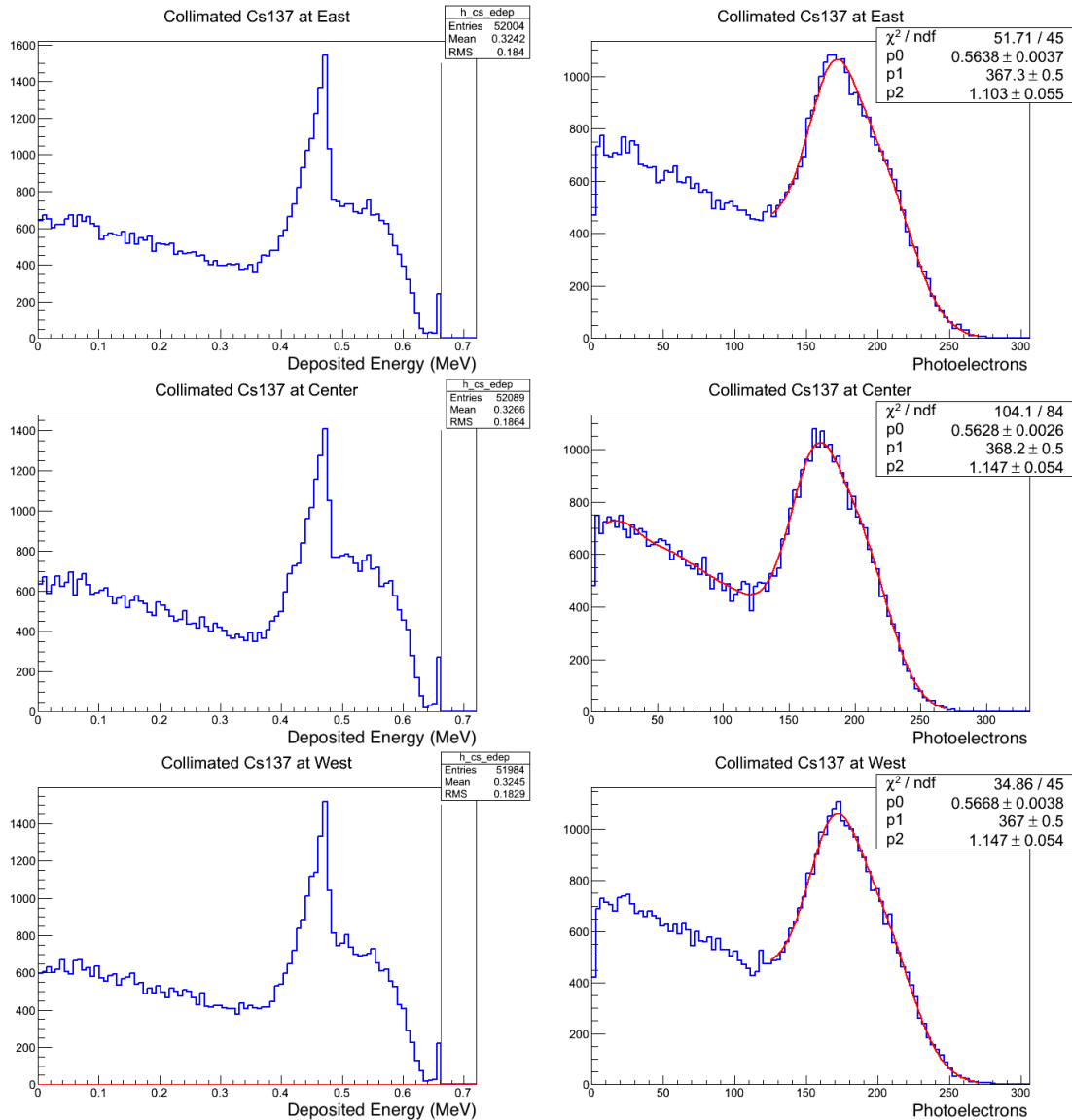


Figure 6.9: Energy spectra for a Monte Carlo simulation of the veto prototype exposed with ^{137}Cs at three different locations. The left column shows the deposited energy spectra, while the right column shows the PE spectra. By convoluting the deposited energy spectra to fit the PE spectra, the light yield can be measured.

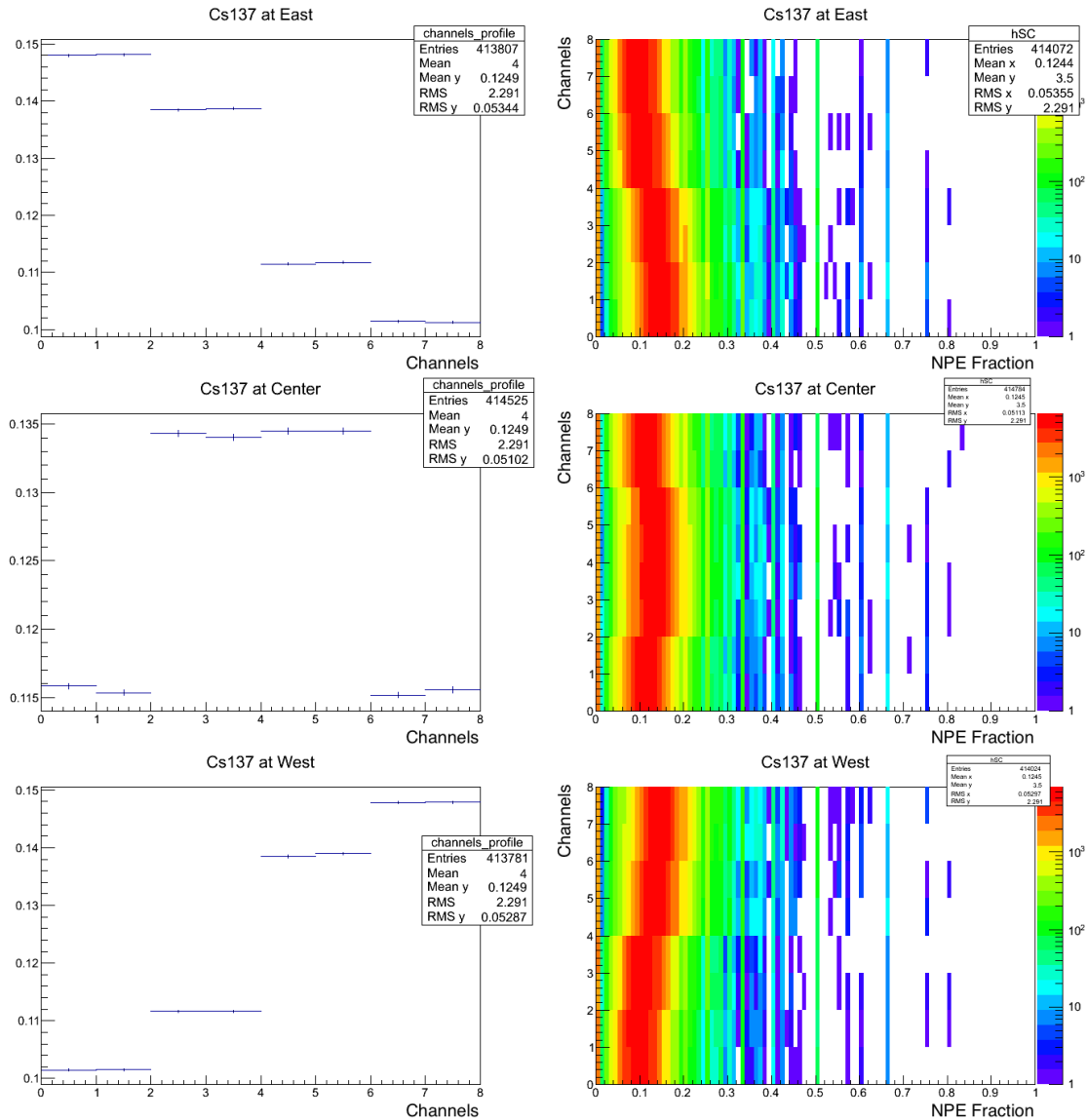


Figure 6.10: The left column shows the fraction of PE response of individual channels over the total PE. The right column shows channel number vs the PE fraction, with the color representing event rate. The channels closer to the source location get harder spectra. The sensitivity of the individual channel response to the source locations can be used to tune the unknown optical parameters with a large batch of simulations.

prototyping, the method discussed in this section will be resumed to train the model parameters for the optical simulation. In addition, the simulation study in this section demonstrated that light yield and energy resolution can be measured with this MC model by convoluting the deposited energy spectrum to fit the PE spectrum.

6.3.3 Demonstration Runs

Data were taken for a variety of radioactive sources. The sources were used to calibrate the SiPM response and the light yield of the prototype. Figure 6.11 shows the measured ^{137}Cs spectrum compared to a Geant4 spectrum smeared using parameters derived from ^{137}Cs data and SiPM response. From this comparison, the light yield is tuned to be 520 PE/MeV to match the shoulder and falling feature between the measured spectrum and Geant4 spectrum.

The energy spectrum is also measured without any radioactive source present. As shown in Figure 6.12, the peak around 16 MeV corresponds to cosmic muons passing through the detector.

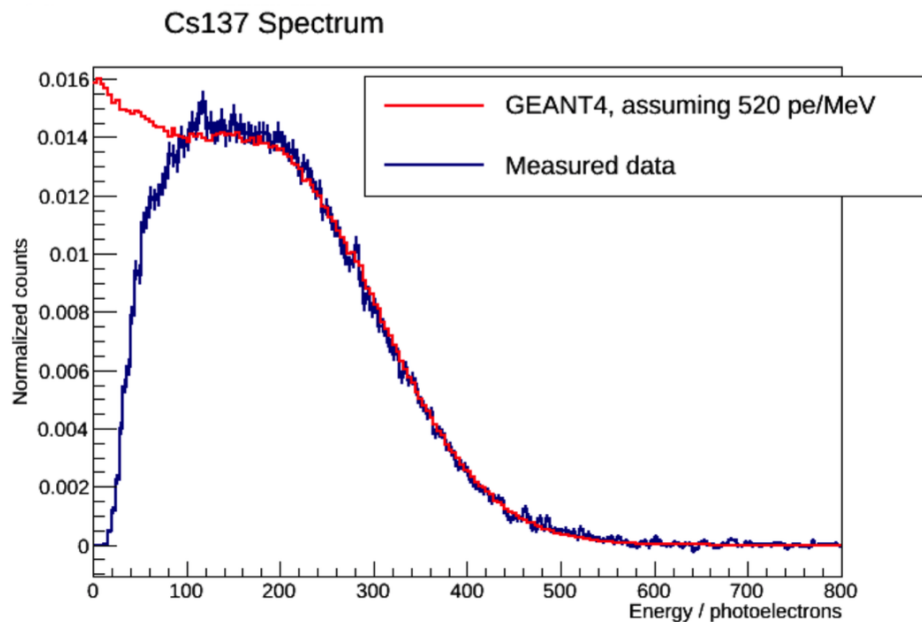


Figure 6.11: The measured spectrum of ^{137}Cs compared to a Geant4 ^{137}Cs spectrum smeared using parameters derived from ^{137}Cs and SiPM response. Figure by Ben Loer, FNAL.

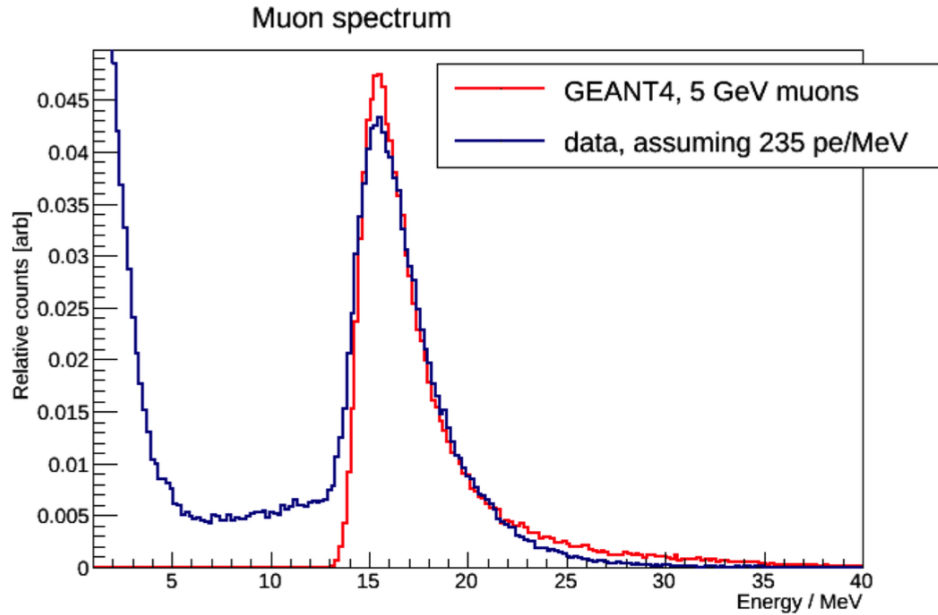


Figure 6.12: The measured energy spectrum for data collected without any radioactive source present. The peak around 16 MeV corresponds to cosmic muons passing through the detector, depositing energy as least ionizing particles. The Geant4 energy spectrum has been convoluted with a smearing function derived from ^{137}Cs data. The energy scale/light yield has been obtained by aligning the data and Monte Carlo peaks by eye. Figure by Ben Loer, FNAL.

Muons are least ionizing particles, and the energy deposition is determined by the path length in the detector scintillator, and estimated to be $\sim 16\text{MeV}$ for the thickness of the liquid scintillator in the prototype. By aligning the peaks of the data and the Monte Carlo, the light yield is tuned to be 235 PE/MeV in the muon run. The true light yield is likely between 0.2-0.5 PE/keV.

When taking data with ^{252}Cf , we were unable to observe the expected 60keV_{ee} peak as the signature of boron neutron captures. The reason is not completely understood, but the large gamma background emitted by the same ^{252}Cf source may be overwhelming the capture signal. It may also be that the energy resolution was too poor to distinguish the neutron capture peak.

At present, since the active neutron veto is not under the baseline plan of SuperCDMS SNOLAB, the work on prototyping has fallen in low priority. If in the future the collaboration is proved to upgrade the passive shield with the active neutron veto, there may be a lot of follow-up on analyzing, understanding the demonstrative runs, and improving the design of the prototype and the full-scale

modules. We may use collimated neutron source to measure the neutron response, or try to shield against gamma rays. We would also need to perform more simulations to reveal potential issues in the system. Finally, with a better understanding of the prototype detector, there may more hints to improve the design for more efficient light collection and better energy resolution.

References

- [1] Scott Dodelson. *Modern cosmology*. San Diego, CA: Academic Press, 2003. URL: <https://cds.cern.ch/record/1282338> (cit. on pp. 1, 9).
- [2] Sean M. Carroll. *Spacetime and geometry: An introduction to general relativity*. Pearson International, 2004. URL: <http://www.slac.stanford.edu/spires/find/books/www?cl=QC6:C37:2004> (cit. on p. 1).
- [3] Planck Collaboration. “Planck 2015 results - I. Overview of products and scientific results”. In: *A&A* 594 (2016), A1. DOI: 10.1051/0004-6361/201527101. URL: <http://dx.doi.org/10.1051/0004-6361/201527101> (cit. on p. 3).
- [4] S. Burles, K. M. Nollett, and Michael S. Turner. “Deuterium and big bang nucleosynthesis”. In: *Nucl. Phys. A* 663 (2000), pp. 861c–864c. DOI: 10.1016/S0375-9474(99)00732-0. arXiv: astro-ph/9903300 [astro-ph] (cit. on pp. 4, 5).
- [5] F. Zwicky. “The redshift of extragalactic nebulae”. In: *Helv. Phys. Acta* 6 (1933). [Gen. Rel. Grav.41,207(2009)], pp. 110–127. DOI: 10.1007/s10714-008-0707-4 (cit. on p. 6).
- [6] Vera C. Rubin and W. Kent Ford Jr. “Rotation of the Andromeda Nebula from a Spectroscopic Survey of Emission Regions”. In: *Astrophys. J.* 159 (1970), pp. 379–403. DOI: 10.1086/150317 (cit. on pp. 6, 7).
- [7] Edvige Corbelli and Paolo Salucci. “The Extended Rotation Curve and the Dark Matter Halo of M33”. In: *Mon. Not. Roy. Astron. Soc.* 311 (2000), pp. 441–447. DOI: 10.1046/j.1365-8711.2000.03075.x. arXiv: astro-ph/9909252 [astro-ph] (cit. on pp. 6, 7).

- [8] Isabelle Paris et al. “The Sloan Digital Sky Survey quasar catalog: ninth data release”. In: *Astron. Astrophys.* 548 (2012), A66. DOI: 10.1051/0004-6361/201220142. arXiv: 1210.5166 [astro-ph.CO] (cit. on p. 6).
- [9] Will Saunders et al. “The PSCz catalogue”. In: *Mon. Not. Roy. Astron. Soc.* 317 (2000), p. 55. DOI: 10.1046/j.1365-8711.2000.03528.x. arXiv: astro-ph/0001117 [astro-ph] (cit. on p. 9).
- [10] Andrew J. S. Hamilton and Max Tegmark. “The Real space power spectrum of the PSCz survey from 0.01 to 300 h Mpc⁻¹”. In: *Mon. Not. Roy. Astron. Soc.* 330 (2002), p. 506. DOI: 10.1046/j.1365-8711.2002.05033.x. arXiv: astro-ph/0008392 [astro-ph] (cit. on p. 9).
- [11] Adam G. Riess et al. “Observational evidence from supernovae for an accelerating universe and a cosmological constant”. In: *Astron. J.* 116 (1998), pp. 1009–1038. DOI: 10.1086/300499. arXiv: astro-ph/9805201 [astro-ph] (cit. on p. 6).
- [12] P. Sikivie. “Experimental Tests of the ”Invisible” Axion”. In: *Phys. Rev. Lett.* 51 (16 Oct. 1983), pp. 1415–1417. DOI: 10.1103/PhysRevLett.51.1415. URL: <http://link.aps.org/doi/10.1103/PhysRevLett.51.1415> (cit. on p. 10).
- [13] Hsin-Chia Cheng, Jonathan L. Feng, and Konstantin T. Matchev. “Kaluza-Klein Dark Matter”. In: *Phys. Rev. Lett.* 89 (21 Oct. 2002), p. 211301. DOI: 10.1103/PhysRevLett.89.211301. URL: <http://link.aps.org/doi/10.1103/PhysRevLett.89.211301> (cit. on p. 10).
- [14] Fumihiro Takayama and Masahiro Yamaguchi. “Gravitino dark matter without R-parity”. In: *Phys. Lett.* B485 (2000), pp. 388–392. DOI: 10.1016/S0370-2693(00)00726-7. arXiv: hep-ph/0005214 [hep-ph] (cit. on p. 10).
- [15] Benjamin W. Lee and Steven Weinberg. “Cosmological Lower Bound on Heavy Neutrino Masses”. In: *Phys. Rev. Lett.* 39 (1977), pp. 165–168. DOI: 10.1103/PhysRevLett.39.165 (cit. on p. 10).
- [16] H.E. Haber and G.L. Kane. “The search for supersymmetry: Probing physics beyond the standard model”. In: *Physics Reports* 117.2 (1985), pp. 75–263. DOI: <http://dx.doi.org/10.>

- 1016/0370-1573(85)90051-1. URL: <http://www.sciencedirect.com/science/article/pii/0370157385900511> (cit. on p. 10).
- [17] Edward W. Kolb and Michael S. Turner. “The Early Universe”. In: *Front. Phys.* 69 (1990), pp. 1–547 (cit. on pp. 10, 11).
- [18] Gerard Jungman, Marc Kamionkowski, and Kim Griest. “Supersymmetric dark matter”. In: *Phys. Rept.* 267 (1996), pp. 195–373. DOI: 10.1016/0370-1573(95)00058-5. arXiv: hep-ph/9506380 [hep-ph] (cit. on p. 11).
- [19] Andrew Hime. “The MiniCLEAN Dark Matter Experiment”. In: *Particles and fields. Proceedings, Meeting of the Division of the American Physical Society, DPF 2011, Providence, USA, August 9-13, 2011*. 2011. arXiv: 1110.1005 [physics.ins-det]. URL: <https://inspirehep.net/record/930736/files/arXiv:1110.1005.pdf> (cit. on pp. 11, 16).
- [20] K. Rielage et al. “Update on the MiniCLEAN Dark Matter Experiment”. In: *Phys. Procedia* 61 (2015), pp. 144–152. DOI: 10.1016/j.phpro.2014.12.024. arXiv: 1403.4842 [physics.ins-det] (cit. on pp. 11, 16).
- [21] P. -A. Amaudruz et al. “DEAP-3600 Dark Matter Search”. In: *Proceedings, 37th International Conference on High Energy Physics (ICHEP 2014): Valencia, Spain, July 2-9, 2014*. Vol. 273-275. 2016, pp. 340–346. DOI: 10.1016/j.nuclphysbps.2015.09.048. arXiv: 1410.7673 [physics.ins-det]. URL: <https://inspirehep.net/record/1324765/files/arXiv:1410.7673.pdf> (cit. on pp. 11, 16).
- [22] D. S. Akerib et al. “The Large Underground Xenon (LUX) Experiment”. In: *Nucl. Instrum. Meth. A* 704 (2013), pp. 111–126. DOI: 10.1016/j.nima.2012.11.135. arXiv: 1211.3788 [physics.ins-det] (cit. on pp. 11, 16).
- [23] E. Aprile et al. “The XENON100 dark matter experiment”. In: *Astroparticle Physics* 35.9 (2012), pp. 573–590. DOI: <http://dx.doi.org/10.1016/j.astropartphys.2012.01.003>. URL: <http://www.sciencedirect.com/science/article/pii/S0927650512000059> (cit. on pp. 11, 16).
- [24] P. Agnes et al. “Results from the first use of low radioactivity argon in a dark matter search”.

- In: *Phys. Rev. D* 93.8 (2016), p. 081101. DOI: 10.1103/PhysRevD.93.081101. arXiv: 1510.00702 [astro-ph.CO] (cit. on pp. 11, 16).
- [25] R. Agnese et al. “Demonstration of Surface Electron Rejection with Interleaved Germanium Detectors for Dark Matter Searches”. In: *Appl. Phys. Lett.* 103 (2013), p. 164105. DOI: 10.1063/1.4826093. arXiv: 1305.2405 [physics.ins-det] (cit. on pp. 11, 16, 27).
- [26] E. Armengaud et al. “First results of the EDELWEISS-II WIMP search using Ge cryogenic detectors with interleaved electrodes”. In: *Phys. Lett. B* 687 (2010), pp. 294–298. DOI: 10.1016/j.physletb.2010.03.057. arXiv: 0912.0805 [astro-ph.CO] (cit. on pp. 11, 16).
- [27] C. E. Aalseth et al. “Results from a Search for Light-Mass Dark Matter with a P-type Point Contact Germanium Detector”. In: *Phys. Rev. Lett.* 106 (2011), p. 131301. DOI: 10.1103/PhysRevLett.106.131301. arXiv: 1002.4703 [astro-ph.CO] (cit. on pp. 11, 16).
- [28] Marco Battaglia, Ian Hinchliffe, and Daniel Tovey. “Cold dark matter and the LHC”. In: *J. Phys. G* 30 (2004), R217–R244. DOI: 10.1088/0954-3899/30/10/R01. arXiv: hep-ph/0406147 [hep-ph] (cit. on p. 12).
- [29] Gianfranco Bertone, Dan Hooper, and Joseph Silk. “Particle dark matter: Evidence, candidates and constraints”. In: *Phys. Rept.* 405 (2005), pp. 279–390. DOI: 10.1016/j.physrep.2004.08.031. arXiv: hep-ph/0404175 [hep-ph] (cit. on p. 12).
- [30] Mark W. Goodman and Edward Witten. “Detectability of Certain Dark Matter Candidates”. In: *Phys. Rev. D* 31 (1985), p. 3059. DOI: 10.1103/PhysRevD.31.3059 (cit. on p. 12).
- [31] Joel R. Primack, David Seckel, and Bernard Sadoulet. “Detection of Cosmic Dark Matter”. In: *Ann. Rev. Nucl. Part. Sci.* 38 (1988), pp. 751–807. DOI: 10.1146/annurev.ns.38.120188.003535 (cit. on p. 12).
- [32] R. W. Schnee. “Introduction to dark matter experiments”. In: *In Physics of the Large and Small: Proceedings of the 2009 Theoretical Advanced Study Institute in Elementary Particle Physics, 629-681 (World Scientific, Singapore) Ed. Csaba Csaki and Scott Dodelson (2010).*

2011. arXiv: 1101.5205 [astro-ph.CO]. URL: <https://inspirehep.net/record/885795/files/arXiv:1101.5205.pdf> (cit. on p. 12).
- [33] J. D. Lewin and P. F. Smith. “Review of mathematics, numerical factors, and corrections for dark matter experiments based on elastic nuclear recoil”. In: *Astropart. Phys.* 6 (1996), pp. 87–112. DOI: 10.1016/S0927-6505(96)00047-3 (cit. on p. 15).
- [34] J. Filippini. “A Search for WIMP Dark Matter Using the First Five-Tower Run of the Cryogenic Dark Matter Search”. PhD thesis. University of California, Berkeley, 2008 (cit. on p. 15).
- [35] David G. Cerdeno and Anne M. Green. “Direct detection of WIMPs”. In: *Particle Dark Matter: Observations, Models and Searches* (2010). arXiv: 1002.1912 [astro-ph.CO] (cit. on p. 15).
- [36] D. S. Akerib et al. “Improved Limits on Scattering of Weakly Interacting Massive Particles from Reanalysis of 2013 LUX Data”. In: *Phys. Rev. Lett.* 116.16 (2016), p. 161301. DOI: 10.1103/PhysRevLett.116.161301. arXiv: 1512.03506 [astro-ph.CO] (cit. on p. 16).
- [37] D. S. Akerib et al. “Results on the Spin-Dependent Scattering of Weakly Interacting Massive Particles on Nucleons from the Run 3 Data of the LUX Experiment”. In: *Phys. Rev. Lett.* 116.16 (2016), p. 161302. DOI: 10.1103/PhysRevLett.116.161302. arXiv: 1602.03489 [hep-ex] (cit. on p. 16).
- [38] Joseph A. Formaggio and C.J. Martoff. “BACKGROUNDS TO SENSITIVE EXPERIMENTS UNDERGROUND”. In: *Annual Review of Nuclear and Particle Science* 54.1 (2004), pp. 361–412. DOI: 10.1146/annurev.nucl.54.070103.181248. eprint: <http://dx.doi.org/10.1146/annurev.nucl.54.070103.181248>. URL: <http://dx.doi.org/10.1146/annurev.nucl.54.070103.181248> (cit. on p. 18).
- [39] Eric B. Norman, Timothy E. Chupp, Kevin T. Lesko, Peter Schwalbach, and Patrick J. Grant. “ $^{26g,m}\text{Al}$ production cross sections from the $^{23}\text{Na}(\alpha, n)^{26}\text{Al}$ reaction”. In: *Nuclear Physics A* 390.3 (1982), pp. 561–572. DOI: [http://dx.doi.org/10.1016/0375-9474\(82\)90283-4](http://dx.doi.org/10.1016/0375-9474(82)90283-4). URL: <http://www.sciencedirect.com/science/article/pii/0375947482902834> (cit.

- on p. 19).
- [40] Eric B. Norman, Timothy E. Chupp, Kevin T. Lesko, Patrick J. Grant, and Gene L. Woodruff. “ ^{22}Na production cross sections from the $^{19}\text{F}(\alpha, n)$ reaction”. In: *Phys. Rev. C* 30 (4 Oct. 1984), pp. 1339–1340. DOI: 10.1103/PhysRevC.30.1339. URL: <http://link.aps.org/doi/10.1103/PhysRevC.30.1339> (cit. on p. 19).
- [41] R. Heaton et al. “” In: *Nucl. Geophys.* V4 (1990), p. 499 (cit. on pp. 19, 20).
- [42] R. K. Heaton, H. W. Lee, B. C. Robertson, E. B. Norman, K. T. Lesko, and B. Sur. “ α -Particle induced high-energy γ -ray yields from light elements”. In: *Nuclear Instruments and Methods in Physics Research A* 364 (Feb. 1995), pp. 317–327. DOI: 10.1016/0168-9002(95)00220-0 (cit. on p. 19).
- [43] D.-M. Mei, C. Zhang, and A. Hime. “Evaluation of (α, n) Induced Neutrons as a Background for Dark Matter Experiments”. In: *Nucl. Instrum. Meth.* A606 (2009), pp. 651–660. DOI: 10.1016/j.nima.2009.04.032. arXiv: 0812.4307 [nucl-ex] (cit. on pp. 20, 21).
- [44] J. Koning, S. Hilaire, and M.C. Duijvestijn. “TALYS: comprehensive nuclear reaction modeling”. In: *Proceedings of the International Conference on Nuclear Data for Science and Technology-ND2004* 769 (2004), p. 1154 (cit. on p. 20).
- [45] Cross Section Evaluation Working Group. *ENDF/B-VI.8 Evaluated Nuclear Data Library*. URL: <http://www.nndc.bnl.gov/endl/b6.8/> (cit. on pp. 20, 40).
- [46] A.J. Koning and D. Rochman. “Modern Nuclear Data Evaluation with the TALYS Code System”. In: *Nuclear Data Sheets* 113.12 (2012), pp. 2841–2934. DOI: 10.1016/j.nds.2012.11.002. URL: <http://www.sciencedirect.com/science/article/pii/S0090375212000889> (cit. on p. 20).
- [47] W.B. Wilson, R.T. Perry, W.S. Charlton, and T.A. Parish. “Sources: A code for calculating (α, n) , spontaneous fission, and delayed neutron sources and spectra”. In: *Progress in Nuclear Energy* 51.4–5 (2009), pp. 608–613. DOI: 10.1016/j.pnucene.2008.11.007. URL: <http://www.sciencedirect.com/science/article/pii/S0149197008001418> (cit. on p. 20).

- [48] S. Scorza et al. “Radiogenic Neutron Code Comparison”. In: *Presentation on AARM Collaboration Meeting* (2015) (cit. on p. 21).
- [49] K. Palladino et al. “Comparison of Radiogenic Neutron Background Calculations”. In: *Presentation on Low Radioactivity Techniques* (2015) (cit. on p. 21).
- [50] Dongming Mei and A. Hime. “Muon-induced background study for underground laboratories”. In: *Phys. Rev. D* 73 (2006), p. 053004. DOI: 10.1103/PhysRevD.73.053004. arXiv: astro-ph/0512125 [astro-ph] (cit. on pp. 21–24, 147).
- [51] C.E. Aalseth et al. “The Majorana Experiment”. In: *Nuclear Physics B - Proceedings Supplements* 217.1 (2011), pp. 44–46. DOI: <http://dx.doi.org/10.1016/j.nuclphysbps.2011.04.063>. URL: <http://www.sciencedirect.com/science/article/pii/S0920563211003021> (cit. on p. 21).
- [52] Ernst-Ingo Esch, T. J. Bowles, A. Hime, A. Pichlmaier, R. Reifarth, and H. Wollnik. “The Cosmic ray muon flux at WIPP”. In: *Nucl. Instrum. Meth.* A538 (2005), pp. 516–525. DOI: 10.1016/j.nima.2004.09.005. arXiv: astro-ph/0408486 [astro-ph] (cit. on p. 23).
- [53] Sharmila Kamat. “Extending the Sensitivity to the Detection of WIMP dark matter with an improved understanding of the Limiting Neutron Backgrounds”. Internal Note. Case Western Reserve University, 2005 (cit. on pp. 23, 58).
- [54] M. Robinson, V. A. Kudryavtsev, R. Luscher, J. E. McMillan, P. K. Lightfoot, N. J. C. Spooner, N. J. T. Smith, and I. Liubarsky. “Measurements of muon flux at 1070 meters vertical depth in the Boulby underground laboratory”. In: *Nucl. Instrum. Meth.* A511 (2003), pp. 347–353. DOI: 10.1016/S0168-9002(03)01973-9. arXiv: hep-ex/0306014 [hep-ex] (cit. on p. 23).
- [55] A. McDolnd et al. “First Neutrino Observations from the Sudbury Neutrino Observatory”. In: *Proceedings of the XIX International Conference on Neutrino Physics & Astrophysics, Sudbury, Canada* (2000). URL: www.sno.phy.queensu.ca/sno/nu2000 (cit. on p. 23).
- [56] C. Zhang and D. -M. Mei. “Measuring Muon-Induced Neutrons with Liquid Scintillation Detector at Soudan Mine”. In: *Phys. Rev. D* 90.12 (2014), p. 122003. DOI: 10.1103/

- PhysRevD.90.122003. arXiv: 1407.3246 [physics.ins-det] (cit. on p. 25).
- [57] I. Abt et al. “The Muon-Induced Neutron Indirect Detection EXperiment, MINIDEX”. In: (2016). arXiv: 1610.01459 [physics.ins-det] (cit. on p. 25).
- [58] Raul Hennings-Yeomans and D. S. Akerib. “A Neutron Multiplicity Meter for Deep Underground Muon-Induced High Energy Neutron Measurements”. In: *Nucl. Instrum. Meth.* A574 (2007), pp. 89–97. DOI: 10.1016/j.nima.2007.01.137. arXiv: astro-ph/0611371 [astro-ph] (cit. on pp. 25, 27).
- [59] Atsuto Suzuki. “Antineutrino Science in KamLAND”. In: *Eur. Phys. J.* C74.10 (2014), p. 3094. DOI: 10.1140/epjc/s10052-014-3094-x. arXiv: 1409.4515 [hep-ex] (cit. on p. 29).
- [60] M. D. Sweany. “Characterization of Neutron Backgrounds for Direct Dark Matter Searches”. PhD thesis. University of California, Davis, 2011 (cit. on pp. 31, 36, 38, 79).
- [61] S. Agostinelli et al. “GEANT4: A Simulation toolkit”. In: *Nucl. Instrum. Meth.* A506 (2003), pp. 250–303. DOI: 10.1016/S0168-9002(03)01368-8 (cit. on p. 36).
- [62] J. Allison et al. “Geant4 developments and applications”. In: *IEEE Trans. Nucl. Sci.* 53 (2006), p. 270. DOI: 10.1109/TNS.2006.869826 (cit. on p. 36).
- [63] J. M. Quesada et al. “Recent Developments In Pre-Equilibrium and De-Excitation Models In Geant4”. In: *Progress in Nuclear Science and Technology* 2 (2011), pp. 936–941 (cit. on p. 40).
- [64] Geant4 Collaboration. *Geant4 9.5 Release Notes*. 2011. URL: <https://geant4.web.cern.ch/geant4/support/ReleaseNotes4.9.5.html> (visited on 12/02/2011) (cit. on p. 40).
- [65] Geant4 Collaboration. *Geant4 Neutron Data Library*. URL: http://geant4.cern.ch/support/datafiles_origin.shtml (cit. on p. 40).
- [66] L. M. Bollinger and G. E. Thomas. “Average-Resonance Method of Neutron-Capture gamma-Ray Spectroscopy: States of Pd-106 , Gd-156 , Gd-158 , Ho-166 , and Er-168”. In: *Phys. Rev.* C2 (1970), pp. 1951–2000. DOI: 10.1103/PhysRevC.2.1951 (cit. on pp. 40, 41).
- [67] P. Kandlakunta and L. Cao. “Gamma-ray rejection, or detection, with gadolinium as a

- converter”. In: *Radiation Protection Dosimetry* 151.3 (2012), pp. 586–590. DOI: 10.1093/rpd/ncs031 (cit. on pp. 40, 41).
- [68] V. A. Kudryavtsev. “Muon simulation codes MUSIC and MUSUN for underground physics”. In: *Comput. Phys. Commun.* 180 (2009), pp. 339–346. DOI: 10.1016/j.cpc.2008.10.013. arXiv: 0810.4635 [physics.comp-ph] (cit. on pp. 43, 58).
- [69] C. Nedlik. *Study of Preferred Afterpulsing Times*. Tech. rep. Syracuse University, Department of Physics, May 2013 (cit. on p. 43).
- [70] Donald E. Groom, Nikolai V. Mokhov, and Sergei I. Striganov. “Muon stopping power and range tables 10-MeV to 100-TeV”. In: *Atom. Data Nucl. Data Tabl.* 78 (2001), pp. 183–356. DOI: 10.1006/adnd.2001.0861 (cit. on p. 67).
- [71] Louis Lyons. *Statistics for Nuclear and Particle Physicists*. 1986 (cit. on pp. 90, 134).
- [72] C. Patrignani and Particle Data Group. “Review of Particle Physics”. In: *Chin. Phys.* C40.10 (2016), p. 100001. DOI: 10.1088/1674-1137/40/10/100001 (cit. on p. 134).
- [73] R. Agnese et al. “Projected Sensitivity of the SuperCDMS SNOLAB experiment”. In: *Submitted to: Phys. Rev. D* (2016). arXiv: 1610.00006 [physics.ins-det] (cit. on p. 151).
- [74] Alex Wright, Pablo Mosteiro, Ben Loer, and Frank Calaprice. “A Highly Efficient Neutron Veto for Dark Matter Experiments”. In: *Nucl. Instrum. Meth.* A644 (2011), pp. 18–26. DOI: 10.1016/j.nima.2011.04.009. arXiv: 1010.3609 [nucl-ex] (cit. on p. 152).
- [75] L. Swiderski, M. Moszynski, D. Wolski, T. Batsch, A. Nassalski, A. Syntfeld-Kazuch, T. Szczesniak, F. Kniest, M. R. Kusner, G. Pausch, J. Stein, and W. Klamra. “Boron-10 Loaded BC523A Liquid Scintillator for Neutron Detection in the Border Monitoring”. In: *IEEE Transactions on Nuclear Science* 55.6 (Dec. 2008), pp. 3710–3716. DOI: 10.1109/TNS.2008.2006172 (cit. on pp. 152, 153).
- [76] Yi-Fen Yen, J.D. Bowman, R.D. Bolton, B.E. Crawford, P.P.J. Delheij, G.W. Hart, T. Haseyama, C.M. Frankle, M. Iinuma, J.N. Knudson, A. Masaike, Y. Masuda, Y. Matsuda, G.E. Mitchell, S.I. Penttilä, N.R. Roberson, S.J. Seestrom, E. Sharapov, H.M. Shimizu, D.A. Smith, S.L. Stephenson, J.J. Szymanski, S.H. Yoo, and V.W. Yuan. “A high-rate 10B-

- loaded liquid scintillation detector for parity-violation studies in neutron resonances”. In: *Nuclear Instruments and Methods in Physics Research Section A: Accelerators, Spectrometers, Detectors and Associated Equipment* 447.3 (2000), pp. 476–489. DOI: [http://dx.doi.org/10.1016/S0168-9002\(99\)01308-X](http://dx.doi.org/10.1016/S0168-9002(99)01308-X). URL: <http://www.sciencedirect.com/science/article/pii/S016890029901308X> (cit. on p. 153).
- [77] Xu Liu. “Experiments and Monte Carlo Analysis for the Optical Properties of the Scintillator in SNO+”. Master Thesis. Queens University, 2010 (cit. on p. 159).
- [78] M. Janecek and W. W. Moses. “Simulating Scintillator Light Collection Using Measured Optical Reflectance”. In: *IEEE Transactions on Nuclear Science* 57.3 (June 2010), pp. 964–970. DOI: 10.1109/TNS.2010.2042731 (cit. on p. 160).

Vita

Author's Name: Yu Chen
Place of Birth: Hohhot, Inner Mongolia, China
Date of Birth: Sept. 1, 1983

Degrees Awarded:

Master of Science, Beijing Normal University, 2009
Bachelor of Science, Beijing Institute of Technology, 2006

Professional Experience:

Research Assistant, Syracuse University Department of Physics, 2011-2016
SuperCDMS Collaboration, 2012-2016
MiniCLEAN Collaboration, 2011-2012
Teaching Assistant, Syracuse University Department of Physics, 2009-2011